UNIVERSIDADE DE SÃO PAULO
INSTITUTO DE FÍSICA DE SÃO CARLOS

Rodrigo Guedes Lang

Phenomenology of the propagation of astroparticles: Lorentz invariance violation and the origin of ultra-high energy cosmic rays

São Carlos

2020

Rodrigo Guedes Lang

Phenomenology of the propagation of astroparticles: Lorentz invariance violation and the origin of ultra-high energy cosmic rays

Thesis presented to the Graduate Program in Physics at the Instituto de Física de São Carlos, Universidade de São Paulo, to obtain the degree of Doctor in Science.

Concentration area: Theoretical and Experimental Physics

Supervisor: Prof. Dr. Luiz Vitor de Souza Filho

Corrected version
(Original version available on the Program Unit)

São Carlos
2020

I AUTHORIZE THE REPRODUCTION AND DISSEMINATION OF TOTAL OR PARTIAL COPIES OF THIS DOCUMENT, BY CONVENTIONAL OR ELECTRONIC MEDIA FOR STUDY OR RESEARCH PURPOSE, SINCE IT IS REFERENCED.

Lang, Rodrigo Guedes
Phenomenology of the propagation of astroparticles: Lorentz invariance violation and the origin of ultra-high energy cosmic rays / Rodrigo Guedes Lang; advisor Luiz Vitor de Souza Filho - corrected version -- São Carlos 2020.
138 p.

Thesis (Doctorate - Graduate Program in Theoretical and Experimental Physics) -- Instituto de Física de São Carlos, Universidade de São Paulo - Brasil , 2020.

1. UHECR. 2. Gamma rays. 3. Lorentz invariance violation. 4. UHECR sources. 5. Anisotropy. I. Souza Filho, Luiz Vitor de, advisor. II. Title.

ACKNOWLEDGEMENTS

This is a scientific thesis. Science, however, is done by people and a person can only be as good as the people in their life. I am lucky to have had numerous great people who directly or indirectly influenced my life and my work so far. I am very thankful to each and every one of them and acknowledge here some of those:

- Above all, my family, who is by far the main foundation behind my achievements. In particular, my parents, Marisa and Hilton, and my brother, Rafael. Ever since I can remember, I have always been encouraged to keep feeding my curiosity and desire to understand things, while still being remembered to enjoy life and do my best to make the lives of people around me better. I am privileged to have a supportive family and I am sure that any personal or professional accomplishments in my life were only possible because they never hesitated to instigate me not to be afraid of being myself and keep following my dreams;
- Vitor, who has guided me through the ways of science for the last 9 years, trusting me and trying to find the paths for me to achieve my best potential. I am lucky that, in a system in which many students are treated as gears in machinery, I was advised by someone who looks at his students as people with their own history and a long future ahead;
- Andrew, who has taught me to look at physics with different eyes and allowed me to open many doors to the unknowns of the Universe;
- São Carlos Astrophysics Group, the best astrophysics group in the whole universe. I doubt that I will ever again find such a fantastic and heart-warming work environment and I am sure that in the last 9 years I wasn't working with colleagues, but with friends that I have made for life. Between the many who have come and gone, leaving their mark on the group, I would like to point three who were essential:
    - Humberto, who has contributed to this thesis with much more than just being our main scientific collaborator, but with being a close friend;
    - Raul, who since the beginning has been of my main role models in astrophysics and who has helped me through a lot more than just work;
    - Pedro, the brother (a younger one, for sure) that astrophysics has gifted me with;
- My friends, of whom I am very proud and who have always lifted me up and made my life light and easy. In special, I would like to thank:

  - Karen, who has taught me (and made me promise never to forget) that before the physicist comes the human being, and before dealing with numbers and data, we will always be dealing with people with emotions and feelings;
  - AdS (and aggregates), who have been crucial in shaping the adult version of myself and who became my family in a new city (and now spread all over the world), making me feel like I have never left home;
  - My friends from TdR, with whom I have now spent (at least) half of my life and became an indissociable part of who I am;
  - Gamma, who won't be able to read this, but has always been on my side and helped me through every day;
- Every teacher and professor that I have had in my life. You have the most important profession of humanity and if I came all the way until here is because I was taught by fantastic people who only made my curiosity and interest in understanding the Universe grow;
- All the staff from IFSC, who has always been extremely competent and hardworking, making life at the institute much easier for many of us;
- DESY-Zeuthen, who has provided me with a first-class infrastructure for developing my work while visiting them. In special, the theory group, in which I was much welcomed and learned a lot;
- The population of Brazil and of the state of São Paulo, who made this work possible through:
  - Fundação de Amparo à Pesquisa do Estado de São Paulo (FAPESP), through grants No.2015/15897-1, No. 2016/24943-0 and No. 2019/01653-4;
  - Conselho Nacional de Desenvolvimento Científico e Tecnológico (CNPq);
  - National Laboratory for Scientific Computing (LNCC/MCTI, Brazil) for providing HPC resources of the SDumont supercomputer, which have contributed to the research results reported within this paper.

“I’m doing science and I’m still alive”
GLaDOS - Aperture Science

ABSTRACT

LANG, R. G. **Phenomenology of the propagation of astroparticles:** Lorentz invariance violation and the origin of ultra-high energy cosmic rays. 2020. 138p. Thesis (Doctor in Science) - Instituto de Física de São Carlos, Universidade de São Paulo, São Carlos, 2020.

In this thesis, we use a phenomenological approach to the propagation of astroparticles in order to study two relevant topics in astrophysics: Lorentz invariance violation (LIV) and the origin of ultra-high energy cosmic rays (UHECR). Lorentz invariance is proposed as a fundamental symmetry of nature according to relativity. However, quantum gravity models assume or accommodate some level of LIV. We present a broad study of the potential of testing LIV with different data sets and experiments in astroparticle physics. Novel techniques are proposed for testing LIV using TeV gamma-ray and UHECR data, in special using data from Imaging Air Cherenkov Telescopes and the Pierre Auger Observatory. No signature of LIV is found and restraining limits are imposed. We present a review of the most common astrophysical tests and a compilation of the currently most restrictive limits of LIV. We also address the long-lasting question about the origin of UHECR. CR are charged particles and, thus, magnetic fields mask the information about the position of their sources. We study how the energy spectrum, composition and distribution of arrival directions can be used to retrieve information about the source distribution. Constraints on the maximum distance of the nearest UHECR source are imposed. We study the arising of a large-scale anisotropy in the form of a dipole measured by the Pierre Auger Observatory and build an understanding of the evolution with energy of the dipole strength.

Keywords: UHECR. Gamma rays. Lorentz invariance violation. UHECR sources. Anisotropy.

RESUMO

LANG, R. G. **Fenomenologia da propagação de astropartículas:** violação da invariância de Lorentz e a origem de raios de cósmicos de altíssima energia. 2020. 138p. Tese (Doutor em Ciências) - Instituto de Física de São Carlos, Universidade de São Paulo, São Carlos, 2020.

Nesta tese, nós usamos um tratamento fenomenológico para a propagação de astropartículas com o intuito de estudar dois relevantes tópicos em astrofísica: violação da invariância de Lorentz (LIV, do inglês *Lorentz invariance violation*) e a origem de raios cósmicos de altíssima energia (UHECR, do inglês *ultra-high energy cosmic rays*). Em relatividade, a invariância de Lorentz é proposta como uma simetria fundamental da natureza. Todavia, modelos de gravitação quântica assumem ou acomodam um certo nível de LIV. Nós apresentamos um amplo estudo do potencial de se testar LIV com diferentes conjuntos de dados e experimentos em astrofísica de partículas. Técnicas inovadoras são propostas para testar LIV usando raios gama com energia da ordem de TeV e UHECR, em especial usando dados de telescópios atmosféricos de Cherenkov e do Observatório Pierre Auger. Nenhum sinal de LIV é encontrado e limites restritivos são impostos. Nós apresentamos uma revisão dos testes de LIV mais comuns em astrofísica de partículas e uma coleção dos limites de LIV mais restritivos da atualidade. Nós também tratamos a questão sobre a origem dos UHECR. Raios cósmicos são partículas carregadas e, portanto, campos magnéticos mascaram a informação sobre a posição de suas fontes. Nós estudamos como o espectro de energia, a composição e a distribuição de direções de chegada podem ser usados para recuperar a informação sobre a distribuição de fontes. Restrições na máxima distância da fonte mais próxima de UHECR são impostas. Nós estudamos o surgimento de uma anisotropia de larga escala na forma de um dipolo medida pelo Observatório Pierre Auger e desenvolvemos um entendimento da evolução com energia da intensidade desse dipolo.

Palavras-chave: Raios cósmicos de altíssima energia. Raios gama. Violação da invariância de Lorentz. Fontes de raios cósmicos de altíssima energia. Anisotropia.

LIST OF FIGURES

Figure 1.1 – Compilation of the energy spectrum of astroparticles measured by several experiments in the past decades. 20

Figure 2.1 – Hillas plot. Possible cosmic ray sources (shaded area) are compared with relation to their magnetic field strength and size. The lines show the combination of B and Γ needed to accelerate a cosmic up to $E = 10^{20}$ eV. 24

Figure 2.2 – Energy loss length as a function of the energy for several interactions of UHECR with the photon background. Dashed and continuous lines show, respectively, the losses for a proton and a nucleus of iron. The gray shaded area shows the region for energy losses larger than the Hubble horizon. 25

Figure 2.3 – Parametrization of the EBL distribution as a function of the background photon wavelength. Each color represents a different EBL model. . . . 26

Figure 2.4 – Design of the Pierre Auger Observatory. Each red dot represents one water Cherenkov tank that composes the surface detector, while the green lines show the field of view of the fluorescence telescopes that compose the fluorescence detector. 28

Figure 2.5 – Compilation of the cosmic ray energy spectrum measured by several experiments. 30

Figure 2.6 – UHECR cosmic ray energy spectrum measured by the Pierre Auger Observatory. The red line shows a fit of the spectrum using a broken power law. The spectral indexes for each region are highlighted. 31

Figure 2.7 – X_{max} distribution for two different compositions. On the left panel, a mixed composition with proton and nitrogen is considered. On the right panel, on the other hand, a mixed composition with proton, helium and iron is considered. The black lines show the total X_{max} distribution for that given composition, while the colored lines show the contribution from each species. 32

Figure 2.8 – First two moments of the X_{max} distribution measured by the Pierre Auger Observatory. The black points represent the experimental data, the black line and square brackets represent, respectively, the statistical and systematic uncertainties. The red and blue lines show the predicted moment for a pure composition of proton and iron, respectively. Three different hadronic interaction models are considered. 33

Figure 2.9 – Large-scale anisotropy dipole measured by the Pierre Auger Observatory. The left panel shows the normalized angular distribution as a function of right ascension, where the thick black line shows a fit function that follows $1 + \delta_\alpha \cos\theta$. The right panel shows the skymap with the normalized flux as a function of the arrival direction in equatorial coordinates. The black star and dashed line shows the galactic center and plane, respectively. 34

Figure 2.10–Evolution of the dipole in right ascension with energy. The left and right panel show, respectively, the dipole amplitude and phase. The gray shaded area shows the results for the large-scale anisotropy dipole for $E > 8$ EeV. 35

Figure 2.11–Upper limits on the flux of neutral particles. The left and right panels show, respectively, the neutrino and photons limits. Shaded areas show the prediction for the fluxes of secondary particles emitted in the GZK effect. The dashed lines on the right panel show the prediction by top-down models. 36

Figure 2.12–Optical depth as a function of the energy. Each of the lines shows the results for different survival probabilities. From bottom to top: e^{-1}, e^{-2}, e^{-3}, and $e^{-4.6}$. 37

Figure 2.13–Mean free path of the pair production as a function of the energy. The labels a, b and c represent different EBL models, while the labels 1, 2 and 3 represent different frequency cutoffs in the radio background. . . 38

Figure 2.14–Differential sensitivity as a function of the energy. Each colored line represents a different experiment/observation time. It is noteworthy that the curve only shows an indication and not a real comparison between different instruments, as the method of calculation and selection criteria are different. 40

Figure 2.15–Angular resolution as a funcion of the energy for 68% containment. Different lines represent different experiments. The expect sensitivity for CTA North is similar to that of CTA South. 41

Figure 6.1 – Attenuation as function of the energy. Each colored line represents a different EBL model, and each panel represents a different redshift. . . 67

Figure 6.2 – Attenuation as function of the energy for the Dominguez EBL model considering LIV for $n = 1$. The dark continuous line represents the LI case. Each colored dashed line represents the attenuation for a different LIV energy scale, and each panel represents a different redshift. 68

Figure 6.3 – Energy spectrum for Mrk 501. The black and red continuous lines represent, respectively, the intrinsic and attenuated LI spectrum. The different dashed lines represent the attenuated spectra considering several LIV energy scales for $n = 1$. The left and the right panel show the spectra using $E_{\text{cut}} = 20$ TeV and $E_{\text{cut}} = 40$ TeV, respectively. The Dominguez model was used for the EBL. 70

Figure 6.4 – Same as fig. 6.3, but for 1ES 0229+200. 70

Figure 6.5 – Simulated detected energy spectrum for Mrk 501 in a LI scenario. The continuous line represents the intrinsic spectrum, and the dashed line represents the predicted attenuated spectrum. The black and red points represent the simulated data for CTA using GammaPy and ctools, respectively. The left and right panels show the cases for $E_{\text{cut}} = 20$ TeV and $E_{\text{cut}} = 40$ TeV, respectively. 71

Figure 6.6 – Same as fig. 6.5, but for a LIV scenario with $E_{\text{LIV}}^{(1)} = 10^{28}$ eV. 71

Figure 6.7 – Same as fig. 6.5, but for 1ES 0229+200. 72

Figure 6.8 – Same as fig. 6.5, but for 1ES 0229+200 in a LIV scenario with $E_{\text{LIV}}^{(1)} = 10^{28}$ eV. 72

Figure 6.9 – Log-likelihood profile as a function of the energy. The red and blue lines show the results for Mrk 501 with $E_{\text{cut}} = 20$ TeV and $E_{\text{cut}} = 40$ TeV, respectively. The gray dashed lines show the difference in the log-likelihood values for 2, 3 and 5σ CL. The black arrows show recent limits for Mrk 501 from H.E.S.S. 74

Figure 7.1 – Simulated integral flux of GZK photons. The arrows show the upper limits on the flux imposed by the Pierre Auger Observatory. Continuous lines show the flux for the rejected LIV scenarios. Dashed lines show the flux for the scenarios in which the data is insensitive to LIV. A pure proton composition is considered. The considered spectral parameters are $\Gamma = 2.3$ and $R_{\text{cut}} = 10^{19.8}$ V 76

Figure 7.2 – Limits on the LIV coefficient as a function of the assumed spectral parameters. The colored areas represent the region of the parameter space that results in the same limit. The left-most region is insensitive to LIV, while the right-most region is reject even in a LI scenario. A pure-proton composition and no evolution of the sources is considered in this example. 77

Figure 7.3 – Same as figure 7.1, but for the mixed composition. 78

Figure 7.4 – Attenuation length for the pion production as a function of the energy. The black line and the blues lines show the results for the LI and various LIV scenarios, respectively. Scenarios with $> 10^{-21}$ result in attenuation lengths larger than 10^5 Mpc for all the considered energies and, thus, are not shown in the plot. 79

Figure 7.5 – Energy threshold in the NRF for the photodisintegration as a function of the energy. The black and blue lines show the results for the LI and various LIV scenarios, respectively. The left and right panels are respectively for a nucleus of helium and iron. 79

Figure 7.6 – Evolution of the fit parameters with respect to the LIV coefficient. The left and right panels show the spectral index and the rigidity cutoff, respectively. Each shade of green represents a different source evolution scenario with $(1 + z)^m$. 81

Figure 7.7 – Evolution of the deviance with respect to the LIV coefficient. The top panel shows the total deviance, while the bottom panel shows the difference in the deviation relative to the LI case. The dashed horizontal lines show the 3σ and 5σ confidence level. Each shade of green represents a different source evolution scenario with $(1 + z)^m$. 82

Figure 7.8 – Evolution of the fit parameters with respect to the LIV coefficient. Each line represents a different combination of astrophysical models. The panels shows the spectral index, rigidity cutoff and integral primary fractions at the source, respectively. The integral primary fractions are for the SPGE model. 83

Figure 7.9 – Evolution of the deviance with respect to the LIV coefficient. Each line represents a different combination of astrophysical models. The top panel shows the total deviance, while the bottom panel shows the difference in the deviation relative to the LI case. The dashed horizontal lines show the 3σ and 5σ confidence level. 84

LIST OF TABLES

Table 6.1 – Spectral parameters considered for the sources. 69
Table 6.2 – Estimated confidence levels for detecting LIV with $E_{\text{LIV}}^{(1)} = 10^{28}$ eV. 73
Table 6.3 – Estimated limits on the LIV energy scale to be imposed by CTA. The limits imposed by H.E.S.S. on Mrk 501 are shown for comparison. 73
Table 7.1 – Combination of astrophysical models considered in this work. 80
Table 7.2 – LIV coefficients that best describe the data for each combination of models. The confidence level is given by $\sigma = \sqrt{D_{\text{LI}} - D}$. 82

CONTENTS

1 INTRODUCTION 19

2 OVERVIEW OF UHE COSMIC RAYS AND VHE GAMMA-RAYS . 23
2.1 UHECR 23
2.1.1 Acceleration 23
2.1.2 Propagation 24
2.1.2.1 Photon background 25
2.1.2.2 Interactions 26
2.1.3 Detection 27
2.1.3.1 Pierre Auger Observatory 27
2.1.3.2 Observables 29
2.1.3.2.1 Energy spectrum 29
2.1.3.2.2 Mass composition 30
2.1.3.2.3 Arrival directions 34
2.1.3.2.4 Upper limits on the flux of neutral particles 35
2.1.4 Open questions 36
2.2 VHE gamma-rays 37
2.2.1 Propagation 37
2.2.2 IACTs and CTA 39

3 LORENTZ INVARIANCE VIOLATION 43

4 LIMITS ON THE LORENTZ INVARIANCE VIOLATION FROM UHECR ASTROPHYSICS 45

5 IMPROVED LIMITS ON LORENTZ INVARIANCE VIOLATION FROM ASTROPHYSICAL GAMMA-RAY SOURCES 57

6 ESTIMATING THE POTENTIAL OF TESTING LIV USING CTA . 67
6.1 Simulation packages 69
6.2 Capability of detecting LIV effects of the same order of current limits 71
6.3 Capability of improving current LIV limits 73

7 TESTING LORENTZ INVARIANCE VIOLATION AT THE PIERRE AUGER OBSERVATORY 75
7.1 Electromagnetic sector 75
7.1.1 Pure-proton composition benchmark 75

7.1.1.1 Mixed composition . . . 77
7.2 Hadronic sector . . . 77
7.2.1 Combined fit of the spectrum and composition under LIV assumptions . . . 80
7.2.1.1 Pure-proton composition benchmark . . . 80
7.2.2 Mixed composition . . . 81

8 LORENTZ INVARIANCE VIOLATION TESTS IN ASTROPARTICLE PHYSICS . . . 85

9 ORIGIN OF UHECR . . . 97

10 REVISITING THE DISTANCE TO THE NEAREST ULTRAHIGH ENERGY COSMIC RAY SOURCE: EFFECTS OF EXTRAGALACTIC MAGNETIC FIELDS . . . 99

11 ULTRAHIGH-ENERGY DIPOLE AND BEYOND . . . 111

12 CONCLUSIONS . . . 125

REFERENCES . . . 129

1 INTRODUCTION

During the years of 1912 and 1913, Austrian physicist Victor Franz Hess (1883-1964) undertook a series of balloon flights going as high as 5 km aiming to decipher the origin of the ionizing radiation measured in the atmosphere by physicists at that time. He has shown that the level of ionization would increase substantially above 1 km reaching at 5 km twice the level observed at sea level (1), which hinted for an extra-terrestrial origin of such radiation. This result was later confirmed in studies by Robert Andrew Millikan (1868-1953) in the 20s, who then coined the term *cosmic rays.* (2) Hess was awarded with the Nobel Prize in Physics in 1936.

A decade later, the understanding of this radiation was further improved when Pierre Victor Auger (1899-1993) detected cosmic radiation events coincident in time but separated by some distance on the surface. He proposed these to be associated with the same initial event, due to the formation of an atmospheric cascade of particles, i.e., the initial particle would collide with a nucleus of the atmosphere, generating a cascade of secondary particles. (3) This cascade effect was later named extensive air-shower (EAS).

Before the advent of human-made accelerators, cosmic rays were the main source for studying elementary particles, which is exemplified by the discovery of the positron in 1932 (4), the muon in 1936 (5,6), and the pion in 1947. (7,8) Nowadays, it is known that these air-showers are formed due to Earth being constantly hit by energetic particles of extra-terrestrial origin. These astroparticles are diverse, being composed mostly of ionized nuclei, photons, electrons, neutrinos, positrons, and anti-nuclei. Throughout this work, the term *cosmic rays* will only be used for charged particles, i.e., ionized nuclei and electrons and their antiparticles, whilst the term *astroparticles* will be used in a more generic way, referring to any kind of extra-terrestrial particle.

The energy spectrum of astroparticles covers a wide range, from a few MeV up to hundreds of EeV, and follows, in a first-order approximation, a power law, decreasing with energy as shown in figure 1.1. The most energetic events detected, with a few hundreds of EeV, are the most energetic known particles in the universe, with energies about seven orders of magnitude higher than those accelerated in the largest human-built accelerator, the Large Hadron Collider (LHC)[*].

---

[*] The comparison with LHC can be done in two forms. When analysing the acceleration power between the sources of UHECR and LHC, the laboratory reference frame (RF) is suitable and a difference of seven orders of magnitude is found (10^{20} eV/10^{13} eV). However, when studying particle physics, it is more appropriate to look at the center-of-mass RF energy. In order to do so, the center-of-mass RF energy of the astroparticle is obtained by considering an interaction between it and an average nucleus of the atmosphere, leading to a difference of around two orders of magnitude.

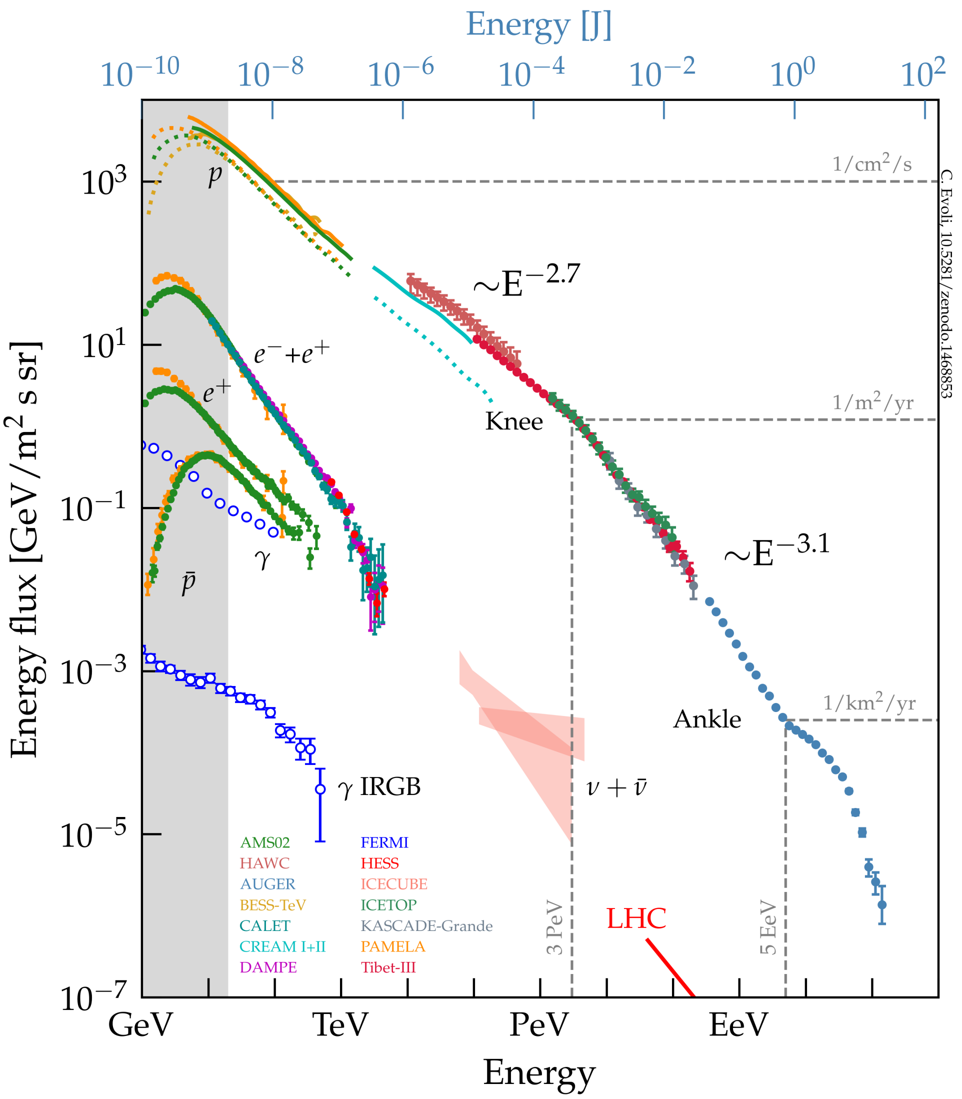

Figure 1.1 – Compilation of the energy spectrum of astroparticles measured by several experiments in the past decades.

Source: EVOLI. (9)

Currently, astroparticle physics has reached unprecedented precision with the advent of complex experiments and large international collaborations of scientists. The wide range of energy and flux intensity, as well as diversity of particles require the use of different experimental techniques and data analysis methods.

For energies up to a few hundreds of GeV, the flux is intense enough so that experiments with an effective area of a few square meters can measure a number of events sufficient to obtain reliable statistics. In this energy range, the most common technique is to use particle detectors on balloon flights or orbital satellites and, in this way, detect the primary astroparticle. The list of major experiments in this range includes PAMELA (10) and AMS-02 (11), satellite cosmic ray detectors, CREAM (12), a cosmic ray detector in balloon flights, and the Fermi-LAT experiment (13), an orbital satellite to study gamma-rays.

For higher energies, the flux intensity drops to a level which requires experiments with an effective area of hundreds or thousands of square kilometers. This is achieved by using ground-based experiments which detect the secondary particles of EAS. Among the most prominent experiments in this energy range are the IceCube Neutrino Observatory (14), a 1 km^3 neutrino detector inside the Antarctic polar ice, the current generation of imaging air Cherenkov telescopes (IACTs), built to detect gamma-rays in the region of hundreds of GeV to tens of TeV, composed of H.E.S.S. (15), VERITAS (16) and MAGIC (17), the HAWC observatory (18), a wide field of view gamma-ray and cosmic rays detector at the TeV region, and the ultra-high energy cosmic rays (UHECR, $E > 10^{18}$ eV) detectors, Pierre Auger Observatory (19) and Telescope Array. (20)

The Pierre Auger Observatory and the next generation of IACTs, the Cherenkov Telescope Array (CTA) (21) as well as the most important results and open questions in UHECRs and TeV gamma-ray astronomy are discussed in more detail in Chapter 2.

Astroparticles have played and still play a crucial role in science, being an important tool for studying astrophysics, astronomy, cosmology, particle physics and even fundamental physics. A few examples of the multi-disciplinary potential of astroparticles include the search for dark matter signatures (22), a multi-messenger detection of events from a neutron star merger (23, 24), including gravitational waves, gamma-rays and neutrinos, and the extension of hadronic interactions models for energies above the LHC range. (25)

In this work, the phenomenology of the propagation of astroparticles is used to study two paramount questions in fundamental physics and astroparticle physics.

First, we discuss the possibility of using astroparticles to test the validity of relativity, due to their high energies and long travel distances. This is done by searching for imprints of Lorentz invariance violation (LIV) in current TeV gamma-ray and UHECR data. LIV and the most important astrophysical tests of it are discussed in Chapter 3. The results obtained in this work regarding LIV are shown in Chapters 6 and 7 and in the form of published articles in Chapters 4, 5, and 8.

Then, we discuss the origin of UHECRs, which remains an open question a century after their discovery. UHECR are charged and, consequently, deviated in the presence of galactic and extra-galactic magnetic fields. Therefore, the CR arrival direction does not necessarily point back to its source. Nevertheless, some residual information is still present, and combining good statistics of data with refined analysis methods may help unveil this question. This problem is discussed in more detail in Chapter 9 and the results obtained in this work are shown in the form of published articles in Chapters 10 and 11.

Finally, the conclusions of this work are addressed in Chapter 12.

2 OVERVIEW OF UHE COSMIC RAYS AND VHE GAMMA-RAYS

As discussed in Chapter 1, astroparticles are diverse in their species and energies and, consequently, so is the case for their detection techniques. In this work, we are mostly interested in ultra-high energy ($E > 10^{18}$ eV) cosmic rays and very-high energy ($10^{11} \lesssim E \lesssim 10^{14}$ eV) gamma-rays. In this chapter, we give an overview of the major results in these two fields as well as the two experiments most used in this work, the Pierre Auger Observatory and the Cherenkov Telescope Array.

2.1 UHECR

2.1.1 Acceleration

The power-law dependency of the cosmic ray energy spectrum and the high energies reached by them are an indication of a non-thermal acceleration process. Historically, two classes of models were proposed to explain this: top-down models, which explained cosmic rays as a product of the decay of more energetic exotic particles, such as topological defects from the early Universe (26, 27), and bottom-up models, in which cosmic rays were accelerated from lower energies up to the highest energies.

The top-down models, however, predict a very intense flux of ultra-high energy photons, which has already been ruled out by upper limits on the photon flux imposed by the Pierre Auger Observatory, as discussed in the next sections.

The bottom-up models, on the other hand, are mostly stochastic models, in which charged particles are accelerated to ultra-high energies in magnetized regions. The first idea was suggested by Fermi in 1949 (28) and proposed that charged particles would randomly collide with moving magnetized clouds. The probability of a head-on collision was estimated to be higher, leading to an average energy gain of $\Delta E/E \sim \beta^2 = (v/c)^2$. This was called the second-order Fermi mechanism. Even though a power-law emission is predicted from it, the efficiency of the process is too low and could not describe the density of cosmic rays considering realistic acceleration times.

Later, a second mechanism was proposed, which considered charged particles colliding with multiple shock waves and being accelerated by irregularities on the fields. (29–32) The average energy gain was estimated to be $\Delta E/E \sim \beta$ and, consequently, it was named first-order Fermi mechanism. Its efficiency is higher than that predicted by the second-order mechanism and a power-law emission is also derived. A spectral index of $\Gamma = 2 - 2.3$ is expected. Both mechanisms may be present depending on energy and source type.

As discussed in the next sections, the sources of cosmic rays remain unknown due to their deviation in magnetic fields. A first-order estimation of the maximum power of acceleration, however, can be done by comparing the Larmor radius of a particle in a given magnetic field to the extension of a given source. This was first proposed by Hillas (33) and the plot illustrating this is named Hillas plot after him. Figure 2.1 shows the Hillas plot for 100 EeV protons and iron nuclei. While this approximation show a necessary feature of the source, it is not sufficient, since energy losses in the region must also be taken into account.

While supernova remnants (SNR) seem to be a suitable candidate for galactic sources (34, 35), the extra-galactic sources remain an open question. A few objects can fulfill the criteria, such as starburst galaxies, active galactic nuclei (AGN), gamma-ray bursts (GRB) and neutron stars. Chapters 9-11 discuss analysis methods that may help unveil this mystery.

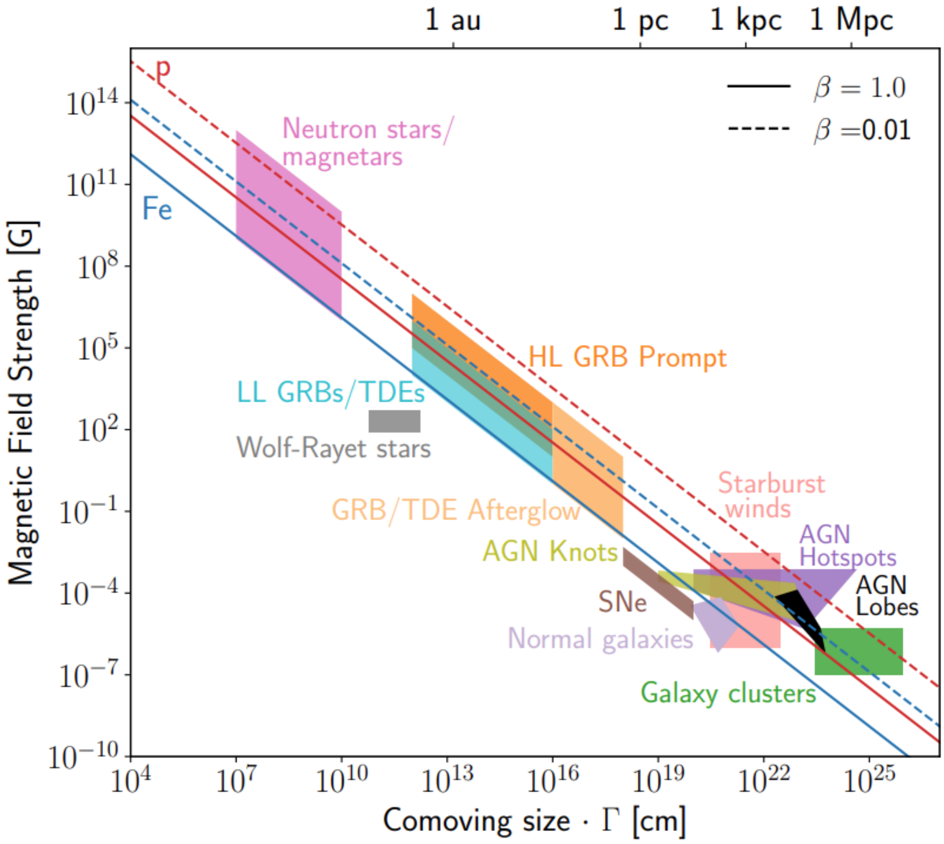

Figure 2.1 – Hillas plot. Possible cosmic ray sources (shaded area) are compared with relation to their magnetic field strength and size. The lines show the combination of B and Γ needed to accelerate a cosmic up to $E = 10^{20}$ eV.

Source: ALVES BATISTA *et al.* (25)

2.1.2 Propagation

Propagating UHECR interact with the photon background, leading to energy-dependent energy losses, which impacts directly the arriving spectrum and composition. (36,

37) Four main processes are present: adiabatic loss (which is not related to interactions with the photon background), pair production, photo-pion production, and photodisintegration. The energy loss of each process for a proton and a nucleus of iron is shown in figure 2.2. Adiabatic losses occur due to the expansion of the universe and affect equally all particles at all energies, being thus the one with less impact on the arriving spectrum.

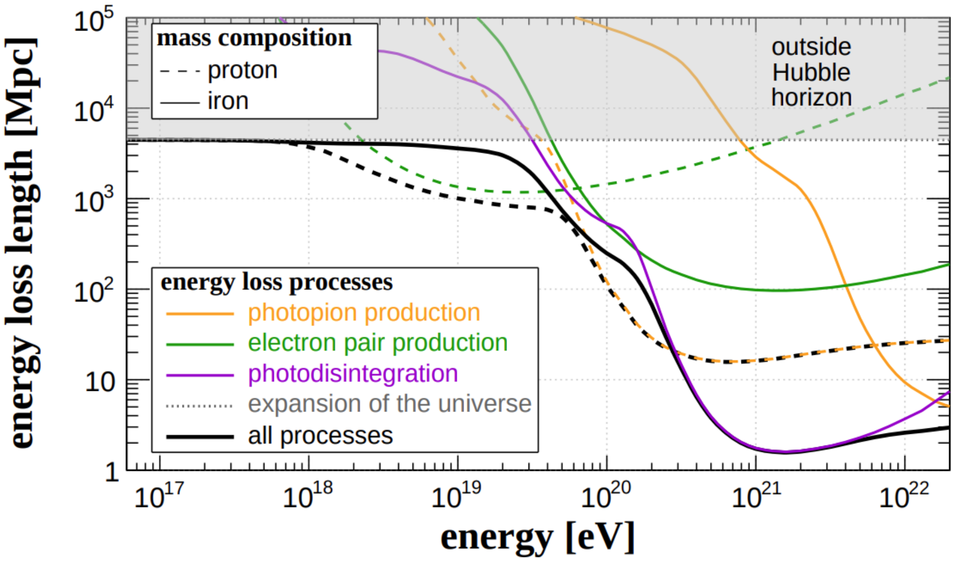

Figure 2.2 – Energy loss length as a function of the energy for several interactions of UHECR with the photon background. Dashed and continuous lines show, respectively, the losses for a proton and a nucleus of iron. The gray shaded area shows the region for energy losses larger than the Hubble horizon.

Source: ALVES BATISTA. (38)

2.1.2.1 Photon background

Photons in a wide energy range populate the universe. Propagating cosmic rays interact with them, which leads to energy loses and shapes the arriving spectrum and composition.

The most abundant photon background is the cosmic microwave background (CMB). Firstly predicted in 1948 (39, 40) and later detected in 1965 (41), it was formed when matter and radiation decoupled in the early stages of the universe and, consequently, contains important pieces of information about its early stages. It is now measured with very high precision and its density can be described by a Planck distribution with $T = (2.7255 \pm 0.0006)$ K. (42)

More energetic photons ($0.01 \lesssim E/\text{eV} \lesssim 1$) form the extra-galactic background light, related to the formation of stars and galaxies. (43) Obtained by modelling the evolution and luminosity of galaxies as well as the presence of dust, the EBL distribution contains many sources of uncertainties. Several competitive models in the literature propose a parametrization for its distribution. (44–49) Some of them are compared in figure 2.3.

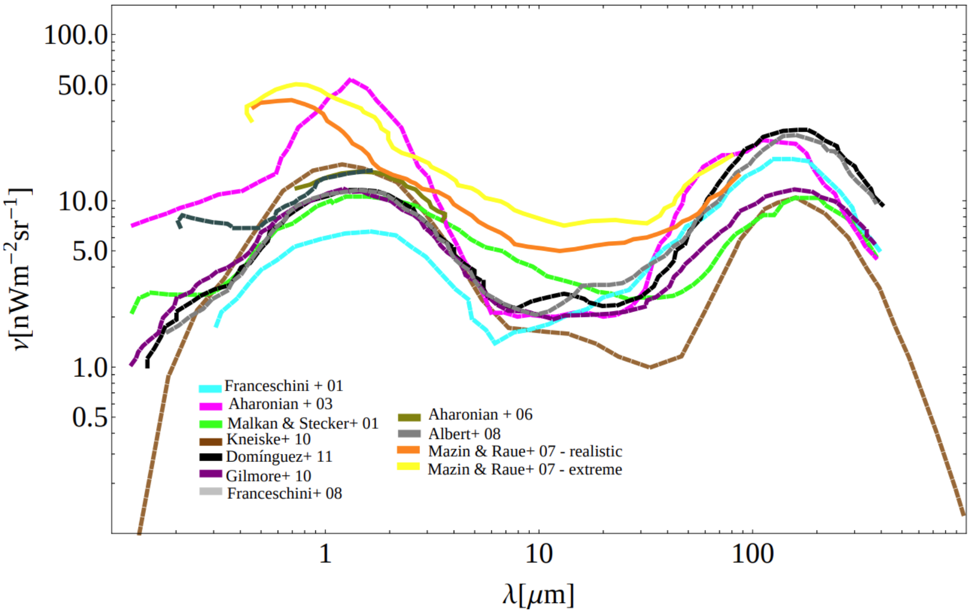

Figure 2.3 – Parametrization of the EBL distribution as a function of the background photon wavelength. Each color represents a different EBL model.

Source: DOS ANJOS. (50)

Finally, for the lower energies, radio background coming from a diffuse background of radio extra-galactic sources is present. It is usually parametrized as a Planck distribution with an effective temperature which depends on the frequency. (51) A cutoff in frequency is also sometimes considered. Even though this background does not play a role in the propagation of UHECR, it is significant for the propagation on UHE photons as discussed later in this chapter.

2.1.2.2 Interactions

For protons, the main energy losses are pair production for $E \lesssim 10^{19.5}$ eV and photo-pion production for $E \gtrsim 10^{19.5}$ eV. For the former, the proton interacts with the photon background, emitting an electron-positron pair and, consequently, losing energy ($p+\gamma \rightarrow p+e^- + e^+$). For the latter, the interaction with the photon background generates a pion, which rapidly decays into two photons or an electron/muon and the correspondent neutrino, depending on its charge ($p+\gamma \rightarrow p/n+\pi^{0/+}$). These secondaries may also be detected by Auger and their predicted fluxes contain important pieces of information for different astrophysical problems, as discussed in the later sections. The most important photon background for these interactions is the CMB.

For a pure proton composition, the pair production could generate a hardening in the spectrum at $E \approx 10^{18.7}$ eV. This is, however, ruled out due to a mixed composition at these energies. This is better explained in the next sections.

As appreciated from figure 2.2, the energy loss length for a proton drops rapidly for $E > 10^{19.5}$ eV leading to propagation horizon and an expected suppression of the flux for higher energies. This was first proposed in parallel by Greisen (52) and Zatsepin and Kuzmin. (53) The effect was named GZK after them. As later discussed, a suppression in the spectrum is indeed seen and its origin may be described by a combination of both the GZK effect and a maximum power of acceleration at sources. However, it is not clear yet how much it is driven by each of these effects.

The energy losses for nuclei are dominated by the photodisintegration, in which the nucleus interacts with the photon background emitting most probably one or two nucleons $({}^{A}N + \gamma \rightarrow {}^{A-1} N + n)$. The most important photon background for this interaction is the EBL. The photodisintegration impacts both the spectrum and composition by generating a large number of lighter cosmic rays.

Similarly to what happens to protons, the energy loss length for nuclei drops for $E \gtrsim 10^{19.5}$ eV, leading to a propagation horizon. These horizons are not only related to the suppression of the arriving spectrum but also to a change in the relative contribution of sources depending on their distances, this is widely discussed in Chapters 9-11.

The propagation considering pair and photo-pion productions is more easily solvable by analytical means. However, when photodisintegration is considered, it becomes more complicated due to new lighter particles being generated, leading to a large number of coupled partial differential equations. The most commonly used approach for calculating the propagation of cosmic rays is through Monte Carlo simulations. Two packages are widely used in the community with such objective: SimProp (54) and CRPropa3. (55) In Ref. (56), the systematics coming from the use of different Monte Carlo codes were evaluated. Several results obtained in this work rely on these softwares.

2.1.3 Detection

2.1.3.1 Pierre Auger Observatory

The Pierre Auger Observatory is the largest cosmic ray observatory ever built. (19) Located in the province of Mendoza, Argentina, it covers an area of 3000 km^2 and uses a hybrid detection technique with a combination of a surface detector (SD) and a fluorescence detector (FD). Currently, the Pierre Auger Collaboration is composed of over 500 scientists from 17 countries.

The surface detector is composed of 1660 water Cherenkov tanks, each with a diameter of 3.6 m, a height of 1.2 m, filled with 12000 liters of pure water and containing three photomultiplier tubes (PMTs). Secondary charged particles that travel faster than the speed of light in water will emit light in the form of Cherenkov radiation, which will then be detected by the PMTs.

The SD stations are distributed in a triangular grid with 1.5 km spacing and a

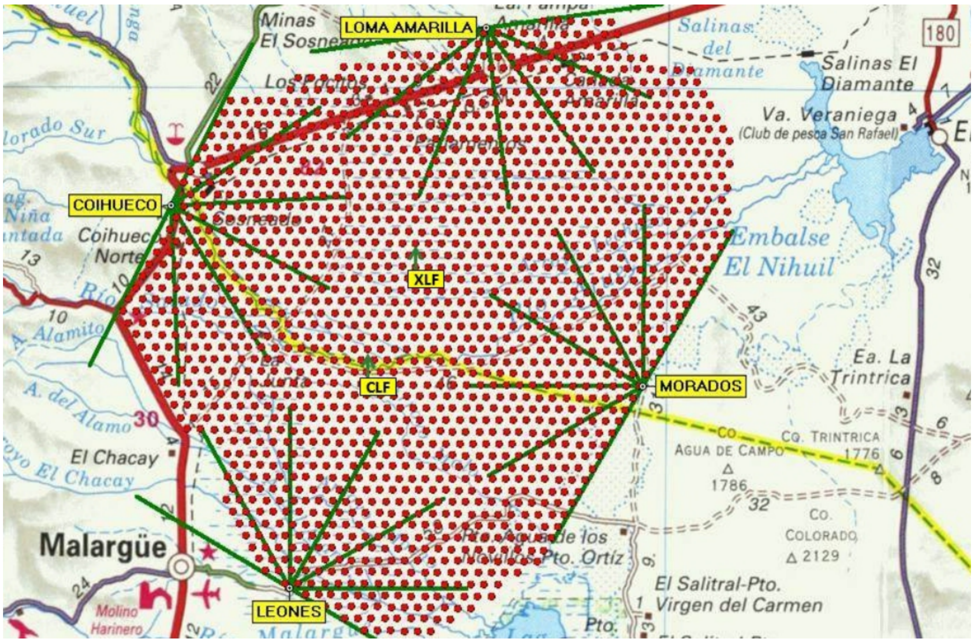
Minas
El Sosneado
LOMA AMARILLA
Salinas del Diamante
180
Salinas El Diamante
Va. Veraniega
(Club de pesca San Rafael)
COIHUECO
Coihueco Norte
Embalse El Nihuil
XLF
CLF
MORADOS
Ea. La Trintrica
El Chacay
AGUA DE CAMPO
1786
CO. TRINTRICA
1776
CO. COLORADO
2129
Malargüe
LEONES
Molino Harinero
El Salitral-Pto. Virgen del Carmen

Figure 2.4 – Design of the Pierre Auger Observatory. Each red dot represents one water Cherenkov tank that composes the surface detector, while the green lines show the field of view of the fluorescence telescopes that compose the fluorescence detector.

Source: AAB *et al.* (19)

smaller inner array with stations separated by 750 m, as shown by the red dots in figure 2.4. The distance between the tanks is such that an average EAS initiated by an EeV cosmic ray can be simultaneously detected by several stations. Less energetic primary particles will generate showers with fewer secondary particles and, consequently, will cover a smaller area. The inner array is, thus, designed to measure lower energies, reaching a detection threshold of $E < 10^{17.5}$ eV.

The SD measures the lateral distribution of the shower, from which both the energy and the arrival direction can be estimated. (57) Since it is not influenced by light of the Sun or the Moon, clouds or rain, the SD has a duty cycle close to 100%.

The fluorescence detector (FD), on the other hand, is composed of 27 fluorescence telescopes, divided in four groups of 6 located in Los Morados, Loma Amarilla, Coihueco and Los Leones, each covering 30° in azimuth (to a total of 180°) and 30° in altitude, starting from 1.5°. Another group with 3 telescopes named High Elevation Auger Telescopes (HEAT) is also built in Coihueco, with an elevated field of view, ranging from 30° to 60° and focusing on the events with lower energies, which develop higher in the atmosphere. All telescopes face the SD array as shown by the green lines in figure 2.4.

Charged secondary particles of the shower induce Nitrogen molecules in the atmosphere to emit fluorescence light in the UV band ($300 - 430$ nm). This light is captured by the fluorescence telescopes with mirrors covering an area of about 13 m^2 and Schmidt optics. The fluorescence light emitted during shower formation is much fainter than that of Moon light. Therefore, the FD can only operate when the Moon is not in its field of view and in clear skies without clouds or rain. This reduces its duty cycle to about 15%.

The FD measures the longitudinal profile of the shower, which is related to the initial particle energy and the number of particles as a function of the depth of the shower in the atmosphere. From that, it is possible to reconstruct the calorimetric energy, the geometry and the depth of shower maximum, X_{max}, which is used to estimate the distribution of primary mass as discussed later. (58, 59)

Both techniques are complementary and contain independent systematic uncertainties. The FD can better reconstruct the energy, however, it has a low duty cycle, limiting the statistics. The SD, on the other hand, can achieve good statistics but is subject to larger systematic uncertainties in the energy reconstruction if not cross-calibrated with the FD. A hybrid design is, thus, essential for improving the capabilities of the experiment and minimizing the systematic uncertainties of the results.

2.1.3.2 Observables

Three main UHECR observables are measured by the Pierre Auger Observatory: the energy spectrum, the mass composition, and the arrival directions. Besides that, the observatory can also detect the flux of neutral secondary particles emitted during propagation, in particular EeV photons and neutrinos. No such event has yet been detected and, consequently, restrictive upper limits on their flux have been imposed. The most up-to-date results of these observables and their implications are discussed in the following sections.

2.1.3.2.1 Energy spectrum

The energy spectrum, i.e., the flux of cosmic rays arriving on Earth as a function of the energy, has been measured by several experiments with energies ranging from hundreds of TeV to hundreds of EeV. As shown in figure 1.1, the steepness of the spectrum causes the flux to drop from a particle per cm^2 per second to less than a particle per km^2 per century. Therefore, experiments of different effective areas and exposures are required to study different ranges of the spectrum.

Figure 2.5 shows a compilation of results from several experiments. As a first-order approximation, it can be described as a power law of the energy, $dN/dE \propto E^{-\Gamma}$. However, as highlighted by multiplying the spectrum by $E^{2.6}$, a few breaks in the spectral index are found, usually called spectral features. The first two features were measured mostly by the KASCADE (61) and KASCADE-Grande (62) experiments and are called first and second knee.

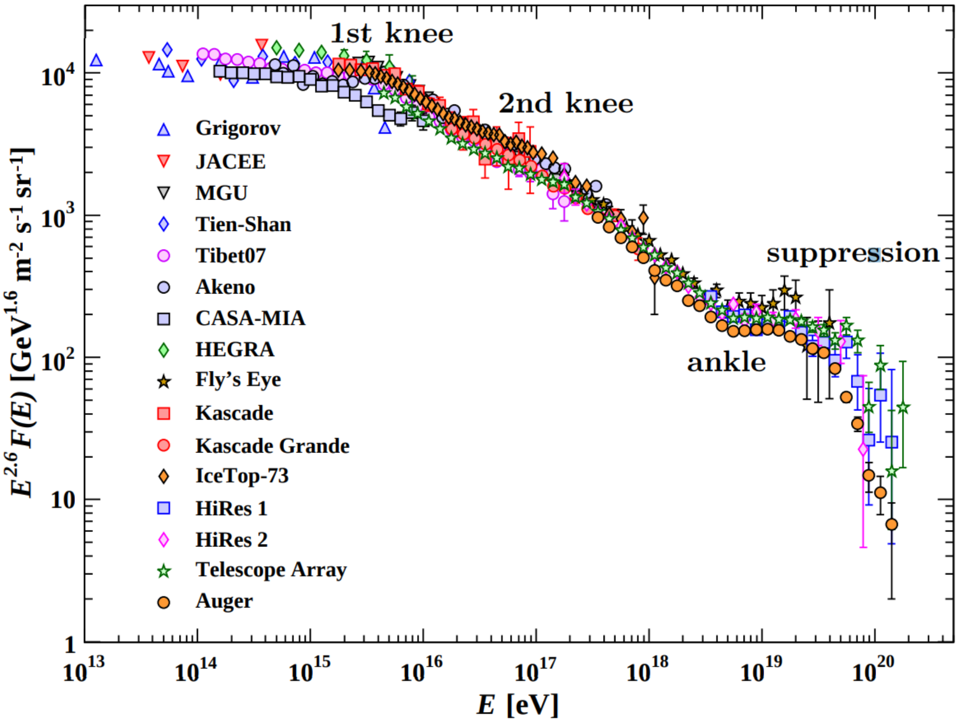

Figure 2.5 – Compilation of the cosmic ray energy spectrum measured by several experiments.

Source: PATRIGNANI *et al.* (60)

The first knee appears at $E \approx 5 \times 10^{15}$ eV, at which the spectral index changes from $\Gamma \approx 2.7$ to $\Gamma \approx 3.0$. The second knee, on the other hand, appears at $E \approx 10^{17}$ eV and also softens the spectral index, changing from $\Gamma \approx 3.0$ to $\Gamma \approx 3.3$.

In particular, the high-energy end of the spectrum, $E > 10^{17}$ eV has been measured with unprecedented statistic by the Pierre Auger Observatory. (57,63) Figure 2.6 shows the latest results from Auger. The last three features of the spectrum are found in this energy range. At $E \approx 5 \times 10^{18}$ eV, the so-called ankle appears as a hardening of the spectrum from $\Gamma \approx 3.3$ to $\Gamma \approx 2.5$. At $E \approx 1.3 \times 10^{19}$ eV, Auger has recently shown the presence of a new feature, softening the spectrum from $\Gamma \approx 2.5$ to $\Gamma \approx 3.0$. Finally, above $E \approx 4.6 \times 10^{19}$ eV, the spectrum is suppressed.

The astrophysical hypotheses for each feature are better understood if the mass composition measurements are analyzed together and, for that reason, they are discussed in the end of next section.

2.1.3.2.2 Mass composition

UHECR are ionized nuclei with their masses ranging from proton ($A = 1$) to iron ($A = 56$). The mass composition is estimated from the distribution of $X_{\max}$. Particles with the same energy and lighter mass are more likely to penetrate deeper into the atmosphere,

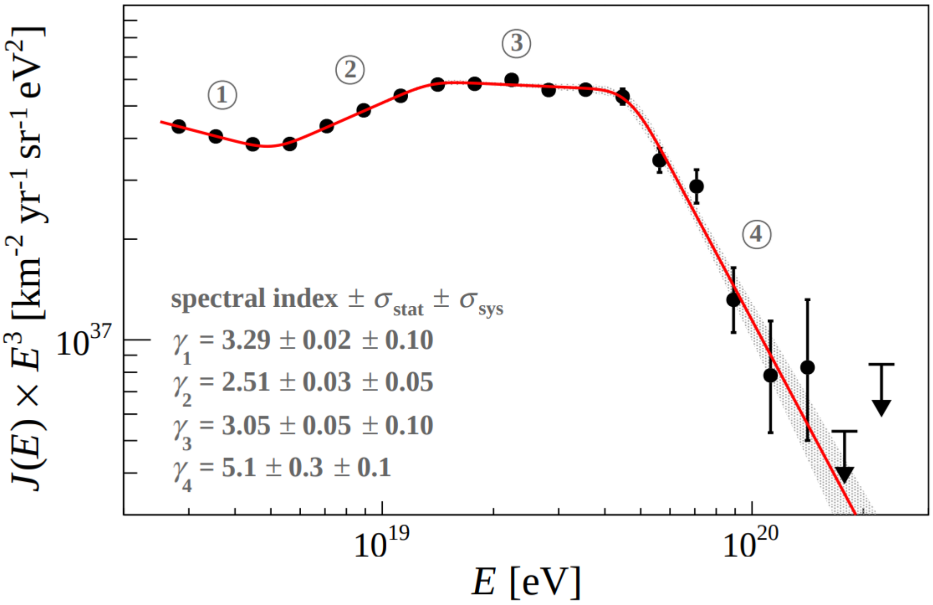

Figure 2.6 – UHECR cosmic ray energy spectrum measured by the Pierre Auger Observatory. The red line shows a fit of the spectrum using a broken power law. The spectral indexes for each region are highlighted.

Source: AAB *et al.* (63)

as one can expect from the superposition model*, and consequently generate a shower with a larger value of $X_{\max}$. However, the mass of the primary cannot be estimated for a single EAS due to its intrinsic stochastic nature, as exemplified by the proton and nitrogen $X_{\max}$ distributions in the left panel of figure 2.7. No conclusion can be drawn from a single measurement. Nevertheless, the distribution of $X_{\max}$ from several measurements contains information of how light/heavy the composition is. Yet, multiple mixed compositions may lead to the same distribution, as shown in figure 2.7. Refer to Ref (64) for an extensive review on composition measurements.

The Pierre Auger Observatory usually compares the first two moments, mean and standard deviation, σ, of the measured $X_{\max}$ distribution in a given energy bin to the mean and standard deviation expected to pure proton and iron compositions. (58, 59) A caveat of composition measurements at these energies, however, comes from the fact that these estimations come from calculations which rely on hadronic interaction models and these are only calibrated up to LHC energies. Different models consider different extrapolations to higher energies, which leads to discrepancies between the models. Three of the most used hadronic interaction models are EPOS-LHC (65), Sibyll 2.3 (66) and QGSJet-II. (67)

Figure 2.8 shows the measurements of Auger for the first two moments of the $X_{\max}$ distribution as a function of the energy. The composition is shown to be non-pure proton and a trend to heavier composition is seen for $E \gtrsim 10^{18.6}$ eV.

---

* A nucleus of energy E and mass A can be approximated as A nuclei with energy E/A.

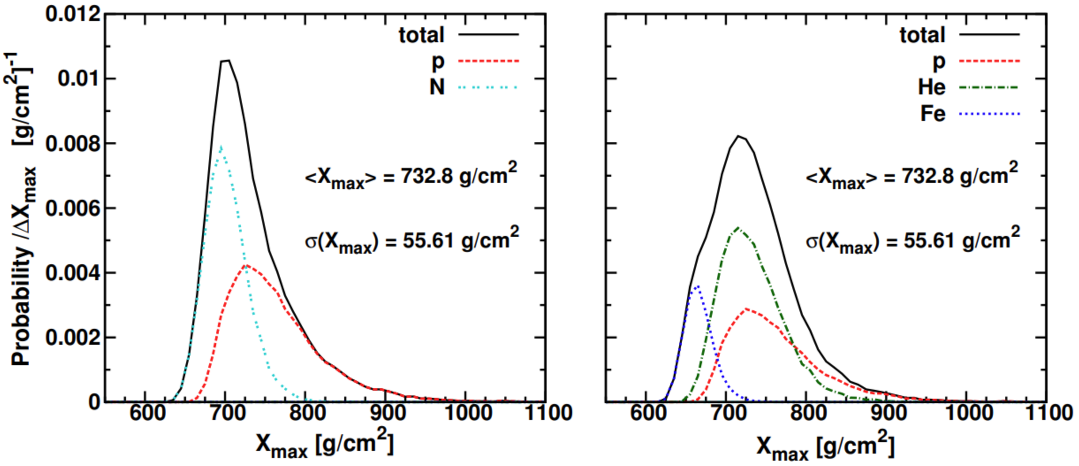

Figure 2.7 – $X_{\rm max}$ distribution for two different compositions. On the left panel, a mixed composition with proton and nitrogen is considered. On the right panel, on the other hand, a mixed composition with proton, helium and iron is considered. The black lines show the total $X_{\rm max}$ distribution for that given composition, while the colored lines show the contribution from each species.

Source: AAB *et al.* (59)

As stated in the previous section, the spectral features are better understood when analyzed in combination with the composition. For the region around the first knee, KASCADE has measured a light composition, mostly dominated by protons (69), whilst for energies around the second knee, KASCADE-Grande has measured a heavy composition. (70) This endorses the hypothesis of the first and second knee being related to a maximum power of acceleration of galactic sources. As cosmic rays are expected to be accelerated by magnetic fields, a rigidity-dependent cutoff is expected in the power of acceleration, i.e., the higher the charge of the CR, the higher the energy up to which a source can accelerate it. The first knee would, thus, be related to the maximum energy that galactic sources can accelerate light cosmic rays, while the second knee would be related to the maximum energy of acceleration for heavy cosmic rays. (71, 72) The change from light to heavy composition after the first knee is a good indication of such process. The factor of ~ 20 between the energy of the second and the first knee is also an evidence for this hypothesis.

As for the ankle, historically, a hypothesis that tried to explain it was known as the dip model and described the ankle as a propagation effect due to protons losing energy via interactions with the photon background. (73) This model considered a pure proton composition for energies around the ankle, which was endorsed by measurements at that time. Nevertheless, this assumption was abdicated due to the precise $X_{\rm max}$ measurements from Auger, which showed a mixed composition at these energies. (68, 74) Currently, the most accepted hypothesis involves a transition from predominant galactic to predominant extra-galactic sources for energies somewhere in the range between the second knee and

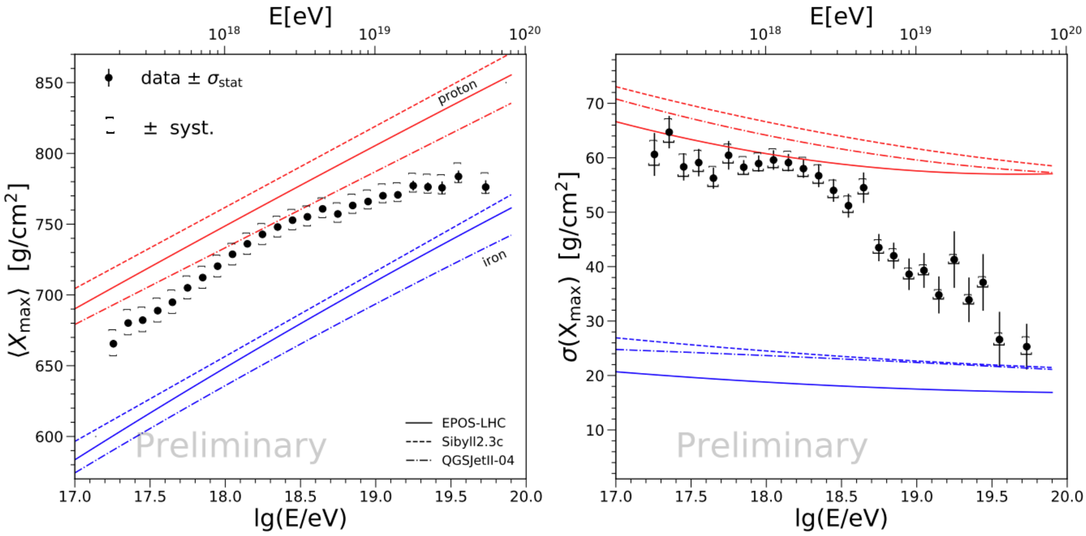

Figure 2.8 – First two moments of the $X_{\max}$ distribution measured by the Pierre Auger Observatory. The black points represent the experimental data, the black line and square brackets represent, respectively, the statistical and systematic uncertainties. The red and blue lines show the predicted moment for a pure composition of proton and iron, respectively. Three different hadronic interaction models are considered.

Source: YUSHKOV *et al.* (68)

the ankle. This is endorsed by the change in composition around this energy, even though the predicted composition depends on the exact transition energy and composition of the extra-galactic component. (75) Another measurement that supports this hypothesis is the evolution of the phase of the measured dipole in the arrival direction distribution as discussed in the next section.

The feature around $E \approx 1.3 \times 10^{19}$ eV was the last to be detected, due to unprecedented statistics achieved by the Pierre Auger Observatory. Its origin is yet to be understood.

Finally, the suppression can be explained by a combination of two effects, the maximum power of acceleration of the sources and the GZK effect, which limits the propagation distance of UHECR. The contribution from each effect substantially depends on assumptions of the models, such as spectral features of the sources and source distribution. A combined fit of energy spectrum and composition from the Pierre Auger has shown a preference for the maximum power of acceleration of the sources. (76) The influence of the spectral assumption to this effect and how it changes with LIV is widely discussed in this work in Chapters 4 and 7. The influence of the source distribution is one of the basis of the work developed in Chapters 9-11.

It is noteworthy to remember that there is a difference between the spectrum and composition at the sources and the spectrum and composition arriving on Earth,

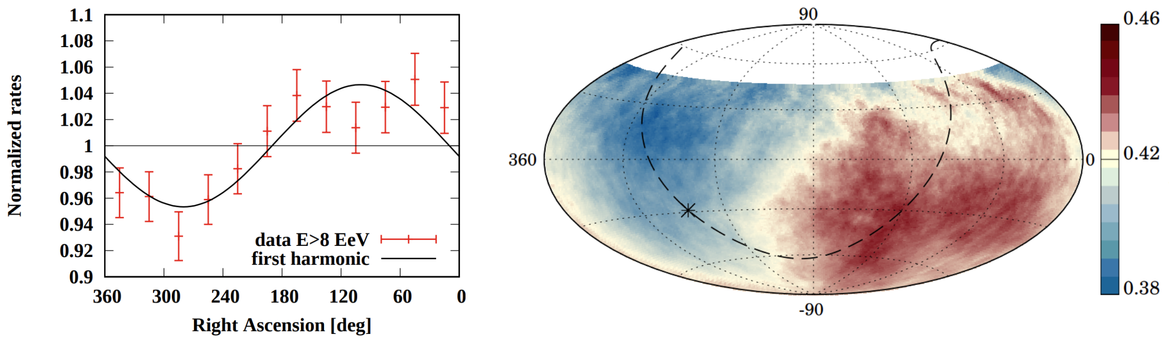

Figure 2.9 – Large-scale anisotropy dipole measured by the Pierre Auger Observatory. The left panel shows the normalized angular distribution as a function of right ascension, where the thick black line shows a fit function that follows $1 + \delta_\alpha \cos\theta$. The right panel shows the skymap with the normalized flux as a function of the arrival direction in equatorial coordinates. The black star and dashed line shows the galactic center and plane, respectively.

Source: AAB *et al.* (77)

which may sometimes be misunderstood. As discussed in the previous section, the initial spectrum and composition are modified due to energy-dependent interactions with the photon background, shaping the arriving ones, which are measured by the experiments.

2.1.3.2.3 Arrival directions

Cosmic rays are charged particles and, consequently, are deviated during propagation in environments with galactic and extra-galactic magnetic fields (GMF and EGMF, respectively). Therefore, the arrival direction of a cosmic ray on Earth does not necessarily point back to its source.

Anisotropy studies conducted by the Pierre Auger Observatory found the data to be highly isotropic for $E < 8$ EeV. For $E > 8$ EeV, however, the angular distribution of arrival directions is well described by a dipole of amplitude $(6.5^{+1.3}_{-0.9})\%$ pointing to right ascension $\alpha_d = (100 \pm 10)^\circ$ and declination $\delta_d = (-24^{+12}_{-13})^\circ$ with a confidence level of more than 5.2σ, i.e., the normalized data is well described by $1 + 0.065 \cos\theta$, where θ is the angle between the considered direction and the dipole direction. (77) This is shown in figure 2.9, which shows the angular distribution as a function of right ascension and the skymap, on which one can see a preferred region of the sky.

A later study from the Pierre Auger Observatory obtained the evolution of the amplitude and phase of the dipole in right ascension, as shown in figure 2.10. A transition from a dipole with a phase that points towards the galactic center to a dipole that points almost outwards it is seen. (78) These results endorse the hypothesis of a transition from

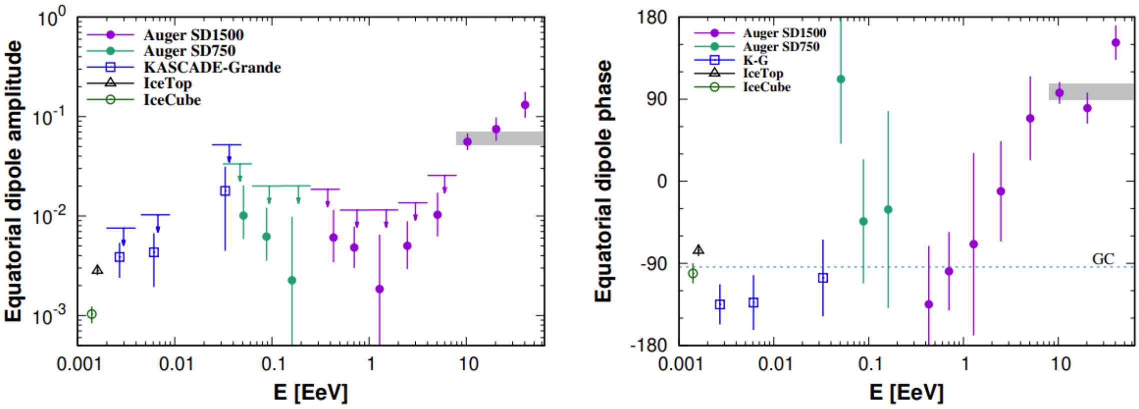

Figure 2.10 – Evolution of the dipole in right ascension with energy. The left and right panel show, respectively, the dipole amplitude and phase. The gray shaded area shows the results for the large-scale anisotropy dipole for $E > 8$ EeV.

Source: AAB *et al.* (78)

predominant galactic to predominant extra-galactic sources in an energy region near the ankle.

Studies trying to correlate anisotropies at the highest energies with catalogs of gamma-ray emitting source have also been done by the Pierre Auger Collaboration. The strongest correlation was found for $E > 39$ EeV and starburst galaxies with a statistical significance of 4.0σ. (79)

Even though new light has been shed on the problem, the quest for the origin of UHECR remains open. This is better discussed in Chapters 9-11.

2.1.3.2.4 Upper limits on the flux of neutral particles

While propagating, UHECR may interact with the photon background and produce pions, which later decay into photons and neutrinos, hereby called GZK photons and GZK neutrinos due to the interaction in which they are created. EAS initiated by these secondary particles may be detected by the Pierre Auger Observatory and separated from cosmic-ray-induced EAS via sophisticated analysis methods which involve the zenith angle and mean $X_{\max}$ of the showers. No GZK photon or neutrino has yet been detected by Auger and, as a consequence, restrictive upper limits on their fluxes were imposed as shown in figure 2.11. (80–82)

For neutrinos, the predictions of theoretical models may rule out some combination of spectral features and source distribution. For photons, the upper limits are such that top-down models that predict that cosmic rays are products of the decay of heavy primordial are ruled out. (81) The upper limits of the photon flux can also be used to study LIV, as discussed in Chapters 4 and 7.

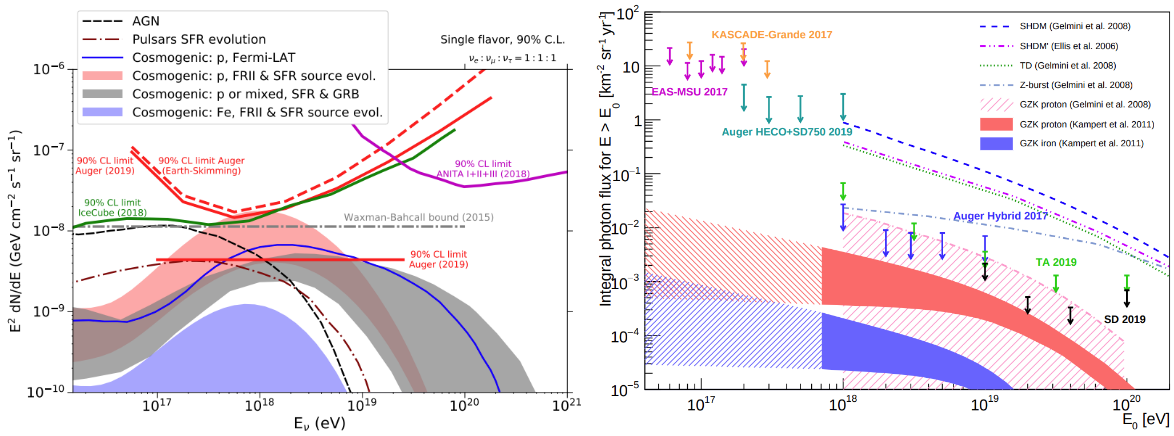

Figure 2.11 – Upper limits on the flux of neutral particles. The left and right panels show, respectively, the neutrino and photons limits. Shaded areas show the prediction for the fluxes of secondary particles emitted in the GZK effect. The dashed lines on the right panel show the prediction by top-down models.

Source (left): PEDREIRA. (80); (right): RAUTENBERG. (81)

2.1.4 Open questions

A long way has been traced from the discovery of cosmic ray until present time. Important questions yet remain open. A few examples are: what is the origin of cosmic rays? What is their composition at the ultra-high energy region? How hadronic interactions behave at these energies? Why is there a large discrepancy in the predicted and measured number of muons in EAS? How exactly are the magnetic fields in our galaxy and in the inter-galactic medium? Can cosmic rays be used to probe fundamental physics in regimes not accessible on Earth? A detailed review of these questions can be found in Ref. (25).

Both Telescope Array and the Pierre Auger Observatory are currently undergoing upgrades which will help astrophysicists answer these questions, (83) The upgrade of Auger involves the equipment of the SD stations with radio antennas in order to decrease the systematic uncertainties of the energy and mass reconstruction (84) and the so-called AugerPrime. (85) This major update can be divided into four components: an upgrade of the electronics of the SD, an update in the operation mode of the FD in order to increase its duty cycle to ∼ 20% and the installation of scintilator surface detectors (SDD) and underground muon detectors (UMD) in order to provide precise measurements of the muonic component of EAS.

Future experiments which aim to further develop the knowledge of the field have also been proposed, such as GRAND (86), a ground-based array of radio antennas covering ∼ 200.000 km^2 and POEMMA (87), a space-based experiment relying in UV telescopes placed in two orbiting satellites.

As previously stated, this work focus on contributing to two of these questions.

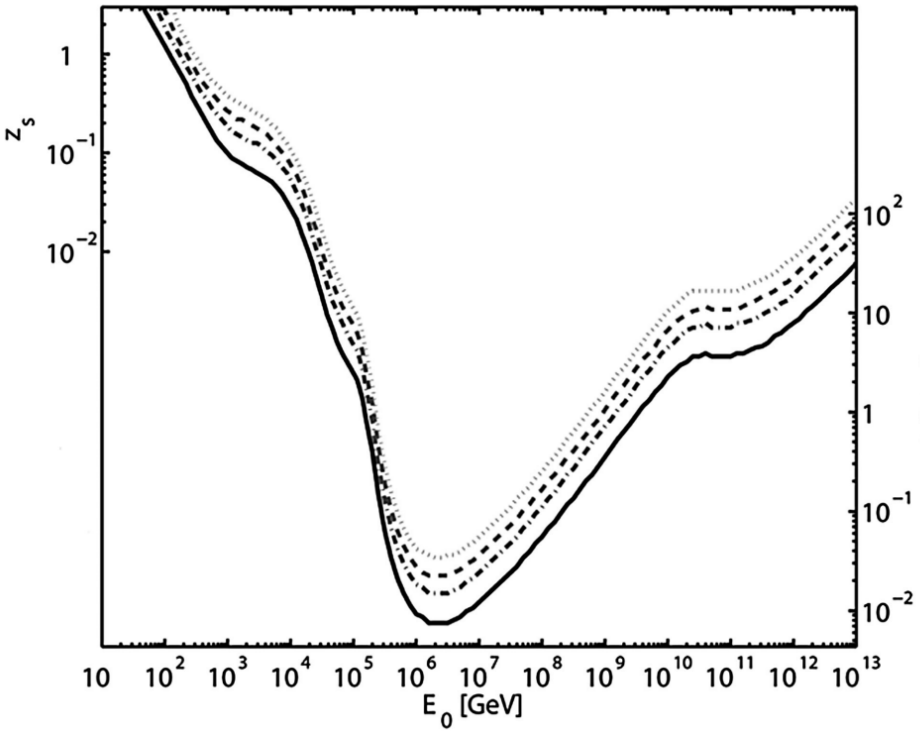

Figure 2.12 – Optical depth as a function of the energy. Each of the lines shows the results for different survival probabilities. From bottom to top: e^{-1}, e^{-2}, e^{-3}, and $e^{-4.6}$.

Source: DE ANGELIS *et al.* (51)

“Can cosmic rays be used to probe fundamental physics in regime not accessible on Earth?” - This is discussed in Chapters 3, 4 and 7.

“What are the origins of UHECR?” - This is discussed in Chapters 9-11.

2.2 VHE gamma-rays

2.2.1 Propagation

The transparency of the universe to gamma-rays depend strongly on their energy. While propagating, gamma-rays may interact with the photon background and be absorbed via pair production ($\gamma + \gamma_{\mathrm{bg}} \to e^+ + e^-$). (51) Figure 2.12 shows the optical depth of this interaction, i.e., the distance at which a given fraction of the gamma-rays are absorbed due to pair production, for energies ranging from GeV to EeV.

Up to ~ 100 GeV the universe is quite transparent and gamma-rays coming from high redshifts are still expected to reach Earth. Starting from a few hundreds of GeV to a few TeV, however, the optical depth drops rapidly and creates a horizon which prevents the detection of far sources in this energy region.

The energy threshold of the pair production depends directly on the energy of the propagating gamma-ray. As shown in figure 2.13, photons in the GeV-TeV range can only

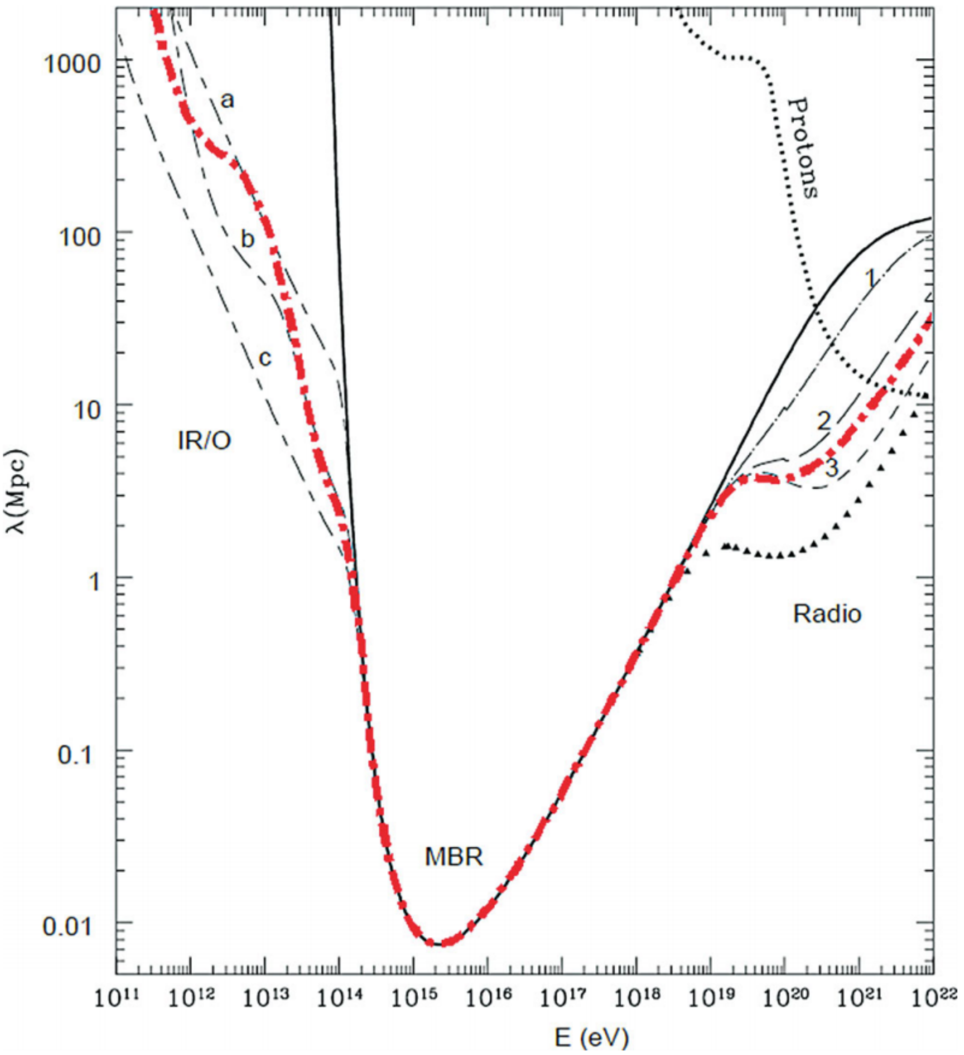

Figure 2.13 – Mean free path of the pair production as a function of the energy. The labels a, b and c represent different EBL models, while the labels 1, 2 and 3 represent different frequency cutoffs in the radio background.

Source: DE ANGELIS *et al.* (51)

interact with the most energetic background, i.e., the EBL. In the PeV-EeV range, photons interact mostly with the CMB. And finally, for the ultra-high energies ($E > 10^{18}$ eV), the radio background dominates the interaction.

The energy spectrum arriving on Earth, $J_{\mathrm{Earth}}(E)$, can be obtained simply by multiplying the intrinsic spectrum on the source, $J_{\mathrm{s}}(E)$, by an attenuation factor, $a(E)$, given by

$$J_{\mathrm{Earth}}(E) = a(E) J_{\mathrm{s}}(E) = e^{-D/\lambda(E)} J_{\mathrm{s}}(E), \tag{2.1}$$

where D is the distance of the source and $\lambda(E)$ is the mean free path of the pair production. For TeV measurements, this usually implies in a prominent suppression of the measured spectrum, masking the true form of the intrinsic spectrum. As discussed in the previous section, the parametrization of the EBL distribution contains a lot of uncertainties, which are reflected in the process of reconstructing the intrinsic spectrum from the measured data. (88)

The propagation of gamma-rays and the effects of LIV on it are widely discussed in Chapters 4-7.

2.2.2 IACTs and CTA

The flux of gamma-rays with energies up to hundreds of GeV is so intense that it is possible to study them using experiments with an effective area of a few square meters. Such small detectors can be put in space-based experiments, allowing the detection of the primary particle, which reduces the uncertainties coming from the interactions with the atmosphere. (13) Nevertheless, for higher energies the flux drops to a level in which ground-based experiments are necessary.

One of the main techniques used by ground-based gamma-ray experiments is that of Imaging Air Cherenkov Telescopes (IACT). (89) A gamma-ray entering the atmosphere may collide with a photon from the Coulomb field of a nucleus of the air generating a cascade of secondary particles. This is similar to the EAS generated by cosmic rays, but only the electromagnetic component of the shower is present, while a cosmic-ray-induced EAS will also have a hadronic component. Charged secondary particles traveling faster than the speed of light on air will then emit a flash Cherenkov radiation, which is collected by large telescopes. Finally, through the study of the characteristics of the image formed in the telescope and preferably a stereo reconstruction, the gamma-ray energy and arrival direction are estimated. EAS initiated by protons, which constitute the bulk of the background for this technique, are separated via machine-learning-based characterization of the image in the telescope. (90)

The current generation of IACTs is composed mainly by three experiments. H.E.S.S., a five-telescope array located in Namibia (15), VERITAS, a four-telescope array located in the United States of America (16) and MAGIC, a two-telescope array located in the Canary Islands. (17) The Cherenkov Telescope Array (CTA) is an advanced project for the next generation of IACTs with ~ 100 telescopes in two different sites: CTA South in Chile and CTA North in the Canary Islands. (21, 22)

As shown in figure 2.14, CTA will provide an improvement of at least an order of magnitude in sensitivity, which is defined as the weakest flux the experiment can detect given some observation time and statistical criteria. The energy range covered by CTA will also be broader than that of the current generation, ranging from 20 GeV to at least 300 TeV. This will be possible by the employment of three sizes of telescope: small-sized telescope (SST), medium-sized telescope (MST) and large-sized telescope (LST). The limitations of the experiment are different at the lowest and the highest energies. For the

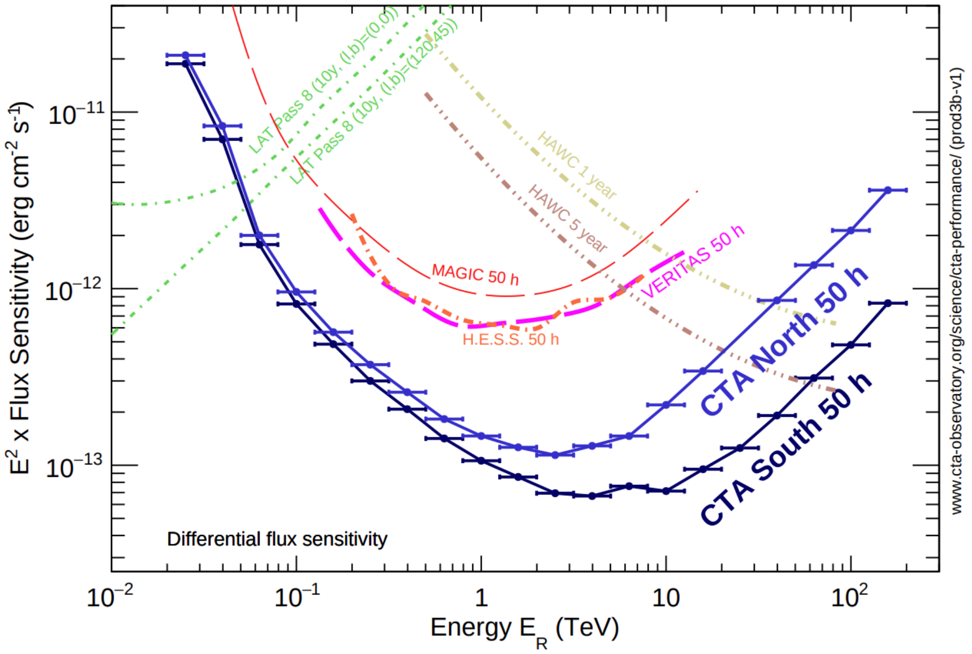

Figure 2.14 – Differential sensitivity as a function of the energy. Each colored line represents a different experiment/observation time. It is noteworthy that the curve only shows an indication and not a real comparison between different instruments, as the method of calculation and selection criteria are different.

Source: ACHARYA *et al.* (22)

lowest, the flux is intense enough so that fewer telescopes are sufficient to obtain good statistics. The light of the EAS, however, is much fainter and, consequently, telescopes with larger area of collection are needed. For the highest energies, on the other hand, the EAS are intense so that smaller telescopes can be used. Nevertheless, the flux is much weaker, requiring a large number of telescopes covering a wide area. The three sizes of telescopes will, thus, focus on different energy ranges: the LST is designed for the lowest energies, the SST for the highest energies, and the MST for the intermediate energies.

The angular resolution will also to be improved, as shown in figure 2.15. This improvement comes mostly from the use of multiple telescopes in the reconstruction, but also from better cameras and optical design. A better angular resolution is desired for studying the morphology of the sources and reducing source confusion.

The science case for CTA (22) involves the majority of the most important questions in gamma-ray astronomy, such as a multi-messenger approach for understanding the acceleration of cosmic rays, the search for signatures of dark matter, probing extreme environments such as jets and relativistic outflows, and exploring frontiers in fundamental physics. (91)

This work joins the efforts to study the last topic. The potential of testing LIV with CTA is estimated in Chapter 6, while the search of signatures of LIV in data measured by current IACTs is presented in Chapter 5.

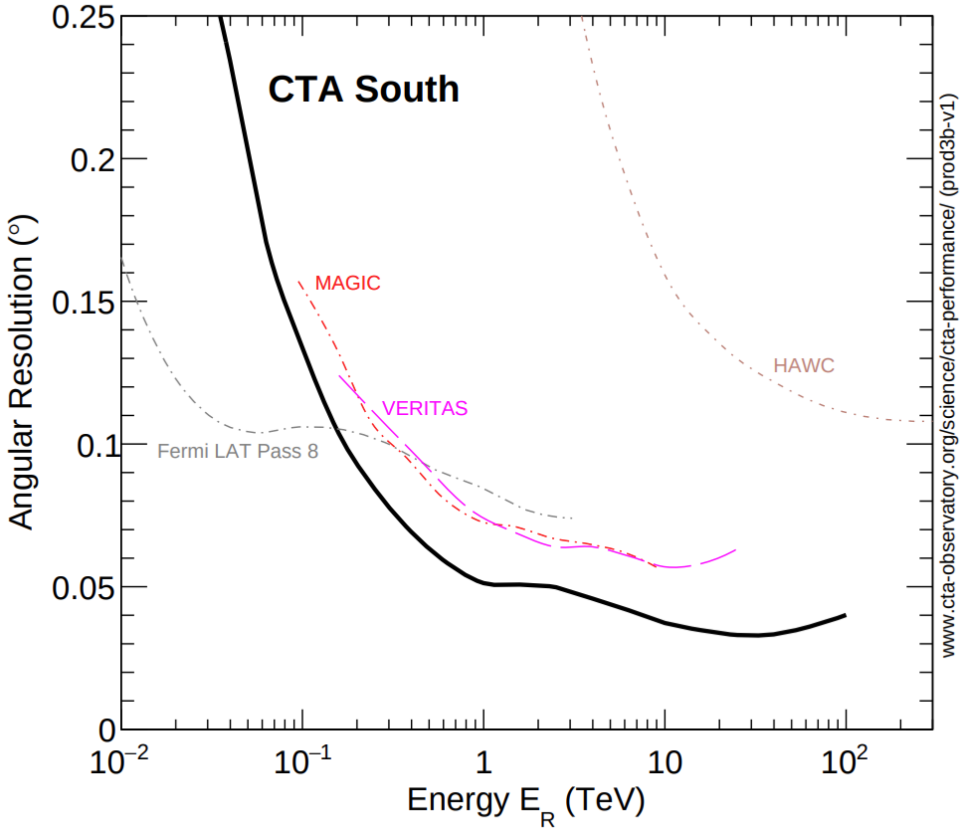

Figure 2.15 – Angular resolution as a funcion of the energy for 68% containment. Different lines represent different experiments. The expect sensitivity for CTA North is similar to that of CTA South.

Source: ACHARYA *et al.* (22)

3 LORENTZ INVARIANCE VIOLATION

The development of relativity in the beginning of the last century is one of the cornerstones in modern physics. It expands the regime of validity of Newtonian physics to high energies by considering inertial reference frames (IRF) which relate to one another via Lorentz transformations instead of Galilean transformation. Two of its main pillars, the universality of the speed of light, c, which is the same for all massless particles in every IRF and also an assymptotic limit for the maximum attainable velocity by a massive particle, and the Lorentz invariant $s^2 = E^2 - p^2$, which has the same value in every IRF.

Over the last century, relativity has succeeded a great deal of experimental tests. Nevertheless, theoretical models of a quantum theory of gravitation may give rise or accommodate some level of Lorentz invariance violation (LIV). (92–95) Hence, searches for signatures of LIV play a fundamental role in experimental and fundamental physics.

In a phenomenological approach, most theoretical models converge to a generalization of the dispersion relation (96) given by[*]

$$E_a^2 = p_a^2 + m_a^2 + \sum_{n=0}^{\infty} \delta_{a,n} S_a^{(n+2)}, \tag{3.1}$$

where E, p and m denote, respectively, the particle energy, momentum and mass, $\delta_{a,n}$ denotes the LIV coefficient of order n, which modulates the intensity of the violation, and a identifies the particle species. S can be chosen to be either the energy or the momentum. However, for massless or very energetic massive particles, this choice is redundant and E is used.

When considering a phenomenological approach, it is usual to only assume LIV effects on a single particle species (or class of particles) and a single order, n, leaving $\delta_{a,n}$ as a free parameter to be either measured or constrained.

In some effective field theories, it is also common to use $\delta_{a,n} = \eta_{a,n}/M_{\mathrm{Pl}}$, where $M_{\mathrm{Pl}} \approx 1.22 \times 10^{28}$ eV is the Planck scale. One may also define a LIV energy scale, $E_{\mathrm{LIV}}^{(n)} = |\delta_{\gamma,n}|^{1/n}$ for $n > 0$. When photons are considered, the scenarios for $\delta_{\gamma,n} < 0$ and $\delta_{\gamma,n} > 0$ are called subluminal and superluminal, respectively.

Since the effects of LIV are expected to be suppressed up to the highest energies, astroparticles play a crucial role in the search of its signatures. (97–99) This is mainly due to their high energies, but also due to the high level of precision achieved by current instruments and the accumulation of effects over a long distance and time.

---

[*] Throughout this work, natural units, i.e., $c = 1$ are used, unless stated otherwise.

The modification of the dispersion relation due to LIV may lead to several effects which would leave imprints in the data, such as time delay between photons of different energies due to a dependency of the speed of light on energy (100, 101), photon decay, which would be forbidden by energy-momentum conservation in Lorentz invariant (LI) scenario (102–104), emission of vacuum Cherenkov (102), modifications in the development of EAS (105, 106) and changes in the kinematics of interactions during astroparticle propagation. (88, 107–112) Over the last decades, several instruments and datasets have been used to search for signatures of these effects. Nevertheless, no significant evidence of LIV has yet been found, leading to very restrictive limits on the LIV coefficients and, consequently, on the effect.

In this work, we focus mostly on the changes of kinematics of interactions during propagation of GZK photons, gamma-rays and UHECR.

In Chapter 4, we present a search for LIV using the propagation of GZK photons. If subluminal LIV is considered, the mean free path of these particles increases significantly. For some combinations of astrophysical models and LIV coefficients, the predicted flux is larger than the upper limits on the photon flux imposed by the Pierre Auger Observatory, resulting in upper limits on the LIV effect. The dependency on the hypothesis for the UHECR sources, such as spectral parameters and composition, is discussed for the first time in the literature.

In Chapter 5, we propose an innovative and robust technique for testing LIV using multiple TeV gamma-ray spectra. Applying this technique to a dataset composed of 111 spectra from 38 sources allowed us to impose the most constraining LIV subluminal limits from TeV gamma-ray astrophysics.

In Chapter 6, we estimate the potential of testing LIV using CTA, the next generation of IACTs. The possibility of detecting LIV effects just above present limits is discussed, as well as the potential to significantly improve these limits if no LIV effect is present.

In Chapter 7, we search for imprints of LIV in the propagation of UHECR and GZK photons using the data from the Pierre Auger Observatory. A combined fit of energy spectrum and composition is done considering several LIV hypotheses and limits using GZK photons are updated.

Finally, in Chapter 8, we present a review of the most common astrophysical tests of LIV, as well as a compilation of the most up-to-date limits.

4 LIMITS ON THE LORENTZ INVARIANCE VIOLATION FROM UHECR ASTROPHYSICS

THE ASTROPHYSICAL JOURNAL, 853:23 (10pp), 2018 January 20 https://doi.org/10.3847/1538-4357/aa9f2c

© 2018. The American Astronomical Society. All rights reserved.

Limits on the Lorentz Invariance Violation from UHECR Astrophysics

Rodrigo Guedes Lang[1], Humberto Martínez-Huerta[1,2], and Vitor de Souza[1]
[1] Instituto de Física de São Carlos, Universidade de São Paulo, Av. Trabalhador São-carlense 400, São Carlos, Brazil; rodrigo.lang@usp.br
[2] Departamento de Física, Centro de Investigación y de Estudios Avanzados del I.P.N., Apartado Postal 14-740, 07000, Ciudad de México, México

Received 2017 September 14; revised 2017 November 30; accepted 2017 November 30; published 2018 January 18

Abstract

In this paper, the Lorentz invariance violation (LIV) is introduced in the calculations of photon propagation in the universe. LIV is considered in the photon sector, and the mean-free path of the $\gamma\gamma \rightarrow e^+e^-$ interaction is calculated. The corresponding photon horizon, including LIV effects, is used to predict major changes in the propagation of photons with energy above 10^{18} eV. The flux of GZK photons on Earth, considering LIV, is calculated for several source models of ultra-high-energy cosmic rays (UHECRs). The predicted flux of GZK gamma-rays is compared to the new upper limits on the photon flux obtained by the Pierre Auger Observatory in order to impose upper limits on the LIV coefficients of order $n = 0$, 1, and 2. The limits on the LIV coefficients derived here are more realistic than previous works and in some cases more restrictive. The analysis resulted in LIV upper limits in the photon sector of $\delta_{\gamma,0}^{\text{limit}} \sim -10^{-20}$, $\delta_{\gamma,1}^{\text{limit}} \sim -10^{-38}\,\text{eV}^{-1}$, and $\delta_{\gamma,2}^{\text{limit}} \sim -10^{-56}\,\text{eV}^{-2}$ in the astrophysical scenario, which best describes UHECR data.

Key words: astroparticle physics – cosmic rays – relativistic processes

1. Introduction

Astroparticle physics has recently reached the status of precision science due to (a) the construction of new observatories operating innovative technologies, (b) the detection of large numbers of events and sources, and (c) the development of clever theoretical interpretations of the data. Two observational windows have produced very important results in the last decade. The ultra-high energy cosmic rays ($E > EeV$) studied by the Pierre Auger and the Telescope Array Observatories (The Pierre Auger Collaboration 2015; Tinyakov 2014) improved our knowledge of the most extreme phenomena known in nature. The GeV–TeV gamma-ray experiments FERMI/LAT (Atwood et al. 2009), H.E.S.S. (The H.E.S.S. Collaboration 2006), MAGIC (The MAGIC Collaboration 2016), and VERITAS (J. Holder for the VERITAS Collaboration 2011) gave a new perspective on gamma-ray production and propagation in the universe. The operation of the current instruments and the construction of future ones (Zhen 2010; The CTA Consortium 2011; Haungs et al. 2015) guarantee the production of even more precise information in the decades to come.

Lorentz invariance (LI) is one of the pillars of modern physics and it has been tested in several experimental approaches (Mattingly 2005). Astroparticle physics has been proposed as an appropriate test environment for possible Lorentz invariance violation (LIV) given the large energy of the particles, the large propagation distances, the accumulation of small interaction effects, and recently the precision of the measurements (Amelino-Camelia et al. 1998; Jacobson et al. 2003; Stecker & Scully 2005, 2009; Ellis et al. 2006, 2008; Galaverni & Sigl 2008a, 2008b; The MAGIC Collaboration 2008; Liberati & Maccione 2009; Ellis & Mavromatos 2013; Fairbairn et al. 2014; Biteau & Williams 2015; Chang et al. 2016; Tavecchio & Bonnoli 2016; Xu & Ma 2016; Rubtsov et al. 2017).

Effective field theories with some Lorentz violation can derive in measurable effects in the data taking by astroparticle physics experiments; nonetheless, in this paper, LIV is introduced in the astroparticle physics phenomenology through the polynomial correction of the dispersion relation in the photon sector and is focused on the gamma-ray propagation and pair production effects with LIV. Other phenomena like vacuum birefringence, photon decay, vacuum Cherenkov radiation, photon splitting, synchrotron radiation, and helicity decay have also been used to set limits on LIV effects on the photon sector but are beyond the scope of this paper; for a review, see Liberati & Maccione (2009), Bluhm (2014), and Rubtsov et al. (2017).

Lorentz invariant gamma-ray propagation in the intergalactic photon background was studied previously in detail by De Angelis et al. (2013), a similar approach is followed in Section 2, but LIV is allowed in the interaction of high energy photons with the background light and their consequences are studied. The process $\gamma\gamma \rightarrow e^+e^-$ is the only one considered to violate LI, and, as a similar approach used in Galaverni & Sigl (2008a), such LIV correction can lead to a correction of the LI energy threshold of the production process. The latter phenomena modifies the mean-free path of the interaction and therefore the survival probability of a photon propagating through the background light, which depends on the LIV coefficients. This dependence is calculated in Section 2 and the mean-free path and the photon horizon are shown for several LIV coefficients and different orders of the LIV expansion in the photon energy dispersion relation.

In Section 3, the mean-free path of the photo-production process considering LIV is implemented in a Monte Carlo propagation code in order to calculate the effect of the derived LIV in the flux of ultra-high energy photons arriving on Earth due to the GZK effect (Greisen 1966; Zatsepin & Kuz'min 1966) and considering several models for the sources of cosmic rays. Section 3 quantifies the influence of the astrophysical models concerning mass composition, energy spectra shape, and source distribution. These dependencies have been largely neglected in previous studies and it is shown here that they influence the GZK photon flux by as much as four orders of magnitude.

In Section 4, the propagated GZK photon flux for each model is compared to recent upper limits on the flux of photons obtained by the Pierre Auger Observatory. For some astrophysical models, the Auger data is used to set restrictive limits on the LIV coefficients. The astrophysical model used to describe the primary cosmic-ray flux has a very large influence on the flux of GZK photons and therefore on the LIV limits imposed. Finally, in Section 5, the conclusions are presented.

2. Photon Horizon Including LIV Effects

One of the most commonly used mechanisms to introduce LIV in particle physics phenomenology is based on the polynomial correction in the dispersion relation of a free propagating particle, mainly motivated by an extra term in the Lagrangian density that explicitly breaks Lorentz symmetry, see, for instance, Amelino-Camelia et al. (1998), Coleman & Glashow (1999), Ahluwalia (1999), Amelino-Camelia (2001), Jacobson et al. (2003), Galaverni & Sigl (2008a, 2008b), Maccione & Liberati (2008), Liberati & Maccione (2011), Jacob & Piran (2008), and Zou et al. (2017). In these models, the corrected expression for the dispersion relation is given by the following equation:

$$E_a^2 - p_a^2 = m_a^2 + \delta_{a,n} E_a^{n+2}, \qquad (1)$$

where a denotes the particle with mass m_a and four-momenta (E_a, p_a). For simplicity, natural units are used in this work. The LIV coefficient, $\delta_{a,n}$, parametrizes the particle dependent LIV correction, where n expresses the correction order, which can be derived from the series expansion or from a particular model for such an order, see, for instance, the case of $n = 0$ (Coleman & Glashow 1997, 1999; Klinkhamer & Schreck 2008), $n = 1$ (Myers & Pospelov 2003), or a generic n (Vasileiou et al. 2013). The LIV parameter of the order of n, δ_n, is frequently considered to be inversely proportional to some LIV energy scale $E_{\mathrm{LIV}}^{(n)}$. Different techniques have been implemented in the search of LIV signatures in astroparticle physics and some of them have been used to derive strong constraints to the LIV energy scale (Amelino-Camelia et al. 1998; Maccione & Liberati 2008; Bi et al. 2009; The H.E.S.S. Collaboration 2011; Otte 2012; Vasileiou et al. 2013; Benjamin Zitzer for the VERITAS Collaboration 2014; Schreck 2014; Biteau & Williams 2015; Martínez-Huerta & Pérez-Lorenzana 2017; Rubtsov et al. 2017).

The threshold analysis of the pair production process, considering the LIV corrections from Equation (1) on the photon sector is discussed in the Appendix and leads to corrections of the LI energy threshold of the process. In the following, $\epsilon_{\mathrm{th}}^{\mathrm{LIV}}$ stands for the minimum energy of the cosmic background (CB) photon in the pair production process with LIV. The latter effect can lead to changes in the optical depth, $\tau_\gamma(E_\gamma, z)$, which quantifies how opaque to photons the universe is. The survival probability, i.e., the probability that a photon, γ, emitted with a given energy, E_γ, and at a given redshift, z, reaches Earth without interacting with the background, is given by

$$P_{\gamma\to\gamma}(E_\gamma, z) = e^{-\tau_\gamma(E_\gamma, z)}. \qquad (2)$$

The photon horizon is the distance (z_h) for which $\tau_\gamma(E_\gamma, z_h) = 1$. z_h defines, as a function of the energy of the photon, the redshift at which an emitted photon will have probability $P_{\gamma\to\gamma} = 1/e$ of reaching Earth. The evaluation of the photon horizon is of extreme importance because it summarizes the visible universe as a function of the energy of the emitted photon. In this section, the photon horizon is calculated including LIV effects. The argument presented in De Angelis et al. (2013) is followed here.

In the intergalactic medium, the $\gamma\gamma_{\mathrm{CB}} \to e^+e^-$ interaction is the main contribution to determine the photon horizon. In the approximation where cosmological effects are negligible, the mean-free path, $\lambda(E_\gamma)$, of this interaction is given by

$$\lambda(E_\gamma) = \frac{cz}{H_0 \tau_\gamma(E_\gamma, z)}, \qquad (3)$$

where $H_0 = 70$ km s^{-1} Mpc^{-1} is the Hubble constant and c is the speed of light in a vacuum. The optical depth is obtained by

$$\tau_\gamma(E_\gamma, z) = \int_0^z dz \frac{c}{H_0(1+z)\sqrt{\Omega_\Lambda + \Omega_M(1+z)^3}} \times \int_{-1}^{1} d(\cos\theta)\frac{1-\cos\theta}{2} \times \int_{\epsilon_{\mathrm{th}}^{\mathrm{LIV}}}^{\infty} d\epsilon\, n_\gamma(\epsilon, z)\sigma(E_\gamma, \epsilon, z), \qquad (4)$$

where θ is the angle between the direction of propagation of both photons $\theta = [-\pi, +\pi]$, $\Omega_\Lambda = 0.7$ is the dark energy density, $\Omega_M = 0.3$ is the matter density, σ is the cross section of the interaction, and $\epsilon_{\mathrm{th}}^{\mathrm{LIV}}$ is the threshold energy of the interaction as given by Equation (13).

$n_{\gamma_{\mathrm{CB}}}$ is the background photon density. The dominant backgrounds are the extra-galactic background light (EBL) for $E_\gamma < 10^{14.5}$ eV, the cosmic background microwave radiation (CMB) for $10^{14.5}$ eV $< E_\gamma < 10^{19}$ eV and the radio background (RB) for $E_\gamma > 10^{19}$ eV. In the calculations presented here, the Gilmore model (Gilmore & Ramirez-Ruiz 2010) was used for the EBL. Since LIV effects in the photon horizon are expected only at the highest energies ($E_\gamma > 10^{16}$ eV), using different models of EBL would not change the results. For the RB, the data from Gervasi et al. (2008) with a cutoff at 1 MHz were used. Different cutoffs in the RB data lead to different photon horizons as shown in De Angelis et al. (2013). Since no new effect shows up in the LIV calculation due to the RB cutoff, only the 1 MHz cutoff will be presented.

It is usual for studies such as the one presented here, in which the threshold of an interaction is shifted, causing a modification of the mean-free path, to neglect direct effects in the cross section, σ, when solving Equation (4). However, an implicit change of the cross section is taken into account given its dependence on the energy threshold $\epsilon_{\mathrm{th}}^{\mathrm{LIV}}$ (Breit & Wheeler 1934).

Figures 1–3 show the mean-free path for $\gamma\gamma_{\mathrm{CB}} \to e^+e^-$ as a function of the energy of the photon, E_γ, for several LIV coefficients with $n = 0$, $n = 1$, and $n = 2$, respectively. The main effect is an increase in the mean-free path that becomes stronger the larger the photon energy, E_γ, and the LIV coefficient are. Consequently, fewer interactions happen and the photon, γ, will have a higher probability of traveling farther than it would have in an LI scenario. Similar effects due to LIV are seen for $n = 0$, $n = 1$, and $n = 2$. The LIV coefficients are treated as free parameters; therefore, there is no way to compare the importance of the effect between the orders $n = 0$,

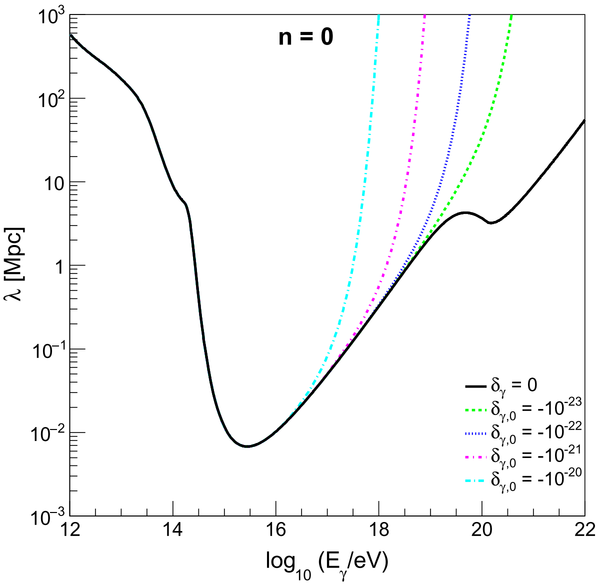

Figure 1. Mean-free path (λ) for $\gamma\gamma_{\rm CB} \to e^{+}e^{-}$ as a function of the energy of the photon (E_γ) shown for several LIV coefficients for $n = 0$. The Gilmore model (Gilmore & Ramirez-Ruiz 2010) for EBL and the Gervasi et al. (Gervasi et al. 2008) model for the RB with a cutoff at 1 MHz were used. The black continuous line is the LI scenario. The colored lines represent different values for the LIV coefficients. The colored lines coincide with the black line for $\log(E_\gamma/eV) < 15$.

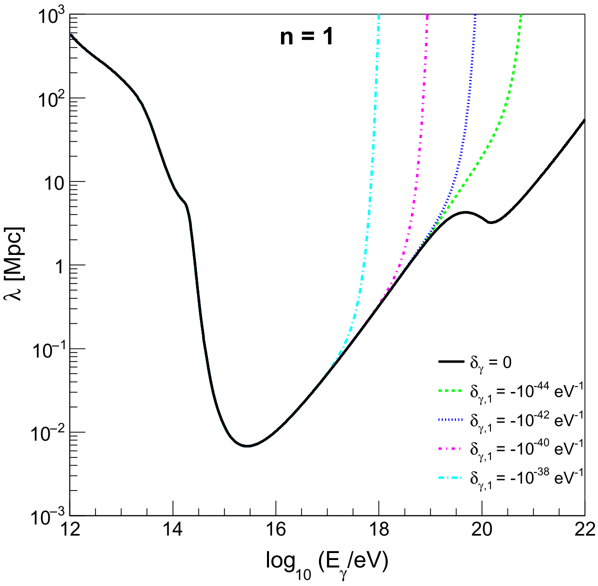

Figure 2. Mean-free path (λ) for $\gamma\gamma_{\rm CB} \to e^{+}e^{-}$ as a function of the energy of the photon (E_γ) shown for several LIV coefficients for $n = 1$. The Gilmore model (Gilmore & Ramirez-Ruiz 2010) for EBL and the Gervasi et al. (Gervasi et al. 2008) model for the RB with a cutoff at 1 MHz were used. The black continuous line is the LI scenario. The colored lines represent different values for the LIV coefficients. The colored lines coincide with the black line for $\log(E_\gamma/eV) < 15$.

$n = 1$, and $n = 2$, each order must be limited independently. Note that $\delta_{\gamma,n}$ units depend on n.

The LIV effect becomes more tangible in Figure 4 in which the photon horizon (z_h) is shown as a function of E_γ for $n = 0$.

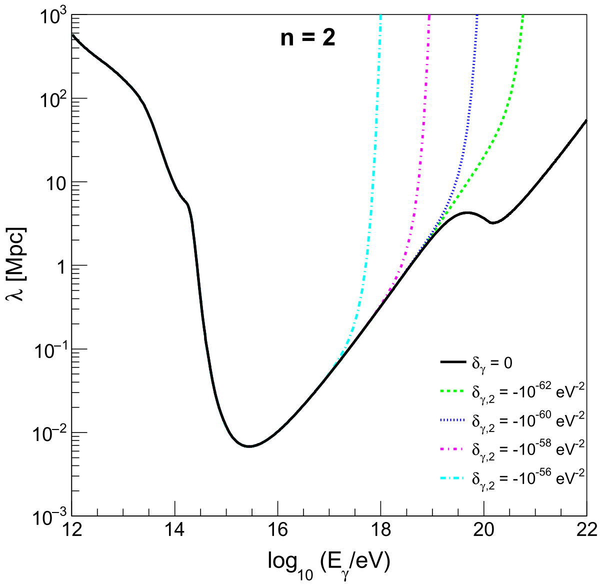

Figure 3. Mean-free path (λ) for $\gamma\gamma_{\rm CB} \to e^{+}e^{-}$ as a function of the energy of the photon (E_γ) shown for several LIV coefficients for $n = 2$. The Gilmore model (Gilmore & Ramirez-Ruiz 2010) for EBL and the Gervasi et al. (Gervasi et al. 2008) model for the RB with a cutoff at 1 MHz were used. The black continuous line is the LI scenario. The colored lines represent different values for the LIV coefficients. The colored lines coincide with the black line for $\log(E_\gamma/eV) < 15$.

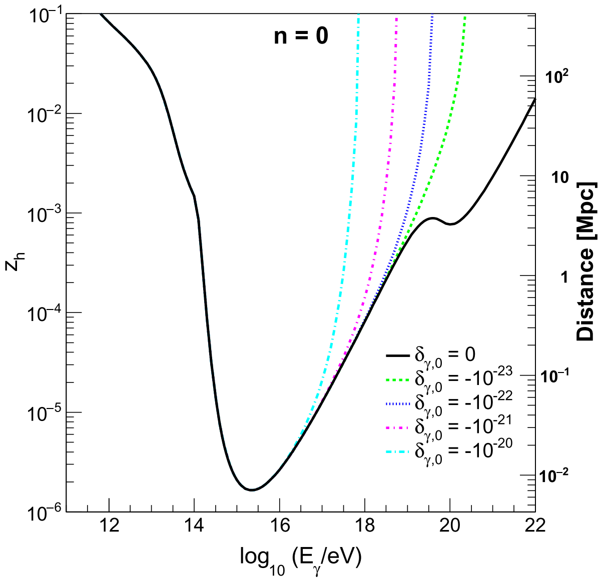

Figure 4. Photon horizon (z_h) as a function of the photon energy (E_γ) for different LIV coefficients with $n = 0$. The right axis shows the equivalent distance obtained using the same assumptions used in Equation (4). The Gilmore model (Gilmore & Ramirez-Ruiz 2010) for EBL and the Gervasi et al. (Gervasi et al. 2008) model for the RB with a cutoff at 1 MHz were used. The black continuous line represents the LI scenario. The colored lines represent different values for the LIV coefficients. The colored lines coincide with the black line for $\log(E_\gamma/eV) < 15$.

For energies above $E_\gamma > 10^{16.5}$ eV and the given LIV values, the photon horizon increases when LIV is taken into account, increasing the probability that a distant source emitting high energy photons produces a detectable flux at Earth. Similar results are found for $n = 1$ and $n = 2$.

3. Flux of GZK Photons Including LIV Effects

Even though the effects of LIV on the propagation of high energy photons are strong, they cannot be directly measured and, therefore, used to probe LIV models. In order to do that, in this section, the flux of GZK photons on Earth considering LIV is obtained and compared to the upper limits on the photon flux from the Pierre Auger Observatory (Carla Bleve for the Pierre Auger Collaboration 2015; The Pierre Auger Collaboration 2017a).

UHECRs interact with the photon background producing pions (photo-pion production). Pions decay shortly after production, generating EeV photons among other particles. The effect of this interaction chain suppresses the primary UHECR flux and generates a secondary flux of photons (Gelmini et al. 2007). The effect was named GZK after the authors of the original papers (Greisen 1966; Zatsepin & Kuz'min 1966). The EeV photons (GZK photons) also interact with the background photons as described in the previous sections.

In order to consider LIV in the GZK photon calculation, the CRPropa3/EleCa (Settimo & Domenico 2015; Batista et al. 2016) codes were modified. The mean-free paths calculated in Section 2 were implemented in these codes and the propagation of the particles was simulated. The resulting flux of GZK photons is, however, extremely dependent on the assumptions about the sources of cosmic rays, such as the injected energy spectra, mass composition, and the distribution of sources in the universe. Therefore, four different models for the injected spectra of cosmic rays at the sources and five different models for the evolution of sources with redshift are considered in the calculations presented below.

3.1. Models of UHECR Sources

No source of UHECR was ever identified and correlation studies with types of sources are not conclusive. Several source types and mechanisms of particle production have been proposed. The amount of GZK photons produced in the propagation of the particles depends significantly on the source model used. In this paper, four UHECR source models are used to calculate the corresponding GZK photons. The models are used as illustrations of the differences in the production of GZK photons; an analysis of the validity of the models and their compatibility with experimental data is beyond the scope of this paper. However, it is important to note that strong constrains to the source models can be set by new measurements (The Pierre Auger Collaboration 2017b). The models used here are labeled as follows:

1. $\boldsymbol{C_1}$: Aloisio et al. (2014);
2. $\boldsymbol{C_2}$: Unger, Farrar, & Anchordoqui (2015)—Fiducial model (Unger et al. 2015);
3. $\boldsymbol{C_3}$: Unger et al. (2015) with the abundance of galactic nuclei from (Olive & Group 2014);
4. $\boldsymbol{C_4}$: Berezinsky, Gazizov, & Grigorieva (2007)—Dip model (Berezinsky et al. 2006).

All four models propose the energy spectrum at the source to be a power-law distribution of the energy with a rigidity cutoff:

$$\frac{dN}{dE_s} = \begin{cases} E_s^{-\Gamma}, & \text{for } R_s < R_{\text{cut}} \\ E_s^{-\Gamma} e^{1-R_s/R_{\text{cut}}}, & \text{for } R_s \geqslant R_{\text{cut}} \end{cases}, \tag{5}$$

where the spectral index, Γ, and the rigidity cutoff, R_{cut}, are parameters given by each model. Five different species of nuclei (H, He, N, Si, and Fe) are considered in these models and their fraction (fH, fHe, fN, fSi, and fFe) are given in Table 1.

The composition of UHECR has a strong influence on the generated flux GZK photons and, therefore, on the possibility to set limits on LIV effects. The models chosen in this study range from very light (C_4) to very heavy (C_2) passing by intermediate compositions C_1 and C_3. Heavier compositions produce less GZK photons and therefore are less prone to reveal LIV effects.

Figure 5 shows the dependence of the GZK photon flux on the source model used. The integral of the GZK photon fluxes for the LIV case of $\delta_{\gamma,0} = 10^{-20}$ are shown as a function of energy. The use of different LIV coefficients results in a shift up and down in the integral flux for each source model, having negligible changes in each ratio. The dependence on the model is of several orders of magnitude and should be considered in studies trying to impose limits on LIV coefficients. The capability to restrict LIV effects is proportional to the GZK photon flux generated in each model assumption.

3.2. Models of Source Distribution

Figure 4 shows how the photon horizon increases significantly when LIV is considered. Therefore, the source distribution in the universe is an important input in GZK photon calculations usually neglected in previous studies. Five different models of source evolution(R_n) are considered here.

1. $\boldsymbol{R_1}$: sources are uniformly distributed in a comoving volume;
2. $\boldsymbol{R_2}$: sources follow the star formation distribution given in Hopkins & Beacom (2006). The evolution is proportional to $(1+z)^{3.4}$ for $z < 1$, to $(1+z)^{-0.26}$ for $1 \leqslant z < 4$ and to $(1+z)^{-7.8}$ for $z \geqslant 4$;
3. $\boldsymbol{R_3}$: sources follow the star formation distribution given in Yüksel et al. (2008). The evolution is proportional to $(1+z)^{3.4}$ for $z < 1$, to $(1+z)^{-0.3}$ for $1 \leqslant z < 4$ and to $(1+z)^{-3.5}$ for $z \geqslant 4$;
4. $\boldsymbol{R_4}$: sources follow the GRB rate evolution from Le & Dermer (2007). The evolution is proportional to $(1 + 8z)/[1 + (z/3)^{1.3}]$;
5. $\boldsymbol{R_5}$: sources follow the GRB rate evolution from Le & Dermer (2007). The evolution is proportional to $(1 + 11z)/[1 + (z/3)^{0.5}]$.

Figure 6 shows the ratio of sources as a function of redshift for the five source distributions considered. The source evolution uniformly distributed in a comoving volume is shown only for comparison. It is clear that even astrophysical motivated evolutions are different for redshifts larger than two. Charged particles produced in sources farther than redshifts equal to one have a negligible probability of reaching Earth; however, the GZK photons produced in their propagation could travel farther if LIV is considered.

Table 1
Parameters of the Four Source Models Used in This Paper

Model	Γ	$\log_{10}(R_{\mathrm{cut}}/V)$	*f*H	*f*He	*f*N	*f*Si	*f*Fe
C_1	1	18.699	0.7692	0.1538	0.0461	0.0231	0.00759
C_2	1	18.5	0	0	0	1	0
C_3	1.25	18.5	0.365	0.309	0.121	0.1066	0.098
C_4	2.7	∞	1	0	0	0	0

Note. Γ is the spectral index, R_{cut} is the rigidity cutoff and *f*H, *f*He, *f*N, *f*Si, and *f*Fe are the fractions of each nuclei.

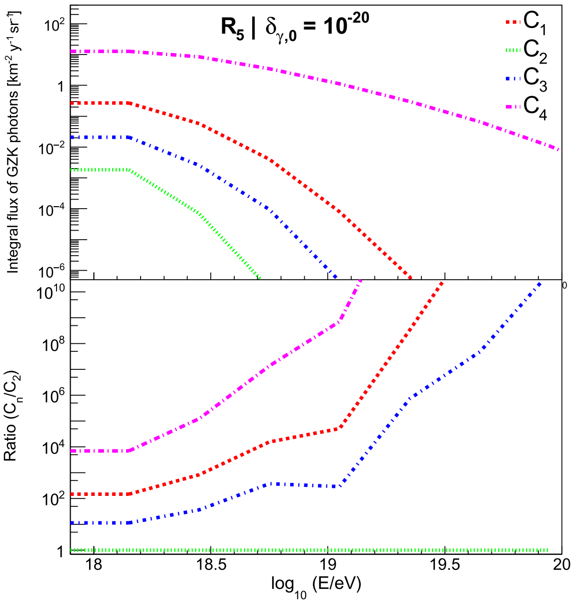

Figure 5. Integral flux of GZK photons as a function of the photon energy for each source model. Each line represents a different model C_n. All cases are for the source evolution model R_5 and LIV coefficient $\delta_{\gamma,0} = 10^{-20}$. The top panel shows the integral flux, while the bottom panel show the ratio to the one that produces less photons, C_2.

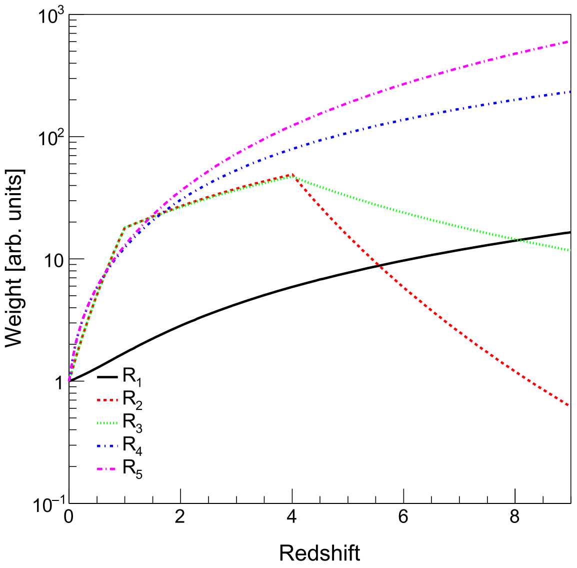

Figure 6. Source evolution with redshift. Each line represents one of the models R_n, see the text for details of the models.

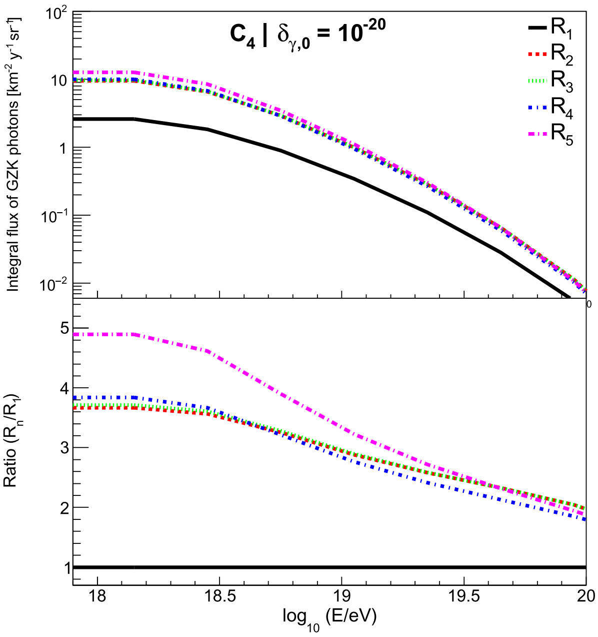

Figure 7. Integral flux of GZK photons as a function of the photon energy for each source evolution model. Each line represents a different model R_n. All cases are for the source model C_4 and LIV coefficient $\delta_{\gamma,0} = 10^{-20}$. The top panel shows the integral flux, while the bottom panel shows the ratio to the simplest case, R_1.

Figure 7 shows the effect of the source evolution in the prediction of GZK photons including LIV effects. Once more, the use of different LIV coefficients results in a shift up an down in the integral flux for each source evolution model, having negligible changes in each ratio. The differences for each source evolution model are as large as 500% at $E = 10^{18}$ eV. The capability to restrict LIV effects is proportional to the GZK photon flux generated in each model assumption.

4. Limits on LIV Coefficients

The GZK photon flux of the five astrophysical models shown above are considered together with the upper limits on the photon flux imposed by the Pierre Auger Observatory to set limits on the LIV coefficients. The simulations considered sources up to 9500 Mpc ($z \approx 8.88$). The reference results are for model C_3R_5, as this is the model that best describes current UHECR data. The three orders of LIV ($n = 0$, 1, and 2) are considered for each astrophysical model C_i. Two limiting cases are also considered: LI and maximum LIV, labeled as $\delta_\gamma = 0$ and $\delta_\gamma \to -\infty$, respectively. The Lorentz invariant case (LI) is shown for comparison. The maximum LIV case ($\delta_\gamma \to -\infty$) represents the limit in which the mean-free path of the

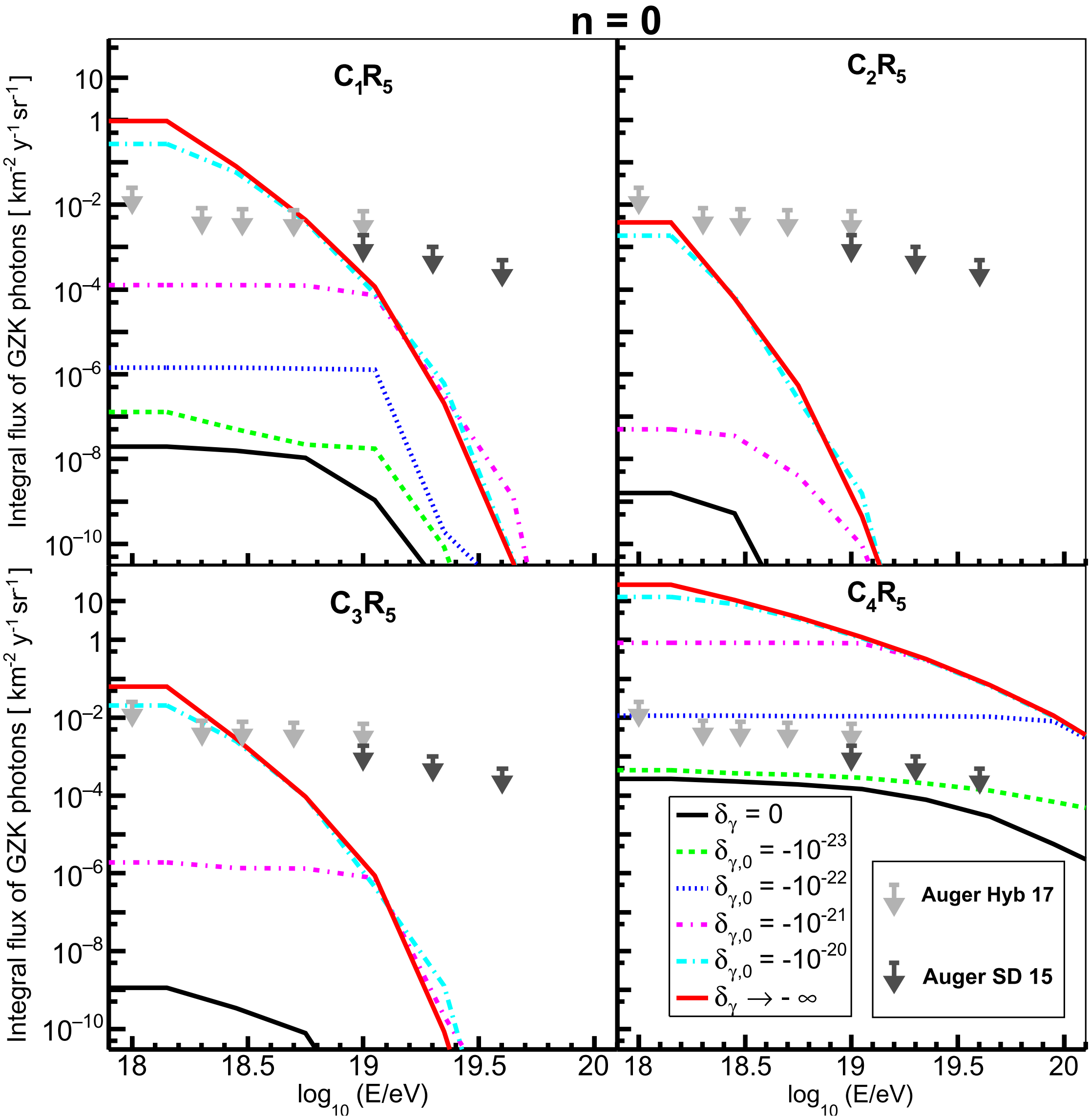

Figure 8. Integral flux of GZK photons as a function of the photon energy, considering LIV effects for $n = 0$. The black continuous line represents the LI scenario. The colored lines represent different values for the LIV coefficients. The red line represents the limit LIV case. The arrows represent the upper limits from the Pierre Auger Observatory. Each panel represents a source model, C_1R_5, C_2R_5, C_3R_5, C_4R_5, respectively.

photon–photon interaction goes to infinity at all energies and therefore no interaction happens. These two cases bracket the possible LIV solutions. The UHECR flux reaching Earth was normalized to the flux measured by the Pierre Auger Observatory (Inés Valiño for the Pierre Auger Collaboration 2015) at $E = 10^{18.75}$ eV, which sets the normalization of the GZK photon flux produced in the propagation of these particles.

Figures 8–10 show the results of the calculations. For some LIV coefficients, models C_1R_5, C_3R_5, and C_4R_5 produces more GZK photons than the upper limits imposed by Auger, therefore, upper limits on the LIV coefficients can be imposed. Model C_2R_5 produces less GZK photons than the upper limits imposed by Auger even for the extreme scenario $\delta_\gamma \to -\infty$; therefore, no limits on the LIV coefficients could be imposed. Table 2 shows the limits imposed in this work for each source model and LIV order.

Table 3 shows the limits imposed by other works for the photons sector for comparison. The direct comparison of the results obtained here (C_3R_5) is only possible with Galaverni & Sigl (2008a; first line in Table 3) because of the similar technique based on GZK photons. The differences between the calculations presented here and the limits imposed in Galaverni & Sigl (2008a) can be explained by (a) the different assumptions considered in the $\gamma\gamma$ interactions with LIV, (b) the different astrophysical models used, and (c) the upper limit on the GZK photon flux used. In Galaverni & Sigl (2008a), the limits were obtained by calculating the energy in which the interaction of a high energy photon with a background photon at the peak of the CMB, i.e., with energy $\epsilon = 6 \times 10^{-4}$ eV, becomes kinematically forbidden. In this work, a more complete approach was used, where the energy threshold was calculated, the mean-free path was obtained by integrating the

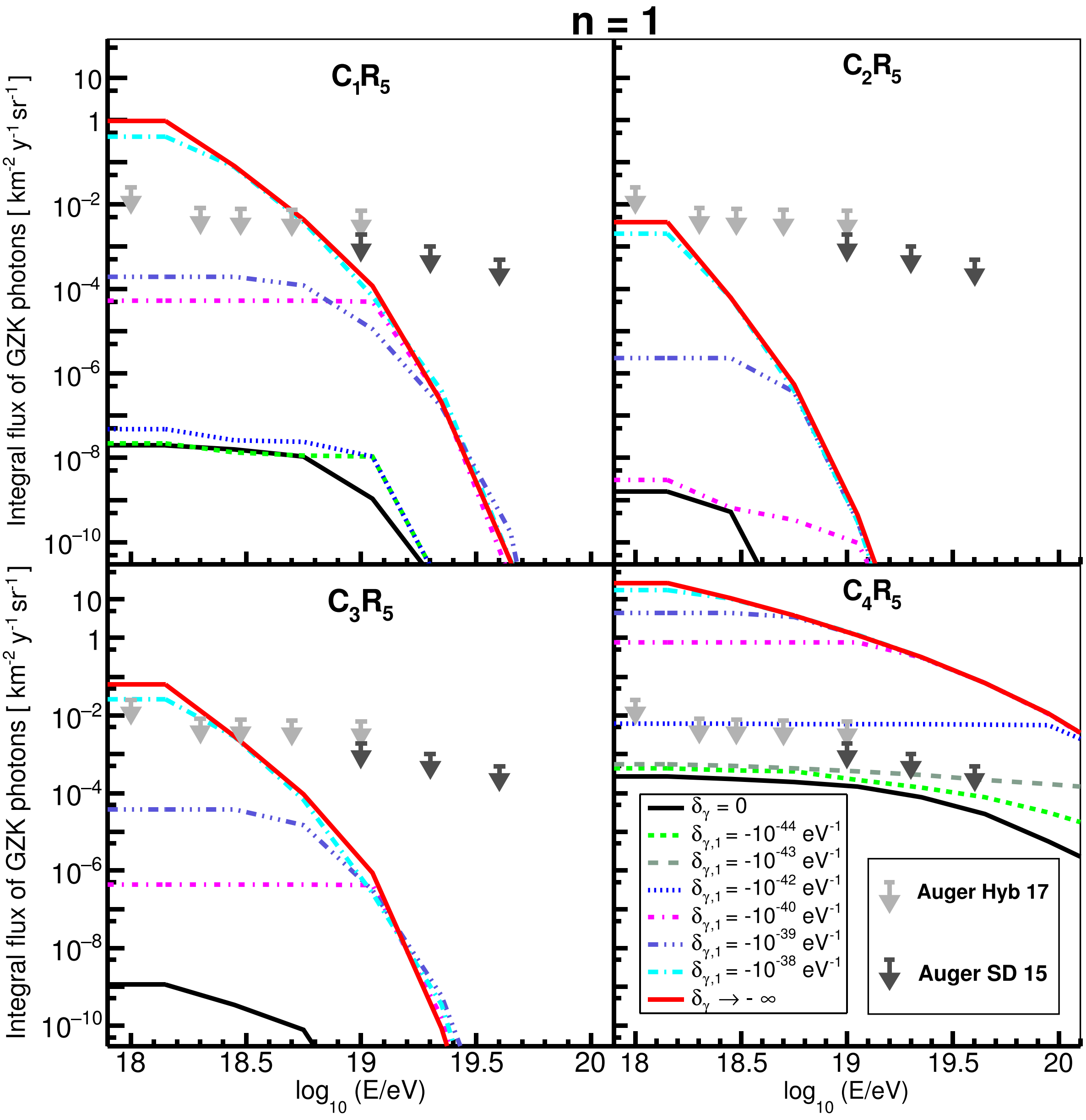

Figure 9. Integral flux of GZK photons as a function of the photon energy, considering LIV effects for $n = 1$. The black continuous line represents the LI scenario. The colored lines represent different values for the LIV coefficients. The red line represents the limit LIV case. The arrows represent the upper limits from the Pierre Auger Observatory. Each panel represents a source model, C_1R_5, C_2R_5, C_3R_5, C_4R_5, respectively.

whole background photon spectrum and the propagation was simulated, obtaining the intensity of the flux of GZK photons. The astrophysical scenario used in Galaverni & Sigl (2008a) was a pure proton composition with energy spectrum normalized by the AGASA measurement (The AGASA Collaboration 2006) and index $\Gamma = 2.6$. The source distribution was not specified in the study. However, this astrophysical scenario is ruled out by the $X_{\max}$ measurements from the Pierre Auger Observatory (The Pierre Auger Collaboration 2014a, 2014b). In the calculations presented here, the LIV limits were updated using astrophysical scenarios compatible to the Auger $X_{\max}$ data. Finally, in this paper, new GZK photon limits published by Auger are used. The LIV limits presented here are, therefore, more realistic and up to date.

The other values in Table 3 are shown for completeness. The second and third entries are based on energy dependent arrival time of TeV photons: (a) a PKS 2155−304 flare measured with H.E.S.S. (The H.E.S.S. Collaboration 2011) and (b) GRB 090510 measured with *Fermi*-LAT (Vasileiou et al. 2013). Entry H.E.S.S.—Mrk 501 (2017) (Lorentz & Brun 2017) in Table 3 is based on the kinematics of the interactions of photons from Mrk 501 with the background. All of the studies shown in Table 3 assume LIV only in the photon sector. However, the systematics of the measurements and the energy

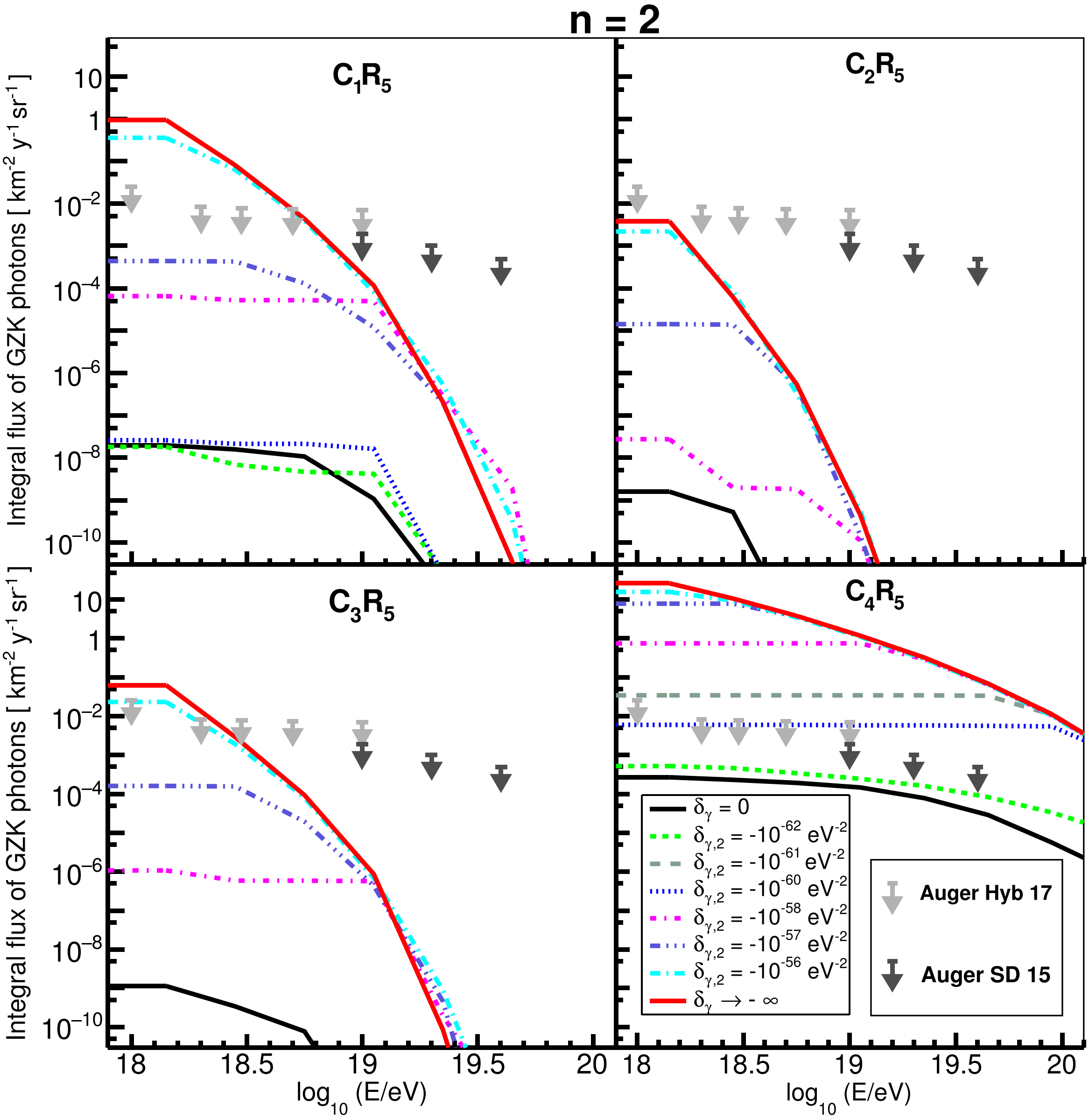

Figure 10. Integral flux of GZK photons as a function of the photon energy considering LIV effects for $n = 2$. The black continuous line represents the LI scenario. The colored lines represent different values for the LIV coefficients. The red line represents the limit LIV case. The arrows represent the upper limits from the Pierre Auger Observatory. Each panel represents a source model, C_1R_5, C_2R_5, C_3R_5, C_4R_5, respectively.

Table 2
Limits on the LIV Coefficients Imposed by This Work for Each Source Model and LIV Order (n)

Model	$\delta_{\gamma,0}^{\rm limit}$	$\delta_{\gamma,1}^{\rm limit}$ (eV^{-1})	$\delta_{\gamma,2}^{\rm limit}$ (eV^{-2})
C_1R_5	$\sim -10^{-20}$	$\sim -10^{-38}$	$\sim -10^{-56}$
C_2R_5	…	…	…
C_3R_5	$\sim -10^{-20}$	$\sim -10^{-38}$	$\sim -10^{-56}$
C_4R_5	$\sim -10^{-22}$	$\sim -10^{-42}$	$\sim -10^{-60}$

Note. Model C_3R_5 is pointed out as containing the reference values of this paper because it describes better the current UHECR data.

Table 3
Limits on the LIV Coefficients Imposed by Other Works Based on Gamma-Ray Propagation

Model	$\delta_{\gamma,0}^{\rm limit}$	$\delta_{\gamma,1}^{\rm limit}$ (eV^{-1})	$\delta_{\gamma,2}^{\rm limit}$ (eV^{-2})
Galaverni & Sigl (2008a)	…	-1.97×10^{-43}	-1.61×10^{-63}
H.E.S.S.—PKS 2155−304 (2011)	…	-4.76×10^{-28}	-2.44×10^{-40}
Fermi—GRB 090510 (2013)	…	-1.08×10^{-29}	-5.92×10^{-41}
H.E.S.S.—Mrk 501 (2017)	…	-9.62×10^{-29}	-4.53×10^{-42}

Note. First line shows a previous result, which can be compared to the calculations presented here in Table 2. The last three lines are shown for completeness. These limits are based on gamma-ray arrival time and are not directly comparable to the ones in Table 2.

of photons (TeV photons versus EeV photons) are very different and a direct comparison between the GZK photon calculations shown here and the time of arrival of TeV photon is not straightforward.

5. Conclusions

In this paper, the effect of possible LIV in the propagation of photons in the universe is studied. The interaction of a high energy photon traveling in the photon background was solved under LIV in the photon sector hypothesis. The mean-free path of the $\gamma\gamma_{\text{CB}} \rightarrow e^{+}e^{-}$ interaction was calculated considering LIV effects. Moderate LIV coefficients introduce a significant change in the mean-free path of the interaction as shown in Section 2 and Figures 1–3. The corresponding LIV photon horizon was calculated as shown in Figure 4.

The dependence of the integral flux of GZK photons on the model for the sources of UHECRs is discussed in Section 3 and shown in Figures 5 and 7. The flux changes several orders of magnitude for different injection spectra models. A difference of about 500% is also found for different source evolution models. Previous LIV limits were calculated using GZK photons generated by source models currently excluded by the data (Galaverni & Sigl 2008a). The calculations presented here show LIV limits based on source models compatible with current UHECR data. In particular, model C_3R_5 was shown to describe the energy spectrum, composition, and arrival direction of UHECR (Unger et al. 2015) and therefore is chosen as our reference result.

The calculated GZK photon fluxes were compared to most updated upper limits from the Pierre Auger Observatory and are shown in Figures 8–10. For some of the models, it was possible to impose limits on the LIV coefficients, as shown in Table 2. It is important to note that the LIV limits shown in Table 2 were derived from astrophysical models of UHECR, compatible to the most updated data. The limits presented here are several orders of magnitude more restrictive than previous calculations based on the arrival time of TeV photons (The H.E.S.S. Collaboration 2011; Vasileiou et al. 2013); however, the comparison is not straightforward due to different systematics of the measurements and energy of the photons.

R.G.L. is supported by FAPESP (2014/26816-0, 2016/24943-0). H.M.H. acknowledges IFSC/USP for their hospitality during the developments of this work, Abdel Pérez Lorenzana for enlightening discussions, and the support from Conacyt Mexico under grant 237004 and the Brazilian agency FAPESP (2017/03680-3). V.d.S. thanks the Brazilian population support via FAPESP (2015/15897-1) and CNPq. This work has partially made use of the computing facilities of the Laboratory of Astroinformatics (IAG/USP, NAT/Unicsul), whose purchase was made possible by the Brazilian agency FAPESP (2009/54006-4) and the INCT-A. The authors acknowledge the National Laboratory for Scientific Computing (LNCC/MCTI, Brazil) for providing HPC resources of the SDumont supercomputer, which have contributed to the research results reported within this paper (http://sdumont.lncc.br).

Software: CRPropa3 (Batista et al. 2016, as developed on https://github.com/CRPropa/CRPropa3, EleCa (Settimo & Domenico 2015).

Appendix
Description of the LIV Model

Equation (1) leads to unconventional solutions of the energy threshold in particle production processes of the type $AB \rightarrow CD$. In this paper, the $\gamma\gamma_{\text{CB}} \rightarrow e^{+}e^{-}$ interaction is considered. From now on, the symbol γ refers to a high energy gamma-ray with energy $E_\gamma = [10^9, 10^{22}]$ eV that propagates in the universe and interacts with the CB photons, γ_{CB}, with energy $\epsilon = [10^{-11}, 10]$ eV.

Considering LIV in the photon sector, the specific dispersion relations can be written as

$$\begin{aligned} E_\gamma^2 - p_\gamma^2 &= \delta_{\gamma,n}\, E_\gamma^{n+2}, \\ \epsilon^2 - p_{\gamma_{\text{CB}}}^2 &= \delta_{\gamma,n}\, \epsilon^{n+2}, \end{aligned} \tag{6}$$

where $\delta_{\gamma,n}$ is the n-order LIV coefficient in the photon sector and therefore taken to be the same in both dispersion relations. The standard LI dispersion relation for the electron–positron pair follows: $E_{e^\pm}^2 - p_{e^\pm}^2 = m_e^2$.

Taking into account the inelasticity (K) of the process ($E_{e^-} = KE_\gamma$) and imposing energy–momentum conservation in the interaction, the following expression for a head-on collision with collinear final momenta can be written to leading order in $\delta_{\gamma,n}$

$$\begin{aligned} &4\epsilon E_\gamma - m_e^2\left(\frac{1}{K(1-K)} - \frac{m_e^2}{2K(1-K)(E_\gamma+\epsilon)^2}\right) \\ &= -\delta_{\gamma,n}E_\gamma^{n+2}\left[1 + \frac{\epsilon^{n+2}}{E_\gamma^{n+2}} - \frac{\epsilon}{E_\gamma}\left(1 + \frac{\epsilon^n}{E_\gamma^n}\right)\right]. \end{aligned} \tag{7}$$

In the ultra relativistic limit $E_\gamma \gg m_e$ and $E_\gamma \gg \epsilon$, this equation reduces to

$$\delta_{\gamma,n}E_\gamma^{n+2} + 4E_\gamma\epsilon - m_e^2\frac{1}{K(1-K)} = 0. \tag{8}$$

Equation (8) implies two scenarios: (I) $\delta_{\gamma,n} > 0$ the photo-production threshold energy is shifted to lower energies and (II) $\delta_{\gamma,n} < 0$ the threshold takes place at higher energies than that expected in an LI regime, except for scenarios below a critical value for delta, where the photo-production process is forbidden. Notice that, if $\delta_{\gamma,n} = 0$ in Equation (8) the LI regime is recovered. In the LI regime, it is possible to define $E_\gamma^{\text{LI}} = \frac{m_e^2}{4\epsilon K(1-K)}$. The math can be simplified by the introduction of the dimensionless variables

$$x_\gamma = \frac{E_\gamma}{E_\gamma^{\text{LI}}}, \tag{9}$$

and

$$\Lambda_{\gamma,n} = \frac{E_\gamma^{\text{LI}\,(n+1)}}{4\epsilon}\delta_{\gamma,n}. \tag{10}$$

Then, Equation (8) takes the form

$$\Lambda_{\gamma,n}x_\gamma^{n+2} + x_\gamma - 1 = 0. \tag{11}$$

Studying the values of $\delta_{\gamma,n}$ for which Equation (11) has a solution, one can set the extreme allowed LIV coefficient (Galaverni & Sigl 2008b; Martínez-Huerta & Pérez-Lorenzana 2017). The limit LIV coefficient ($\delta_{\gamma,n}^{\text{lim}}$) for which the interaction

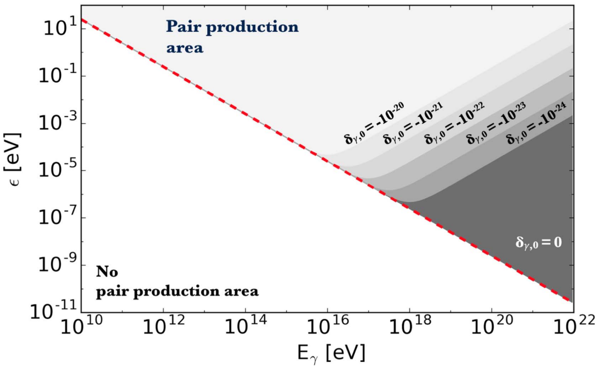

Figure 11. Allowed regions for the pair production in the $\gamma\gamma_{\rm CB} \rightarrow e^{+}e^{-}$ interaction considering LIV effects. The high energy photon (E_γ) and background photon (ϵ) parameter space is shown divided in gray regions for each value of $\delta_{\gamma,0}$. The gray areas are cumulative from darker to lighter gray. The red dashed line is a reference for $\delta_{\gamma,0} = 0$ (LI case).

is kinematically allowed for a given E_γ and ϵ is given by

$$\delta_{\gamma,n}^{\rm lim} = -4 \frac{\epsilon}{E_{\gamma}^{{\rm LI}\,(n+1)}} \frac{(n+1)^{n+1}}{(n+2)^{n+2}}. \qquad (12)$$

Equation (11) has real solutions for x_γ only if $\delta_{\gamma,n} > \delta_{\gamma,n}^{\rm lim}$. Therefore, under the LIV model considered here, if $\delta_{\gamma,n} < \delta_{\gamma,n}^{\rm lim}$, high energy photons would not interact with background photons of energy ϵ.

For a given E_γ and $\delta_{\gamma,n}$ the threshold background photon energy ($\epsilon_{\rm th}^{\rm LIV}$) including LIV effects is

$$\epsilon_{\rm th}^{\rm LIV} = \frac{m_e^2}{4E_\gamma K(1-K)} - \frac{\delta_{\gamma,n} E_\gamma^{n+1}}{4}. \qquad (13)$$

The superscript LIV is used for emphasis. In the paper, $\epsilon_{\rm th}^{\rm LIV}$ as given by Equation (13) will be used for the calculations of the mean-free path of the $\gamma\gamma_{\rm CB} \rightarrow e^{+}e^{-}$ interaction. Figure 11 shows the allowed parameter space of E_γ and ϵ for different values of $\delta_{\gamma,0}$. The gray areas are cumulative from darker to lighter gray.

ORCID iDs

Rodrigo Guedes Lang https://orcid.org/0000-0003-0492-5628
Humberto Martínez-Huerta https://orcid.org/0000-0001-7714-0704
Vitor de Souza https://orcid.org/0000-0003-0865-233X

References

Ahluwalia, D. V. 1999, Natur, 398, 199
Aloisio, R., Berezinsky, V., & Blasi, P. 2014, JCAP, 10, 020
Amelino-Camelia, G. 2001, Natur, 410, 1065
Amelino-Camelia, G., Ellis, J. R., Mavromatos, N. E., Nanopoulos, D. V., & Sarkar, S. 1998, Natur, 393, 763
Atwood, W. B., et al. 2009, ApJ, 697, 1071
Batista, R. A., Dundovic, A., Erdmann, M., et al. 2016, JCAP, 05, 038
Benjamin Zitzer for the VERITAS Collaboration 2014, Proc. ICRC (Rio de Janeiro), 33, 1147
Berezinsky, V., Gazizov, A., & Grigorieva, S. 2006, PhRvD, 74, 043005
Bi, X.-J., Cao, Z., Li, Y., & Yuan, Q. 2009, PhRvD, 79, 083015
Biteau, J., & Williams, D. A. 2015, ApJ, 812, 60
Bluhm, R. 2014, in Springer Handbook of Spacetime, ed. A. Ashtekar & V. Petkov (Berlin: Springer), 485
Breit, G., & Wheeler, J. A. 1934, PhRv, 46, 1087
Carla Bleve for the Pierre Auger Collaboration 2015, Proc. ICRC (The Hague), 34, 1103
Chang, Z., Li, X., Lin, H.-N., et al. 2016, ChPhC, 40, 045102
Coleman, S., & Glashow, S. L. 1999, PhRvD, 59, 116008
Coleman, S. R., & Glashow, S. L. 1997, PhLB, 405, 249
De Angelis, A., Galanti, G., & Roncadelli, M. 2013, MNRAS, 432, 3245
Ellis, J., Mavromatos, N., Nanopoulos, D., Sakharov, A., & Sarkisyan, E. 2006, APh, 25, 402
Ellis, J., Mavromatos, N., Nanopoulos, D., Sakharov, A., & Sarkisyan, E. 2008, APh, 29, 158
Ellis, J., & Mavromatos, N. E. 2013, APh, 43, 50
Fairbairn, M., Nilsson, A., Ellis, J., Hinton, J., & White, R. 2014, JCAP, 1406, 005
Galaverni, M., & Sigl, G. 2008a, PhRvL, 100, 021102
Galaverni, M., & Sigl, G. 2008b, PhRvD, 78, 063003
Gelmini, G., Kalashev, O., & Semikoz, D. V. 2007, APh, 28, 390
Gervasi, M., Tartari, A., Zannoni, M., Boella, G., & Sironi, G. 2008, ApJ, 682, 223
Gilmore, R., & Ramirez-Ruiz, E. 2010, ApJ, 721, 709
Greisen, K. 1966, PhRvL, 16, 748
Haungs, A., Medina-Tanco, G., & Santangelo, A. 2015, ExA, 40, 1
Hopkins, A. M., & Beacom, J. F. 2006, ApJ, 651, 142
Inés Valiño for the Pierre Auger Collaboration 2015, Proc. ICRC (The Hague), 34, 271
J. Holder for the VERITAS Collaboration 2011, Proc. ICRC (Beijing), 32, 137
Jacob, U., & Piran, T. 2008, JCAP, 01, 031
Jacobson, T., Liberati, S., & Mattingly, D. 2003, PhRvD, 67, 124011
Klinkhamer, F. R., & Schreck, M. 2008, PhRvD, 78, 085026
Le, T., & Dermer, C. D. 2007, ApJ, 661, 394
Liberati, S., & Maccione, L. 2009, ARNPS, 59, 245
Liberati, S., & Maccione, L. 2011, JPhCS, 314, 012007
Lorentz, M., & Brun, P. 2017, EPJWC, 136, 03018
Maccione, L., & Liberati, S. 2008, JCAP, 0808, 027
Martínez-Huerta, H., & Pérez-Lorenzana, A. 2017, PhRvD, 95, 063001
Mattingly, D. 2005, LRR, 8, 5
Myers, R. C., & Pospelov, M. 2003, PhRvL, 90, 211601
Olive, K., & Group, P. D. 2014, ChPhC, 38, 090001
Otte, A. N. 2012, Proc. ICRC (Beijing), 32, 256
Rubtsov, G., Satunin, P., & Sibiryakov, S. 2017, JCAP, 1705, 049
Schreck, M. 2014, in Proc. 6th Meeting on CPT and Lorentz Symmetry, ed. A. Kostelecky (Singapore: World Scientific), 176
Settimo, M., & Domenico, M. D. 2015, APh, 62, 92
Stecker, F. W., & Scully, S. T. 2005, APh, 23, 203
Stecker, F. W., & Scully, S. T. 2009, NJPh, 11, 085003
Tavecchio, F., & Bonnoli, G. 2016, A&A, 585, A25
The AGASA Collaboration 2006, NuPhs, 151, 3
The CTA Consortium 2011, ExA, 32, 193
The H.E.S.S. Collaboration 2006, A&A, 457, 899
The H.E.S.S. Collaboration 2011, APh, 34, 738
The MAGIC Collaboration 2008, PhLB, 668, 253
The MAGIC Collaboration 2016, APh, 72, 61
The Pierre Auger Collaboration 2014a, PhRvD, 90, 122005
The Pierre Auger Collaboration 2014b, PhRvD, 90, 122006
The Pierre Auger Collaboration 2015, NIMPA, 798, 172
The Pierre Auger Collaboration 2017a, JCAP, 04, 009
The Pierre Auger Collaboration 2017b, JCAP, 04, 038
Tinyakov, P. 2014, NIMPA, 742, 29
Unger, M., Farrar, G. R., & Anchordoqui, L. A. 2015, PhRvD, 92, 123001
Vasileiou, V., Jacholkowska, A., Piron, F., et al. 2013, PhRvD, 87, 122001
Xu, H., & Ma, B.-Q. 2016, APh, 82, 72
Yüksel, H., Kistler, M. D., Beacom, J. F., & Hopkins, A. M. 2008, ApJL, 683, L5
Zatsepin, G. T., & Kuz'min, V. A. 1966, ZhPmR, 4, 114
Zhen, C. 2010, ChPhC, 34, 249
Zou, X.-B., Deng, H.-K., Yin, Z.-Y., & Wei, H. 2017, Phys. Lett. B, 776, 284

5 IMPROVED LIMITS ON LORENTZ INVARIANCE VIOLATION FROM ASTROPHYSICAL GAMMA-RAY SOURCES

PHYSICAL REVIEW D **99,** 043015 (2019)

Improved limits on Lorentz invariance violation from astrophysical gamma-ray sources

Rodrigo Guedes Lang,[*] Humberto Martínez-Huerta,[†] and Vitor de Souza[‡]
Instituto de Física de São Carlos, Universidade de São Paulo,
Avenue Trabalhador São-carlense 400, CEP 13566-590 São Carlos, SP, Brasil

(Received 16 August 2018; published 28 February 2019)

Lorentz invariance (LI) has a central role in science and its violation (LIV) at some high-energy scale has been related to possible solutions for several of the most intriguing puzzles in nature such as dark matter, dark energy, cosmic rays generation in extreme astrophysical objects and quantum gravity. We report on a search for LIV signal based on the propagation of gamma rays from astrophysical sources to Earth. An innovative data analysis is presented which allowed us to extract unprecedented information from the most updated data set composed of 111 energy spectra of 38 different sources measured by current gamma-ray observatories. No LIV signal was found, and we show that the data are best described by LI assumption. We derived limits for the LIV energy scale at least 3 times better than the ones currently available in the literature for subluminal signatures of LIV in high-energy gamma rays.

DOI: 10.1103/PhysRevD.99.043015

I. INTRODUCTION

Lorentz invariance (LI) is one of the pillars of fundamental physics and its violation (LIV) has been proposed by several quantum gravity and effective field theories [1–12]. Astroparticles have proven to be a sensitive probe for LIV and its signatures in the photon sector have been searched through arrival time delay, photon splitting, spontaneous emission, shift in the pair production energy threshold and many others effects [13–40]. In particular, the strongest limits for subluminal signatures of LIV based on the propagation of high-energy gamma rays have been imposed using the energy spectra of TeV gamma-ray sources [31,36,37] and the time delay of TeV gamma-rays emitted by gamma-ray bursts (GRBs) [41].

The framework summarized in the next section shows how the interaction of gamma rays with background photons on the way from the source to Earth modulates the intrinsic energy spectrum emitted by the source. The modulation of the spectrum is considerably different if the interactions in the propagation are taken to be LI or LIV. Previous works have shown how to extract the effect of the propagation from the measured energy spectrum allowing us to identify the assumption (LI or LIV) which best describes the data [31,36,37]. These analyses have been limited mainly by (a) poor knowledge of the extra-Galactic background light (EBL), (b) large uncertainties in the intrinsic energy spectra functional form, (c) scarce data and (d) not fully optimized analysis procedures.

In this work, a new analysis method is proposed to help overcoming these limitations and to contribute in improving the power to search for LIV signatures in TeV gamma-ray energy spectra. Moreover, the most updated data set available in the literature was analyzed: 111 energy spectra from 38 different sources. Two selection steps are implemented in this analysis. First, a selection procedure is developed to choose the relevant measured spectra. We show that only 18 spectra from 6 sources out of the 111 spectra from 38 sources have power to constrain LIV beyond the current limits. This selection procedure developed here can be used in any future analysis to evaluate which new measured spectrum is relevant to impose LIV limits. Second, the analysis method developed in Sec. III considers carefully each measured point of each spectrum, rejecting any data that could bias the result towards a faked positive LIV signal. The use of the most complete data set combined with an innovative analysis procedure resulted in the best LIV limits derived so far using this framework as shown in Sec. IV. The limitations of the method developed here are tested in Appendix B in which we shown that the results are robust under (a) poor knowledge of the EBL, (b) large uncertainties in the intrinsic energy spectra functional form, (c) energy resolution, (d) selection of spectra and (e) energy bins selection used in the calculation of the intrinsic energy spectra.

II. LIV IN THE GAMMA-RAY ASTROPHYSICS FRAMEWORK

Subluminal LIV in the photon sector can be described as a polynomial correction of the dispersion relation:

---

[*] rodrigo.lang@usp.br
[†] humbertomh@ifsc.usp.br
[‡] vitor@ifsc.usp.br

© 2019 American Physical Society

$$E_\gamma^2 - p_\gamma^2 = -\frac{E_\gamma^{(n+2)}}{(E_{\mathrm{LIV}}^{(n)})^n}, \tag{1}$$

where E_γ is the energy and p_γ the momentum of the gamma ray. Natural units are used in this work (c = 1). $E_{\mathrm{LIV}}^{(n)}$ is the LIV energy scale for each correction order n. $E_{\mathrm{LIV}}^{(n)}$ is the parameter to be constrained in this analysis because it modulates the effect and is used to derive the energy beyond which the energy dispersion relation departures from LI. Only the two leading orders $n = 1, 2$ are considered hereafter. Best current limits at 2σ confidence level for subluminal signatures of LIV in high-energy gamma rays are $E_{\mathrm{LIV}}^{(1)} = 9.27 \times 10^{28}$ eV [41] and $E_{\mathrm{LIV}}^{(2)} = 8.7 \times 10^{20}$ eV [36].

On their way to Earth, TeV gamma rays interact with the EBL photons creating pairs:

$\gamma + \gamma_{\mathrm{EBL}} \to e^+ + e^-$ [42]. In the next section, we use the EBL model of Franceschini [43] as implemented in Ref. [44] and the influence of other models [45,46] is tested in Appendix B 1. Successive interactions attenuate the emitted gamma-ray flux as described by

$$a(E, z) = e^{-\tau}(E, z) = \frac{J_{\mathrm{meas}}(E)}{J_{\mathrm{int}}(E, z)}, \tag{2}$$

where J_{meas} is the measured spectrum at Earth and J_{int} is the intrinsic spectrum emitted by the source. $a(E, z)$ is called attenuation and τ is the optical depth.

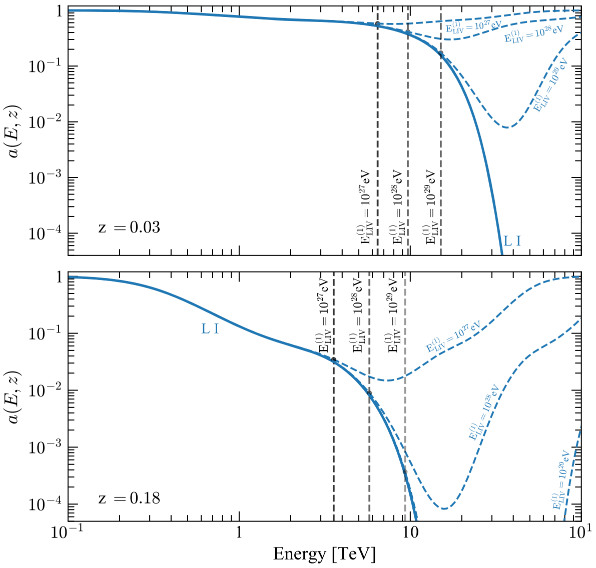

FIG. 1. Examples of attenuation as a function of gamma-ray energy. Upper and bottom panels correspond to a source at z = 0.03 and 0.18, respectively. Four cases are shown for LI and LIV with $E_{\mathrm{LIV}}^{(1)} = 10^{27}$, 10^{28} and 10^{29} eV. Dashed vertical lines shows the energy in which the LIV attenuation is 10% higher than the LI attenuation.

If LIV is considered, the pair-production energy threshold increases and the gamma rays have less probability to interact with the EBL photons. As a consequence, the optical depth decreases and the gamma ray propagates farther in the Universe [35,42]. Figure 1 shows an example of this effect in the attenuation of gamma rays from two sources at z = 0.03 and 0.18 as a function of the energy. Four cases were calculated assuming LI and LIV with $E_{\mathrm{LIV}}^{(1)} = 10^{27}$, 10^{28} and 10^{29} eV. The interaction suppresses the flux at the highest energies. When LI is considered, there is a steep and definitive drop in the attenuation curve. However, when LIV is considered, the interaction becomes less probable for the highest energetic gamma rays which can propagate further causing a recovery of the flux. The intensity of the effect depends on the energy of the gamma ray, on the LIV energy scale and on the distance of the source. In the next section, a method is developed to deal with these dependencies and extract the LIV energy scale ($E_{\mathrm{LIV}}^{(n)}$) which best describes the data.

III. ANALYSIS METHOD AND DATA SELECTION

The use of multiple sources at different distances can be combined by proper analysis methods to improve the search for a LIV signal. Each measured energy spectrum contributes with a given strength to the analysis efficiency. Selecting only the relevant data helps to increase the statistics power without adding systematic effects. We considered here every energy spectrum measured by each observatory as independent measurements.

Figure 1 shows that there is an energy window of interest in between the abrupt fall of the LI attenuation and the recovery in the LIV curve ranging from a few up to hundreds of TeV depending on the source distance. In this energy range it is easier to differentiate the LI from the LIV assumption. Gamma-ray observatories have continuously coverage from hundreds of GeV to few TeV and the upper energy threshold is given by collection area. Therefore LIV studies are usually limited by the maximum energy which can be measured by the experiments.

In summary, only two quantities determine the contribution of a measured spectrum in searching for a LIV signal: the distance of the source and the maximum energy measured in that spectrum, (E_{max}). The distance of the source controls the amount of modulation in the spectrum and E_{max} sets how much data is available in the energy window of interest. Based on this discussion, we propose to select measurements in which the attenuation ratio between LIV and LI assumptions at E_{max} differs by at least 10%: $a_{\mathrm{LIV}}/a_{\mathrm{LI}} > 1.1$. These points are illustrated by the horizontal dashed lines in Fig. 1.

Figure 2 summarizes the spectrum selection procedure. Dashed curves show the distances (z) as a function of energy for which $a_{\mathrm{LIV}}/a_{\mathrm{LI}} > 1.1$. Each curve was calculated for a different value of $E_{\mathrm{LIV}}^{(1)}$ as shown. The black crosses and the red stars show the distance of the source and

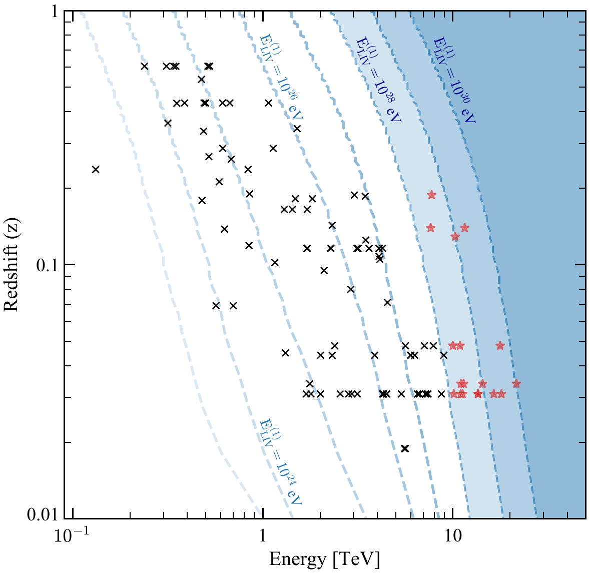

FIG. 2. Distance as a function of energy for which $a_{\rm LIV}/a_{\rm LI} > 1.1$ are shown as dashed lines for several $E_{\rm LIV}^{(1)}$ values. Black crosses and the red stars show the distance and $E_{\rm max}$ of all 111 measured energy spectra used in this work as taken from the TeVCat catalog [47]. Red stars show the spectra with power to set a LIV energy scale limit more stringent than the current available one. The selected spectra are shown in Appendix A.

$E_{\rm max}$ of all 111 measured energy spectra used in this work. The measurements were taken from the TeVCat catalog [47] and confirmed in the original publications. An energy spectrum is useful to set a limit of $E_{\rm LIV}^{(1)}$ if its ($E_{\rm max}$, z) point is on the right side of the corresponding $E_{\rm LIV}^{(1)}$ line. Given that we aim at setting limits on $E_{\rm LIV}^{(1)}$ more stringent than the ones already available in the literature ($E_{\rm LIV}^{(1)} \sim 10^{28}$ eV), we have selected only 18 spectra from 6 sources [37,48–60], shown as red stars in Fig. 2 for further considerations in this analysis. In Appendix A, these selected spectra are discriminated in Table II, and in Appendix B 4, we also show the effect of including other 11 spectra from 3 sources [50,61–66] in the analysis and we prove our hypothesis that the latter are useless to improve the search for a LIV signal.

Once the relevant energy spectra are chosen, the standard analysis procedure follows four steps: (I) from the measured spectra, calculate the intrinsic spectra using the LI attenuation at the distance of each source, (II) model the intrinsic spectra with a functional form, (III) using the model of the intrinsic spectra calculate the spectra at Earth supposing several LIV energy scales, (IV) compare the calculated LIV spectra on Earth with the measured spectra on Earth and set which value of LIV energy scale best describes the data.

We consider here a more carefully analysis of the first step. If LIV is true in nature, the highest energetic gamma rays measured on Earth interacted in its way under LIV, therefore, the assumption of step (I) can be false. In other words, the measured spectrum can not be deattenuated under LI assumption to calculate the intrinsic spectrum if finding a LIV signal is the target of the analysis. Apparently, this point has been neglected in previous studies of this kind and its consequence is to artificially produce a LIV signal or artificially improve the LIV energy scale limits.

We have taken care of that by using only points in each energy spectrum which could not be differentiated between a LI and LIV propagation as explained below. We define a fiducial LI region in each measured energy spectrum as the energy range in which the measured flux cannot distinguish between LI and LIV propagation. The fiducial LI region of each spectrum is constituted by the set of energy bins that fulfills the following condition:

$$\frac{a_{\rm LIV}}{a_{\rm LI}} \leq \frac{J_{\rm meas}(E) + \rho\sigma(J_{\rm meas}(E))}{J_{\rm meas}(E)}, \tag{3}$$

where $a_{\rm LIV}$ and $a_{\rm LI}$ are the LIV and LI attenuation, respectively. $J_{\rm meas}$ and $\sigma(J_{\rm meas})$ are the measured flux and its statistical uncertainty, respectively. ρ is an input parameter of the analysis taken as $\rho = 1$. In Appendix B 5, we test larger values of ρ and show that the results presented here are robust under reasonable choices of ρ.

According to the condition in Eq. (3), bins in which the difference in $a_{\rm LIV}$ and $a_{\rm LI}$ are larger than the statistical uncertainty of the measured flux are discarded in the reconstruction of the intrinsic spectrum. Only points satisfying the condition are used to calculate the intrinsic spectrum. These points can be safely deattenuated using $a_{\rm LI}$ (analysis step I) to calculate the intrinsic flux at the source avoiding the introduction of spurious LIV signal.

We modeled the intrinsic spectrum at the source by a simple power law and by a power law with an exponential cutoff (analysis step II). As shown in Appendix B 2, the data are better described when a power law with an exponential cutoff:

$$J_{\rm int}(E) = A\left(\frac{E}{E_0}\right)^{-\Gamma} e^{-E/E_{\rm cut}}, \tag{4}$$

where the normalization A, the spectral index Γ and the energy cutoff $E_{\rm cut}$ are free parameters. E_0 is a reference energy taken to be $E_0 = 1$ TeV. The best fitted parameters (A, Γ and $E_{\rm cut}$) and its one sigma statistical uncertainties are considered in the next step of the analysis.

The fitted intrinsic spectra are propagated back to Earth under the assumption of LIV (analysis step III). The calculated energy spectra on Earth is defined as $J_{\rm cal} = a_{\rm LIV} \times J_{\rm int}$ for several LIV energy scales. We varied $E_{\rm LIV}^{(1)}$ from 4×10^{27} eV to 10^{30} eV in log steps of 0.0041 and $E_{\rm LIV}^{(2)}$ from 2×10^{20} eV to 10^{22} eV in log steps of 0.0041. Note that the LI scenario corresponds to $E_{\rm LIV}^{(n)} \to \infty$. The most important experimental feature in the measured energy spectrum is the energy resolution of the detection. We have considered an energy resolution of 10%. Each bin in $J_{\rm cal}$ was smeared by a Gaussian with width equal to 10% of the bin energy using a forward-folding technique. In Appendix B 3, we tested other values of the energy resolution and show that the conclusions presented here are not changed if reasonable values of the energy resolution are considered.

At this point in the analysis, for each of the 18 measured spectra, we have calculated several $J_{\rm cal}$ spectra covering (a) many $E_{\rm LIV}^{(n)}$ values and (b) many possibilities of intrinsic spectra inside the one sigma uncertainty of the best fitted values. Each one of these $J_{\rm cal}$ spectra is finally compared to the measured $J_{\rm meas}$ spectra using a log-likelihood statistical test (analysis step IV). In this test, all measured points in the energy spectra are used. For each $E_{\rm LIV}^{(n)}$, the log-likelihood value ($2\mathcal{L}$) of all 18 spectra are summed. It is only here that all 18 spectra contribute together to limit one value of $E_{\rm LIV}^{(n)}$. Upper limits in the measured flux have also been used in the log-likelihood calculation and they play a very important role in limiting the recover of the LIV flux.

Without loss of generality, we have chosen to analyze only the two limiting cases within the one sigma uncertainty best fitted parameters of the intrinsic spectra. We show only the bracketing solutions of the intrinsic spectra which have the lowest and highest values of $2\mathcal{L}$. We named these solutions LIV-disfavored and LIV-favored, respectively. The variation of $2\mathcal{L}$ with $E_{\rm LIV}^{(n)}$ determines the presence of a LIV signal or the LIV energy scale limits as analyzed in details in the next section.

IV. NEW LIV LIMITS

Figure 3 shows the variation of the log-likelihood value with $E_{\rm LIV}^{(n)}$ for $n = 1$ and $n = 2$ for LIV-disfavored and LIV-favored cases. The discontinuity in one curve in Fig. 3 is a consequence of the analysis procedure explained in the last section. The discontinuity is caused by the inclusion of an extra point in the fiducial LI region when the $E_{\rm LIV}^{(n)}$ moves upwards. The minimum log-likelihood value ($\mathcal{L}_{\rm min}$) was found when the maximum $E_{\rm LIV}^{(n)}$ is considered. The tendency of $2(\mathcal{L} - \mathcal{L}_{\rm min})$ in Fig. 3 shows the log-likelihood difference vanishing with $E_{\rm LIV}^{(n)} \to \infty$ which corresponds to the LI case. In conclusion, the data set formed by the 18 energy spectra considered here is best described by a LI model.

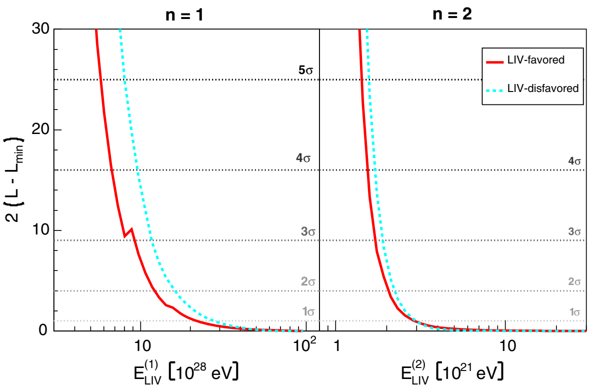

FIG. 3. Log-likelihood value as a function of the LIV energy scale. Left plot is for $n = 1$ and right plot for $n = 2$. The red full and cyan dashed line represent the LIV-favored and LIV-disfavored cases, respectively. The horizontal dashed lines represent the 1, 2, 3, 4 and 5σ rejection confidence levels.

TABLE I. Limits on the LIV energy scale imposed by this analysis. Only the most conservative limits are shown corresponding to the LIV-favored case.

	2σ	3σ	5σ
$E_{\rm LIV}^{(1)}$ [10^{28} eV]	12.08	9.14	5.73
$E_{\rm LIV}^{(2)}$ [10^{21} eV]	2.38	1.69	1.42

Thus, it is possible to impose limits on the LIV energy scale. The LIV model corresponding to a given $E_{\rm LIV}^{(n)}$ can be excluded with a confidence level (CL) given by $\sigma = \sqrt{2(\mathcal{L} - \mathcal{L}_{\rm min})}$ as shown by the dashed horizontal lines

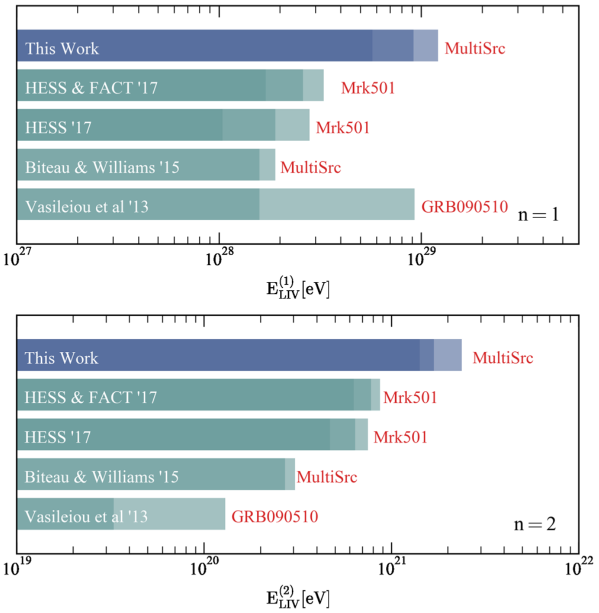

FIG. 4. Comparison of the best limits imposed on the LIV energy scale. Left panel for $n = 1$ and right panel for $n = 2$. Shades of blue and green correspond to 2, 3 an 5σ CL. Only the most conservative limits of our analysis are shown corresponding to the LIV-favored case. This work and Biteau and Williams' s 15 are based on multiple sources (MultiSrc), the latter of which are translated to the photon sector and to the quadratic term. The other limits are based on specific measurement of one source as appointed.

in Fig. 3. Table I shows the limits imposed by this analysis for $E^{(1)}_{\rm LIV}$ and $E^{(2)}_{\rm LIV}$ with 2σ, 3σ and 5σ CL. We show the limits for most conservative scenario based on the LIV-favored case.

Figure 4 compares the LIV energy scale limits presented in this work with the best limits in the literature: (a) the best limits from spectral analysis of a single TeV source imposed by the Markarian 501 measurements from HESS and FACT [36,37], (b) the best limits from spectral analysis of multiple TeV sources [31], and (c) the best limits from time delay analysis of gamma-ray bursts (GRB) imposed by the GRB090510 measurements from MAGIC [41]. The limits imposed in this work are at least 3 times better than the ones presented in previous works.

The comparison between the results presented here and limits obtained from the nonobservation of ultra-high-energy (UHE) photons is not straightforward. LIV limits imposed with TeV gamma rays and UHE photons are independent and complementary analysis. Some analysis using upper limits on UHE photon photon flux are more constraining than the TeV gamma-ray limits shown here, however they are strongly dependent on the astrophysical assumptions considered [35].

V. CONCLUSIONS

In this work, we propose a new analysis procedure for searching LIV signatures using multiple TeV measured energy spectra. The analysis method developed here includes (a) a procedure to select the relevant measured spectra and (b) a procedure to select which bins in each measured energy spectrum should be considered to calculate the intrinsic energy spectrum of the source. Both selections minimized the systematic bias of the analysis and allowed us to obtain a very robust result irrespective of the issues which traditionally penalized the LIV studies, such as poor knowledge of the EBL, large uncertainties in the intrinsic energy spectra functional form, scarce data and energy resolution. The influence of these limitations and the possible biases introduced by the new criteria are evaluated in Appendix B, where we show that our conclusions are valid despite these limitations and biases.

Throughout the paper we consider only subluminal LIV in the photon sector to allow the comparison with a large set of previous studies. If LIV in the electron sector is also considered (pair-production), the LIV parameter $1/\mathrm{E}_{\rm LIV}$ becomes a linear combination of the LIV contributions from the different particle species [32]. In the most common scenario, photons dominate over electrons, and the derived results in this work remain the same. In the second most common scenarios, LIV is universal for photons and electrons, and a factor of $1/(1-1/2^n)$ should be considered in the final results [67]. The superluminal propagation of photons is not considered in the paper because its consequences would require a specific data analysis, probably different from the one used in this paper.

We applied this analysis method to the most updated gamma-ray TeV data set. We considered 111 measured energy spectra from 38 sources; only 18 measured spectra from 6 sources were shown to significantly contribute to restricting the LIV energy scale beyond the current limits. We conclude that the data set is best described by LI assumption, and we impose strict limits to the LIV energy scale. Figure 4 summarizes the results. At 5σ exclusion CL, the LIV energy scale limits imposed here are 3.3 times better than the best limits from previous TeV spectra analysis and 3.6 times better than the best limits from previous time delay analysis.

ACKNOWLEDGMENTS

The authors acknowledge FAPESP support No. 2015/15897-1, No. 2016/24943-0, and No. 2017/03680-3. The authors also acknowledge the National Laboratory for Scientific Computing (LNCC/MCTI, Brazil) for providing HPC resources of the SDumont supercomputer, which have contributed to the research results reported within this paper (http://sdumont.lncc.br).

APPENDIX A: SELECTED SPECTRA

This section contains the list of sources used in this analysis.

TABLE II. List of spectra 18 spectra from 6 sources out of the 111 spectra from 38 sources that fulfill the selection criteria according to the procedure proposed in the paper. Columns show the name and redshift of the source, the experiment that measured the spectra and a specification of the measured spectrum as in the original publication shown as reference in the last column.

Source	Redshift	Experiment	Spectrum	Reference
Markarian 421	0.031	HEGRA	1999–2000	[48]
			2000–2001	[48]
		HESS	2000	[49]
		VERITAS	2006–2008 (low)	[50]
			2006–2008 (mid)	[50]
		TACTIC	2005–2006	[51]
			2009–2010	[52]
Markarian 501	0.034	TACTIC	2005–2006	[53]
		ARGO-YBJ	2008–2011	[54]
			2011 (flare)	[54]
		HESS	2014 (flare)	[37]
1ES 1959 + 650	0.048	Whipple	2002 (flare)	[55]
		HEGRA	2002 (low)	[56]
			2002 (high)	[56]
H 1426 + 428	0.129	HEGRA	1999–2000	[57]
1ES 0229 + 200	0.1396	HESS	2005–2006	[58]
		VERITAS	2010–2011	[59]
1ES 0347-121	0.188	VERITAS	2006	[60]

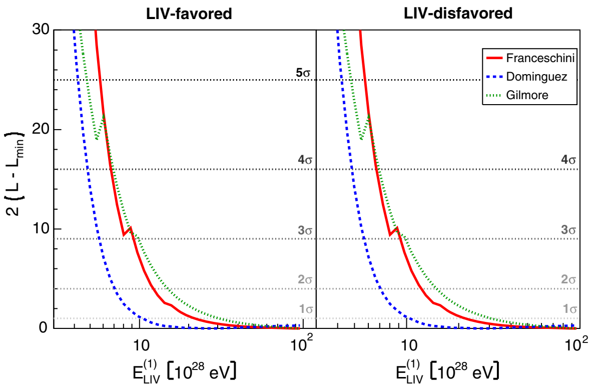

FIG. 5. Log-likelihood value as a function of the LIV energy scale for $n = 1$. Left plot shows the LIV-favored case and the right plot shows the LIV-disfavored case. Red lines show the results for the Franceschini model, green lines for Gilmore model and blue lines for the Dominguez model. The horizontal dashed lines represent the 1, 2, 3, 4 and 5σ confidence levels.

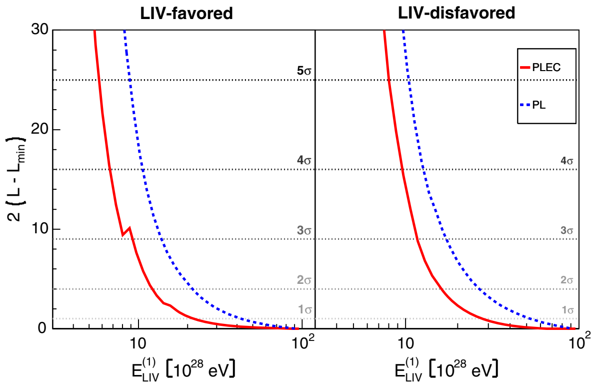

FIG. 6. Log-likelihood value as a function of the LIV energy scale for $n = 1$. Left plot shows the LIV-favored case and the right plot shows the LIV-disfavored case. The cyan and the red lines show, respectively, the results for the power law and power law with an exponential cutoff parametrizations. The horizontal dashed lines represent the 1, 2, 3, 4 and 5σ confidence levels.

APPENDIX B: EVALUATION OF THE SYSTEMATIC EFFECTS AND OF THE LIMITATIONS OF THIS ANALYSIS

In this section, we evaluate the influence of systematic effects and of the limitations of this analysis in the conclusions of the work. We compare different possible choices to the benchmark model presented in Sec. IV. The main sources of systematics and limitations of the analysis are

(i) Choices of the EBL models;
(ii) Model of the intrinsic spectrum;
(iii) Energy resolution;
(iv) Selection of spectra;
(v) Selection of energy bins to be used in the calculation of the intrinsic energy spectra.

The three first items are common to all LIV analysis based on the propagation of TeV gamma rays. The last two items are particular to the method proposed here. Below, we show the impact of different choices in the results.

1. EBL models

The uncertainties in the EBL spectrum are still large [31,46]. The reference model (Franceschini [43]) was chosen to allow the direct comparison of our results with previous works. At least two other EBL models are also used in the literature: Dominguez [46] and Gilmore [45]. We repeated our analysis using these two models and the results are shown in Fig. 5 and in Table III. The same overall behavior of the log-likelihood curves is obtained and the numerical values of $E_{\mathrm{LIV}}^{(n)}$ at the same confidence level are compatible to the reference analysis.

TABLE III. Limits on the LIV energy scale imposed by this work for different EBL models.

	Franceschini			Dominguez			Gilmore		
	2σ	3σ	5σ	2σ	3σ	5σ	2σ	3σ	5σ
$E_{\mathrm{LIV}}^{(1)}$ [10^{28} eV]	12.08	9.14	5.73	6.85	5.62	4.17	14.89	9.80	4.74
$E_{\mathrm{LIV}}^{(2)}$ [10^{21} eV]	2.38	1.69	1.42	1.56	1.40	1.14	2.17	1.78	1.31

2. Model of the intrinsic spectrum

We evaluate here the choice of a power law with an exponential cutoff (PLEC) to model the intrinsic spectrum

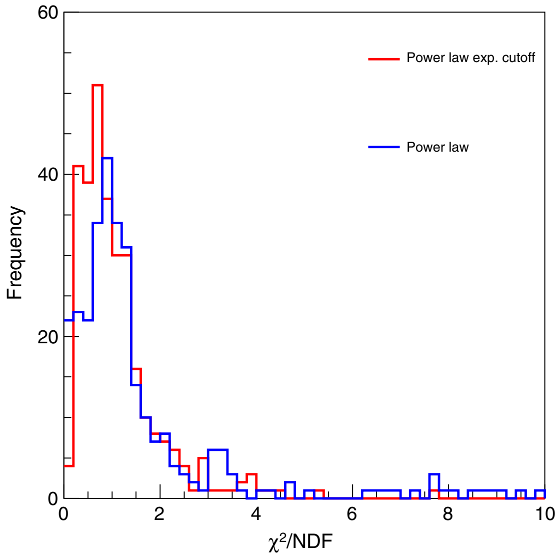

FIG. 7. Distribution of χ^2/NDF for the fitted intrinsic spectrum. The blue line represents the distribution obtained using a simple power law parametrization and the red line represents the results using a power law with an exponential cutoff.

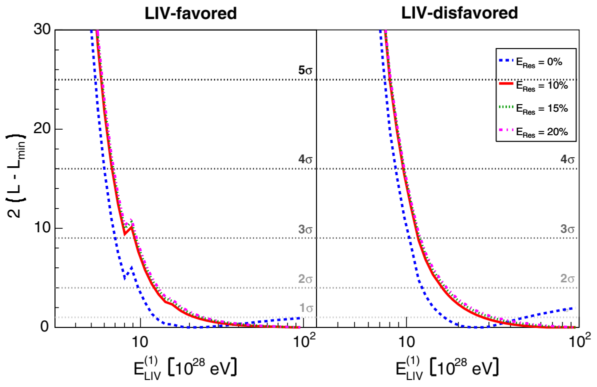

FIG. 8. Log-likelihood value as a function of the LIV energy scale for $n = 1$. Left plot shows the LIV-favored case and the right plot shows the LIV-disfavored case. The different colored lines show the results for different energy resolutions. The horizontal dashed lines represent the 1, 2, 3, 4 and 5σ confidence levels.

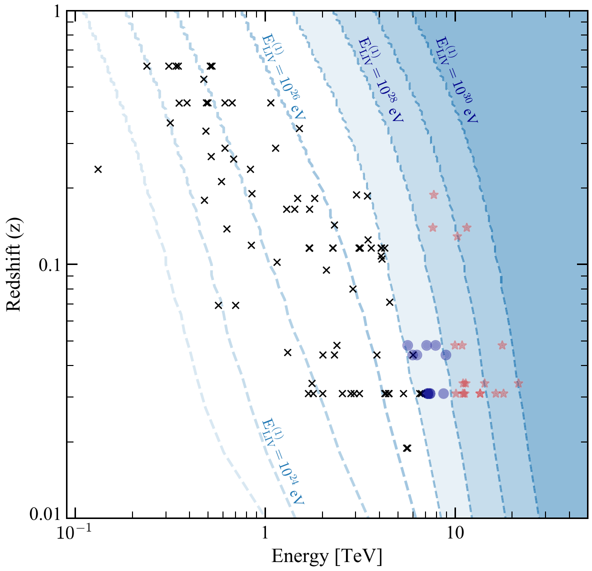

FIG. 9. Distance as a function of energy for which $a_{\mathrm{LIV}}/a_{LI} > 1.1$ are shown as dashed lines for several $E_{\mathrm{LIV}}^{(1)}$ values. Black crosses, blue circles and the red stars show the distance and $E_{\max}$ of all 111 measured energy spectra studied in this work. Reference data set A is composed by the red stars. Data set B analyzed in this section is composed of blue circles and red starts.

of the sources. This functional shape is motivated by acceleration theory of particles in the source which generate the gamma-ray flux. We test its possible bias by repeating the fit with a simple power law (PL) function. Figure 6 shows the resulting log-likelihood profile using each parametrization and Fig. 7 shows the distribution of χ^2/NDF for the reconstructed spectra using both the PL and the PLEC parametrizations.

The spectra are better reconstructed using the PLEC parametrization, with a mean χ^2/NDF of 1.12 and a standard deviation of 0.92, while the PL results in a mean χ^2/NDF of 2.04 with a standard deviation of 3.09. The limits using the PLEC parametrization are also more conservative. The PLEC parametrization contemplates a wider range of possibilities for the bins not used in the reconstruction, including the simple power law. Therefore, using a simple power law for the intrinsic spectra could bias the analysis due to both a bad reconstruction and assuming the behavior of the most energetic bins, where LIV effects emerge.

3. Energy resolution

The reference analysis considers an energy resolution of 10%. We evaluate the effect of this choice by repeating the

TABLE IV. List of spectra added in this section to evaluate the influence of the spectra choice in the procedure proposed in the paper. Columns show the name and redshift of the source, the experiment that measured the spectra and a specification of the measured spectrum as in the original publication shown as reference in the last column.

Source	Redshift	Experiment	Spectrum	Reference
Markarian 421	0.031	VERITAS	2006–2008 (highC)	[50]
			2006–2008 (very_high)	[50]
		ARGO-YBJ	2007–2010 (flux 1)	[61]
		ARGO-YBJ	2007–2010 (flux 3)	[61]
		ARGO-YBJ	2007–2010 (flux 4)	[61]
1ES 2344 + 514	0.044	Whipple	1995 (b)	[62]
		VERITAS	2007–2008 (low)	[63]
			2007–2015	[64]
1ES 1959 + 650	0.048	VERITAS	2007–2011	[65]
			2015	[66]
			2016	[66]

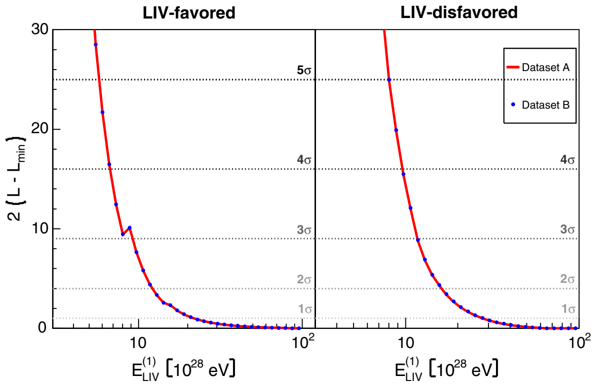

FIG. 10. Log-likelihood value as a function of the LIV energy scale for $n = 1$. The red and blue lines show the results using data sets A and B, respectively. Both lines overlap. The horizontal dashed lines represent the 1, 2, 3, 4 and 5σ confidence levels.

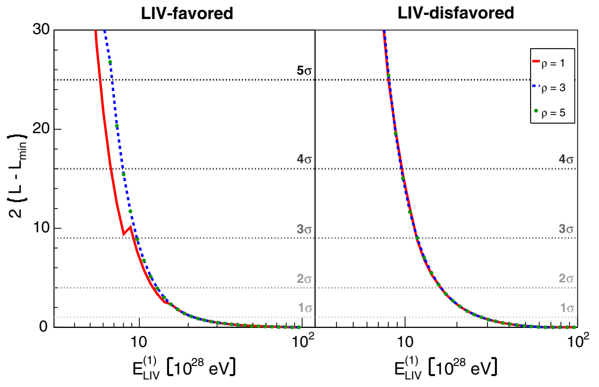

FIG. 11. Log-likelihood value as a function of the LIV energy scale for $n = 1$. Left plot shows the LIV-favored case and the right plot shows the LIV-disfavored case. The colored lines show the results for different values of ρ. The horizontal dashed lines represent the 1, 2, 3, 4 and 5σ confidence levels.

analysis with energy resolution of 0%, 15% and 20%. The log-likelihood test is shown in Fig. 8. The difference is small for energy resolutions of 10%, 15% and 20%. If perfect energy reconstruction is considered (energy resolution 0%) the analysis bias the results towards a LIV signal. This happens because the bin migration induced by the resolution artificially increases the flux at the highest energies, which mimics the LIV effect.

4. Selection of spectra

The selection procedure presented in the paper chose a subset of 18 measured spectra from 6 sources to be considered in our analysis as is shown in Fig. 9 by the red star. We tested the effect of including other measured spectra in the final result. We arbitrarily included the next 11 spectra from 3 sources in the data analysis shown as blue circles in Fig. 9 and listed in Table IV. The original data set used in III is named here data set A and previously listed in Table II. The 29 spectra composed by the original 18 plus 11 arbitrarily added to explore the systematics is named data set B. The corresponding log-likelihood test of the two data sets A and B is shown in Fig. 10. The curves overlap, we show data set B as blue points for visualization purpose. There was no significant change in the results by adding the extra 11 spectra which proves the efficiency of the selection procedure proposed in Sec. III of the paper.

5. Selection of bins in each measured spectrum

The energy region used to reconstruct the intrinsic spectrum was defined in Eq. (3) and depends on the factor ρ. The reference results were obtained using $\rho = 1$ which means we excluded from the intrinsic spectrum reconstruction any energy bin for which the difference between the LI and the LIV attenuation is larger than the error in the measured flux. We evaluate here the systematic effect in the results derived from the choice of $\rho = 1$. We repeated the analysis considering $\rho = 3$ and $\rho = 5$. The ρ parameter sets the tolerance for the difference between LI and LIV attenuations. The number of bins used to reconstruct the intrinsic spectrum increases with ρ.

Figure 11 shows the log-likelihood test using $\rho = 1, \rho = 3$ and $\rho = 5$. The test confirms that the overall shape of the log-likelihood curves does not depend on the choice of ρ. If the curves overlap, points were used to plot continuous functions for visualization purpose. Most important, this test shows that $\rho = 1$ leads to the most conservative LIV limit and that previous analysis which did not take into account this selection might have overestimated the LIV limit.

---

[1] Y. Nambu, Suppl. Prog. Theor. Phys. **E68**, 190 (1968).
[2] V. A. Kostelecky and S. Samuel, Phys. Rev. D **39**, 683 (1989).
[3] D. Colladay and V. A. Kostelecky, Phys. Rev. D **58**, 116002 (1998).
[4] J. Ellis, N. E. Mavromatos, and D. V. Nanopoulos, Phys. Rev. D **61**, 027503 (1999).
[5] R. Gambini and J. Pullin, Phys. Rev. **59**, 124021 (1999).
[6] G. Amelino-Camelia, Nature (London) **410**, 1065 (2001).
[7] J. Alfaro, Phys. Rev. Lett. **94**, 221302 (2005).

[8] R. Potting, J. Phys. Conf. Ser. **447**, 012009 (2013).

[9] B. Audren, D. Blas, J. Lesgourgues, and S. Sibiryakov, J. Cosmol. Astropart. Phys. 08 (2013) 039.

[10] *Springer Handbook of Spacetime*, edited by R. Bluhm (Springer, Berlin, 2014), pp. 485–507, DOI: 10.1007/978-3-642-41992-8_23.

[11] G. Calcagni, Eur. Phys. J. C **77**, 291 (2017).

[12] D. Bettoni, A. Nusser, D. Blas, and S. Sibiryakov, J. Cosmol. Astropart. Phys. 05 (2017) 024.

[13] S. Liberati and L. Maccione, Annu. Rev. Nucl. Part. Sci. **59**, 245 (2009).

[14] S. R. Coleman and S. L. Glashow, Phys. Lett. B **405**, 249 (1997).

[15] G. Amelino-Camelia, J. R. Ellis, N. E. Mavromatos, D. V. Nanopoulos, and S. Sarkar, Nature (London) **393**, 763 (1998).

[16] S. R. Coleman and S. L. Glashow, Phys. Rev. D **59**, 116008 (1999).

[17] F. W. Stecker and S. L. Glashow, Astropart. Phys. **16**, 97 (2001).

[18] F. W. Stecker, Astropart. Phys. **20**, 85 (2003).

[19] T. Jacobson, S. Liberati, and D. Mattingly, Phys. Rev. D **67**, 124011 (2003).

[20] F. W. Stecker and S. T. Scully, Astropart. Phys. **23**, 203 (2005).

[21] J. R. Ellis, N. E. Mavromatos, D. V. Nanopoulos, A. S. Sakharov, and E. K. G. Sarkisyan, Astropart. Phys. **25**, 402 (2006); **29**, 158(E) (2008).

[22] M. Galaverni and G. Sigl, Phys. Rev. Lett. **100**, 021102 (2008).

[23] M. Galaverni and G. Sigl, Phys. Rev. D **78**, 063003 (2008).

[24] J. Albert *et al.* (MAGIC Collaboration and Other Contributors), Phys. Lett. B **668**, 253 (2008).

[25] F. W. Stecker and S. T. Scully, New J. Phys. **11**, 085003 (2009).

[26] H. Xu and B.-Q. Ma, Astropart. Phys. **82**, 72 (2016).

[27] Z. Chang, X. Li, H.-N. Lin, Y. Sang, P. Wang, and S. Wang, Chin. Phys. C **40**, 045102 (2016).

[28] J. Ellis and N. E. Mavromatos, Astropart. Phys. **43**, 50 (2013).

[29] M. Fairbairn, A. Nilsson, J. Ellis, J. Hinton, and R. White, J. Cosmol. Astropart. Phys. 06 (2014) 005.

[30] F. Tavecchio and G. Bonnoli, Astron. Astrophys. **585**, A25 (2016).

[31] J. Biteau and D. A. Williams, Astrophys. J. **812**, 60 (2015).

[32] H. Martínez-Huerta and A. Pérez-Lorenzana, Phys. Rev. D **95**, 063001 (2017).

[33] G. Rubtsov, P. Satunin, and S. Sibiryakov, J. Cosmol. Astropart. Phys. 05 (2017) 049.

[34] H. Martínez-Huerta (HAWC Collaboration), Proc. Sci. ICRC2017 (**2018**) 868.

[35] R. G. Lang, H. Martínez-Huerta, and V. de Souza, Astrophys. J. **853**, 23 (2018).

[36] G. Cologna *et al.* (FACT and H.E.S.S. Collaborations), AIP Conf. Proc. **1792**, 050019 (2017).

[37] M. Lorentz and P. Brun (H.E.S.S. Collaboration), EPJ Web Conf. **136**, 03018 (2017).

[38] C. Pfeifer, Phys. Lett. B **780**, 246 (2018).

[39] J. Ellis, R. Konoplich, N. E. Mavromatos, L. Nguyen, A. S. Sakharov, and E. K. Sarkisyan-Grinbaum, arXiv:1807.00189.

[40] H. Abdalla and M. Böttcher, Astrophys. J. **865**, 159 (2018).

[41] V. Vasileiou, A. Jacholkowska, F. Piron, J. Bolmont, C. Couturier, J. Granot, F. W. Stecker, J. Cohen-Tanugi, and F. Longo, Phys. Rev. D **87**, 122001 (2013).

[42] A. De Angelis, G. Galanti, and M. Roncadelli, Mon. Not. R. Astron. Soc. **432**, 3245 (2013).

[43] A. Franceschini, G. Rodighiero, and M. Vaccari, Astron. Astrophys. **487**, 837 (2008).

[44] M. Meyer, EBLtable module, https://github.com/me-manu/ebltable.

[45] R. C. Gilmore, R. S. Somerville, J. R. Primack, and A. Dominguez, Mon. Not. R. Astron. Soc. **422**, 3189 (2012).

[46] A. Dominguez *et al.*, Mon. Not. R. Astron. Soc. **410**, 2556 (2011).

[47] S. Wakely and D. Horan, TeVCat catalog, http://tevcat.uchicago.edu/.

[48] F. Aharonian *et al.* (HEGRA Collaboration), Astron. Astrophys. **393**, 89 (2002).

[49] F. Aharonian *et al.* (H.E.S.S. Collaboration), Astron. Astrophys. **437**, 95 (2005).

[50] V. A. Acciari *et al.*, Astrophys. J. **738**, 25 (2011).

[51] M. Sharma, J. Nayak, M. K. Koul, S. Bose, A. Mitra, V. K. Dhar, A. K. Tickoo, and R. Koul, Nucl. Instrum. Methods Phys. Res., Sect. A **770**, 42 (2015).

[52] P. Chandra *et al.*, J. Phys. G **39**, 045201 (2012).

[53] S. V. Godambe *et al.*, J. Phys. G **35**, 065202 (2008).

[54] B. Bartoli *et al.* (ARGO-YBJ Collaboration), Astrophys. J. **758**, 2 (2012).

[55] M. K. Daniel *et al.* (VERITAS Collaboration), Astrophys. J. **621**, 181 (2005).

[56] F. Aharonian, A. Akhperjanian, and M. Beilicke (HEGRA Collaboration), Astron. Astrophys. **406**, L9 (2003).

[57] F. Aharonian *et al.* (HEGRA Collaboration), Astron. Astrophys. **403**, 523 (2003).

[58] F. Aharonian *et al.* (H.E.S.S. Collaboration), Astron. Astrophys. **475**, L9 (2007).

[59] E. Aliu *et al.*, Astrophys. J. **782**, 13 (2014).

[60] F. Aharonian *et al.* (H.E.S.S. Collaboration), Astron. Astrophys. **473**, L25 (2007).

[61] B. Bartoli *et al.* (ARGO-YBJ Collaboration), Astrophys. J. **734**, 110 (2011).

[62] M. Schroedter *et al.*, Astrophys. J. **634**, 947 (2005).

[63] V. A. Acciari *et al.*, Astrophys. J. **738**, 169 (2011).

[64] C. Allen *et al.* (VERITAS Collaboration), Mon. Not. R. Astron. Soc. **471**, 2117 (2017).

[65] E. Aliu *et al.* (VERITAS Collaboration), Astrophys. J. **775**, 3 (2013).

[66] M. Santander (VERITAS Collaboration), Proc. Sci. ICRC2017 (**2017**) 622.

[67] H. Martínez-Huerta, R. G. Lang, and V. de Souza, arXiv:1901.03205.

6 ESTIMATING THE POTENTIAL OF TESTING LIV USING CTA

As previously discussed in Chapter 2, TeV gamma-rays are absorbed by the interaction with photons of the EBL, which shapes the arriving spectrum. A way of quantifying the effect is to calculate the attenuation, $a(E) = e^{-\tau}$, given by

$$a(E) = \frac{J_{\mathrm{Earth}}(E)}{J_{\mathrm{s}}(E)} = e^{-\tau} = e^{-D/\lambda(E)}, \tag{6.1}$$

where J_{Earth} and J_{s} are, respectively, the arriving spectrum on Earth and the intrinsic spectrum at the source, D is distance of the source and λ is the mean free path of the pair production, for which the EBL is the main background at these energies. Nevertheless, there are several sources of uncertanties related to the parametrization of the EBL distribution and competitive models in the literature differ between themselves.

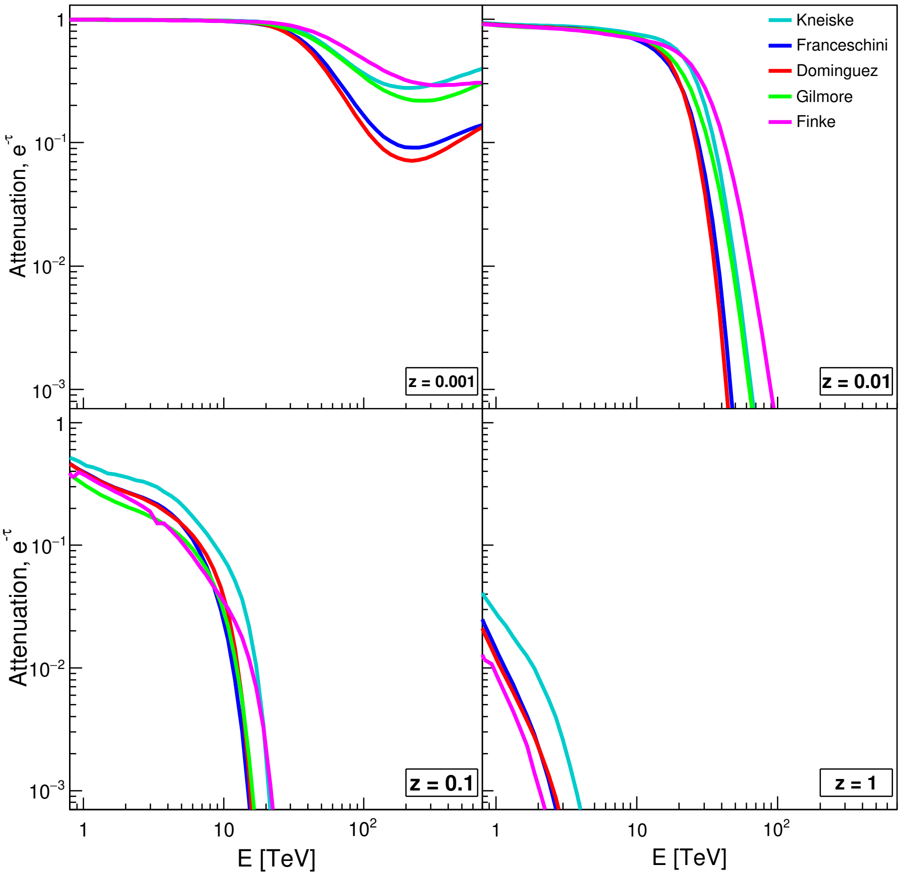

Figure 6.1 – Attenuation as function of the energy. Each colored line represents a different EBL model, and each panel represents a different redshift.

Source: By the author.

Figure 6.1 shows the attenuation as a function of the energy from 5 different EBL models, Kneiske (44), Franceschini (45), Dominguez (48), Gilmore (47) and Finke (46), and 4 representative distances of the sources, given by their redshift, $z = \{10^{-3}, 10^{-2}, 10^{-1}, 1\}$. The attenuation remains close to 1, i.e., almost no absorption of the intrinsic spectrum, up to a given energy at which it drops rapidly, creating a strong suppression in the arriving spectrum. This energy is strongly dependent on the redshift and the farther the source, the lower the energy of the suppression.

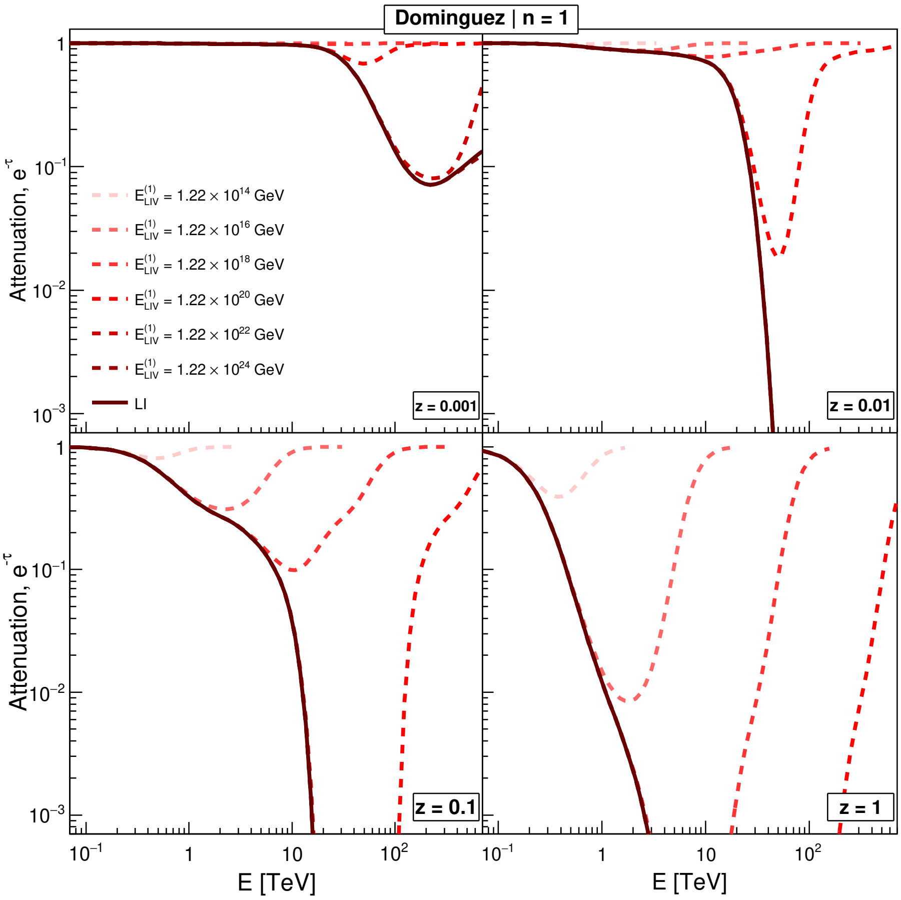

Figure 6.2 – Attenuation as function of the energy for the Dominguez EBL model considering LIV for $n = 1$. The dark continuous line represents the LI case. Each colored dashed line represents the attenuation for a different LIV energy scale, and each panel represents a different redshift.

Source: By the author.

The attenuation considering LIV is obtained following the calculations described in Chapter 4. Figure 6.2 shows the results using the Dominguez EBL model and considering subluminal LIV with $n = 1$. If some level of LIV is present, a recovery in the attenuation is seen, which implies in fewer gamma-rays being absorbed and, thus, a recovery of the arriving spectrum. The energy at which the effect becomes relevant is dictated by the LIV coefficient (or correspondingly the energy scale). Similar results are found for other EBL models and LIV orders, n.

As discussed in Chapter 5 and performed by previous works, imprints of this effect in TeV gamma-ray spectra can be searched to test LIV. This type of analysis is limited by the sensitivity and energy range of the experiment. CTA is expected to provide a considerable improvement in both features, being thus a great candidate for future LIV tests.

In this work, we estimate the potential of studying LIV with CTA. Two scenarios are considered and the response of the observatory is simulated for two different sources, Markarian 501 (Mrk 501), a blazar at $z = 0.034$ and 1ES 0229+200, a BL Lac object at $z = 0.139$. Both their intrinsic spectra have been parametrized by a power law with an exponential cutoff,

$$\frac{dN}{dE}(E) = N_0 \left(\frac{E}{E_0}\right)^{-\Gamma} e^{-E/E_{\text{cut}}}, \tag{6.2}$$

where the normalization, N, the reference energy, E_0, and the spectral index, Γ, for each source are shown in table 6.1. Two cutoff energies are considered for each source, $E_{\text{cut}} = 20$ TeV and $E_{\text{cut}} = 40$ TeV. Observation times of 10 and 100 hours are considered for Mrk 501 and 1ES 0229+200, respectively, which is similar to the observation times used in current experiments.

Table 6.1 – Spectral parameters considered for the sources.

Source	N_0 [TeV^{-1}cm^{-2}s^{-1}]	E_0 [TeV]	Γ	z
Mrk 501	4.243×10^{-12}	5.014	2.36	0.034
1ES 0229+200	1.447×10^{-12}	1.636	1.45	0.139

Source: By the author.

Figures 6.3 and 6.4 show the calculated arriving spectrum for several LIV energy scales. As expected, a recovery in the spectrum is found when LIV is considered.

Two scenarios were considered. In the first, we assume LIV of the same order of current limits, i.e., $E_{\text{LIV}}^{(1)} = 10^{28}$ eV and simulate the capability of CTA detecting this signature. In the second, on the other hand, we assume no LIV and estimate the limits that could be imposed by CTA.

6.1 Simulation packages

There are currently two main simulation packages for the CTA consortium: ctools and GammaPy. In this work, we obtained the response of the observatory using ctools. In parallel, Dr. Humberto Martínez-Huerta has done the simulations using GammaPy.

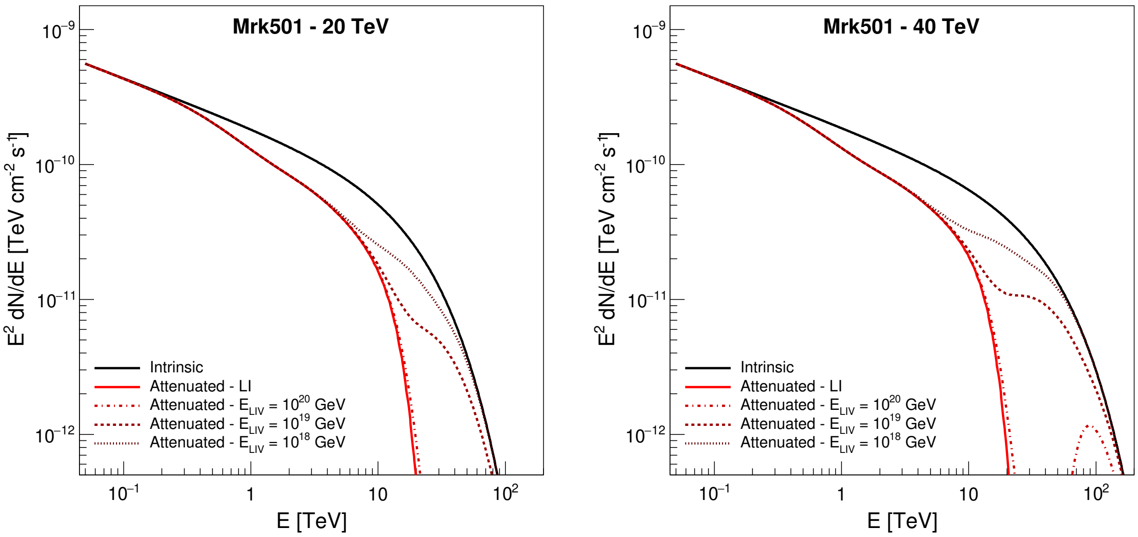

Figure 6.3 – Energy spectrum for Mrk 501. The black and red continuous lines represent, respectively, the intrinsic and attenuated LI spectrum. The different dashed lines represent the attenuated spectra considering several LIV energy scales for $n = 1$. The left and the right panel show the spectra using $E_{\rm cut} = 20$ TeV and $E_{\rm cut} = 40$ TeV, respectively. The Dominguez model was used for the EBL.

Source: By the author.

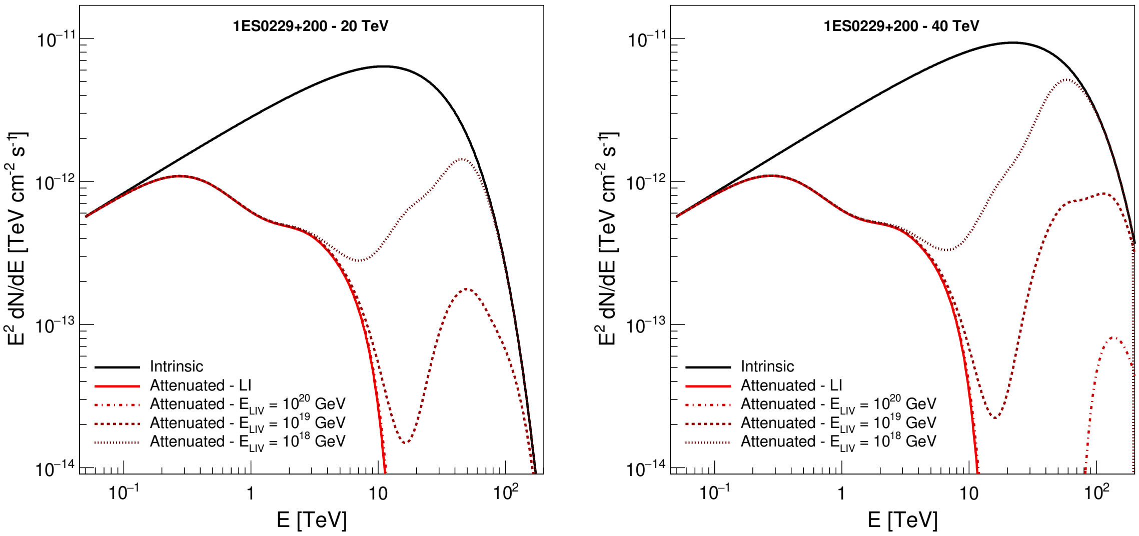

Figure 6.4 – Same as fig. 6.3, but for 1ES 0229+200.

Source: By the author.

Figures 6.5-6.8 show the comparison of the obtained results for each combination of source, energy cutoff and LIV scenario. In all cases, there is good agreement between the results using ctools and GammaPy and the predicted spectra.

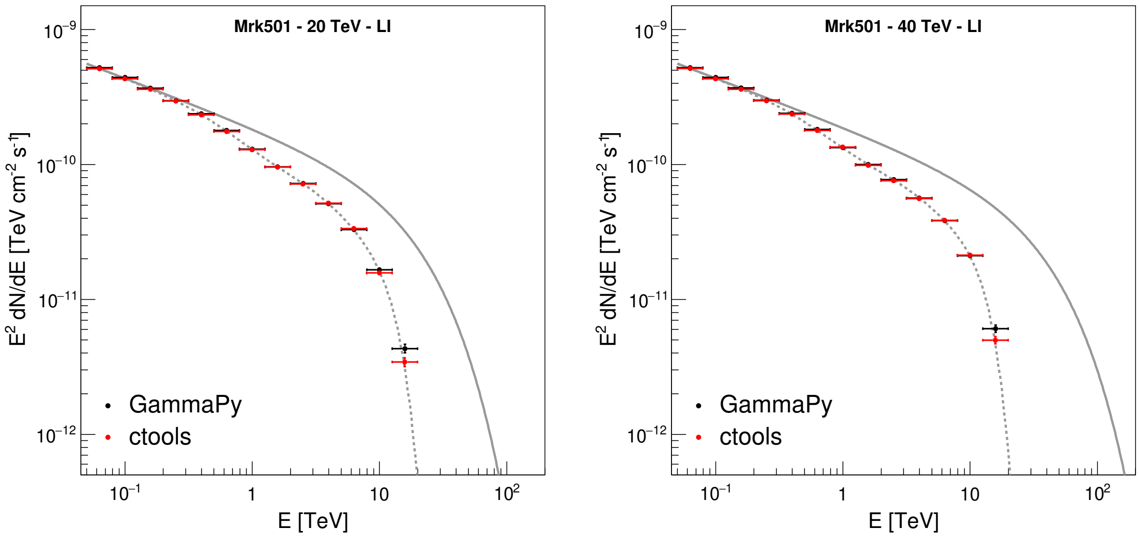

Figure 6.5 – Simulated detected energy spectrum for Mrk 501 in a LI scenario. The continuous line represents the intrinsic spectrum, and the dashed line represents the predicted attenuated spectrum. The black and red points represent the simulated data for CTA using GammaPy and ctools, respectively. The left and right panels show the cases for $E_{\text{cut}} = 20$ TeV and $E_{\text{cut}} = 40$ TeV, respectively.

Source: By the author.

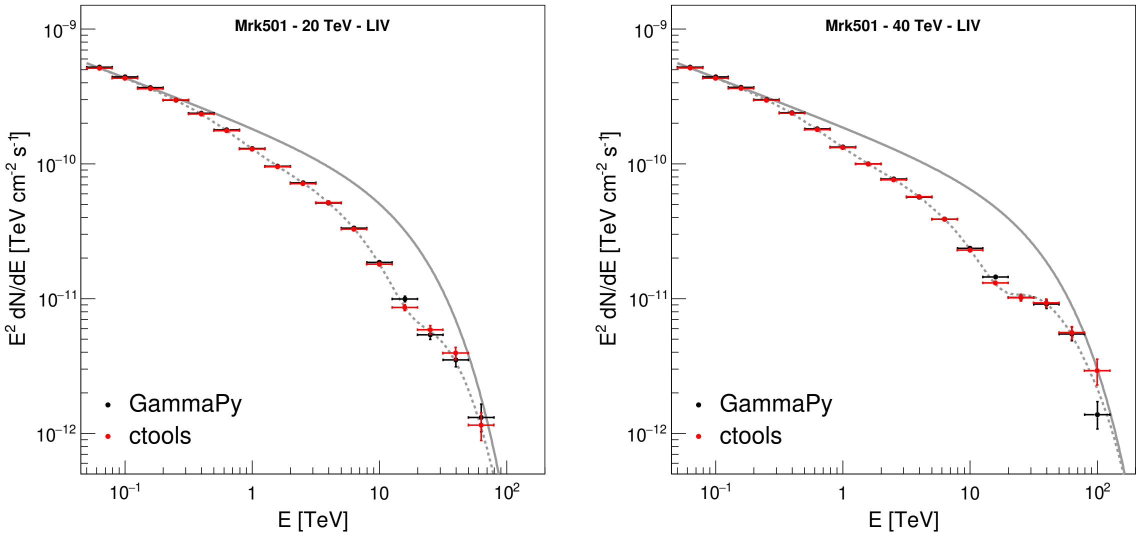

Figure 6.6 – Same as fig. 6.5, but for a LIV scenario with $E_{\text{LIV}}^{(1)} = 10^{28}$ eV.

Source: By the author.

6.2 Capability of detecting LIV effects of the same order of current limits

For the first case, we have considered $E_{\text{LIV}}^{(1)} = 10^{28}$ eV and simulated the capability of CTA differentiating it from a LI scenario. The predicted measured spectra for both the LIV and LI were simulated and the rejection of the LI scenario by the simulated

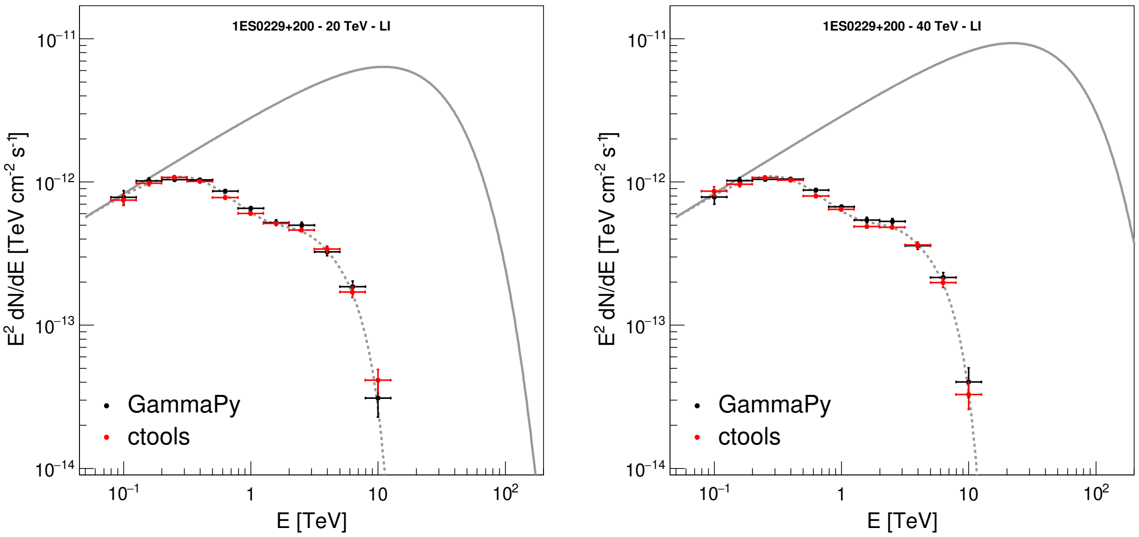

Figure 6.7 – Same as fig. 6.5, but for 1ES 0229+200.

Source: By the author.

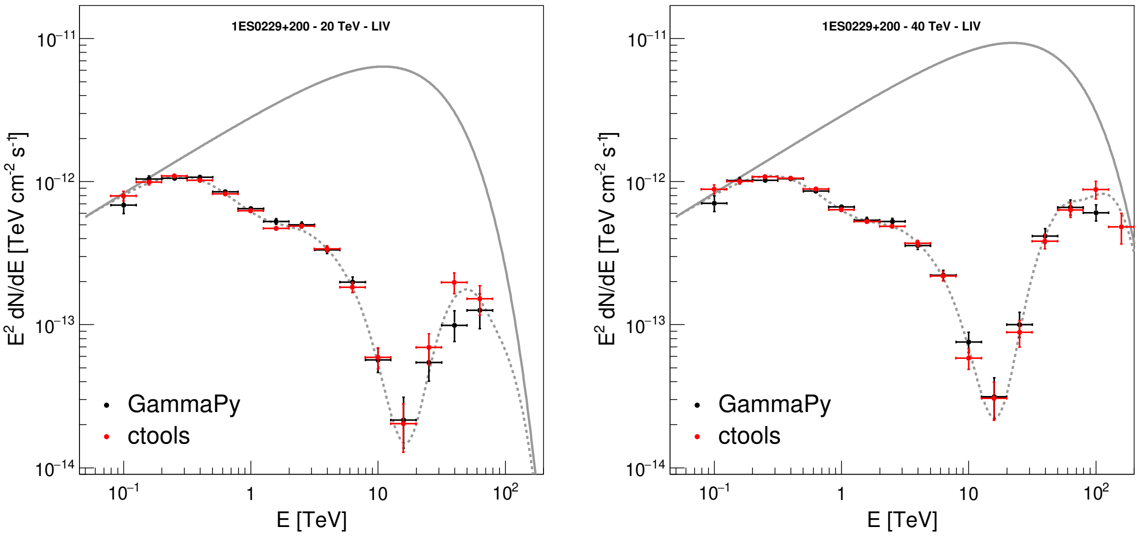

Figure 6.8 – Same as fig. 6.5, but for 1ES 0229+200 in a LIV scenario with $E_{\text{LIV}}^{(1)} = 10^{28}$ eV.

Source: By the author.

measurements was obtained via a log-likelihood statistical test. The confidence level of rejection is given by

$$\sigma = \sqrt{2\left(\mathcal{L}_{\text{LIV}} - \mathcal{L}_{\text{LI}}\right)}, \tag{6.3}$$

where $2\mathcal{L}$ is the log-likelihood value. Table 6.2 shows the results for Mrk 501. If this level of LIV is present, CTA will surely be capable of detecting it. The significance of detection will strongly depend on the LIV energy scale and the case considered here, $E_{\text{LIV}}^{(1)} = 10^{28}$ eV, is just an example scenario.

Table 6.2 – Estimated confidence levels for detecting LIV with $E_{\mathrm{LIV}}^{(1)} = 10^{28}$ eV.

Source	E_{cut} [TeV]	σ
Mrk 501	20	51
	40	79

Source: By the author.

6.3 Capability of improving current LIV limits

The second case considered assumes no LIV and estimates the limits that can be imposed by CTA. In order to do that, the simulated measured data considering no LIV is compared to predictions of the spectrum for several LIV energy scales via a log-likelihood statistical analysis.

Figure 6.9 shows the log-likelihood profile for Mrk 501. The simulated data is best described, i.e., the smallest value of $2\mathcal{L}$ is found by a LI assumption ($E_{\mathrm{LIV}}^{(1)} \rightarrow \infty$). Limits of the LIV scale can be imposed with a confidence level given by $\sigma = \sqrt{2(\mathcal{L} - \mathcal{L}_{\mathrm{best}})}$. Table 6.3 summarizes the limits for both Mrk 501 and 1ES 0229+200. Current limits imposed by H.E.S.S. using Mrk 501 are shown for comparison and enforce the great potential of CTA to test LIV.

Table 6.3 – Estimated limits on the LIV energy scale to be imposed by CTA. The limits imposed by H.E.S.S. on Mrk 501 are shown for comparison.

Source	E_{cut} [TeV]	$E_{\mathrm{LIV}}^{(1)}$ [10^{28} eV]			$E_{\mathrm{LIV}}^{(2)}$ [10^{21} eV]		
		2σ	3σ	5σ	2σ	3σ	5σ
Mrk 501	20	3.6	3.2	2.6	1.7	1.5	0.8
	40	9.1	7.2	5.0	4.7	3.8	2.6
1ES 0229+200	20	3.5	2.0	0.8	1.7	1.2	0.6
	40	6.2	3.6	1.4	2.4	1.7	0.8
H.E.S.S. limits		2.8	1.9	1.04	0.75	0.64	0.47

Source: By the author.

This work assisted as a minor contribution to an article from the CTA consortium, which aims to estimate the sensitivity of CTA for probing cosmology and fundamental physics using gamma-ray propagation. (113) The results here presented were used to evaluate the systematic uncertainties coming from the use of different simulation packages. This article has been submitted to the *Journal of Cosmology and Astrophysics* (JCAP) and is currently under peer review.

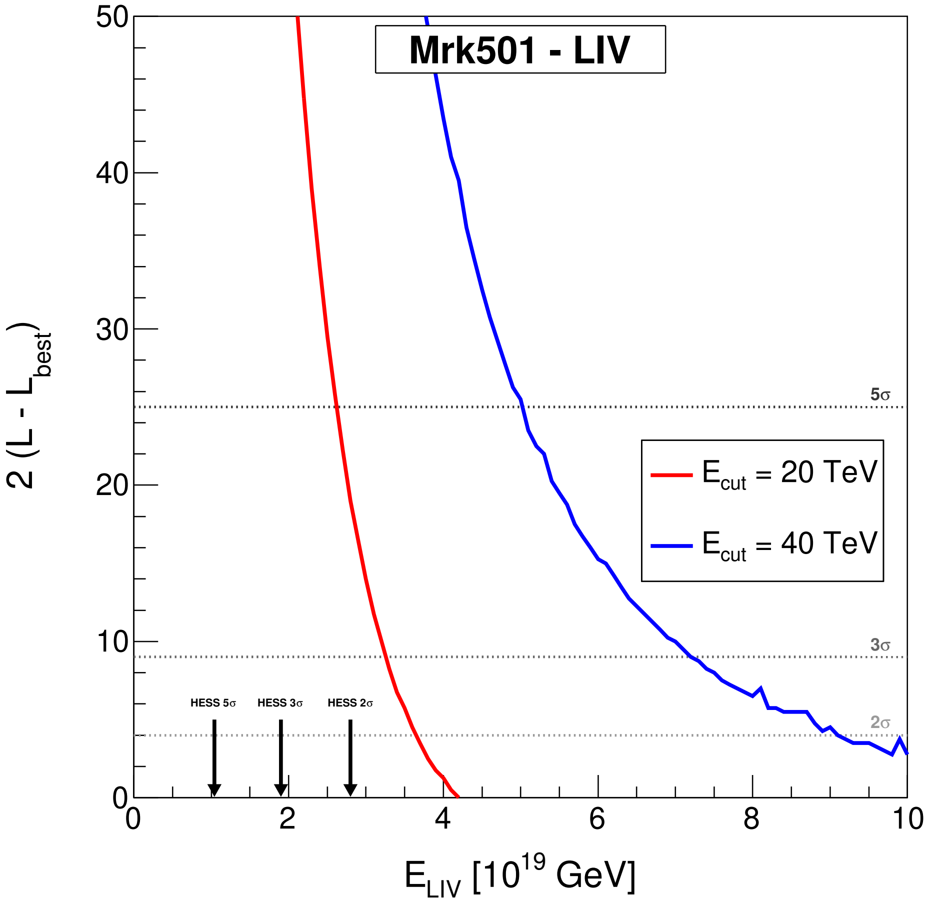

Figure 6.9 – Log-likelihood profile as a function of the energy. The red and blue lines show the results for Mrk 501 with $E_{\mathrm{cut}} = 20$ TeV and $E_{\mathrm{cut}} = 40$ TeV, respectively. The gray dashed lines show the difference in the log-likelihood values for 2, 3 and 5σ CL. The black arrows show recent limits for Mrk 501 from H.E.S.S.

Source: By the author.

7 TESTING LORENTZ INVARIANCE VIOLATION AT THE PIERRE AUGER OBSERVATORY

In this chapter, we use different datasets from the Pierre Auger Observatory to test LIV. This work was developed within the Pierre Augar Collaboration and is meant to be published as a collaboration paper, which is in final stages of preparation. The results presented in this thesis are based on the calculations, simulations and analyses performed by the author, with the exception of the fits, that were done by Dr. Denise Boncioli.

As discussed in the previous chapters, the effects of LIV are expected to be suppressed up to the highest energies. The Pierre Auger Observatory, being the largest UHECR detector is, thus, expected to play an important role in these studies.

Two different and independent scenarios are treated: subluminal LIV in the electromagnetic sector and LIV in the hadronic sector. For the first, the upper limits on the flux of EeV photons are used, similarly to what is done in Chapter 4. For the second, a combined fit of the energy spectrum and mass composition considering LIV in the propagation is done for the first time in the literature.

7.1 Electromagnetic sector

We use the formalism and implementation for LIV in the propagation of GZK photons presented in Chapter 4. In addition to the results already presented in that chapter, two cases are considered: a pure-proton composition benchmark and a mixed composition. For both cases, the spectral parameters of the UHECR sources are those found to best fit the data from the Pierre Auger Observatory.

7.1.1 Pure-proton composition benchmark

The pure-proton composition benchmark provides us with a didactic example for better understanding the dependency of the results on the assumptions about the UHECR sources. For this case, the source parameters were found by fitting the spectrum for $E > 10^{18}$ eV and are given by ($\Gamma = 2.3$, $R_{\text{cut}} = 10^{19.8}$ V). An evolution of the sources with redshift that follows $(1+z)^m$ was considered. Different values of m ranging from -4 to 4 were tested. The data is best described with a strong source evolution, $m = 4$, which also increases the flux of GZK photons.

Similarly to what was done in Chapter 4, the integral flux of GZK photons was obtained for several LIV coefficients as well as the two limiting cases, $\delta_\gamma = 0$ (LI), and $\delta_\gamma \to -\infty$, for which no interaction happens at all for the considered energies. Figure 7.1 shows the results for $n = 0$. For some of the LIV coefficients assumed, the predicted flux is more intense than the upper limits, leading to limits on the LIV coefficients. In this

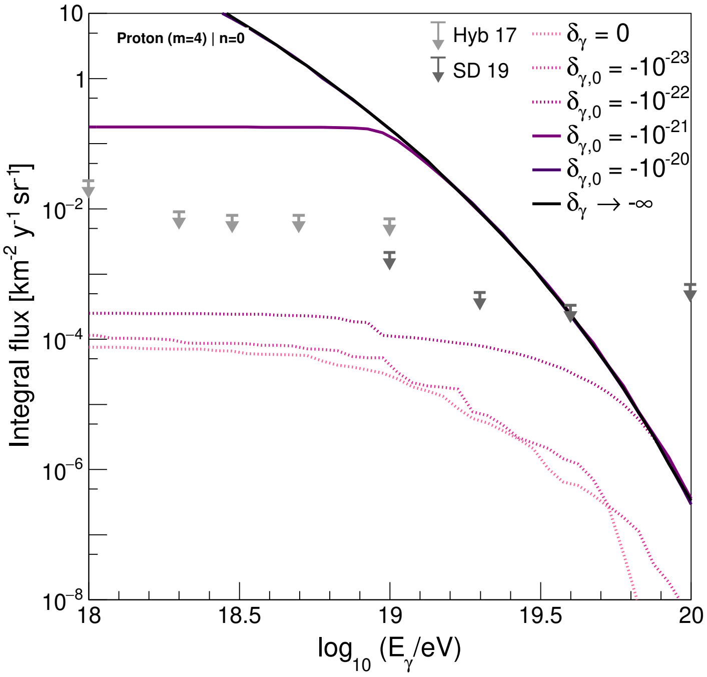

Figure 7.1 – Simulated integral flux of GZK photons. The arrows show the upper limits on the flux imposed by the Pierre Auger Observatory. Continuous lines show the flux for the rejected LIV scenarios. Dashed lines show the flux for the scenarios in which the data is insensitive to LIV. A pure proton composition is considered. The considered spectral parameters are $\Gamma = 2.3$ and $R_{\text{cut}} = 10^{19.8}$ V

Source: By the author.

example scenario, limits of $\delta_{\gamma,0} > -10^{-21}$, $\delta_{\gamma,1} > -10^{-40}$ eV^{-1} and $\delta_{\gamma,2} > -10^{-58}$ eV^{-2} could be imposed.

These limits are several orders of magnitude more restrictive than the upper limits on subluminal LIV from TeV gamma-ray astronomy. Nevertheless, as argued before, these results depend strongly on the assumptions about the sources. This is better illustrated in figure 7.2, which shows the limits for a pure-proton composition, a source evolution of $m = 0$, and every combination of (Γ, R_{cut}). The limits become weaker for lower rigidity cutoffs and higher spectral indexes. For some combinations, the data is insensitive to LIV. In these cases, the vast majority of UHECR does not reach energies high enough to produce pions, that would later decay into GZK photons. On the other direction of the parameter space, the predicted flux is so intense that even for the LI case, that region of the parameter space is ruled out. Other orders of LIV, n, lead to similar results. For other primaries, the results are similar but shifted to higher rigidity cutoffs for heavier primaries. Therefore, a lighter composition is more promising for testing LIV.

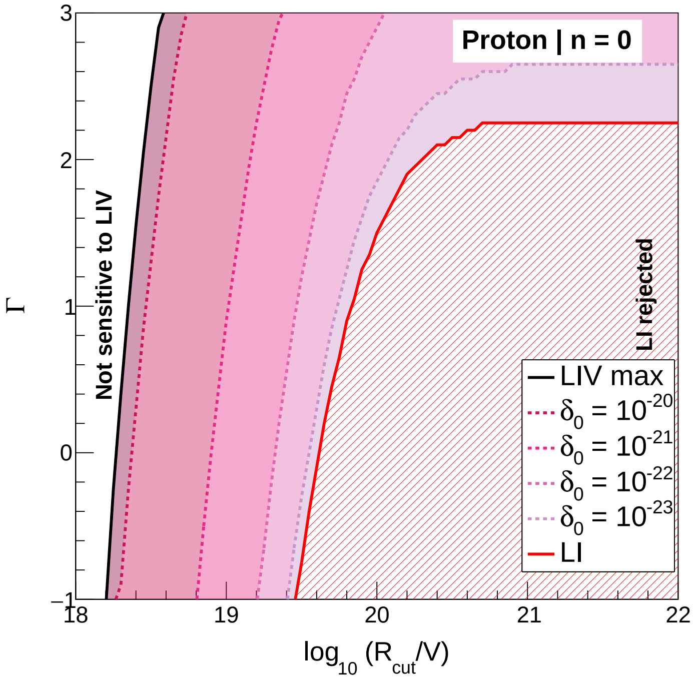

Figure 7.2 – Limits on the LIV coefficient as a function of the assumed spectral parameters. The colored areas represent the region of the parameter space that results in the same limit. The left-most region is insensitive to LIV, while the right-most region is reject even in a LI scenario. A pure-proton composition and no evolution of the sources is considered in this example.

Source: By the author.

7.1.1.1 Mixed composition

A more realistic astrophysical scenario comes from the results of the combined fit of spectrum and composition performed by the Pierre Auger Collaboration. (76) Figure 7.3 shows the results for the SPGE model of that study (these models are best described in the following section). Not even the prediction from the most extreme case, $\delta_\gamma \to -\infty$, is more intense than the upper limits. The data is, thus, insensitive to LIV. This is the case for all the astrophysical scenarios from Ref (76) and for $n = 1$ and $n = 2$. This is mostly due to a low rigidity cutoff and a mixed composition, as shown in figure 7.2.

7.2 Hadronic sector

For the second independent scenario, the propagation of UHECR is modified by considering LIV in the hadronic sector. This has been the subject of previous works. (107, 110, 112, 114, 115) We propose further development of these analyses by considering for the first time a mixed composition and a combined fit of both the energy spectrum and mass composition under LIV assumptions.

The effect of LIV in the dominant energy losses, i.e., photo-pion production and

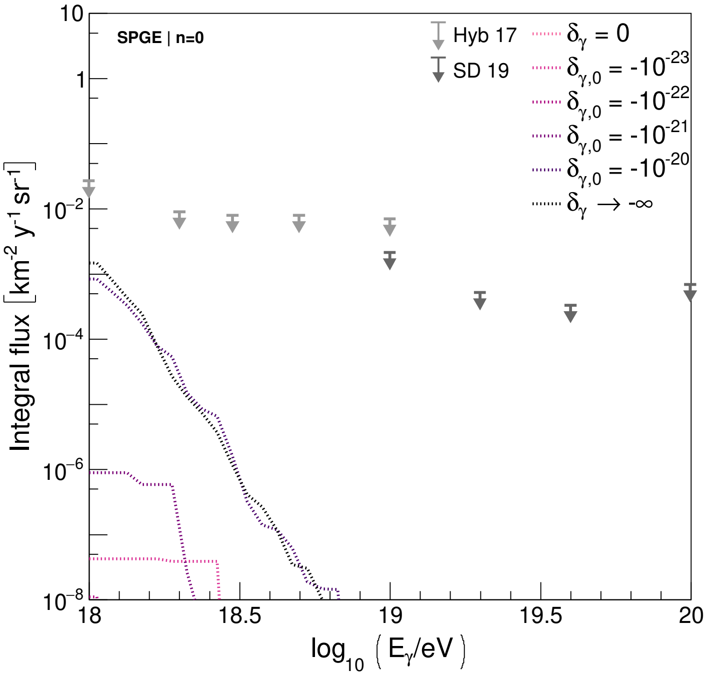

Figure 7.3 – Same as figure 7.1, but for the mixed composition.

Source: By the author.

photodisintegration are obtained. The modified kinematics are calculated following the procedure developed in Ref. (116).

The LIV coefficient of protons, nuclei and pions can be reduced a single coefficient, $\delta_{\mathrm{had}} = \delta_p = \delta_\pi/2 = A^n \delta_A$, where A is the atomic mass of the nucleus. The relation between δ_p and δ_π is justified by the argument that the LIV effect on the pion production depends on $\delta_\pi - \delta_p$. (110) Taking $\delta_p = \delta_\pi/2$ leads to effects of the same order in pion production and photodisintegration. The relation between δ_p and δ_A, on the other hand, is endorsed by the superposition model:

$$E_A^2 = m_A^2 + p_A^2 + \sum_{n=0}^{\infty} \delta_{A,n} E_A^{(n+2)} \implies \tag{7.1}$$

$$A^2 E_p^2 = A^2 m_p^2 + A^2 p_N^2 + \sum_{n=0}^{\infty} A^{(n+2)} \delta_{A,n} E_p^{(n+2)} \implies \tag{7.2}$$

$$\delta_{p,n} = A^n \delta_{A,n}. \tag{7.3}$$

Figures 7.4 and 7.5 show, respectively, the attenuation length for the pion production and the energy threshold in the nucleus reference frame (NRF) for the photodisintegration. The effects of LIV on both interactions are similar, an increase above a critical energy, which depends on $\delta_{\mathrm{had},0}$, resulting in fewer interactions during propagation. Similar results are found for other LIV orders, n, and other primaries.

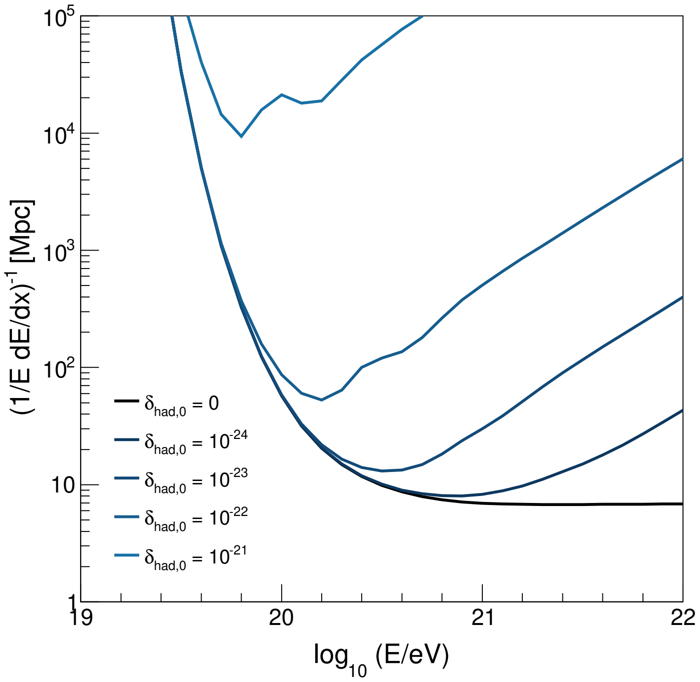

Figure 7.4 – Attenuation length for the pion production as a function of the energy. The black line and the blues lines show the results for the LI and various LIV scenarios, respectively. Scenarios with $> 10^{-21}$ result in attenuation lengths larger than 10^5 Mpc for all the considered energies and, thus, are not shown in the plot.

Source: By the author.

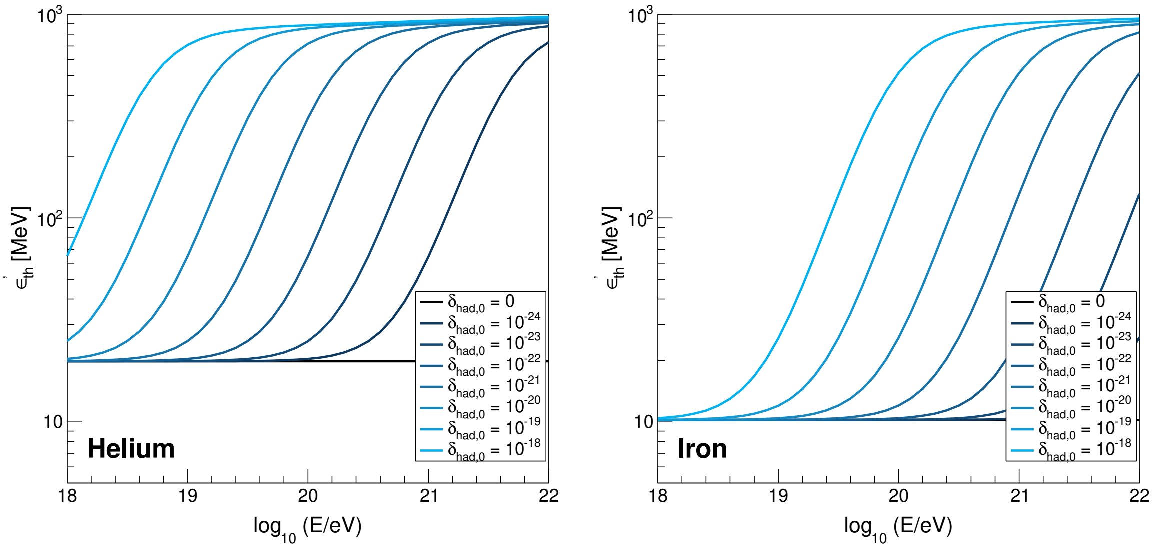

Figure 7.5 – Energy threshold in the NRF for the photodisintegration as a function of the energy. The black and blue lines show the results for the LI and various LIV scenarios, respectively. The left and right panels are respectively for a nucleus of helium and iron.

Source: By the author.

7.2.1 Combined fit of the spectrum and composition under LIV assumptions

In order to find the LIV coefficient that best describes the data, we follow the procedure for a combined fit of the energy spectrum and mass composition from Ref (76). The propagation of UHECR, however, is simulated under different LIV assumptions. The modified interactions were implemented on SimProp v2.4. (54) The simulations were performed considering 5 representative primaries (H, He, N, Si and Fe). The sources were divided into 7 redshift intervals: [0,0.01), [0.01,0.05), [0.05,0.1), [0.1,0.2), [0.2,0.3), [0.3,0.5) and [0.5,2.5). An energy range of $10^{17.5} < E/\text{eV} < 10^{22}$ was considered and 10^5 events were simulated for each primary and redshift interval. In order to estimate the dependency of the result on the astrophysical models, different models for the EBL, photo-nuclear cross section, and hadronic interaction were considered, as listed in table 7.1.

Table 7.1 – Combination of astrophysical models considered in this work.

Scenario	Nuclear cross sections	EBL model	Hadronic interactions
SPGE	PSB (117, 118)	Gilmore (47)	EPOS-LHC (65)
STGE	Talys (119)	Dominguez (48)	EPOS-LHC
SPDE	PSB	Gilmore	EPOS-LHC
SPGS	PSB	Gilmore	Sibyll 2.3c (66)

Source: By the author.

The combined fit of the simulated arriving energy spectrum and mass composition follows the same procure of Ref (76) and uses up-to-date data from Refs. (68, 120). The spectrum at the sources is defined as

$$\left.\frac{dN}{dE}\right|_A = J_0 f_A \left(\frac{E}{10^{18}\ \text{eV}}\right)^{-\Gamma} \times \begin{cases} 1, & \text{for } R < R_{\text{cut}} \\ e^{(1-R/R_{\text{cut}})}, & \text{for } R \geq R_{\text{cut}} \end{cases}, \tag{7.4}$$

where the normalization, J_0, the spectral index, Γ, the rigidity cutoff, R_{cut}, and four of the primary fractions, f_A, are free parameters of the fit. The X_{max} distributions are parametrized by Gumbel functions. (121)

Two cases are also considered in this analysis: an illustrative pure-proton composition benchmark and a mixed composition.

7.2.1.1 Pure-proton composition benchmark

Previous works on LIV in the propagation of UHECR considered a pure-proton composition. (107, 110, 114, 115) Even though such assumption is ruled out by X_{max} measurements, we first consider the same assumption as an illustrative way of comparing to these results. For this case, only the energy spectrum is fitted for $E > 10^{18}$ eV and different source evolutions are considered.

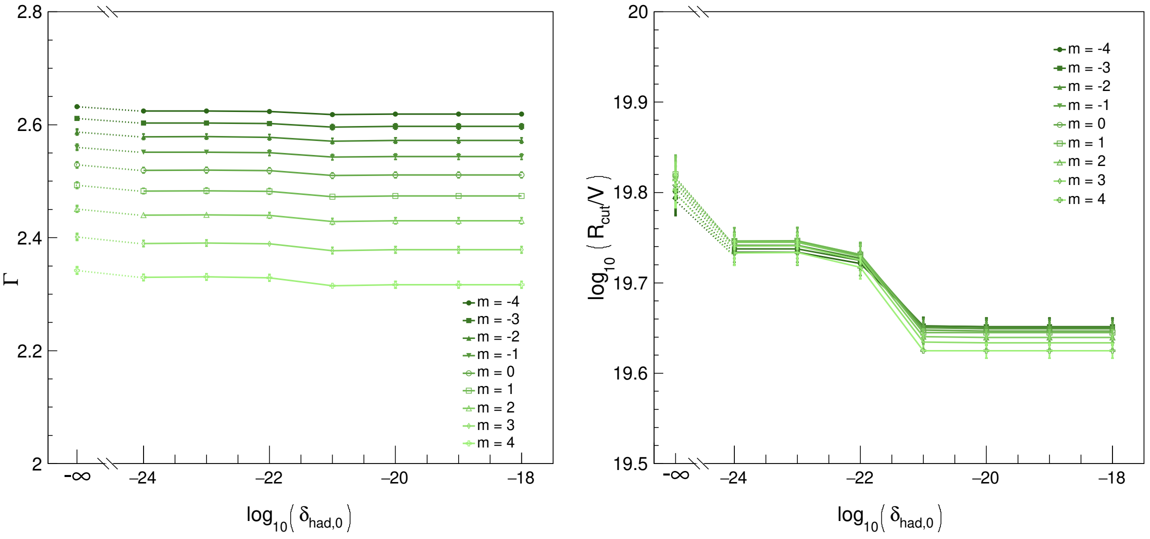

Figure 7.6 – Evolution of the fit parameters with respect to the LIV coefficient. The left and right panels show the spectral index and the rigidity cutoff, respectively. Each shade of green represents a different source evolution scenario with $(1 + z)^m$.

Source: By the author.

Figure 7.6 shows the evolution of the fit parameters with $\delta_{\mathrm{had},0}$. Both the spectral index and the rigidity cutoff slightly drop for strong LIV. Figure 7.7, on the other hand, shows the evolution of the deviance, a generalized form of the χ^2, with $\delta_{\mathrm{had},0}$. The lower the deviance, the better the data is described. The LI case is taken as a reference and the confidence level (CL) is obtained via $\sigma = \sqrt{|D - D_{\mathrm{LI}}|}$.

For every source evolution considered, the data is best described by $\delta_{\mathrm{had},0} = 10^{-23}$ with more than 3σ CL. Limits on the LIV coefficient were imposed for $\delta^{3\sigma}_{\mathrm{had},0} < 10^{-22}$ and $\delta^{5\sigma}_{\mathrm{had},0} < 10^{-21}$. These results are compatible with previous LIV works. Nevertheless, the deviance for the fit is bad and the X_{max} data cannot be described.

7.2.2 Mixed composition

Further development of previous analyses is proposed here by considering a more realistic mixed composition and estimating the dependency on astrophysical model assumptions. For each value of $\delta_{\mathrm{had},0}$, both the energy spectrum and X_{max} distributions were fitted. Figure 7.8 shows the evolution of the fitted parameters with LIV. For strong LIV, the scenarios converge to a spectral index close to 2, which is consistent with Fermi acceleration.

Figure 7.9, on the other hand, shows the evolution of the deviance. The data is best described by some level of LIV, as shown in table 7.2. This shows that the data favors a scenario with fewer interactions during propagation. That could be an indication of a LIV signal, but can also be caused by other features not covered by the simplistic astrophysical

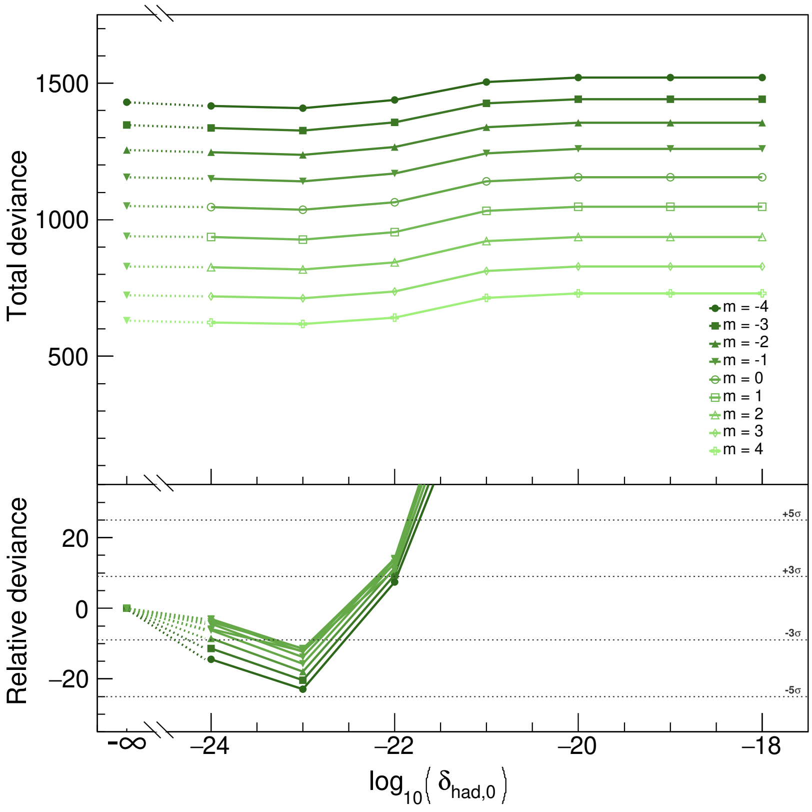

Figure 7.7 – Evolution of the deviance with respect to the LIV coefficient. The top panel shows the total deviance, while the bottom panel shows the difference in the deviation relative to the LI case. The dashed horizontal lines show the 3σ and 5σ confidence level. Each shade of green represents a different source evolution scenario with $(1 + z)^m$.

Source: By the author.

Table 7.2 – LIV coefficients that best describe the data for each combination of models. The confidence level is given by $\sigma = \sqrt{D_{\text{LI}} - D}$.

Scenario	$\delta_{\text{had},0}^{\text{best}}$	CL
SPGE	10^{-21}	5.8σ
STGE	10^{-20}	6.2σ
SPDE	10^{-20}	5.4σ
SPGS	10^{-21}	5.3σ

Source: By the author.

model considered for the sources, such as a higher relative contribution from very local sources.

Limits on $\delta_{\text{had},0}$ can also be imposed due to the increase of the deviance for strong LIV. For all the combinations of models considered, the limits imposed are $\delta_{\text{had},0}^{5\sigma} < 10^{-19}$. The limits on the LIV coefficients of higher order can be estimated by considering that

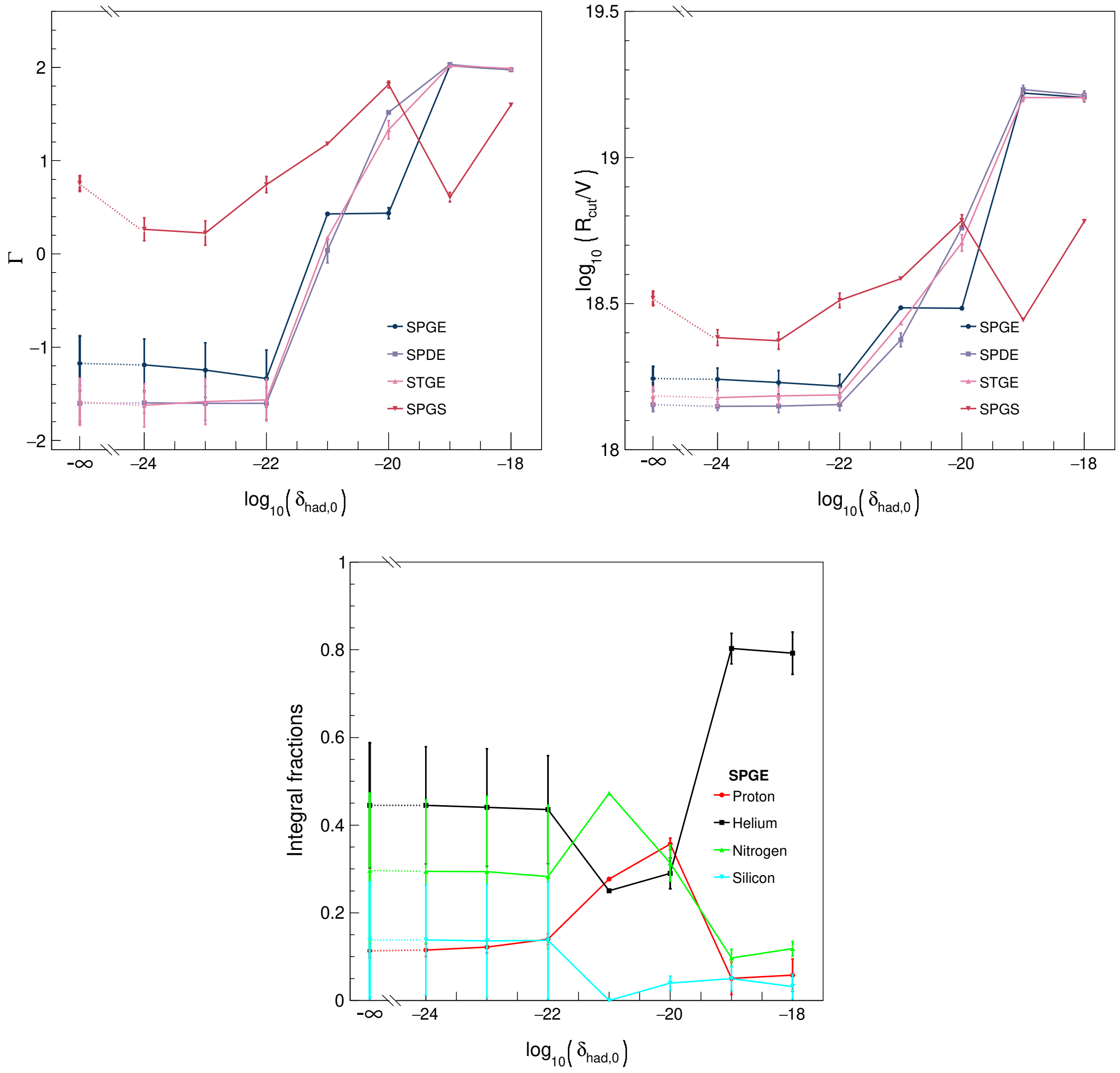

Figure 7.8 – Evolution of the fit parameters with respect to the LIV coefficient. Each line represents a different combination of astrophysical models. The panels shows the spectral index, rigidity cutoff and integral primary fractions at the source, respectively. The integral primary fractions are for the SPGE model.

Source: By the author.

LIV effects are dominated by the most energetic particles. With that,

$$\delta_{\text{had},0} E_{\text{cut}}^{2} = \delta_{\text{had,n}} E_{\text{cut}}^{(n+2)} \implies \delta_{\text{had,n}} = \delta_{\text{had},0} E_{\text{cut}}^{-n}. \tag{7.5}$$

For the limits imposed in this work, this approximation leads to $\delta_{\text{had},0}^{5\sigma} \lesssim 10^{-38}$ eV^{-1} and $\delta_{\text{had},2}^{5\sigma} \lesssim 10^{-57}$ eV^{-2}.

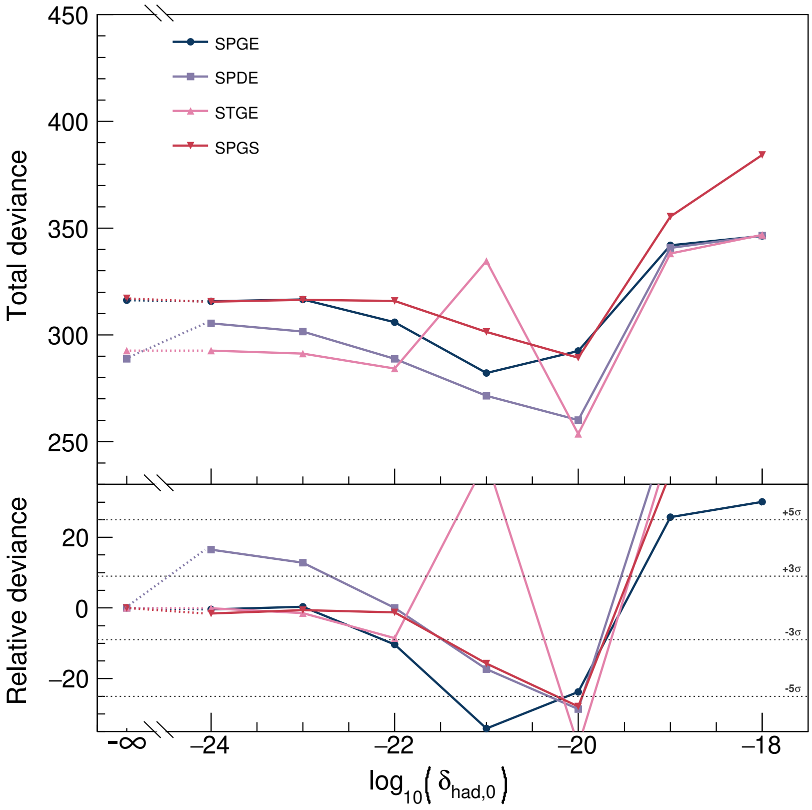

Figure 7.9 – Evolution of the deviance with respect to the LIV coefficient. Each line represents a different combination of astrophysical models. The top panel shows the total deviance, while the bottom panel shows the difference in the deviation relative to the LI case. The dashed horizontal lines show the 3σ and 5σ confidence level.

Source: By the author.

8 LORENTZ INVARIANCE VIOLATION TESTS IN ASTROPARTICLE PHYSICS

The Astrophysical Journal, 853:23 (10pp), 2018 January 20
https://doi.org/10.3847/1538-4357/aa9f2c
© 2018. The American Astronomical Society. All rights reserved.

Limits on the Lorentz Invariance Violation from UHECR Astrophysics

Rodrigo Guedes Lang[1], Humberto Martínez-Huerta[1,2], and Vitor de Souza[1]
[1] Instituto de Física de São Carlos, Universidade de São Paulo, Av. Trabalhador São-carlense 400, São Carlos, Brazil; rodrigo.lang@usp.br
[2] Departamento de Física, Centro de Investigación y de Estudios Avanzados del I.P.N., Apartado Postal 14-740, 07000, Ciudad de México, México
Received 2017 September 14; revised 2017 November 30; accepted 2017 November 30; published 2018 January 18

Abstract

In this paper, the Lorentz invariance violation (LIV) is introduced in the calculations of photon propagation in the universe. LIV is considered in the photon sector, and the mean-free path of the $\gamma\gamma \rightarrow e^+e^-$ interaction is calculated. The corresponding photon horizon, including LIV effects, is used to predict major changes in the propagation of photons with energy above 10^{18} eV. The flux of GZK photons on Earth, considering LIV, is calculated for several source models of ultra-high-energy cosmic rays (UHECRs). The predicted flux of GZK gamma-rays is compared to the new upper limits on the photon flux obtained by the Pierre Auger Observatory in order to impose upper limits on the LIV coefficients of order $n = 0$, 1, and 2. The limits on the LIV coefficients derived here are more realistic than previous works and in some cases more restrictive. The analysis resulted in LIV upper limits in the photon sector of $\delta_{\gamma,0}^{\rm limit} \sim -10^{-20}$, $\delta_{\gamma,1}^{\rm limit} \sim -10^{-38}\,{\rm eV}^{-1}$, and $\delta_{\gamma,2}^{\rm limit} \sim -10^{-56}\,{\rm eV}^{-2}$ in the astrophysical scenario, which best describes UHECR data.

Key words: astroparticle physics – cosmic rays – relativistic processes

1. Introduction

Astroparticle physics has recently reached the status of precision science due to (a) the construction of new observatories operating innovative technologies, (b) the detection of large numbers of events and sources, and (c) the development of clever theoretical interpretations of the data. Two observational windows have produced very important results in the last decade. The ultra-high energy cosmic rays ($E > EeV$) studied by the Pierre Auger and the Telescope Array Observatories (The Pierre Auger Collaboration 2015; Tinyakov 2014) improved our knowledge of the most extreme phenomena known in nature. The GeV–TeV gamma-ray experiments FERMI/LAT (Atwood et al. 2009), H.E.S.S. (The H.E.S.S. Collaboration 2006), MAGIC (The MAGIC Collaboration 2016), and VERITAS (J. Holder for the VERITAS Collaboration 2011) gave a new perspective on gamma-ray production and propagation in the universe. The operation of the current instruments and the construction of future ones (Zhen 2010; The CTA Consortium 2011; Haungs et al. 2015) guarantee the production of even more precise information in the decades to come.

Lorentz invariance (LI) is one of the pillars of modern physics and it has been tested in several experimental approaches (Mattingly 2005). Astroparticle physics has been proposed as an appropriate test environment for possible Lorentz invariance violation (LIV) given the large energy of the particles, the large propagation distances, the accumulation of small interaction effects, and recently the precision of the measurements (Amelino-Camelia et al. 1998; Jacobson et al. 2003; Stecker & Scully 2005, 2009; Ellis et al. 2006, 2008; Galaverni & Sigl 2008a, 2008b; The MAGIC Collaboration 2008; Liberati & Maccione 2009; Ellis & Mavromatos 2013; Fairbairn et al. 2014; Biteau & Williams 2015; Chang et al. 2016; Tavecchio & Bonnoli 2016; Xu & Ma 2016; Rubtsov et al. 2017).

Effective field theories with some Lorentz violation can derive in measurable effects in the data taking by astroparticle physics experiments; nonetheless, in this paper, LIV is introduced in the astroparticle physics phenomenology through the polynomial correction of the dispersion relation in the photon sector and is focused on the gamma-ray propagation and pair production effects with LIV. Other phenomena like vacuum birefringence, photon decay, vacuum Cherenkov radiation, photon splitting, synchrotron radiation, and helicity decay have also been used to set limits on LIV effects on the photon sector but are beyond the scope of this paper; for a review, see Liberati & Maccione (2009), Bluhm (2014), and Rubtsov et al. (2017).

Lorentz invariant gamma-ray propagation in the intergalactic photon background was studied previously in detail by De Angelis et al. (2013), a similar approach is followed in Section 2, but LIV is allowed in the interaction of high energy photons with the background light and their consequences are studied. The process $\gamma\gamma \rightarrow e^+e^-$ is the only one considered to violate LI, and, as a similar approach used in Galaverni & Sigl (2008a), such LIV correction can lead to a correction of the LI energy threshold of the production process. The latter phenomena modifies the mean-free path of the interaction and therefore the survival probability of a photon propagating through the background light, which depends on the LIV coefficients. This dependence is calculated in Section 2 and the mean-free path and the photon horizon are shown for several LIV coefficients and different orders of the LIV expansion in the photon energy dispersion relation.

In Section 3, the mean-free path of the photo-production process considering LIV is implemented in a Monte Carlo propagation code in order to calculate the effect of the derived LIV in the flux of ultra-high energy photons arriving on Earth due to the GZK effect (Greisen 1966; Zatsepin & Kuz'min 1966) and considering several models for the sources of cosmic rays. Section 3 quantifies the influence of the astrophysical models concerning mass composition, energy spectra shape, and source distribution. These dependencies have been largely neglected in previous studies and it is shown here that they influence the GZK photon flux by as much as four orders of magnitude.

In Section 4, the propagated GZK photon flux for each model is compared to recent upper limits on the flux of photons obtained by the Pierre Auger Observatory. For some astrophysical models, the Auger data is used to set restrictive limits on the LIV coefficients. The astrophysical model used to describe the primary cosmic-ray flux has a very large influence on the flux of GZK photons and therefore on the LIV limits imposed. Finally, in Section 5, the conclusions are presented.

2. Photon Horizon Including LIV Effects

One of the most commonly used mechanisms to introduce LIV in particle physics phenomenology is based on the polynomial correction in the dispersion relation of a free propagating particle, mainly motivated by an extra term in the Lagrangian density that explicitly breaks Lorentz symmetry, see, for instance, Amelino-Camelia et al. (1998), Coleman & Glashow (1999), Ahluwalia (1999), Amelino-Camelia (2001), Jacobson et al. (2003), Galaverni & Sigl (2008a, 2008b), Maccione & Liberati (2008), Liberati & Maccione (2011), Jacob & Piran (2008), and Zou et al. (2017). In these models, the corrected expression for the dispersion relation is given by the following equation:

$$E_a^2 - p_a^2 = m_a^2 + \delta_{a,n} E_a^{n+2}, \tag{1}$$

where a denotes the particle with mass m_a and four-momenta (E_a, p_a). For simplicity, natural units are used in this work. The LIV coefficient, $\delta_{a,n}$, parametrizes the particle dependent LIV correction, where n expresses the correction order, which can be derived from the series expansion or from a particular model for such an order, see, for instance, the case of $n = 0$ (Coleman & Glashow 1997, 1999; Klinkhamer & Schreck 2008), $n = 1$ (Myers & Pospelov 2003), or a generic n (Vasileiou et al. 2013). The LIV parameter of the order of n, δ_n, is frequently considered to be inversely proportional to some LIV energy scale $E_{\rm LIV}^{(n)}$. Different techniques have been implemented in the search of LIV signatures in astroparticle physics and some of them have been used to derive strong constraints to the LIV energy scale (Amelino-Camelia et al. 1998; Maccione & Liberati 2008; Bi et al. 2009; The H.E.S.S. Collaboration 2011; Otte 2012; Vasileiou et al. 2013; Benjamin Zitzer for the VERITAS Collaboration 2014; Schreck 2014; Biteau & Williams 2015; Martínez-Huerta & Pérez-Lorenzana 2017; Rubtsov et al. 2017).

The threshold analysis of the pair production process, considering the LIV corrections from Equation (1) on the photon sector is discussed in the Appendix and leads to corrections of the LI energy threshold of the process. In the following, $\epsilon_{\rm th}^{\rm LIV}$ stands for the minimum energy of the cosmic background (CB) photon in the pair production process with LIV. The latter effect can lead to changes in the optical depth, $\tau_\gamma\,(E_\gamma, z)$, which quantifies how opaque to photons the universe is. The survival probability, i.e., the probability that a photon, γ, emitted with a given energy, E_γ, and at a given redshift, z, reaches Earth without interacting with the background, is given by

$$P_{\gamma\to\gamma}(E_\gamma, z) = e^{-\tau_\gamma(E_\gamma, z)}. \tag{2}$$

The photon horizon is the distance (z_h) for which $\tau_\gamma(E_\gamma, z_h) = 1$. z_h defines, as a function of the energy of the photon, the redshift at which an emitted photon will have probability $P_{\gamma\to\gamma} = 1/e$ of reaching Earth. The evaluation of the photon horizon is of extreme importance because it summarizes the visible universe as a function of the energy of the emitted photon. In this section, the photon horizon is calculated including LIV effects. The argument presented in De Angelis et al. (2013) is followed here.

In the intergalactic medium, the $\gamma\gamma_{\rm CB} \to e^+e^-$ interaction is the main contribution to determine the photon horizon. In the approximation where cosmological effects are negligible, the mean-free path, $\lambda\,(E_\gamma)$, of this interaction is given by

$$\lambda(E_\gamma) = \frac{cz}{H_0 \tau_\gamma(E_\gamma, z)}, \tag{3}$$

where $H_0 = 70$ km s^{-1} Mpc^{-1} is the Hubble constant and c is the speed of light in a vacuum. The optical depth is obtained by

$$\begin{aligned}\tau_\gamma(E_\gamma, z) = &\int_0^z dz \frac{c}{H_0(1+z)\sqrt{\Omega_\Lambda + \Omega_M(1+z)^3}}\\ &\times \int_{-1}^{1} d(\cos\theta)\frac{1-\cos\theta}{2}\\ &\times \int_{\epsilon_{\rm th}^{\rm LIV}}^{\infty} d\epsilon\, n_\gamma(\epsilon, z)\sigma(E_\gamma, \epsilon, z),\end{aligned} \tag{4}$$

where θ is the angle between the direction of propagation of both photons $\theta = [-\pi, +\pi]$, $\Omega_\Lambda = 0.7$ is the dark energy density, $\Omega_M = 0.3$ is the matter density, σ is the cross section of the interaction, and $\epsilon_{\rm th}^{\rm LIV}$ is the threshold energy of the interaction as given by Equation (13).

$n_{\gamma_{\rm CB}}$ is the background photon density. The dominant backgrounds are the extra-galactic background light (EBL) for $E_\gamma < 10^{14.5}$ eV, the cosmic background microwave radiation (CMB) for $10^{14.5}$ eV $< E_\gamma < 10^{19}$ eV and the radio background (RB) for $E_\gamma > 10^{19}$ eV. In the calculations presented here, the Gilmore model (Gilmore & Ramirez-Ruiz 2010) was used for the EBL. Since LIV effects in the photon horizon are expected only at the highest energies ($E_\gamma > 10^{16}$ eV), using different models of EBL would not change the results. For the RB, the data from Gervasi et al. (2008) with a cutoff at 1 MHz were used. Different cutoffs in the RB data lead to different photon horizons as shown in De Angelis et al. (2013). Since no new effect shows up in the LIV calculation due to the RB cutoff, only the 1 MHz cutoff will be presented.

It is usual for studies such as the one presented here, in which the threshold of an interaction is shifted, causing a modification of the mean-free path, to neglect direct effects in the cross section, σ, when solving Equation (4). However, an implicit change of the cross section is taken into account given its dependence on the energy threshold $\epsilon_{\rm th}^{\rm LIV}$ (Breit & Wheeler 1934).

Figures 1–3 show the mean-free path for $\gamma\gamma_{\rm CB} \to e^+e^-$ as a function of the energy of the photon, E_γ, for several LIV coefficients with $n = 0$, $n = 1$, and $n = 2$, respectively. The main effect is an increase in the mean-free path that becomes stronger the larger the photon energy, E_γ, and the LIV coefficient are. Consequently, fewer interactions happen and the photon, γ, will have a higher probability of traveling farther than it would have in an LI scenario. Similar effects due to LIV are seen for $n = 0$, $n = 1$, and $n = 2$. The LIV coefficients are treated as free parameters; therefore, there is no way to compare the importance of the effect between the orders $n = 0$,

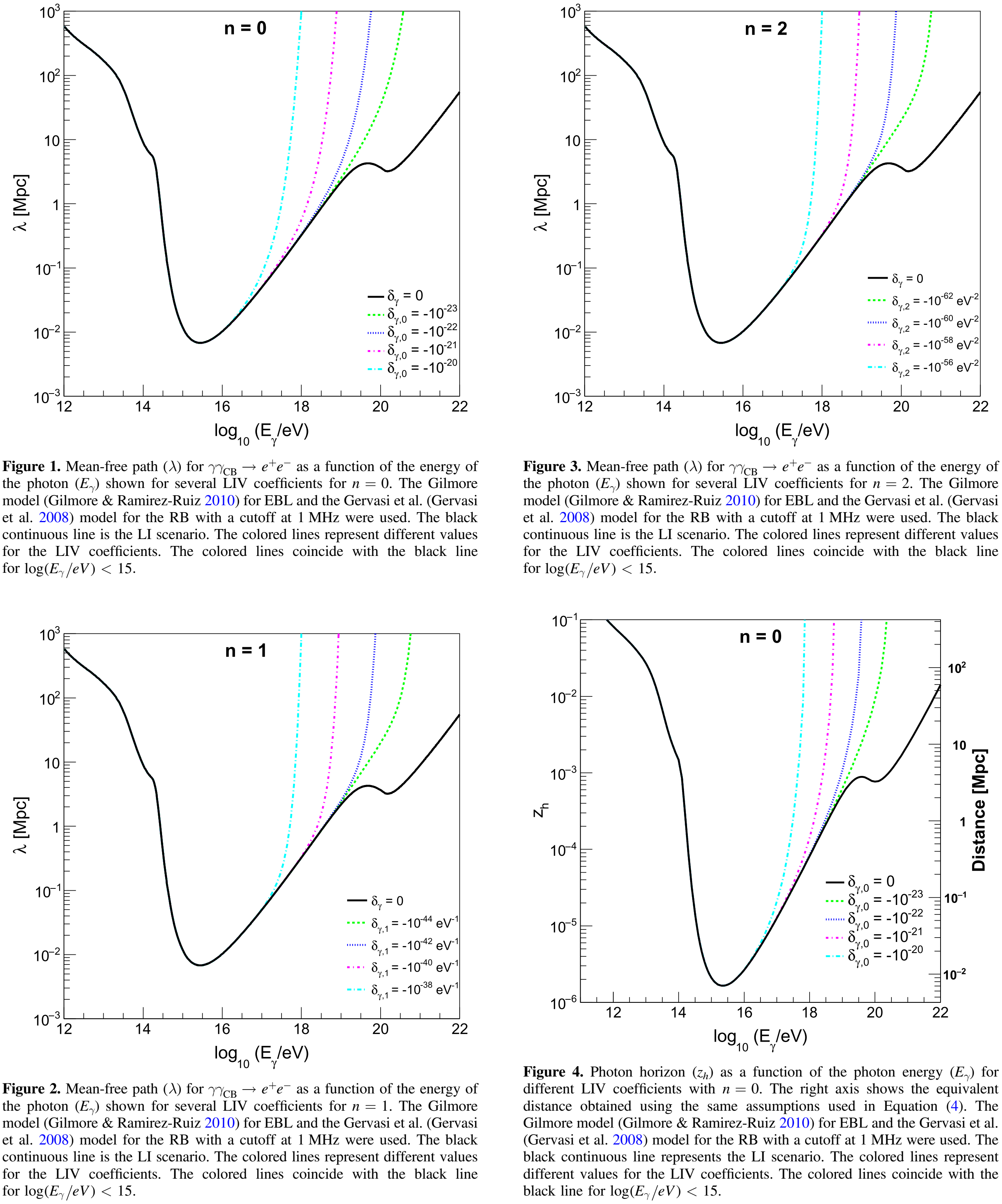

Figure 1. Mean-free path (λ) for $\gamma\gamma_{\rm CB} \rightarrow e^+e^-$ as a function of the energy of the photon (E_γ) shown for several LIV coefficients for $n = 0$. The Gilmore model (Gilmore & Ramirez-Ruiz 2010) for EBL and the Gervasi et al. (Gervasi et al. 2008) model for the RB with a cutoff at 1 MHz were used. The black continuous line is the LI scenario. The colored lines represent different values for the LIV coefficients. The colored lines coincide with the black line for $\log(E_\gamma/eV) < 15$.

Figure 2. Mean-free path (λ) for $\gamma\gamma_{\rm CB} \rightarrow e^+e^-$ as a function of the energy of the photon (E_γ) shown for several LIV coefficients for $n = 1$. The Gilmore model (Gilmore & Ramirez-Ruiz 2010) for EBL and the Gervasi et al. (Gervasi et al. 2008) model for the RB with a cutoff at 1 MHz were used. The black continuous line is the LI scenario. The colored lines represent different values for the LIV coefficients. The colored lines coincide with the black line for $\log(E_\gamma/eV) < 15$.

Figure 3. Mean-free path (λ) for $\gamma\gamma_{\rm CB} \rightarrow e^+e^-$ as a function of the energy of the photon (E_γ) shown for several LIV coefficients for $n = 2$. The Gilmore model (Gilmore & Ramirez-Ruiz 2010) for EBL and the Gervasi et al. (Gervasi et al. 2008) model for the RB with a cutoff at 1 MHz were used. The black continuous line is the LI scenario. The colored lines represent different values for the LIV coefficients. The colored lines coincide with the black line for $\log(E_\gamma/eV) < 15$.

Figure 4. Photon horizon (z_h) as a function of the photon energy (E_γ) for different LIV coefficients with $n = 0$. The right axis shows the equivalent distance obtained using the same assumptions used in Equation (4). The Gilmore model (Gilmore & Ramirez-Ruiz 2010) for EBL and the Gervasi et al. (Gervasi et al. 2008) model for the RB with a cutoff at 1 MHz were used. The black continuous line represents the LI scenario. The colored lines represent different values for the LIV coefficients. The colored lines coincide with the black line for $\log(E_\gamma/eV) < 15$.

$n = 1$, and $n = 2$, each order must be limited independently. Note that $\delta_{\gamma,n}$ units depend on n.

The LIV effect becomes more tangible in Figure 4 in which the photon horizon (z_h) is shown as a function of E_γ for $n = 0$. For energies above $E_\gamma > 10^{16.5}$ eV and the given LIV values, the photon horizon increases when LIV is taken into account, increasing the probability that a distant source emitting high energy photons produces a detectable flux at Earth. Similar results are found for $n = 1$ and $n = 2$.

3. Flux of GZK Photons Including LIV Effects

Even though the effects of LIV on the propagation of high energy photons are strong, they cannot be directly measured and, therefore, used to probe LIV models. In order to do that, in this section, the flux of GZK photons on Earth considering LIV is obtained and compared to the upper limits on the photon flux from the Pierre Auger Observatory (Carla Bleve for the Pierre Auger Collaboration 2015; The Pierre Auger Collaboration 2017a).

UHECRs interact with the photon background producing pions (photo-pion production). Pions decay shortly after production, generating EeV photons among other particles. The effect of this interaction chain suppresses the primary UHECR flux and generates a secondary flux of photons (Gelmini et al. 2007). The effect was named GZK after the authors of the original papers (Greisen 1966; Zatsepin & Kuz'min 1966). The EeV photons (GZK photons) also interact with the background photons as described in the previous sections.

In order to consider LIV in the GZK photon calculation, the CRPropa3/EleCa (Settimo & Domenico 2015; Batista et al. 2016) codes were modified. The mean-free paths calculated in Section 2 were implemented in these codes and the propagation of the particles was simulated. The resulting flux of GZK photons is, however, extremely dependent on the assumptions about the sources of cosmic rays, such as the injected energy spectra, mass composition, and the distribution of sources in the universe. Therefore, four different models for the injected spectra of cosmic rays at the sources and five different models for the evolution of sources with redshift are considered in the calculations presented below.

3.1. Models of UHECR Sources

No source of UHECR was ever identified and correlation studies with types of sources are not conclusive. Several source types and mechanisms of particle production have been proposed. The amount of GZK photons produced in the propagation of the particles depends significantly on the source model used. In this paper, four UHECR source models are used to calculate the corresponding GZK photons. The models are used as illustrations of the differences in the production of GZK photons; an analysis of the validity of the models and their compatibility with experimental data is beyond the scope of this paper. However, it is important to note that strong constrains to the source models can be set by new measurements (The Pierre Auger Collaboration 2017b). The models used here are labeled as follows:

1. C_1: Aloisio et al. (2014);
2. C_2: Unger, Farrar, & Anchordoqui (2015)—Fiducial model (Unger et al. 2015);
3. C_3: Unger et al. (2015) with the abundance of galactic nuclei from (Olive & Group 2014);
4. C_4: Berezinsky, Gazizov, & Grigorieva (2007)—Dip model (Berezinsky et al. 2006).

All four models propose the energy spectrum at the source to be a power-law distribution of the energy with a rigidity cutoff:

$$\frac{dN}{dE_s} = \begin{cases} E_s^{-\Gamma}, & \text{for } R_s < R_{\text{cut}} \\ E_s^{-\Gamma} e^{1-R_s/R_{\text{cut}}}, & \text{for } R_s \geqslant R_{\text{cut}} \end{cases}, \tag{5}$$

where the spectral index, Γ, and the rigidity cutoff, R_{cut}, are parameters given by each model. Five different species of nuclei (H, He, N, Si, and Fe) are considered in these models and their fraction (fH, fHe, fN, fSi, and fFe) are given in Table 1.

The composition of UHECR has a strong influence on the generated flux GZK photons and, therefore, on the possibility to set limits on LIV effects. The models chosen in this study range from very light (C_4) to very heavy (C_2) passing by intermediate compositions C_1 and C_3. Heavier compositions produce less GZK photons and therefore are less prone to reveal LIV effects.

Figure 5 shows the dependence of the GZK photon flux on the source model used. The integral of the GZK photon fluxes for the LIV case of $\delta_{\gamma,0} = 10^{-20}$ are shown as a function of energy. The use of different LIV coefficients results in a shift up and down in the integral flux for each source model, having negligible changes in each ratio. The dependence on the model is of several orders of magnitude and should be considered in studies trying to impose limits on LIV coefficients. The capability to restrict LIV effects is proportional to the GZK photon flux generated in each model assumption.

3.2. Models of Source Distribution

Figure 4 shows how the photon horizon increases significantly when LIV is considered. Therefore, the source distribution in the universe is an important input in GZK photon calculations usually neglected in previous studies. Five different models of source evolution(R_n) are considered here.

1. R_1: sources are uniformly distributed in a comoving volume;
2. R_2: sources follow the star formation distribution given in Hopkins & Beacom (2006). The evolution is proportional to $(1+z)^{3.4}$ for $z < 1$, to $(1+z)^{-0.26}$ for $1 \leqslant z < 4$ and to $(1+z)^{-7.8}$ for $z \geqslant 4$;
3. R_3: sources follow the star formation distribution given in Yüksel et al. (2008). The evolution is proportional to $(1+z)^{3.4}$ for $z < 1$, to $(1+z)^{-0.3}$ for $1 \leqslant z < 4$ and to $(1+z)^{-3.5}$ for $z \geqslant 4$;
4. R_4: sources follow the GRB rate evolution from Le & Dermer (2007). The evolution is proportional to $(1 + 8z)/[1 + (z/3)^{1.3}]$;
5. R_5: sources follow the GRB rate evolution from Le & Dermer (2007). The evolution is proportional to $(1 + 11z)/[1 + (z/3)^{0.5}]$.

Figure 6 shows the ratio of sources as a function of redshift for the five source distributions considered. The source evolution uniformly distributed in a comoving volume is shown only for comparison. It is clear that even astrophysical motivated evolutions are different for redshifts larger than two. Charged particles produced in sources farther than redshifts equal to one have a negligible probability of reaching Earth; however, the GZK photons produced in their propagation could travel farther if LIV is considered.

Table 1
Parameters of the Four Source Models Used in This Paper

Model	Γ	$\log_{10}(R_{\mathrm{cut}}/V)$	*f*H	*f*He	*f*N	*f*Si	*f*Fe
C_1	1	18.699	0.7692	0.1538	0.0461	0.0231	0.00759
C_2	1	18.5	0	0	0	1	0
C_3	1.25	18.5	0.365	0.309	0.121	0.1066	0.098
C_4	2.7	∞	1	0	0	0	0

Note. Γ is the spectral index, R_{cut} is the rigidity cutoff and *f*H, *f*He, *f*N, *f*Si, and *f*Fe are the fractions of each nuclei.

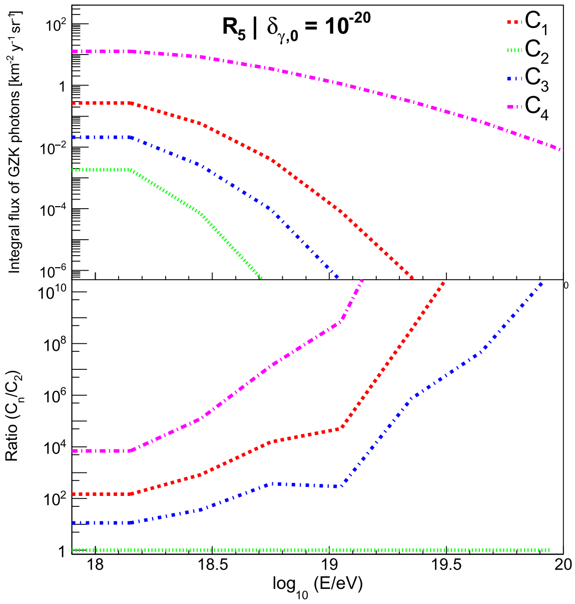

Figure 5. Integral flux of GZK photons as a function of the photon energy for each source model. Each line represents a different model C_n. All cases are for the source evolution model R_5 and LIV coefficient $\delta_{\gamma,0} = 10^{-20}$. The top panel shows the integral flux, while the bottom panel show the ratio to the one that produces less photons, C_2.

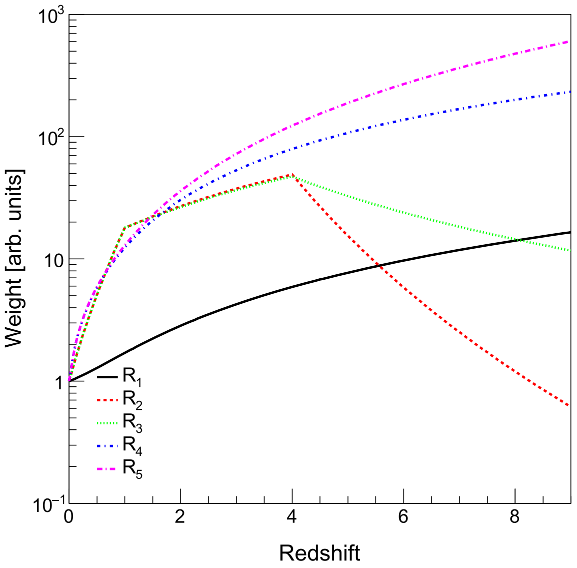

Figure 6. Source evolution with redshift. Each line represents one of the models R_n, see the text for details of the models.

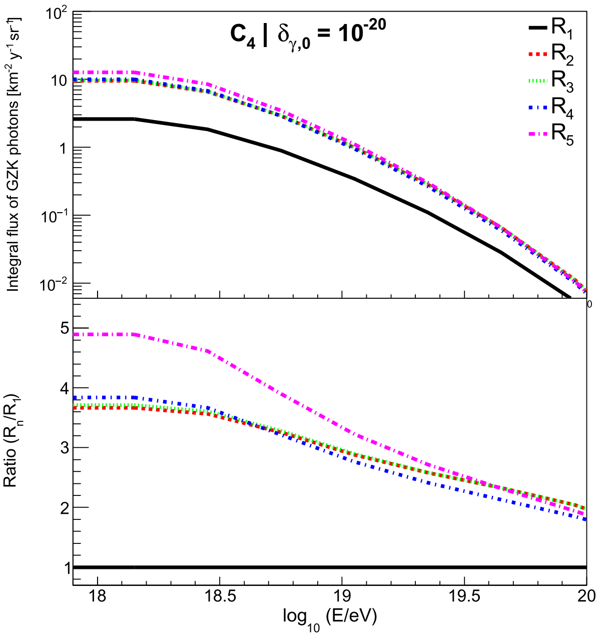

Figure 7. Integral flux of GZK photons as a function of the photon energy for each source evolution model. Each line represents a different model R_n. All cases are for the source model C_4 and LIV coefficient $\delta_{\gamma,0} = 10^{-20}$. The top panel shows the integral flux, while the bottom panel shows the ratio to the simplest case, R_1.

Figure 7 shows the effect of the source evolution in the prediction of GZK photons including LIV effects. Once more, the use of different LIV coefficients results in a shift up an down in the integral flux for each source evolution model, having negligible changes in each ratio. The differences for each source evolution model are as large as 500% at $E = 10^{18}$ eV. The capability to restrict LIV effects is proportional to the GZK photon flux generated in each model assumption.

4. Limits on LIV Coefficients

The GZK photon flux of the five astrophysical models shown above are considered together with the upper limits on the photon flux imposed by the Pierre Auger Observatory to set limits on the LIV coefficients. The simulations considered sources up to 9500 Mpc ($z \approx 8.88$). The reference results are for model C_3R_5, as this is the model that best describes current UHECR data. The three orders of LIV ($n = 0$, 1, and 2) are considered for each astrophysical model C_i. Two limiting cases are also considered: LI and maximum LIV, labeled as $\delta_\gamma = 0$ and $\delta_\gamma \to -\infty$, respectively. The Lorentz invariant case (LI) is shown for comparison. The maximum LIV case ($\delta_\gamma \to -\infty$) represents the limit in which the mean-free path of the

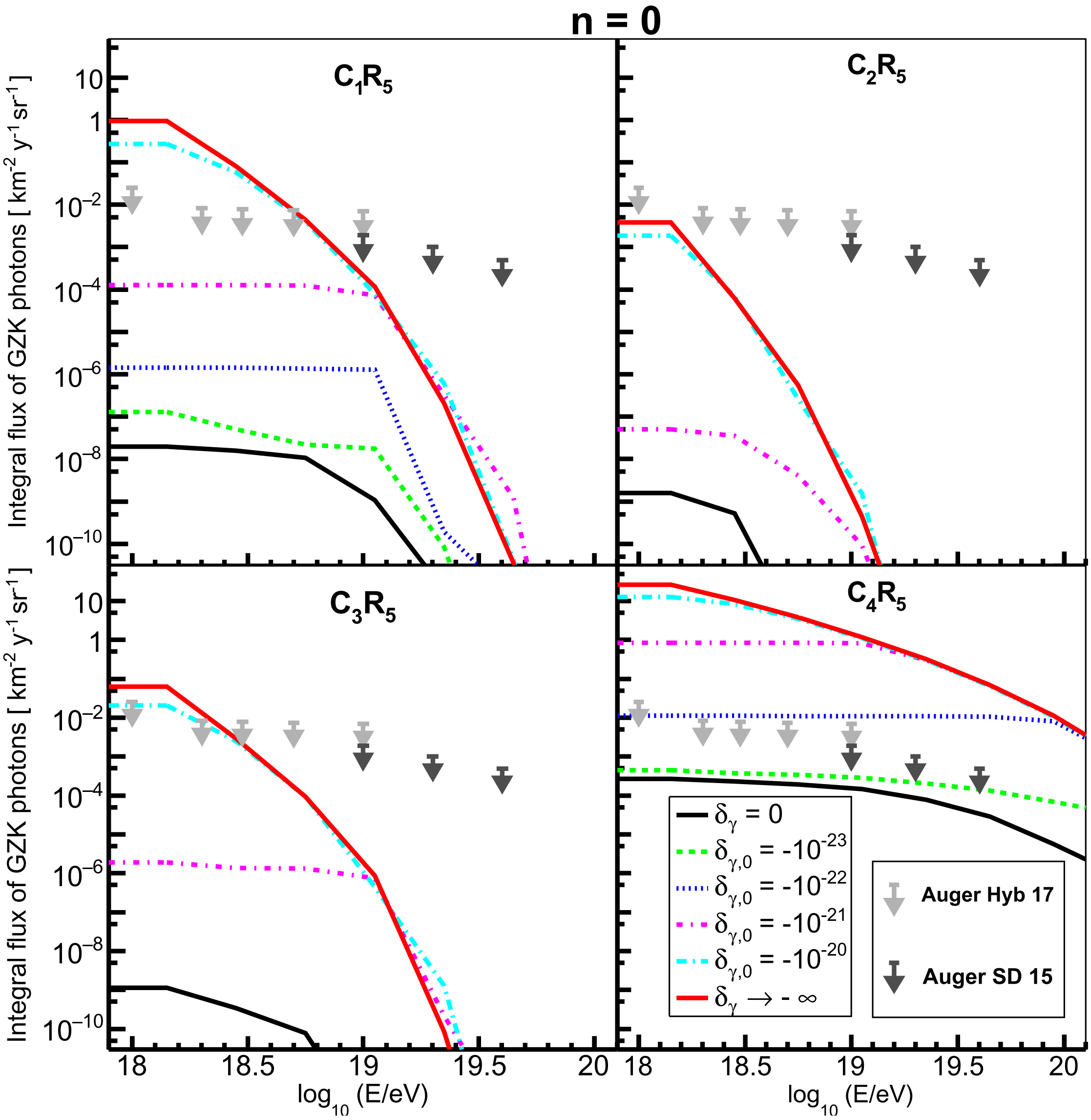

Figure 8. Integral flux of GZK photons as a function of the photon energy, considering LIV effects for $n = 0$. The black continuous line represents the LI scenario. The colored lines represent different values for the LIV coefficients. The red line represents the limit LIV case. The arrows represent the upper limits from the Pierre Auger Observatory. Each panel represents a source model, C_1R_5, C_2R_5, C_3R_5, C_4R_5, respectively.

photon–photon interaction goes to infinity at all energies and therefore no interaction happens. These two cases bracket the possible LIV solutions. The UHECR flux reaching Earth was normalized to the flux measured by the Pierre Auger Observatory (Inés Valiño for the Pierre Auger Collaboration 2015) at $E = 10^{18.75}$ eV, which sets the normalization of the GZK photon flux produced in the propagation of these particles.

Figures 8–10 show the results of the calculations. For some LIV coefficients, models C_1R_5, C_3R_5, and C_4R_5 produces more GZK photons than the upper limits imposed by Auger, therefore, upper limits on the LIV coefficients can be imposed. Model C_2R_5 produces less GZK photons than the upper limits imposed by Auger even for the extreme scenario $\delta_\gamma \to -\infty$; therefore, no limits on the LIV coefficients could be imposed. Table 2 shows the limits imposed in this work for each source model and LIV order.

Table 3 shows the limits imposed by other works for the photons sector for comparison. The direct comparison of the results obtained here (C_3R_5) is only possible with Galaverni & Sigl (2008a; first line in Table 3) because of the similar technique based on GZK photons. The differences between the calculations presented here and the limits imposed in Galaverni & Sigl (2008a) can be explained by (a) the different assumptions considered in the $\gamma\gamma$ interactions with LIV, (b) the different astrophysical models used, and (c) the upper limit on the GZK photon flux used. In Galaverni & Sigl (2008a), the limits were obtained by calculating the energy in which the interaction of a high energy photon with a background photon at the peak of the CMB, i.e., with energy $\epsilon = 6 \times 10^{-4}$ eV, becomes kinematically forbidden. In this work, a more complete approach was used, where the energy threshold was calculated, the mean-free path was obtained by integrating the

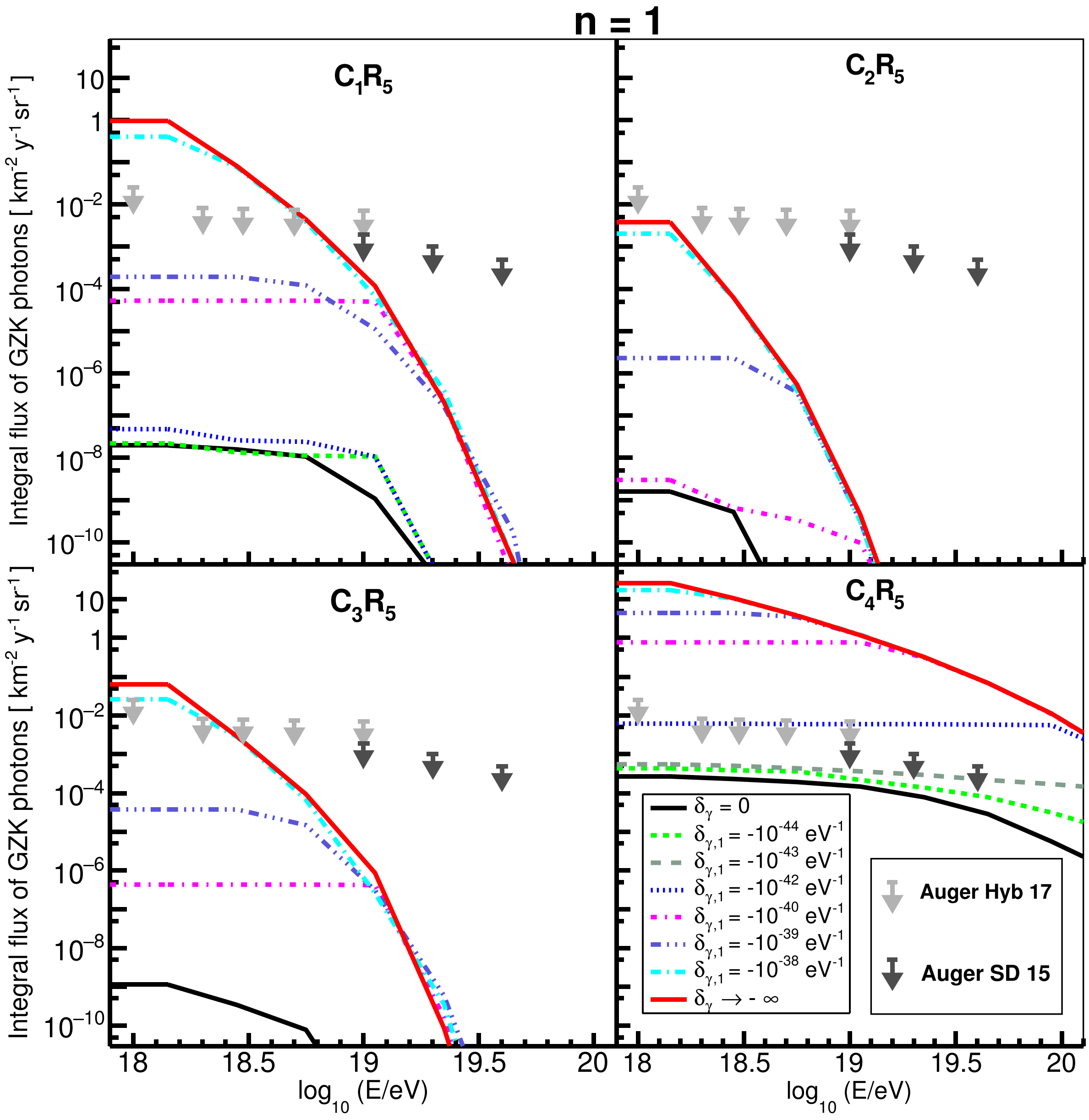

Figure 9. Integral flux of GZK photons as a function of the photon energy, considering LIV effects for $n = 1$. The black continuous line represents the LI scenario. The colored lines represent different values for the LIV coefficients. The red line represents the limit LIV case. The arrows represent the upper limits from the Pierre Auger Observatory. Each panel represents a source model, C_1R_5, C_2R_5, C_3R_5, C_4R_5, respectively.

whole background photon spectrum and the propagation was simulated, obtaining the intensity of the flux of GZK photons. The astrophysical scenario used in Galaverni & Sigl (2008a) was a pure proton composition with energy spectrum normalized by the AGASA measurement (The AGASA Collaboration 2006) and index $\Gamma = 2.6$. The source distribution was not specified in the study. However, this astrophysical scenario is ruled out by the $X_{\max}$ measurements from the Pierre Auger Observatory (The Pierre Auger Collaboration 2014a, 2014b). In the calculations presented here, the LIV limits were updated using astrophysical scenarios compatible to the Auger $X_{\max}$ data. Finally, in this paper, new GZK photon limits published by Auger are used. The LIV limits presented here are, therefore, more realistic and up to date.

The other values in Table 3 are shown for completeness. The second and third entries are based on energy dependent arrival time of TeV photons: (a) a PKS 2155−304 flare measured with H.E.S.S. (The H.E.S.S. Collaboration 2011) and (b) GRB 090510 measured with *Fermi*-LAT (Vasileiou et al. 2013). Entry H.E.S.S.—Mrk 501 (2017) (Lorentz & Brun 2017) in Table 3 is based on the kinematics of the interactions of photons from Mrk 501 with the background. All of the studies shown in Table 3 assume LIV only in the photon sector. However, the systematics of the measurements and the energy

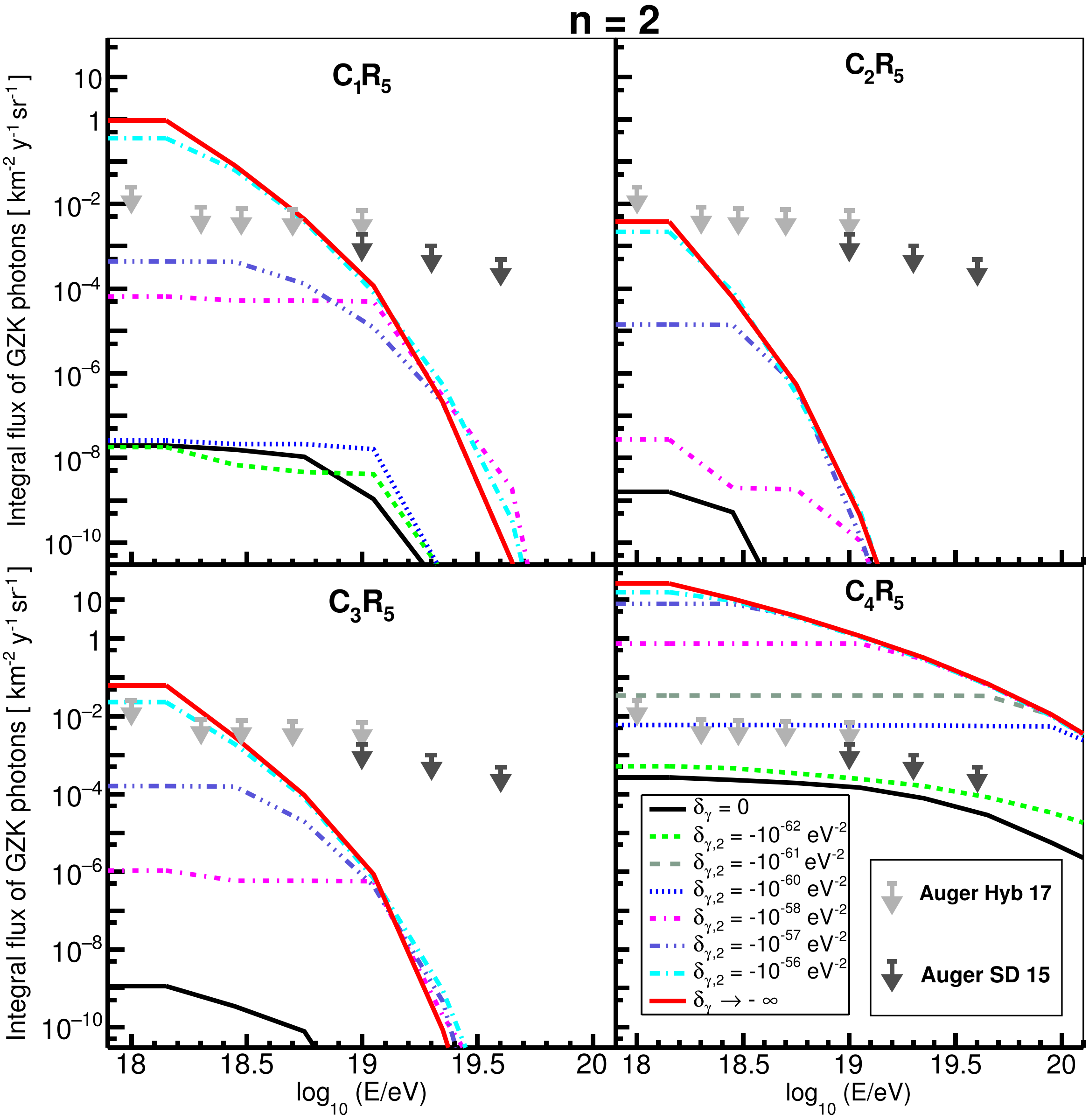

Figure 10. Integral flux of GZK photons as a function of the photon energy considering LIV effects for $n = 2$. The black continuous line represents the LI scenario. The colored lines represent different values for the LIV coefficients. The red line represents the limit LIV case. The arrows represent the upper limits from the Pierre Auger Observatory. Each panel represents a source model, C_1R_5, C_2R_5, C_3R_5, C_4R_5, respectively.

Table 2
Limits on the LIV Coefficients Imposed by This Work for Each Source Model and LIV Order (n)

Model	$\delta_{\gamma,0}^{\text{limit}}$	$\delta_{\gamma,1}^{\text{limit}}$ (eV^{-1})	$\delta_{\gamma,2}^{\text{limit}}$ (eV^{-2})
C_1R_5	$\sim -10^{-20}$	$\sim -10^{-38}$	$\sim -10^{-56}$
C_2R_5	⋯	⋯	⋯
C_3R_5	$\sim -10^{-20}$	$\sim -10^{-38}$	$\sim -10^{-56}$
C_4R_5	$\sim -10^{-22}$	$\sim -10^{-42}$	$\sim -10^{-60}$

Note. Model C_3R_5 is pointed out as containing the reference values of this paper because it describes better the current UHECR data.

Table 3
Limits on the LIV Coefficients Imposed by Other Works Based on Gamma-Ray Propagation

Model	$\delta_{\gamma,0}^{\text{limit}}$	$\delta_{\gamma,1}^{\text{limit}}$ (eV^{-1})	$\delta_{\gamma,2}^{\text{limit}}$ (eV^{-2})
Galaverni & Sigl (2008a)	⋯	-1.97×10^{-43}	-1.61×10^{-63}
H.E.S.S.—PKS 2155−304 (2011)	⋯	-4.76×10^{-28}	-2.44×10^{-40}
Fermi—GRB 090510 (2013)	⋯	-1.08×10^{-29}	-5.92×10^{-41}
H.E.S.S.—Mrk 501 (2017)	⋯	-9.62×10^{-29}	-4.53×10^{-42}

Note. First line shows a previous result, which can be compared to the calculations presented here in Table 2. The last three lines are shown for completeness. These limits are based on gamma-ray arrival time and are not directly comparable to the ones in Table 2.

of photons (TeV photons versus EeV photons) are very different and a direct comparison between the GZK photon calculations shown here and the time of arrival of TeV photon is not straightforward.

5. Conclusions

In this paper, the effect of possible LIV in the propagation of photons in the universe is studied. The interaction of a high energy photon traveling in the photon background was solved under LIV in the photon sector hypothesis. The mean-free path of the $\gamma\gamma_{\rm CB} \rightarrow e^+e^-$ interaction was calculated considering LIV effects. Moderate LIV coefficients introduce a significant change in the mean-free path of the interaction as shown in Section 2 and Figures 1–3. The corresponding LIV photon horizon was calculated as shown in Figure 4.

The dependence of the integral flux of GZK photons on the model for the sources of UHECRs is discussed in Section 3 and shown in Figures 5 and 7. The flux changes several orders of magnitude for different injection spectra models. A difference of about 500% is also found for different source evolution models. Previous LIV limits were calculated using GZK photons generated by source models currently excluded by the data (Galaverni & Sigl 2008a). The calculations presented here show LIV limits based on source models compatible with current UHECR data. In particular, model C_3R_5 was shown to describe the energy spectrum, composition, and arrival direction of UHECR (Unger et al. 2015) and therefore is chosen as our reference result.

The calculated GZK photon fluxes were compared to most updated upper limits from the Pierre Auger Observatory and are shown in Figures 8–10. For some of the models, it was possible to impose limits on the LIV coefficients, as shown in Table 2. It is important to note that the LIV limits shown in Table 2 were derived from astrophysical models of UHECR, compatible to the most updated data. The limits presented here are several orders of magnitude more restrictive than previous calculations based on the arrival time of TeV photons (The H.E.S.S. Collaboration 2011; Vasileiou et al. 2013); however, the comparison is not straightforward due to different systematics of the measurements and energy of the photons.

R.G.L. is supported by FAPESP (2014/26816-0, 2016/24943-0). H.M.H. acknowledges IFSC/USP for their hospitality during the developments of this work, Abdel Pérez Lorenzana for enlightening discussions, and the support from Conacyt Mexico under grant 237004 and the Brazilian agency FAPESP (2017/03680-3). V.d.S. thanks the Brazilian population support via FAPESP (2015/15897-1) and CNPq. This work has partially made use of the computing facilities of the Laboratory of Astroinformatics (IAG/USP, NAT/Unicsul), whose purchase was made possible by the Brazilian agency FAPESP (2009/54006-4) and the INCT-A. The authors acknowledge the National Laboratory for Scientific Computing (LNCC/MCTI, Brazil) for providing HPC resources of the SDumont supercomputer, which have contributed to the research results reported within this paper (http://sdumont.lncc.br).

Software: CRPropa3 (Batista et al. 2016, as developed on https://github.com/CRPropa/CRPropa3, EleCa (Settimo & Domenico 2015).

Appendix
Description of the LIV Model

Equation (1) leads to unconventional solutions of the energy threshold in particle production processes of the type $AB \rightarrow CD$. In this paper, the $\gamma\gamma_{\rm CB} \rightarrow e^+e^-$ interaction is considered. From now on, the symbol γ refers to a high energy gamma-ray with energy $E_\gamma = [10^9, 10^{22}]$ eV that propagates in the universe and interacts with the CB photons, $\gamma_{\rm CB}$, with energy $\epsilon = [10^{-11}, 10]$ eV.

Considering LIV in the photon sector, the specific dispersion relations can be written as

$$E_\gamma^2 - p_\gamma^2 = \delta_{\gamma,n}\, E_\gamma^{n+2},$$
$$\epsilon^2 - p_{\gamma_{\rm CB}}^2 = \delta_{\gamma,n}\, \epsilon^{n+2}, \qquad (6)$$

where $\delta_{\gamma,n}$ is the n-order LIV coefficient in the photon sector and therefore taken to be the same in both dispersion relations. The standard LI dispersion relation for the electron–positron pair follows: $E_{e^\pm}^2 - p_{e^\pm}^2 = m_e^2$.

Taking into account the inelasticity (K) of the process ($E_{e^-} = KE_\gamma$) and imposing energy–momentum conservation in the interaction, the following expression for a head-on collision with collinear final momenta can be written to leading order in $\delta_{\gamma,n}$

$$4\epsilon E_\gamma - m_e^2\left(\frac{1}{K(1-K)} - \frac{m_e^2}{2K(1-K)(E_\gamma+\epsilon)^2}\right)$$
$$= -\delta_{\gamma,n}E_\gamma^{n+2}\left[1 + \frac{\epsilon^{n+2}}{E_\gamma^{n+2}} - \frac{\epsilon}{E_\gamma}\left(1 + \frac{\epsilon^n}{E_\gamma^n}\right)\right]. \qquad (7)$$

In the ultra relativistic limit $E_\gamma \gg m_e$ and $E_\gamma \gg \epsilon$, this equation reduces to

$$\delta_{\gamma,n}E_\gamma^{n+2} + 4E_\gamma\epsilon - m_e^2\frac{1}{K(1-K)} = 0. \qquad (8)$$

Equation (8) implies two scenarios: (I) $\delta_{\gamma,n} > 0$ the photo-production threshold energy is shifted to lower energies and (II) $\delta_{\gamma,n} < 0$ the threshold takes place at higher energies than that expected in an LI regime, except for scenarios below a critical value for delta, where the photo-production process is forbidden. Notice that, if $\delta_{\gamma,n} = 0$ in Equation (8) the LI regime is recovered. In the LI regime, it is possible to define $E_\gamma^{\rm LI} = \frac{m_e^2}{4\epsilon K(1-K)}$. The math can be simplified by the introduction of the dimensionless variables

$$x_\gamma = \frac{E_\gamma}{E_\gamma^{\rm LI}}, \qquad (9)$$

and

$$\Lambda_{\gamma,n} = \frac{E_\gamma^{{\rm LI}\,(n+1)}}{4\epsilon}\delta_{\gamma,n}. \qquad (10)$$

Then, Equation (8) takes the form

$$\Lambda_{\gamma,n}x_\gamma^{n+2} + x_\gamma - 1 = 0. \qquad (11)$$

Studying the values of $\delta_{\gamma,n}$ for which Equation (11) has a solution, one can set the extreme allowed LIV coefficient (Galaverni & Sigl 2008b; Martínez-Huerta & Pérez-Lorenzana 2017). The limit LIV coefficient ($\delta_{\gamma,n}^{\rm lim}$) for which the interaction

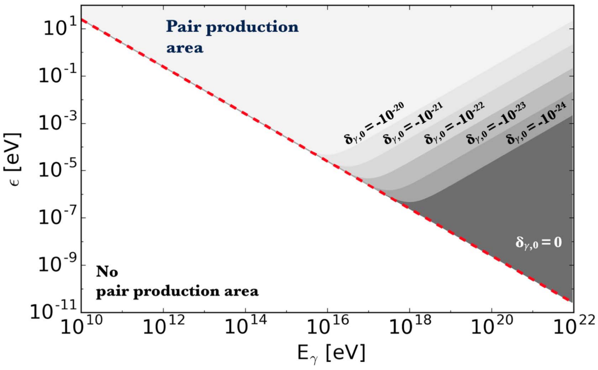

Figure 11. Allowed regions for the pair production in the $\gamma\gamma_{\rm CB} \rightarrow e^+e^-$ interaction considering LIV effects. The high energy photon (E_γ) and background photon (ϵ) parameter space is shown divided in gray regions for each value of $\delta_{\gamma,0}$. The gray areas are cumulative from darker to lighter gray. The red dashed line is a reference for $\delta_{\gamma,0} = 0$ (LI case).

is kinematically allowed for a given E_γ and ϵ is given by

$$\delta_{\gamma,n}^{\rm lim} = -4\frac{\epsilon}{E_\gamma^{{\rm LI}\,(n+1)}}\frac{(n+1)^{n+1}}{(n+2)^{n+2}}. \qquad (12)$$

Equation (11) has real solutions for x_γ only if $\delta_{\gamma,n} > \delta_{\gamma,n}^{\rm lim}$. Therefore, under the LIV model considered here, if $\delta_{\gamma,n} < \delta_{\gamma,n}^{\rm lim}$, high energy photons would not interact with background photons of energy ϵ.

For a given E_γ and $\delta_{\gamma,n}$ the threshold background photon energy ($\epsilon_{\rm th}^{\rm LIV}$) including LIV effects is

$$\epsilon_{\rm th}^{\rm LIV} = \frac{m_e^2}{4E_\gamma K(1-K)} - \frac{\delta_{\gamma,n}E_\gamma^{n+1}}{4}. \qquad (13)$$

The superscript LIV is used for emphasis. In the paper, $\epsilon_{\rm th}^{\rm LIV}$ as given by Equation (13) will be used for the calculations of the mean-free path of the $\gamma\gamma_{\rm CB} \rightarrow e^+e^-$ interaction. Figure 11 shows the allowed parameter space of E_γ and ϵ for different values of $\delta_{\gamma,0}$. The gray areas are cumulative from darker to lighter gray.

ORCID iDs

Rodrigo Guedes Lang https://orcid.org/0000-0003-0492-5628
Humberto Martínez-Huerta https://orcid.org/0000-0001-7714-0704
Vitor de Souza https://orcid.org/0000-0003-0865-233X

References

Ahluwalia, D. V. 1999, Natur, 398, 199
Aloisio, R., Berezinsky, V., & Blasi, P. 2014, JCAP, 10, 020
Amelino-Camelia, G. 2001, Natur, 410, 1065
Amelino-Camelia, G., Ellis, J. R., Mavromatos, N. E., Nanopoulos, D. V., & Sarkar, S. 1998, Natur, 393, 763
Atwood, W. B., et al. 2009, ApJ, 697, 1071
Batista, R. A., Dundovic, A., Erdmann, M., et al. 2016, JCAP, 05, 038
Benjamin Zitzer for the VERITAS Collaboration 2014, Proc. ICRC (Rio de Janeiro), 33, 1147
Berezinsky, V., Gazizov, A., & Grigorieva, S. 2006, PhRvD, 74, 043005
Bi, X.-J., Cao, Z., Li, Y., & Yuan, Q. 2009, PhRvD, 79, 083015
Biteau, J., & Williams, D. A. 2015, ApJ, 812, 60
Bluhm, R. 2014, in Springer Handbook of Spacetime, ed. A. Ashtekar & V. Petkov (Berlin: Springer), 485
Breit, G., & Wheeler, J. A. 1934, PhRv, 46, 1087
Carla Bleve for the Pierre Auger Collaboration 2015, Proc. ICRC (The Hague), 34, 1103
Chang, Z., Li, X., Lin, H.-N., et al. 2016, ChPhC, 40, 045102
Coleman, S., & Glashow, S. L. 1999, PhRvD, 59, 116008
Coleman, S. R., & Glashow, S. L. 1997, PhLB, 405, 249
De Angelis, A., Galanti, G., & Roncadelli, M. 2013, MNRAS, 432, 3245
Ellis, J., Mavromatos, N., Nanopoulos, D., Sakharov, A., & Sarkisyan, E. 2006, APh, 25, 402
Ellis, J., Mavromatos, N., Nanopoulos, D., Sakharov, A., & Sarkisyan, E. 2008, APh, 29, 158
Ellis, J., & Mavromatos, N. E. 2013, APh, 43, 50
Fairbairn, M., Nilsson, A., Ellis, J., Hinton, J., & White, R. 2014, JCAP, 1406, 005
Galaverni, M., & Sigl, G. 2008a, PhRvL, 100, 021102
Galaverni, M., & Sigl, G. 2008b, PhRvD, 78, 063003
Gelmini, G., Kalashev, O., & Semikoz, D. V. 2007, APh, 28, 390
Gervasi, M., Tartari, A., Zannoni, M., Boella, G., & Sironi, G. 2008, ApJ, 682, 223
Gilmore, R., & Ramirez-Ruiz, E. 2010, ApJ, 721, 709
Greisen, K. 1966, PhRvL, 16, 748
Haungs, A., Medina-Tanco, G., & Santangelo, A. 2015, ExA, 40, 1
Hopkins, A. M., & Beacom, J. F. 2006, ApJ, 651, 142
Inés Valiño for the Pierre Auger Collaboration 2015, Proc. ICRC (The Hague), 34, 271
J. Holder for the VERITAS Collaboration 2011, Proc. ICRC (Beijing), 32, 137
Jacob, U., & Piran, T. 2008, JCAP, 01, 031
Jacobson, T., Liberati, S., & Mattingly, D. 2003, PhRvD, 67, 124011
Klinkhamer, F. R., & Schreck, M. 2008, PhRvD, 78, 085026
Le, T., & Dermer, C. D. 2007, ApJ, 661, 394
Liberati, S., & Maccione, L. 2009, ARNPS, 59, 245
Liberati, S., & Maccione, L. 2011, JPhCS, 314, 012007
Lorentz, M., & Brun, P. 2017, EPJWC, 136, 03018
Maccione, L., & Liberati, S. 2008, JCAP, 0808, 027
Martínez-Huerta, H., & Pérez-Lorenzana, A. 2017, PhRvD, 95, 063001
Mattingly, D. 2005, LRR, 8, 5
Myers, R. C., & Pospelov, M. 2003, PhRvL, 90, 211601
Olive, K., & Group, P. D. 2014, ChPhC, 38, 090001
Otte, A. N. 2012, Proc. ICRC (Beijing), 32, 256
Rubtsov, G., Satunin, P., & Sibiryakov, S. 2017, JCAP, 1705, 049
Schreck, M. 2014, in Proc. 6th Meeting on CPT and Lorentz Symmetry, ed. A. Kostelecky (Singapore: World Scientific), 176
Settimo, M., & Domenico, M. D. 2015, APh, 62, 92
Stecker, F. W., & Scully, S. T. 2005, APh, 23, 203
Stecker, F. W., & Scully, S. T. 2009, NJPh, 11, 085003
Tavecchio, F., & Bonnoli, G. 2016, A&A, 585, A25
The AGASA Collaboration 2006, NuPhs, 151, 3
The CTA Consortium 2011, ExA, 32, 193
The H.E.S.S. Collaboration 2006, A&A, 457, 899
The H.E.S.S. Collaboration 2011, APh, 34, 738
The MAGIC Collaboration 2008, PhLB, 668, 253
The MAGIC Collaboration 2016, APh, 72, 61
The Pierre Auger Collaboration 2014a, PhRvD, 90, 122005
The Pierre Auger Collaboration 2014b, PhRvD, 90, 122006
The Pierre Auger Collaboration 2015, NIMPA, 798, 172
The Pierre Auger Collaboration 2017a, JCAP, 04, 009
The Pierre Auger Collaboration 2017b, JCAP, 04, 038
Tinyakov, P. 2014, NIMPA, 742, 29
Unger, M., Farrar, G. R., & Anchordoqui, L. A. 2015, PhRvD, 92, 123001
Vasileiou, V., Jacholkowska, A., Piron, F., et al. 2013, PhRvD, 87, 122001
Xu, H., & Ma, B.-Q. 2016, APh, 82, 72
Yüksel, H., Kistler, M. D., Beacom, J. F., & Hopkins, A. M. 2008, ApJL, 683, L5
Zatsepin, G. T., & Kuz'min, V. A. 1966, ZhPmR, 4, 114
Zhen, C. 2010, ChPhC, 34, 249
Zou, X.-B., Deng, H.-K., Yin, Z.-Y., & Wei, H. 2017, Phys. Lett. B, 776, 284

9 ORIGIN OF UHECR

Cosmic rays are charged particles and, consequently, are deviated in the presence of galactic and extra-galactic magnetic fields. Therefore, their arrival direction does not necessarily point back to their sources. For that reason, a century after their discovery, no definitive answer has yet been found for the question about their sources.

In this work, we join the efforts to move towards an answer to this century-long question by building an understanding on how the distribution of UHECR sources affects the data measured by experiments.

As discussed in Chapter 2, there are three main observables in UHECR experiments: energy spectrum, composition and arrival direction. Phenomenological models usually try to describe both the energy spectrum and composition together. In most approaches, sources are considered to be uniformly distributed and emitting cosmic rays following a power law with a rigidity cutoff,

$$\frac{dN}{dE} = N_0 E^{-\Gamma} e^{-R/R_{\text{cut}}}, \tag{9.1}$$

where the normalization, N_0, the spectral index, Γ, and the rigidity cutoff, $R_{\text{cut}} = E_{\text{cut}}/Z$, are usually taken to be the same at all sources. While this may be a strong assumption, considering unique spectral parameters would lead to an impracticable number of free parameters. In such approach, the spectral parameters and composition at the sources which describe well the data are found. (76,122,123) Nevertheless, not much can be concluded about the distribution of sources, which is either treated as homogeneously distributed or following a source evolution with redshift given by $(1+z)^m$.

Going in a different direction, studies have proposed the main bulk of UHECR to come from the contribution of a single source. (124,125)

Ref. (126) has further delved into understanding the radial distribution of UHECR sources by evaluating the contribution to the spectrum from sources in different distance shells. The need for local sources of UHECR with distances of tens of Mpc, depending on composition, was shown. This result comes from the steep horizon which arises from the energy-dependent propagation losses discussed in Chapter 2.

In Chapter 10, we further improve this analysis. A new fast and robust semi-analytical method for the propagation of UHECR in the presence of turbulent magnetic fields is proposed and the contribution to the spectrum from sources at each distance shell under different magnetic field assumptions is studied. This leads to updates in the constraints on the distance to the nearest UHECR source.

The distribution of arrival directions, on the other hand, is intrinsically related to the distribution, both angular and radial, of UHECR sources. While anisotropy studies at the highest energies are used to try to find correlations between excesses in the arrival direction distribution and the position of candidate sources (79, 127), the large-scale dipole may also contain crucial pieces of information.

As discussed in Chapter 1, the angular distribution of arrival directions for $E > 8$ EeV measured by the Pierre Auger Observatory is well described by a dipole of intensity $\delta = 0.065^{+0.013}_{-0.009}$ pointing outwards the galactic center, i.e., the normalized angular distribution is well described by $1 + \delta \cos\theta$, with θ being the angle between the arrival direction and the dipole direction. (77) The evolution of the phase and amplitude of the dipole in right-ascension when more energy bins are considered was also measured by Auger (78) and corroborates the hypothesis of a transition from predominant galactic to predominant extra-galactic sources.

Understanding the origin of the dipolar behavior as well as its evolution with energy is of paramount importance for moving towards an answer to the origin of UHECR. The arising of a dipolar distribution of arrival directions of UHECR coming from a single source in an environment with turbulent EGMF was discussed in previous works through the use of Monte Carlo simulations. (128) The amplitude of the dipole for a angular distribution resulting from an ensemble of sources under a diffusive regime was also obtained. (129–132)

In Chapter 11, we further develop the understanding of the arising of the dipolar behavior. We propose an analytical calculation of the poles and power spectrum of the angular distribution for a single source under turbulent EGMF. The regime of validity of the diffusive assumption is discussed. We also combine such calculations with the semi-analytical method for the propagation proposed in Chapter 10 to obtain the evolution of the dipole with energy for an ensemble of sources.

10 REVISITING THE DISTANCE TO THE NEAREST ULTRAHIGH ENERGY COSMIC RAY SOURCE: EFFECTS OF EXTRAGALACTIC MAGNETIC FIELDS

PHYSICAL REVIEW D **102,** 063012 (2020)

Revisiting the distance to the nearest ultrahigh energy cosmic ray source: Effects of extragalactic magnetic fields

Rodrigo Guedes Lang[*]
Instituto de Física de São Carlos, Universidade de São Paulo,
Av. Trabalhador São-Carlense, 400 São Carlos, SP, Brazil

Andrew M. Taylor
DESY, D-15738 Zeuthen, Germany

Markus Ahlers
Niels Bohr International Academy and Discovery Center, Niels Bohr Institute,
University of Copenhagen, Blegdamsvej 17, DK-2100 Copenhagen, Denmark

Vitor de Souza
Instituto de Física de São Carlos, Universidade de São Paulo,
Av. Trabalhador São-Carlense, 400 São Carlos, SP, Brazil

(Received 28 May 2020; accepted 12 August 2020; published 11 September 2020)

We update the constraints on the location of the nearest ultrahigh energy cosmic ray (UHECR) source. By analyzing recent data from the Pierre Auger Observatory using state-of-the-art CR propagation models, we reaffirm the need of local sources with a distance less than 25–100 Mpc, depending on mass composition. A new fast semianalytical method for the propagation of UHECR in environments with turbulent magnetic fields is developed. The onset of an enhancement and a low-energy magnetic horizon of cosmic rays from sources located within a particular distance range is demonstrated. We investigate the distance to the nearest source, taking into account these magnetic field effects. The results obtained highlight the robustness of our constrained distances to the nearest source.

DOI: 10.1103/PhysRevD.102.063012

I. INTRODUCTION

The origin of ultrahigh energy cosmic rays (UHECR) remains an open question even a century after their discovery [1]. Deflections of cosmic rays in extragalactic and galactic magnetic fields scramble their arrival direction and, consequently, mask the location of their sources. Only for the most energetic events ($E \gtrsim 10^{19.5}$ eV), some residual information about their origin can still be present in their arrival direction distribution. In particular, a recent analysis of data from the Pierre Auger Observatory [2] has revealed a strong large-scale dipole anisotropy at the level of 6.5% above 8 EeV [3] (see also [4,5]). In addition, the data above 39 EeV show hints of a cross-correlation with γ-ray data, in particular, for the subsample of starburst galaxies [6]. While these results can be considered important milestones toward the identification of UHECR sources, the overall data are presently inconclusive. We refer to the recent reviews [7,8] for further details.

The energy spectrum of UHECR, on the other hand, has been measured with unprecedented statistics [9], revealing two important features: a hardening of the spectral index at $E = 10^{18.8}$ eV, the so-called ankle, and a suppression for $E > 10^{19.7}$ eV [10], which may be explained by either a maximum power of acceleration of the sources or energy losses during the propagation or a combination of both [11]. During their propagation, UHECR interact with the photon background and lose energy via e^-e^+ pair production, pion production, and photodisintegration, the latter of which leads to a change in the particle species [12,13]. These losses are energy dependent, with the highest energies ($E \gtrsim 10^{19.5}$ eV) being dominated by pion production for a proton and by photodisintegration for heavier nuclei, the GZK effect, named after Greisen, Zatsepin and Kuzmin who first predicted it [14,15]. These propagation effects create an energy-dependent horizon, dictating a maximum distance from which UHECR of a given energy are expected to come from [16–19]. As a consequence, the energy spectrum also contains information about the distance distribution of the sources of UHECR, which might be helpful in deciphering their origins.

In this work, we investigate the role played by the local sources of UHECR on the observed spectrum. First, in Sec. II, we revisit the work of Ref. [20] that constrained the distance to the nearest source for an environment with no magnetic fields. This study is updated here by analyzing

---

[*] rodrigo.lang@usp.br

© 2020 American Physical Society

recent data from the Pierre Auger Observatory using the state-of-the-art Monte Carlo propagation code, CRPropa 3 [21]. We also discuss the stability and systematic uncertainties of the fit. We develop the analysis by discussing the combined effects of a distance to the nearest source and extragalactic turbulent magnetic fields. In Sec. III A, we describe a semianalytical approximation for the propagation of UHECR in turbulent extragalactic magnetic fields that provides an efficient method of studying the effect of a magnetic horizon in the cosmic ray data analysis. In Sec. III B, we explore the effects of the distance to the nearest source in the low-energy end of the spectrum for different magnetic field scenarios. The maximum distance to the nearest source is again constrained for such scenarios. Finally, we conclude in Sec. IV.

II. DISTANCE TO THE NEAREST SOURCE

Nearby UHECR sources are necessary to explain the high-energy end of the cosmic ray spectrum ($E \gtrsim 10^{19.5}$ eV) due to the energy-loss horizon of these particles. A better understanding of this requirement may provide additional information about the UHECR source distribution. We update the work of Ref. [20] by analyzing recent UHECR data from the Pierre Auger Observatory.

We consider spatially uniform distributions of sources that accelerate UHECR at a constant rate. The injection spectrum follows a power law with spectral index Γ and a rigidity-dependent exponential cutoff, $\exp(-R/R_{\max})$. We assume a pure mass composition at the sources, with five representative primaries, ^{1}H, ^{4}He, ^{14}N, ^{28}Si, and ^{56}Fe. Such a species range has an approximately uniform spacing in $\ln A$, where A is the atomic mass. We start as in Ref. [20] by neglecting the effects of magnetic fields and consider the robustness of the results under more general conditions in the following section. In the absence of magnetic fields, the use of an one-dimensional (1D) UHECR propagation treatment is justified.

Using the state-of-the-art Monte Carlo propagation code CRPropa 3, we obtain the arriving spectrum from an ensemble of sources. A simple example scenario with $\Gamma = 2$ and $R_{\max} = 10^{21}$ V is considered in order to qualitatively highlight these effects. Figures 1 and 2 show the spectra originating from different distance shells as well as the resulting spectrum for a given distance to the nearest source, $D_{\min}$, for the two extreme primaries, proton and iron. Each distance shell dominates a different energy range in such a way that local sources contribute the most to the very end of the spectrum and, thus, large values of $D_{\min}$ lead to a strong suppression of the flux, which is not compatible with the data.

A. Analysis method

To quantify the proximity of the most local UHECR sources, we fit for each primary the spectral data of the Pierre Auger Observatory [10] using a simple χ^2 test. We test different values of the minimum energy bin of the fit, $E_{\min}^{\mathrm{fit}}$. For each value of $E_{\min}^{\mathrm{fit}}$ and $D_{\min}$, the spectral parameters, Γ and $R_{\max}$, as well as the normalization are taken as free parameters and fitted to the data. We account for the systematic uncertainties by performing a scan in the energy scale from −14% to 14%. The effects of $D_{\min}$ due to propagation losses reveal themselves at the highest energies, at which the particles propagate almost ballistically in the magnetic fields.

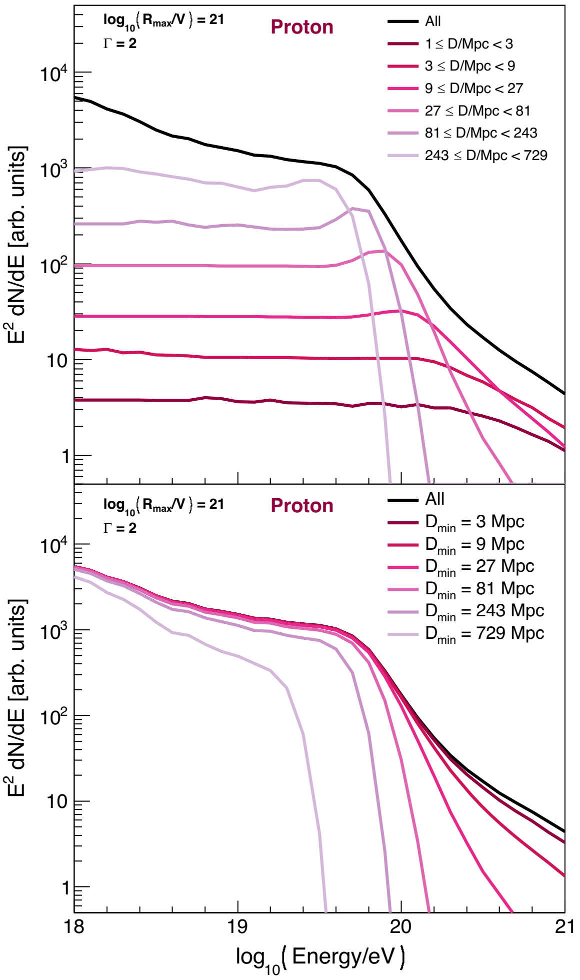

FIG. 1. Example spectrum of cosmic rays divided into distance shells with protons as primaries. On the top panel, the black line represents the total flux, while the colored lines represent the contribution of each distance shell. On the bottom panel, on the other hand, each colored line shows the total flux for a given distance to the nearest source, $D_{\min}$.

The distance to the nearest source has much stronger effects on the measured spectrum than on the measured composition. Similar results are found for every primary. Therefore, a simple fit of the spectral data for a pure

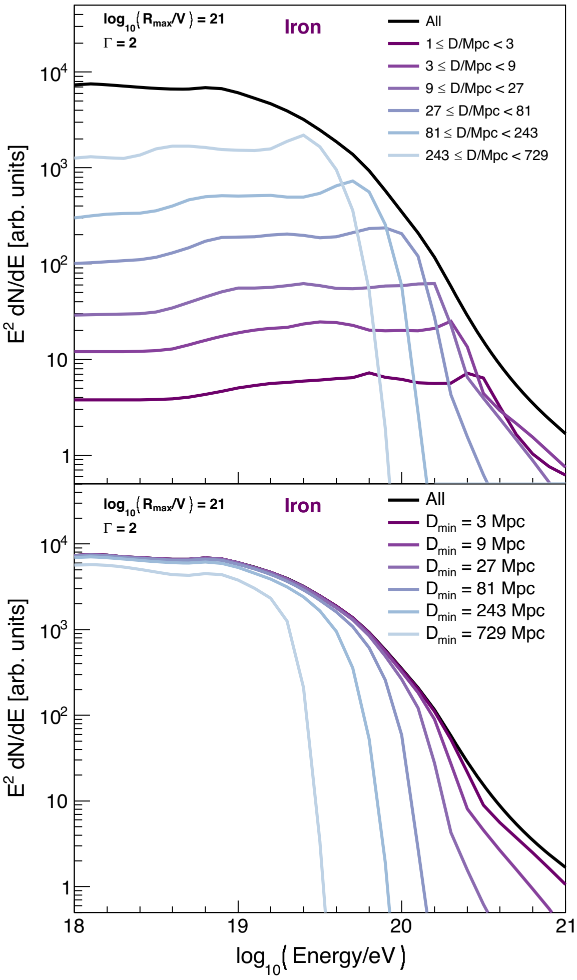

FIG. 2. Same as Fig. 1, but for iron.

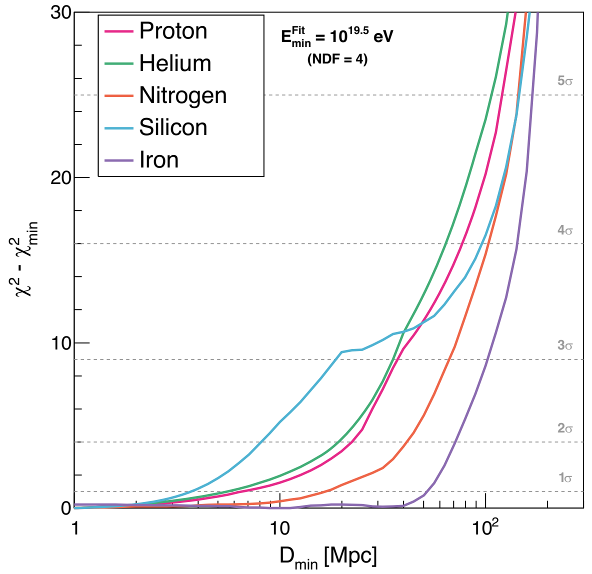

FIG. 3. Value of χ^2 obtained for the best-fit parameters for each distance to the nearest source, D_{min}. The results for $E^{\mathrm{fit}}_{\mathrm{min}} = 10^{19.5}$ eV are shown; similar distributions were obtained for other values of $E^{\mathrm{fit}}_{\mathrm{min}}$. The pink, green, orange, cyan and purple lines represent, respectively, the scenarios with pure proton, helium, nitrogen, silicon, and iron composition at the sources. The confidence level of rejection, σ, is shown for comparison.

composition scenario is sufficient to address the main effects.

B. Maximal distances of the nearest source

Figure 3 shows the evolution of $\Delta\chi^2$ as the value of D_{min} is increased for $E^{\mathrm{fit}}_{\mathrm{min}} = 10^{19.5}$ eV. The data are best described by small values of D_{min}, reinforcing the need for local sources. Large distances to the nearest source can be statistically rejected with a confidence level given by $\sigma = \sqrt{\chi^2 - \chi^2_{\mathrm{min}}}$. The reference rejected distances at 3σ (99.7%) confidence level for $E^{\mathrm{fit}}_{\mathrm{min}} = 10^{19.5}$ eV are shown in Table I. The sudden change in the behavior of the χ^2 distribution for silicon comes from the combination of the dependency of the photodisintegration cross section and energy threshold with the mass and the energy in which the corresponding D_{min} shell is dominant.

Figure 4 shows the resulting spectra for the best-fit scenario, $D^{\mathrm{best}}_{\mathrm{min}}$, as well as the scenario rejected at 3σ confidence level, $D^{3\sigma}_{\mathrm{min}}$. Large distances to the nearest source result in a severe suppression at the highest energies due to the UHECR horizon, which is in disagreement with experimental data. Similar effects on the spectrum were found for helium, nitrogen, and silicon.

C. Systematics

We investigate the systematic uncertainty of the analysis by evaluating the influence of some of the model assumptions in the final result, i.e., $D^{3\sigma}_{\mathrm{min}}$. In particular, we address the minimum energy considered in the fit, $E^{\mathrm{fit}}_{\mathrm{min}}$, the source evolution, and the extragalactic background light model (EBL).

Cosmic rays interact with the background radiation fields, including the EBL, resulting in energy losses.

TABLE I. Reference rejected distances to the nearest source of UHECR at 3σ (99.7%) confidence level and the fitted spectral parameters for such cases. A minimum energy of the fit of $E^{\mathrm{fit}}_{\mathrm{min}} = 10^{19.5}$ eV is considered.

Primary	$D^{3\sigma}_{\mathrm{min}}$ [Mpc]	$\Gamma^{3\sigma}$	$\log_{10}(R^{3\sigma}_{\mathrm{max}}/\mathrm{V})$
p	40	2.8	20
He	40	2.6	23
N	70	2.7	23
Si	31	2.6	23
Fe	100	0.8	19.5

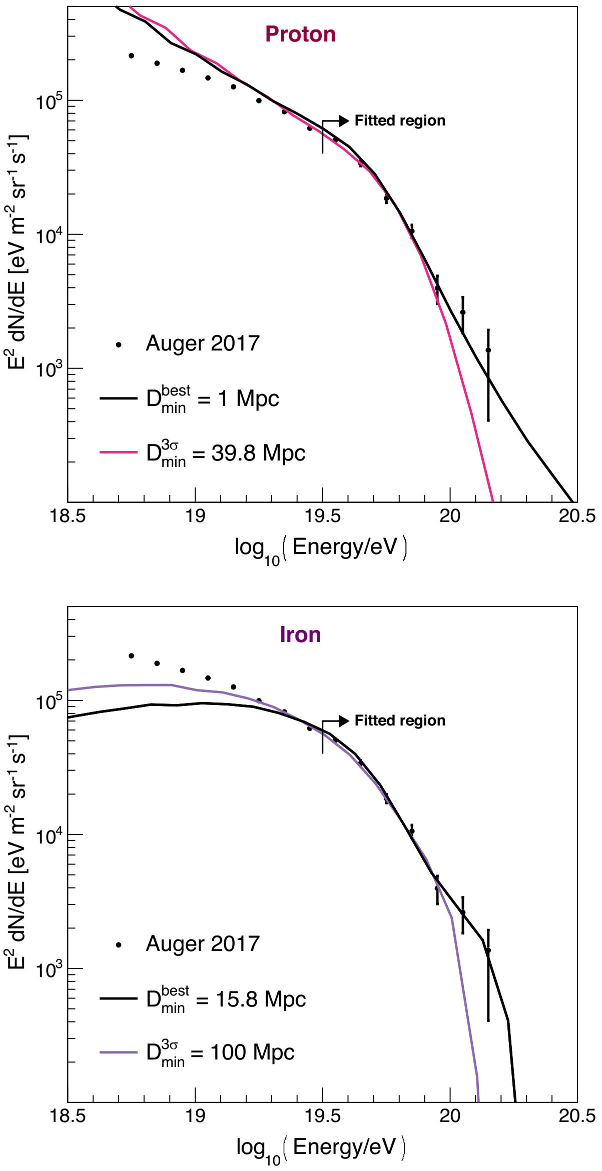

FIG. 4. Spectrum of the best-fit scenario for both $D_{\rm min}^{\rm best}$ and $D_{\rm min}^{3\sigma}$. The top and bottom panels are for pure proton and iron composition, respectively. The black lines show the best-fit spectra for the values of $D_{\rm min}$ which best describes the data, while the colored lines show the best-fit spectra for $D_{\rm min}^{3\sigma}$. The spectral parameters for $D_{\rm min}^{3\sigma}$ are shown in Table I, while the spectral parameters for $D_{\rm min}^{\rm best}$ are ($\Gamma^{\rm best} = 2.8$, $\log_{10}(R_{\rm max}^{\rm best}/{\rm V}) = 20.5$) and ($\Gamma^{\rm best} = 0.8$, $\log_{10}(R_{\rm max}^{\rm best}/{\rm V}) = 19.7$) for proton and iron, respectively.

The EBL distribution, however, is not well understood and several competitive models are used to describe it. In this work, we use the Kneiske model [22] and the upper and lower limits from the Stecker model [23] as representative EBL distributions.

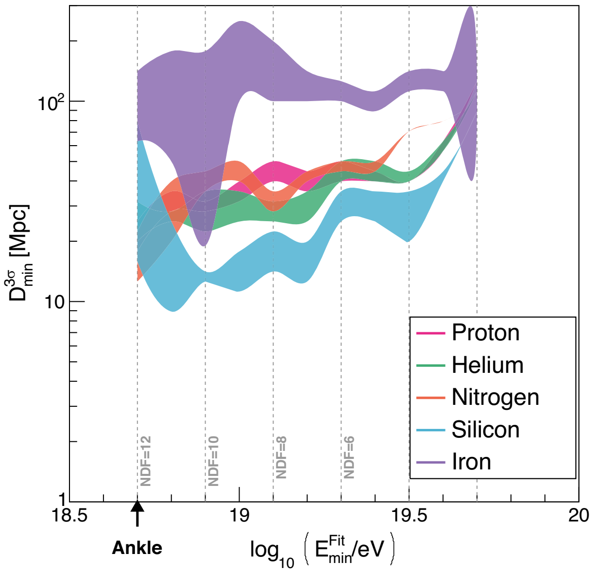

FIG. 5. Upper limits of the distance to the nearest source at 3σ (99.7%) for increasing value of $E_{\rm min}^{\rm fit}$. The pink, green, orange, cyan, and purple lines represent, respectively, the scenarios with pure proton, helium, nitrogen, silicon, and iron primaries. The number of degrees of freedom (NDF) for each $E_{\rm min}^{\rm fit}$ is shown by the dashed gray lines. The area represents the uncertainty coming for the EBL model. The Kneiske model [22] as well as the upper and lower limits on the distribution coming from the Stecker model [23] were considered.

The source evolution is modeled as $(1+z)^k$ and the systematics coming from it are insignificant. Even for a strong source evolution with redshift such as those following star formation rates, in which the number of sources grow with $(1+z)^{3.6}$ for small values of redshift [24,25], the results are exactly the same. This is expected, since the studied effects come from close sources ($z \lesssim 0.02$), for which the density of sources would change only by a factor of $1.02^{3.6} \approx 1.07$.

Figure 5 shows how the value of $D_{\rm min}^{3\sigma}$ changes for different values of $E_{\rm min}^{\rm fit}$ and EBL models for each primary. While the resulting fit parameters depend heavily on the assumptions of the fit [11], the inferred value for $D_{\rm min}^{3\sigma}$ proves to be stable in relation to these parameters, and consequently even a simple fit such as the one proposed here can be used to obtain important insights on the local sources of UHECR. Considerations of more realistic mixed composition would lead to similar conclusions with restrained distances to the nearest source lying somewhere in between the results obtained in this analysis.

III. MAGNETIC FIELDS

We further study the constraints on the distance to the nearest source by investigating the effects of the presence of turbulent extragalactic magnetic fields.

Being charged particles, UHECR are deflected by both galactic and extragalactic magnetic fields. Although this can impact the distribution of arrival directions, it is expected that the total flux from a homogeneous distribution of sources will not be changed by these deflections, as it has previously been deduced from the application of Liouville's theorem [26].

Nevertheless, the relative contribution to the total cosmic ray spectrum from sources in each distance shell is strongly dependent on the extragalactic magnetic field strength. The distance to the nearest source can thus have an impact on both the total arriving spectrum and composition at different energies, for scenarios in which strong extragalactic magnetic fields exist.

In order to further investigate this, we first present a semianalytical method for obtaining the UHECR spectrum and the corresponding contribution of each distance shell in such environments. Subsequently, we discuss the resulting effects and finally study the robustness of the maximum distance to the nearest sources in the presence of extragalactic magnetic fields (EGMF).

A. Semianalytical propagation method

The propagation of ultrahigh energy nuclei is stochastic in nature and, thus, can be studied with Monte Carlo methods. Environments without magnetic fields can be efficiently simulated by adopting simplifying techniques such as performing the simulation in 1D and reweighting the events using the sources energy and distance distributions. Nevertheless, when a general extragalactic magnetic field is considered, a so-called 4D simulation is needed, taking into account the spatial scales and also the time (or redshift) at which the cosmic ray was emitted. This increases the computational cost, due to the extra dimensions considered as well as to the fact that most of the simulated cosmic rays do not arrive at Earth.

If the considered fields are turbulent and isotropic, however, the propagation remains radially symmetric around each source and, thus, a mapping of the 1D Monte Carlo simulation into a 4D result is possible.

In order to do so, it is necessary to obtain the distance distribution of cosmic rays from each source as a function of time, $dN/dr(t, \lambda_{\mathrm{scatt}})$, where $\lambda_{\mathrm{scatt}}(R, B, \lambda_{\mathrm{coh}})$ is the scattering length.

In this work, we use a simple prescription for the scattering length, which is motivated by present limitations in our knowledge of the actual field structures,

$$\lambda_{\mathrm{scatt}} = \begin{cases} \left(\frac{R_L}{\lambda_{\mathrm{coh}}}\right)^{1/3} \lambda_{\mathrm{coh}} & \text{for } R_L < \lambda_{\mathrm{coh}} \\ \left(\frac{R_L}{\lambda_{\mathrm{coh}}}\right)^{2} \lambda_{\mathrm{coh}}, & \text{for } R_L \geq \lambda_{\mathrm{coh}} \end{cases}, \tag{1}$$

where λ_{coh} is the coherence length of the field and R_L is the Larmor radius of the particle given by

$$R_L = \frac{p}{|q|B} \approx \frac{1.081}{Z} \left(\frac{E}{\mathrm{EeV}}\right) \left(\frac{\mathrm{nG}}{B}\right) \mathrm{Mpc}. \tag{2}$$

Three regimes are considered depending on the rigidity, travel time, and magnetic field properties: for short times, the cosmic ray propagates ballistically and a simple delta function is enough to describe the distribution; for large times, the propagation is diffusive and a truncated Gaussian is used, and for the intermediate regime, a Jüttner distribution is needed.

The 1D Monte Carlo simulations are then mapped into a 4D result by an analytic expression for the fraction P of cosmic rays emitted at time t (or equivalently distance $D = ct$ in the 1D simulation) that were emitted at sources in a distance window $(D_{\mathrm{min}}, D_{\mathrm{max}})$, which is given by

$$P = \int_{D_{\mathrm{min}}}^{D_{\mathrm{max}}} \frac{dN}{dr}(t, \lambda_{\mathrm{scatt}}) dr. \tag{3}$$

The distribution dN/dr is explained in details in Appendix A, and an example distribution of this function is shown in Fig. 9. Additionally, the simulation setup, the mapping, and the validation of the method are described in Appendix B. The method obtains results consistent to those obtained by a full 4D simulation, with more than 4 orders of magnitude less computational time and a better control of the simulation parameters.

For the mapping of propagation time to distance, we assume that the scattering length of the cosmic rays remains approximately constant during their propagation. This is reasonable, since the main energy loss mechanism for nuclei is photodisintegration, in which the rigidity may change by a factor of $26/56 \approx 0.5$ in the worst case. For protons at the lowest energies considered, the main energy loss mechanism is the $e^{-}e^{+}$ pair production which has a large loss length and has previously been demonstrated to be safely neglected [19].

B. Spectral effects of extragalactic magnetic fields

In this section, we decipher the various spectral features expected to arise in an environment with magnetic fields, following the procedure described in Sec. III A.

We consider an extragalactic magnetic field with Kolmogorov turbulence power spectrum (see Appendix B for more details). Such a field construction can be fully characterized by its rms field strength, B, and coherence length, λ_{coh}. We illustrate the effects with a representative scenario using $\Gamma = 2$, $R_{\mathrm{max}} = 10^{21}$ V, and $B = 3$ nG. This is an example scenario that qualitatively highlights the effects; more realistic scenarios are considered further on the analysis.

The effects of magnetic fields on the contribution of each distance shell can be seen in the upper panels of Figs. 6 and 7 for proton and iron, respectively. As visible in the individual plots, up to four regimes are present in each shell

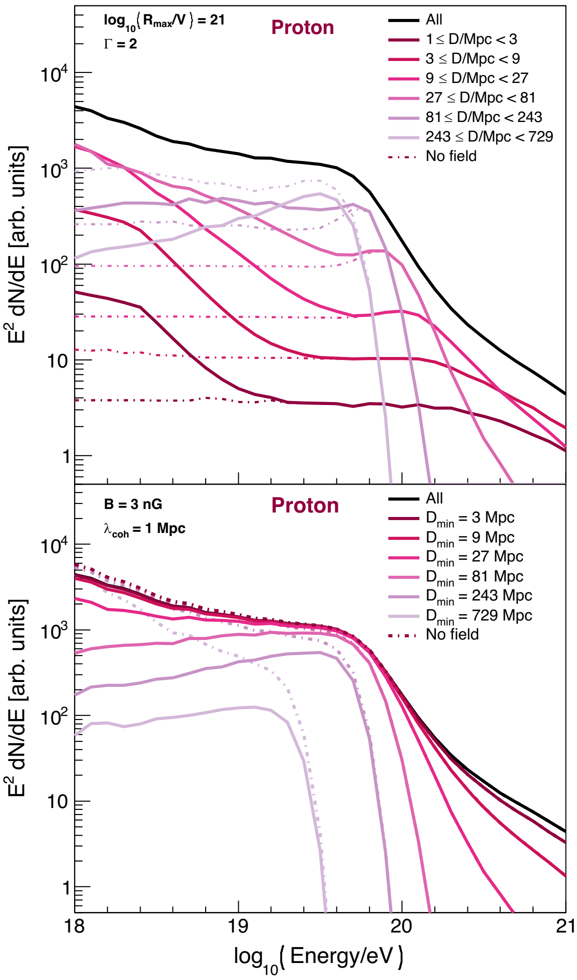

FIG. 6. Spectrum of cosmic rays in an environment with turbulent magnetic fields divided into distance shells for a pure composition of proton at the sources. The parameters of the fields are taken as $B = 3$ nG and $\lambda_{\mathrm{coh}} = 1$ Mpc. On the top panel, each colored line shows the contribution from each distance shell, while the black line shows the total spectrum. On the bottom panel, each colored line represents a scenario with a different distance to the nearest source, D_{min}. The dashed lines show the case with no magnetic fields for comparison.

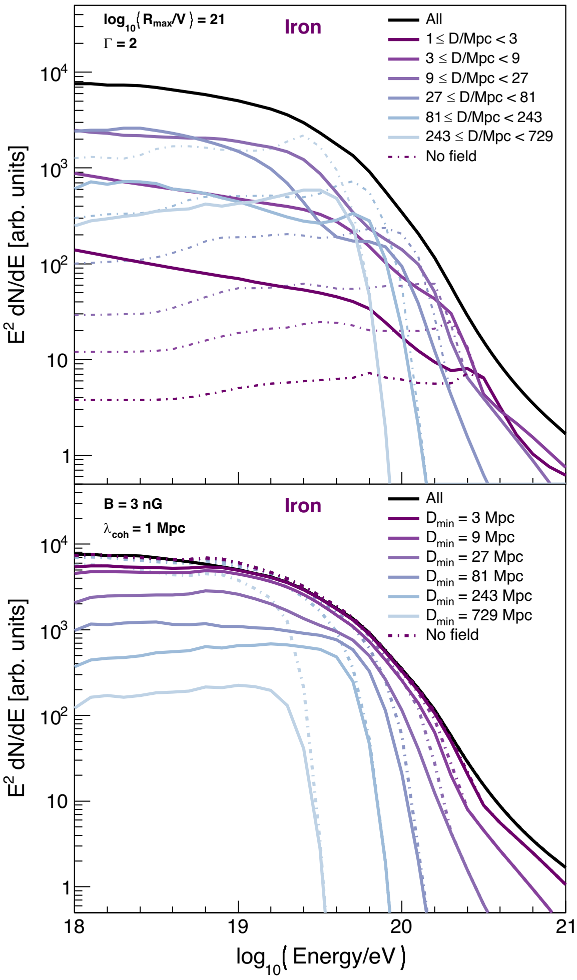

FIG. 7. Same as Fig. 6, but for iron.

and are convoluted with the spectral features coming from energy loss processes. From higher to lower energies, they can be defined as follows:

(1) Ballistic: At the highest energies, the rigidity is sufficiently high, and the propagation distances sufficiently short, such that magnetic field effects do not arise.

(2) Nonresonant scattering enhancement: For lower energies, the cosmic ray number density from a shell increases due to the accumulation of particles scattering over time and their ability to return to a region. In this region, the enhancement scales as E^{-2}.

(3) Resonant scattering enhancement: Due to the energy dependence of the scattering lengths, which is encapsulated in Eq. (1), in this region the enhancement scales as $E^{-1/3}$.

(4) Magnetic horizon: A low-energy magnetic horizon emerges due to the finite age of the Universe.

The farther the shell, the higher the energy up to which these effects are manifest.

In the lower panels of Figs. 6 and 7, the total spectrum for a given distance to the nearest source is shown. The combination of the four effects aforementioned in each shell results in a notable low-energy horizon and a hardening of the spectrum above the ankle and close to GZK energies. For some combinations of field intensity and distance to the nearest source, a significant change in the arriving composition is expected. Such a change may potentially account for the large fraction of protons observed below the ankle [27], though the investigation of such a possibility lies beyond the scope of this study.

C. Distance constraints with magnetic fields

In order to verify the robustness of the results presented in Sec. II, we repeat the fit and constrain the distance to the nearest source under different extragalactic magnetic field assumptions using the method described in Sec. III A. We considered magnetic fields below the upper limits of 3 nG set by observations [28–31]. Additionally, magnetic fields weaker than 0.1 nG have almost no effect within the energy range considered here. Changing λ_{coh} also impacts the final spectrum. The magnitude of the effect scales with $B\sqrt{\lambda_{\mathrm{coh}}}$.

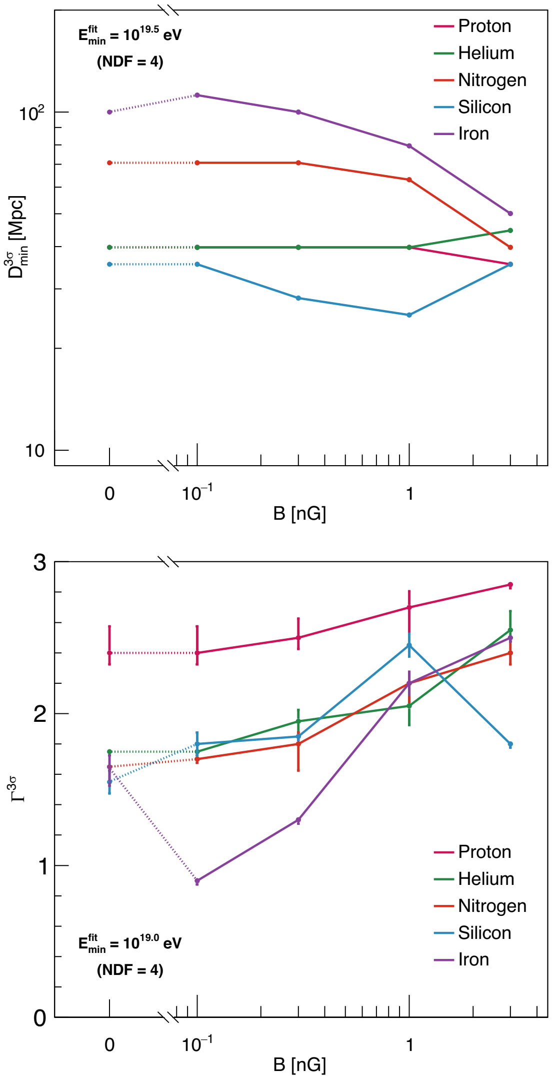

FIG. 8. The top panel shows the evolution of the restrained distance to nearest source, $D_{\mathrm{min}}^{3\sigma}$ with relation to the field strength, B, while the bottom one shows the evolution of the fitted spectral index, Γ, with relation to B. The pink, green, orange, cyan and purple lines represent, respectively, the scenarios with pure proton, helium, nitrogen, silicon, and iron composition at the sources.

Figure 8 shows the evolution of the maximum value of the distance to the nearest source at 3σ confidence level, $D_{\mathrm{min}}^{3\sigma}$, and of the spectral index, Γ, with relation to the field strength, B. In scenarios for extragalactic magnetic fields within the range allowed by observation that we consider, our results for the least constrained primaries, i.e., nitrogen and iron are strengthened and the results obtained for proton, helium, and silicon are confirmed.

Important insight can also be drawn from the evolution of the spectral index, Γ with relation to the field strength, B. For reasonable magnetic field strengths, a softening of the fitted spectral index is found. This is expected in order to compensate for the hardening of the spectrum coming from the magnetic effects described in Sec. III B.

From this analysis, as appreciated from Fig. 8, we conclude that the existence of sources at $D <$ 25–100 Mpc ($z \lesssim 0.02$) are imperative to explain the high-energy end of the spectrum measured by the Pierre Auger Observatory. This corroborates the previous results regarding the need of local sources [20].

IV. CONCLUSIONS

In this work, we have revisited and updated previous studies on the need of local UHECR sources. We have furthered these results by considering the combined effects to the arriving spectrum of magnetic fields and the distance to the nearest UHECR source.

We updated the result of Ref. [20] using new data from the Pierre Auger Observatory and adopting the publicly available Monte Carlo propagation code CRPropa 3. A simple fit to the spectral data of the Pierre Auger Observatory for scenarios considering a pure composition at the sources was performed. The fit becomes inconsistent with the data for large distances to the nearest source, D_{min}. The resulting upper limits at the 3σ confidence level, $D_{\mathrm{min}}^{3\sigma}$, as well as the corresponding fit parameters are shown in Table I. While the fit for proton, helium, nitrogen, and silicon favor the scenario of GZK suppression over the scenario of maximum acceleration power of the sources, i.e., large maximum rigidity and soft spectral instead of low maximum rigidity and hard spectral index, the simulations for iron are well described by both scenarios, but slightly favor the latter.

The stability of the analysis was also addressed for the first time. The fit result was shown to be stable with respect to the initial energy bin of the analysis, the primary composition, and the models adopted for the EBL and source evolution. This contrasts with the spectral parameters, which tend to depend strongly on such hypotheses.

For the first time, we studied the combined effects of a distance to the closest source and the presence of turbulent extragalactic magnetic fields. A semianalytical method for the propagation of UHECR in these turbulent fields was presented. A mapping of a 1D simulation into a 4D simulation using the distance distribution of cosmic rays emitted by a source is used. This method is considerably faster and computationally easier than a full 4D Monte Carlo simulation.

Although turbulent magnetic fields do not change the total flux from a homogeneous distribution of sources, we show how the contribution of each distance shell is affected. Specifically, we highlight four regimes for such alteration effects: ballistic, nonresonant scattering enhancement, resonant scattering enhancement, and a low-energy magnetic horizon. Consequently, introducing a reasonable value of D_{min} results in a low-energy suppression and a hardening in the measured spectrum. We discussed the dependence of the horizon on the primary species and the field properties, a change in the composition measurements for lower energies is also expected.

Finally, we have reanalyzed the data accounting for the effects of magnetic fields. For reasonable values of the field strength, our constraints on the distance to the nearest source are confirmed, or even strengthened depending on the primary. Therefore, we reaffirm the previous results that sources at $D < 25$–100 Mpc are imperative to describe the experimental data from the Pierre Auger Observatory. This is consistent with several astrophysical models that predict that the main bulk of the cosmic ray spectrum can be explained by nearby sources [32–35].

In summary, the interplay between magnetic fields and the distance to the nearest source imprints significant features in the spectrum of UHECR. Complimentary to the arrival directions, which contain information about the angular distribution of UHECR sources, the composition and most importantly the spectral data allow to study their radial distribution.

ACKNOWLEDGMENTS

R. G. L. and V. d. S. acknowledge FAPESP support No. 2015/15897-1, No. 2016/24943-0, and No. 2019/01653-4. M. A. acknowledges support by VILLUM FONDEN under Project No. 18994. R. G. L. and V. d. S. acknowledge the National Laboratory for Scientific Computing (LNCC/MCTI, Brazil) for providing HPC resources of the SDumont supercomputer, which have contributed to the research results reported within this paper (http://sdumont.lncc.br). R. G. L. thanks DESY Zeuthen for all the help and infrastructure provided while visiting the institution.

APPENDIX A: DISTANCE DISTRIBUTIONS

If we consider isotropic random EGMF, the spatial distribution of cosmic rays emitted by a source is only a function of distance, r, the diffusive scattering length, λ_{scatt} (which depends on the cosmic ray rigidity), and propagation time, t. In the following, we discuss the probability distribution to observe a cosmic ray test particle at a radial distance r from its source after the propagation time t.

Three different regimes are considered. For early times, ($\alpha = 3ct/\lambda_{\mathrm{scatt}} < 0.1$), the effects of magnetic fields are still negligible and the propagation is approximately ballistic. A delta distribution is used to describe this regime,

$$\left(\frac{dN}{dr}\right)_{\mathrm{ballistic}} = \delta(r - ct). \tag{A1}$$

On the other hand, for long travel times, $\alpha > 10$ cosmic ray propagation is well described as a diffusive process. To avoid superluminal propagation, $r > ct$, we use the following truncated Gaussian distribution:

$$\left(\frac{dN}{dr}\right)_{\mathrm{diff}} = \begin{cases} Ar^2 e^{-\frac{r^2}{2\sigma^2}} & \text{for } r \leq ct \\ 0 & \text{for } r > ct \end{cases}, \tag{A2}$$

where $\sigma = \sqrt{\lambda_{\mathrm{scatt}} ct/3}$ and A is the normalization constant given by

$$\frac{1}{A} = \sigma^2 \left(\sqrt{\frac{\pi}{2}} \sigma \operatorname{erf}\left(\frac{ct}{2\sigma}\right) - cte^{-\frac{(ct)^2}{2\sigma^2}} \right). \tag{A3}$$

This distribution describes very well the diffusive regime and is relatively well behaved and easy to treat both numerically and analytically. However, its limit in the ballistic regime ($\sigma \to \infty$) is given by

$$\lim_{\sigma \to \infty} \left(\frac{dN}{dr}\right)_{\mathrm{diff}} = \begin{cases} \frac{3r^2}{(ct)^3} & \text{for } r \leq ct \\ 0 & \text{for } r > ct \end{cases}, \tag{A4}$$

which is not a delta distribution as expected (even though it still peaks at $r = ct$). Therefore, the truncated Gaussian distribution does not describe very well the transition between the ballistic and the diffusive regime. Consequently, for the transition regime, i.e., $0.1 < \alpha < 10$, a more complex function is needed and the Jüttner distribution [36,37] is used,

$$\left(\frac{dN}{dr}\right)_{\text{Jüttner}} = \begin{cases} \frac{r^2 \alpha e^{-\alpha/\sqrt{1-(\frac{r}{ct})^2}}}{(ct)^3 K_1(\alpha)(1-(\frac{r}{ct})^2)^2} & \text{for } r \leq ct \\ 0 & \text{for } r > ct \end{cases}, \tag{A5}$$

where $\alpha = 3ct/\lambda_{\mathrm{scatt}}$. The limits of this distribution for small and large α agree with the ballistic and diffusive regimes, respectively. Nevertheless, the Jüttner distribution is much more complex to handle both numerically and analytically.

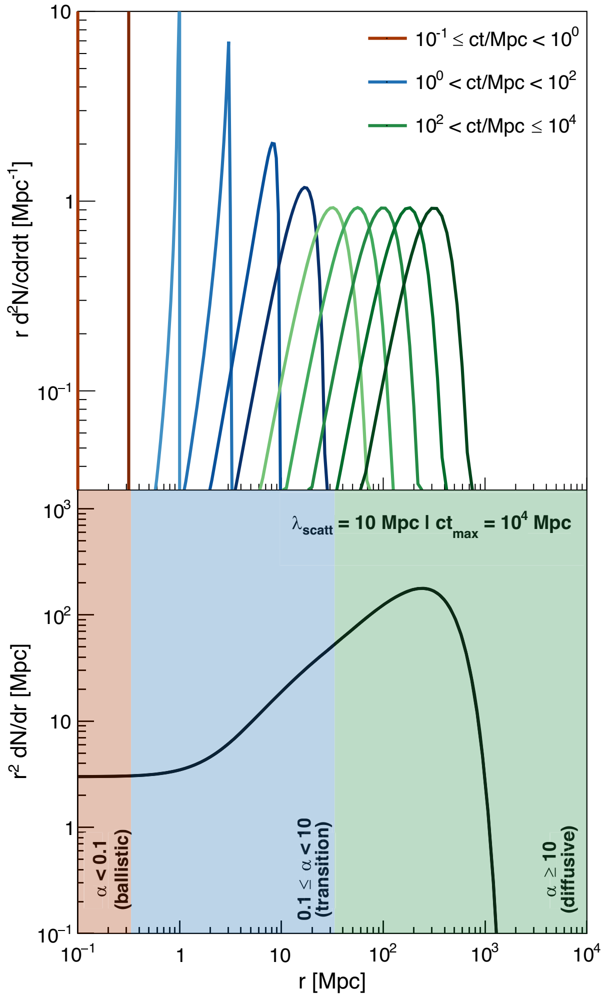

FIG. 9. Distance distribution of cosmic rays emitted by a single source in an environment with turbulent magnetic fields. The top panel shows the time evolution, and each line represents the distribution after a given time with log steps. The bottom panel shows the time integrated distribution. In both panels, red, blue, and green represent, respectively, the ballistic ($\alpha < 0.1$), transition ($0.1 \le \alpha < 10$) and diffusive ($\alpha > 10$) regimes. A scattering length $\lambda_{\rm scatt} = 10$ Mpc was chosen and the age of the Universe was taken as $ct_{\rm max} = 10^4$ Mpc.

Figure 9 shows the time evolution of the cosmic ray spatial distribution as well as its integral over time (lower panel). Each of the regimes, in which a different distribution is considered, is highlighted by a different color. For short distances, the flux behaves as $1/r^2$, for merely geometric reasons. Farther on, on the diffusive regime, the flux behaves as $1/r$, which is due to the accumulation of events over time. Finally, there is a suppression of the flux due to the finite age of the Universe (in this example plot taken as $ct_{\rm max} = 10^4$ Mpc).

APPENDIX B: SIMULATION AND VALIDATION

The simulations were performed with the most widely used package for Monte Carlo simulations of UHECR in the literature, CRPropa 3 [21].[1] The setup consists of a 1D simulation with no magnetic fields for sources with emitting energy $E_s = [1, 10^4]$ EeV and age $ct_s = [1, 3162.2]$ Mpc each with 20 bins per decade in $\log_{10}$.[2] ^{1}H, ^{4}He, ^{14}N, ^{28}Si, and ^{56}Fe were used as primaries. Pion production, e^-e^+ pair production, photodisintegration, and adiabatic losses are considered.

For each combination of initial parameters (E_s, t_s, and primary charge Z_s), a number of detected cosmic rays as a function of the energy, $S(E,(E_s,t_s,Z_s))$, was obtained in the simulations. The final flux for each primary and a shell of sources with $D = (D_{\rm min}, D_{\rm max})$ is then given with an arbitrary normalization by

$$\frac{dN}{dE}(D,E,Z_s) = \sum_{E_s,t_s} S(E,(E_s,t_s,Z_s))\,W_{\rm spec}(E_s,Z_s) \times W_{\rm redshift}(t_s)\,W_{\rm mag}(E_s,t_s,D)\,W_{\rm sim}(E_s,t_s), \qquad \text{(B1)}$$

where $W_{\rm spec}$, $W_{\rm redshift}$, $W_{\rm mag}$, and $W_{\rm sim}$ are, respectively, the weights accounting for spectral features, redshift distribution, magnetic fields, and the simulation binning. We use the following ansatz for the (relative) weights:

$$W_{\rm spec}(E_s,Z_s) \propto E_s^{-\Gamma} e^{E_s/(Z_s R_{\rm max})}, \qquad \text{(B2)}$$

$$W_{\rm redshift}(t_s) \propto (1+z(t_s))^m, \qquad \text{(B3)}$$

$$W_{\rm sim}(E_s,t_s) \propto E_s t_s, \qquad \text{(B4)}$$

where the spectral index, Γ, and the maximum rigidity at the sources, $R_{\rm max}$ are the spectral parameters. The parameter m accounts for the evolution of the source distribution with redshift and the extra term $E_s t_s$ is needed to compensate for the log binning of the simulation.

The effects of the turbulent magnetic fields are introduced by

$$W_{\rm mag} \propto \int_{D_{\rm min}}^{D_{\rm max}} \frac{dN}{dr}(\lambda_{\rm scatt}, t_s)\,dr, \qquad \text{(B5)}$$

where dN/dr is the distribution given in Appendix A and $\lambda_{\rm scatt}$ is given in Eq. (1).

Finally, the overall CR flux is obtained by the sum shells and primaries,

$$\frac{dN}{dE}(E) = \sum_{D,Z_s} f(Z_s)\frac{dN}{dE}(D,E,Z_s), \qquad \text{(B6)}$$

where $f(Z_s)$ is the fraction of the primary at the source.

---

[1] https://crpropa.desy.de.

[2] In a 1D simulation, the age (and consequently travel time) $ct_s = D_s$, where D_s is the distance of the source since all the propagation is ballistic.

We validate our method by a comparison to the results of a full 4D simulation using CRPropa 3 for a simple case scenario. A pure iron composition at the sources and a strong magnetic field ($B = 2.4$ nG, $\lambda_{\mathrm{coh}} = 1$ Mpc) are chosen to enhance the effects of the magnetic fields. No energy losses are taken into account in order to avoid masking the effects from the magnetic fields and speed up the simulations. A scenario with $\Gamma = 2$, $R_{\mathrm{max}} = 10^{21}$ V and $ct_{\mathrm{max}} = 10^4$ Mpc is considered.

Figure 10 shows the contribution from each distance shell to the total flux obtained with each method. The results are consistent with each other. The results from the 4D simulation fluctuate much more due to the low statistics of simulated events for farther sources, even with 10^4 times longer simulations. An easier handling of the magnetic field properties is possible with the semi-analytical approach, since this information is contained on the mapping. For the 4D simulation, on the other hand, it would be necessary to rerun the whole simulation for different field parameters.

Therefore, the proposed method obtains consistent results with a considerably lower computational cost and a better control of the simulation parameters with relation to a full 4D simulation.

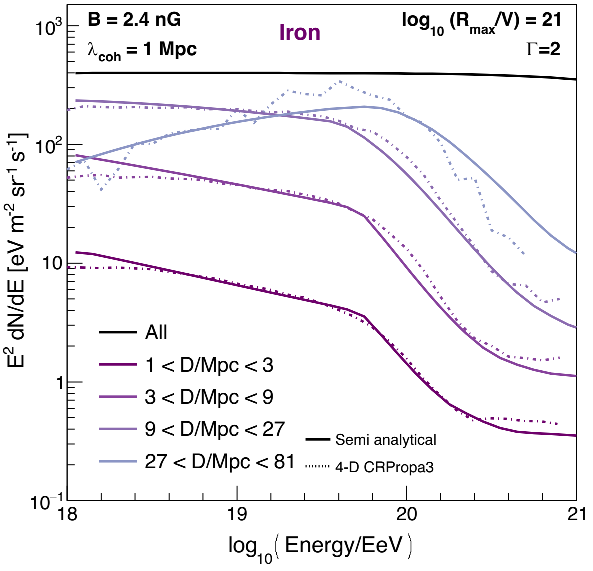

FIG. 10. Comparison of the results of the proposed method and a full 4D simulation. The black line shows the total spectrum, while the different colored lines show the contribution of each distance shell. The continuous and dashed lines represent, respectively, the semianalytical and the full 4D simulation.

---

[1] R. Alves Batista *et al.*, Front. Astron. Space Sci. **6**, 23 (2019).
[2] A. Aab *et al.* (Pierre Auger Collaboration), Nucl. Instrum. Methods Phys. Res., Sect. A **798**, 172 (2015).
[3] A. Aab *et al.* (Pierre Auger Collaboration), Science **357**, 1266 (2017).
[4] M. Ahlers, Astrophys. J. **863**, 146 (2018).
[5] A. Aab *et al.* (Pierre Auger Collaboration), Astrophys. J. **891**, 142 (2020).
[6] A. Aab *et al.* (Pierre Auger Collaboration), Astrophys. J. Lett. **853**, L29 (2018).
[7] M. Ahlers and P. Mertsch, Prog. Part. Nucl. Phys. **94**, 184 (2017).
[8] O. Deligny, Astropart. Phys. **104**, 13 (2019).
[9] J. Abraham *et al.* (Pierre Auger Collaboration), Phys. Lett. B **685**, 239 (2010).
[10] F. Fenu (Pierre Auger Collaboration), Proc. Sci. ICRC2017 (**2018**) 486.
[11] A. Aab *et al.* (Pierre Auger Collaboration), J. Cosmol. Astropart. Phys. 04 (2017) 038; 03 (2018) 02(E)
[12] D. Hooper, S. Sarkar, and A. M. Taylor, Astropart. Phys. **27**, 199 (2007).
[13] D. Allard, Astropart. Phys. **39–40**, 33 (2012).
[14] K. Greisen, Phys. Rev. Lett. **16**, 748 (1966).
[15] G. T. Zatsepin and V. A. Kuzmin, Pis'ma Zh. Eksp. Teor. Fiz. **4**, 114 (1966) [JETP Lett. **4**, 78 (1966)].
[16] M. Lemoine, Phys. Rev. D **71**, 083007 (2005).
[17] R. Aloisio and V. Berezinsky, Astrophys. J. **625**, 249 (2005).
[18] N. Globus, D. Allard, and E. Parizot, Astron. Astrophys. **479**, 97 (2008).
[19] S. Mollerach and E. Roulet, J. Cosmol. Astropart. Phys. 10 (2013) 013.
[20] A. M. Taylor, M. Ahlers, and F. A. Aharonian, Phys. Rev. D **84**, 105007 (2011).
[21] R. Alves Batista *et al.*, J. Cosmol. Astropart. Phys. 05 (2016) 038.
[22] T. M. Kneiske, T. Bretz, K. Mannheim, and D. Hartmann, Astron. Astrophys. **413**, 807 (2004).
[23] F. W. Stecker, S. T. Scully, and M. A. Malkan, Astrophys. J. **827**, 6 (2016); **863**, 112(E) (2018).
[24] A. M. Hopkins and J. F. Beacom, Astrophys. J. **651**, 142 (2006).
[25] H. Yuksel, M. D. Kistler, J. F. Beacom, and A. M. Hopkins, Astrophys. J. Lett. **683**, L5 (2008).
[26] R. Aloisio and V. Berezinsky, Astrophys. J. **612**, 900 (2004).
[27] A. Yushkov, Proc. Sci., ICRC2019 (**2019**) 482.
[28] P. P. Kronberg and M. Simard-Normandin, Nature (London) **263**, 653 (1976).
[29] P. P. Kronberg, Rep. Prog. Phys. **57**, 325 (1994).
[30] P. Blasi, S. Burles, and A. V. Olinto, Astrophys. J. Lett. **514**, L79 (1999).
[31] D. R. Schleicher and F. Miniati, Mon. Not. R. Astron. Soc. **418**, L143 (2011).

[32] T. Wibig and A. W. Wolfendale, Open Astron. J. **2**, 95 (2009).
[33] T. Piran, arXiv:1005.3311.
[34] P. L. Biermann and V. de Souza, Astrophys. J. **746**, 72 (2012).
[35] S. Mollerach and E. Roulet, Phys. Rev. D **99**, 103010 (2019).
[36] F. Jüttner, Ann. Phys. (Berlin) **339**, 856 (1911).
[37] R. Aloisio, V. Berezinsky, and A. Gazizov, Astrophys. J. **693**, 1275 (2009).

11 ULTRAHIGH-ENERGY DIPOLE AND BEYOND

PHYSICAL REVIEW D **103,** 063005 (2021)

Ultrahigh-energy cosmic rays dipole and beyond

Rodrigo Guedes Lang,[1,*] Andrew M. Taylor,[2] and Vitor de Souza[1]
[1]*Instituto de Física de São Carlos, Universidade de São Paulo, Av. Trabalhador São-Carlense, 400, São Carlos, SP, Brazil*
[2]*DESY, D-15738 Zeuthen, Germany*

(Received 3 December 2020; accepted 16 February 2021; published 3 March 2021)

Recent data from the Pierre Auger Observatory has revealed the presence of a large-scale dipole in the arrival direction distribution of ultrahigh-energy cosmic rays (UHECR). In this work, we build up an understanding of the diffusive origin of such a dipolar behavior as well as its dependency on energy and astrophysical source assumptions such as extra-Galactic magnetic field strength and cosmic ray composition. We present a novel analytical approach for calculating the angular distribution of CR coming from a single source and discuss the regimes in which the steady-state dipole result is expected. We also present a semianalytical method for calculating the evolution with energy of the resultant dipole for an ensemble of sources. We show that a local source allows for a strong growth of the dipole with energy over a large energy range. The possibility of a transition from a dipolar to nondipolar regime at the highest energies and its implications for the source density, magnetic field intensity, and cosmic ray composition are discussed.

DOI: 10.1103/PhysRevD.103.063005

I. INTRODUCTION

One of the key unsolved questions in astroparticle physics is the origin of ultrahigh-energy cosmic rays (UHECR, $E > 10^{18}$ eV) [1]. Discovered many decades ago, these nuclei reach Earth almost isotropically. The direction for their sources, however, is hidden by the deflections in the extra-Galactic and Galactic magnetic fields during their propagation. Results from the Pierre Auger Observatory [2] using the most complete UHECR dataset ever collected have revealed the presence of a large-scale dipole in the distribution of arrival directions at energies above 8 EeV. Such a dipole, with a magnitude of 6.5%, was measured with 5.2σ confidence level [3] and points in a direction outwards away from the Galactic center, suggestive of an extra-Galactic origin for cosmic rays at these energies. A more recent analysis from the Pierre Auger collaboration has furthermore revealed that the measured dipole magnitude itself evolves as a function of the energy, suggesting a change in the origin of the dipolar anisotropies from predominantly Galactic to predominantly extra-Galactic in the region between 1 and a few EeV [4].

In a previous work, we have discussed the possibility of using the arriving energy spectrum measured by the Pierre Auger Observatory [5–7] to get insights about the radial distribution of UHECR sources [8]. UHECR interact with the photon background during their propagation, giving rise to an energy-dependent propagation horizon. From this, we estimated the maximum distance to the nearest source which still describes well the data, indicating the need for local sources at 25–100 Mpc.

In this work we further delve into the question about the origin of UHECR by investigating on theoretical grounds the evolution of the dipole magnitude as a function of energy for an ensemble of sources, and evaluating the influence of local sources on this result. Initially, in Sec. II, we develop an analytical approach for calculating the resulting angular distribution of arriving cosmic rays propagating from a single source through an extra-Galactic environment within which turbulent magnetic fields are present. We obtain the amplitude of the dipole and higher poles by expanding this analytical distribution in spherical harmonics. The dependency with the magnetic field strength, the source distance, and the age of activity of the sources are evaluated and discussed. In Sec. III, we use the results for a single source to obtain the evolution of the dipole with the energy expected from an ensemble of sources. In Sec. IV, the results for different source densities, and, consequently, distances to the nearest source, are discussed. The transition from a dipolar to a nondipolar regime is presented for the first time. Finally, in Sec. V, we draw our conclusions.

II. COSMIC RAY ANGULAR DISTRIBUTION FROM A SINGLE SOURCE

Cosmic rays propagating through the extra-Galactic medium are deflected by the extra-Galactic magnetic fields. Such propagation can be considered as each particle having its direction of motion randomized after each scattering length, λ_{scatt}. The scattering length is dependent on the

---

[*] rodrigo.lang@usp.br

2470-0010/2021/103(6)/063005(12)

© 2021 American Physical Society

Larmor radius, R_L, of the particle, and the level of magnetic turbulence at a wavelength matching the Larmor length scale. Appealing to the results of quasilinear theory [9], $\lambda_{\rm scatt} = [B_0^2/\delta B(R_L)^2]R_L$, where $\delta B(\lambda)^2 = d\delta B^2/d\ln\lambda$ denotes the differential energy density in logarithmic wavelength bins. With the energy density in the turbulent modes dominated by the longest wavelengths, the scattering length carries information about the ratio of energies in the coherent magnetic field, to that in the turbulent magnetic field, $B_0^2/\delta B^2$, where $\delta B^2 = \int \delta B(\lambda)^2 d\ln\lambda$ is the summed power of the turbulent modes. Leading to $\delta B(R_L)^2 = (R_L/\lambda_{\rm coh})^{q-1}\delta B^2$, where q is the spectral slope of turbulence (5/3 for Kolmogorov turbulence) and $R_L/\lambda_{\rm coh}$ is the ratio of the particle's Larmor radius to the coherence length of the field. This allows a simple description of the scattering length [10],

$$\lambda_{\rm scatt} = \left(\frac{B_0^2}{\delta B^2}\right)\lambda_{\rm coh}\begin{cases}\left(\frac{R_L}{\lambda_{\rm coh}}\right)^{1/3}, & \text{for } R_L < \lambda_{\rm coh}\\ \left(\frac{R_L}{\lambda_{\rm coh}}\right)^{2}, & \text{for } R_L \geq \lambda_{\rm coh}\end{cases}. \tag{1}$$

No Galactic magnetic field effects are here considered. Throughout we assume $\delta B^2 = B_0^2$.

Consequently, the particles arriving at Earth will not necessarily point back to their original source. Nevertheless, as we discuss next, some residual information about the source position invariably remains encoded in the arrival directions distribution.

The angular distribution of cosmic rays (CR) coming from a single source was previously studied with Monte Carlo simulations in Ref. [11]. As expected from diffusion theory, it was shown that, in the steady-state diffusive regime, achieved for sufficiently long source activity timescales, the normalized angular distribution can be described as $dN/d\cos\theta = 1 + \delta\cos\theta$, where θ is the angle between the source position and the arrival direction (see Fig. 1). In this regime, the dipole amplitude of cosmic rays of a given rigidity emanating from a single source relates to the particle scattering length and the source distance, r_s, as $\delta = \lambda_{\rm scatt}/r_s$.

In this work, we have further developed this calculation and discuss the validity of the steady-state diffusive regime. We propose an analytical approach for obtaining the resultant CR angular distribution following the propagation of CR from their sources to Earth. To achieve this, we utilize earlier insights obtained for describing CR transport in different propagation regimes [8]. We here look into how these different propagation regimes imprint themselves onto the arriving CR angular distribution. Additionally, we test a variety of different source properties, such as the mean source distance and age of source activity.

We start by considering a single source, which emits cosmic rays continuously and isotropically. Each of the particles has a probability of $dl/\lambda_{\rm scatt}$ of having its direction of motion randomized after propagating a small distance dl. Previously, in Ref. [8], we obtained the radial evolution distribution function for cosmic rays emitted in a single pulse, i.e., the radial Green's function from a single source, $d^3N/dr^3|_{\rm G}(r,t)$. Three regimes were noted. For $3ct/\lambda_{\rm scatt} < 0.1$, the propagation is ballistic and a delta distribution can be used. For $3ct/\lambda_{\rm scatt} > 10$, the propagation is diffusive and a truncated Gaussian can be used (truncated in order to prevent super luminal propagation). Finally, for the transition regime, $0.1 \leq 3ct/\lambda_{\rm scatt} \leq 10$, a Jüttner distribution can be used.

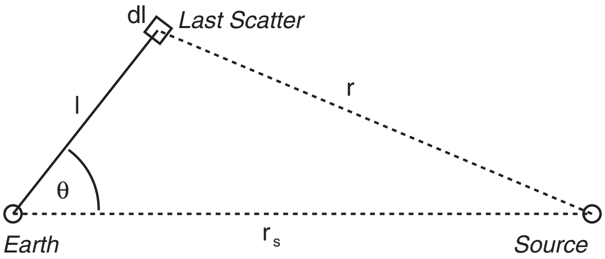

FIG. 1. Diagram depicting the arrival of diffusively propagating particles from a source, focusing on the last scattering the particles make before arriving to Earth.

In order to obtain the angular distribution, we calculate the number of particles arriving to Earth at an angle θ relative to the source direction, in a time interval, dt, and in a small area, dA, i.e., $d^2N/dAdt(\theta)$. The diagram in Fig. 1 illustrates the geometry of the problem. As appreciated from this figure, for a particle to arrive to Earth with a given arrival direction, θ, it must have last scattered somewhere in the line of sight along a path at that angle, and then subsequently have survived all the way to Earth without additional scattering. The number of particles that fulfill these criteria is given by

$$\left.\frac{d^2N}{dAdt}\right|_{\rm diff}(\theta,t) = \int_0^\infty \frac{dl e^{-l/\lambda_{\rm scatt}} n(r(l), t+l)}{\lambda_{\rm scatt}/c}, \tag{2}$$

where $cdt/\lambda_{\rm scatt}$ is the fraction of particles that scattered in the time interval dt, $e^{-l/\lambda_{\rm scatt}}$ is the probability that these particles survived all the way to Earth without interacting again, and $n(r, t+l)$ is the particle density at this location, given by

$$n(r,t) = \int_t^{t_{\rm max}} \frac{dt'}{\tau}\left.\frac{d^3N}{dr^3}\right|_{\rm G}(r,t'), \tag{3}$$

where $d^3N/dr^3|_{\rm G}(r,t)$ are the distributions obtained in Ref. [8], τ^{-1} is the source emissivity taken as constant, $t_{\rm max}$ is the age of activity of the sources, and r is the distance to the source, which relates to the distance to Earth, l, as

$$r^2 = l^2 + r_s^2 - 2lr_s\cos\theta. \tag{4}$$

It is also necessary to take into the account the particles which arrived on Earth having propagated ballistically, i.e., without ever scattering, which are given by

$$\left.\frac{d^2N}{dAdt}\right|_{\mathrm{bal}}(\theta,t) = \delta(\theta)\frac{e^{-r_s/\lambda_{\mathrm{scatt}}}}{\tau 4\pi r_s^2}, \tag{5}$$

where dt/τ is the number of particles emitted in a time interval dt. The delta function assures that such particles can only arrive from the direction of the source, and $e^{-r_s/\lambda_{\mathrm{scatt}}}$ gives the fraction of particles in this regime. Finally, the total number of particles arriving with a direction given by the angle θ, in a time interval dt, and in a small area dA is given by

$$\frac{d^2N}{dAdt}(\theta,t) = \left.\frac{d^2N}{dAdt}\right|_{\mathrm{diff}}(\theta,t) + \left.\frac{d^2N}{dAdt}\right|_{\mathrm{bal}}(\theta,t). \tag{6}$$

At this stage, the angular distribution, $dN/d\cos\theta$, can be obtained by integrating $d^2N/dAdt$ over the exposure of the experiment. However, as the time scale of a human-made experiment is negligible compared to cosmological time scales, the factoring in of the exposure is effectively just a global normalization factor.

Solving this expression numerically, Fig. 2 shows the resulting angular distribution for different values of $\lambda_{\mathrm{scatt}}/r_s$. For large values, the distribution is dominated by the delta distribution coming from the ballistic propagation. For small values, on the other hand, the distribution is mostly uniform, with a small preference for the direction of the source, and can be well described by $1 + \delta\cos\theta$.

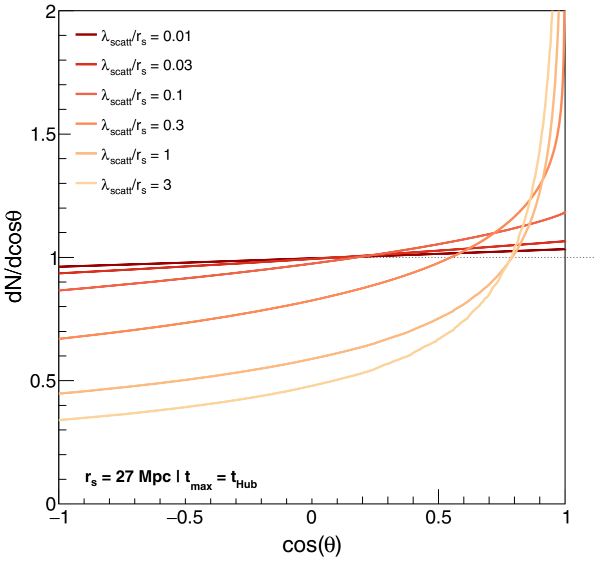

FIG. 2. Normalized angular distribution. Each shade of orange represents a value of $\lambda_{\mathrm{scatt}}/r_s$.

A. Steady-state diffusive regime

For the steady-state diffusive regime ($\lambda_{\mathrm{scatt}}/r_s > r_s/ct_{\mathrm{max}}$), the ballistic term vanishes and the density can be written as $n(r) \propto 1/(\lambda_{\mathrm{scatt}}r)$. The angular distribution is thus given by

$$\frac{dN}{d\cos\theta} \propto \int_0^\infty \frac{dle^{-l/\lambda_{\mathrm{scatt}}}}{r(l)} \approx \frac{\lambda_{\mathrm{scatt}}}{r(\lambda_{\mathrm{scatt}})}$$
$$\approx \frac{\lambda_{\mathrm{scatt}}}{r_s(1-\frac{\lambda_{\mathrm{scatt}}}{r_s}\cos\theta)} \approx \frac{\lambda_{\mathrm{scatt}}}{r_s}\left(1+\frac{\lambda_{\mathrm{scatt}}}{r_s}\cos\theta\right). \tag{7}$$

Therefore, the results obtained in previous works and expected from the diffusive theory for the steady-state regime are verified.

B. Expansion in spherical harmonics

A more quantitative way of studying such distributions is to expand them in spherical harmonics and to look at the behavior of the coefficients. The angular distribution, $dN/d\cos\theta$, can be written in orthogonal functions,

$$\frac{dN}{d\cos\theta} = N\left[1 + \sum_{n=1}^{\infty}\sum_{m=-\ell}^{m=\ell}\Phi_{\ell,m}Y_\ell^m(\phi,\theta)\right]. \tag{8}$$

For the case of a single source in turbulent magnetic fields, no dependency on ϕ is expected if θ is the angle between the source and the arrival direction as shown in Fig. 1 and, consequently, only $m = 0$ is needed. We define the spherical harmonics similarly to what is done in Ref. [11],

$$Y_\ell(\theta) = Y_\ell^0(\theta) = \frac{2\ell+1}{\sqrt{2}}P_\ell(\cos\theta), \tag{9}$$

with $P_\ell(\cos\theta)$ being the Legendre polynomials. With that, the amplitude of the poles, Φ_ℓ, are calculated by

$$\Phi_\ell = \int_{-1}^{1} d\cos\theta\frac{dN}{Nd\cos\theta}\frac{2\ell+1}{\sqrt{2}}P_\ell(\cos\theta), \tag{10}$$

in particular, the amplitude of the dipole is defined as $\delta = \Phi_1$. We can obtain the information about the power in each multiple by performing an angular power spectrum analysis, similarly to Refs. [12–14],

$$C_\ell = \frac{\Phi_\ell^2/(2\ell+1)}{\sum_n \Phi_n^2/(2n+1)}, \tag{11}$$

which leads to

$$0 < C_\ell < 1, \quad \text{for all } \ell$$
$$\sum_{\ell=0}^{\infty} C_\ell = 1. \tag{12}$$

We also define the nondipolarity of the distribution, f_{nondip}, as the power in the multipoles higher than the dipole,

$$f_{\mathrm{nondip}} = 1 - C_0 - C_1, \tag{13}$$

which is negligible for dipolar distributions, i.e., distributions that are well described by $1 + \delta \cos\theta$.

C. Evolution of the coefficients of the spherical harmonics

With these definitions, we can calculate the evolution of the amplitude of the poles, Φ_ℓ, and the power spectrum coefficients, C_ℓ, with $\lambda_{\mathrm{scatt}}/r_s$ for different source distance, r_s, and source activity duration, t_{max}, cases.

The top panel of Fig. 3 shows the values of δ obtained for different source distances. The dashed lines in the figure show the linear relation expected for transport in the steady-state diffusive regime, i.e., $\delta = \lambda_{\mathrm{scatt}}/r_s$ and in the ballistic regime, i.e., $\delta = 3$. For values of $\lambda_{\mathrm{scatt}}/r_s$ between $\sim r_s/ct_{\mathrm{max}}$ and ~ 0.1, agreement with the linear relation result is obtained. In this regime, $\sqrt{3C_1} \sim \Phi_1 = \delta$. However, outside this range a strong departure from this relation is seen.

For sufficiently low values of $\lambda_{\mathrm{scatt}}/r_s$ ($\lambda_{\mathrm{scatt}}/r_s < r_s/ct_{\mathrm{max}}$), the dependency of δ becomes softer than the steady-state result, since the system has insufficient time to reach this state, and the resulting dipole is larger than the steady-state result case. For a given t_{max}, the farther the source, the sooner (in $\lambda_{\mathrm{scatt}}/r_s$) that this departure kicks in. This is due to the finite age of the Universe, which prevents the density of cosmic rays emitted from the source reaching the steady-state value.

For sufficiently high values of $\lambda_{\mathrm{scatt}}/r_s$ ($\lambda_{\mathrm{scatt}}/r_s > 0.3$), on the other hand, the ballistic regime contribution becomes significant. This is measured by the angular power spectrum shown in the bottom panel of Fig. 3. When the power in the higher order poles ($\ell > 1$) becomes non-negligible, the dipole amplitude departures from the linear relation. In this regime, most of the particles do not diffuse at all and, therefore, point directly back to the source. This results in a nondipolar behavior, which is verified by the increasing of the f_{nondip} term.[1] C_0 and C_1 tend to constant small values which follow $C_0 = C_1/3$, as expected from the definition in Eq. (10). This is due to a finite angular resolution.

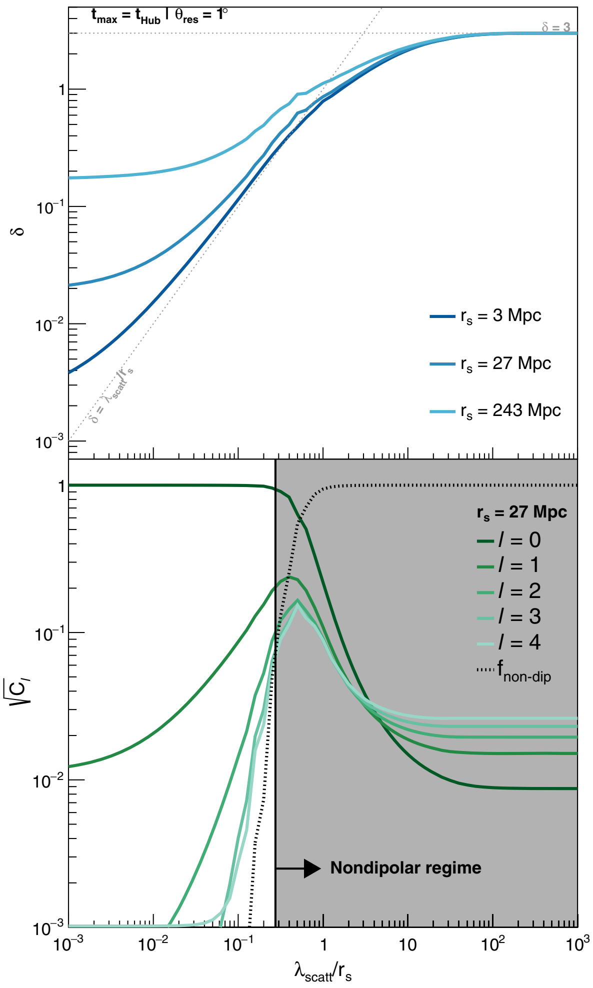

FIG. 3. Evolution of the spherical harmonics expansion terms with $\lambda_{\mathrm{scatt}}/r_s$. The top panel shows the amplitude of the dipole for different distances to source. The bottom panel shows the angular power spectrum for $r_s = 27$ Mpc. The gray dashed lines on the top panel show the results expected for the steady-state diffusive and ballistic regimes, while the black dashed line on the bottom panel shows the term f_{nondip}. The shaded area shows the nondipolar regime, in which $f_{\mathrm{nondip}} > 1\%$. t_{Hub} is the Hubble time.

The effects of the angular resolution, θ_{res}, and time of activity of the sources, are detailed in Appendix A.

III. DIPOLE OF AN ENSEMBLE OF SOURCES

In the previous section, we built an understanding of the angular distribution resulting from a single source of cosmic rays. In this section, we evaluate the evolution with energy of the dipole for an ensemble of sources. This was previously studied in Refs. [15–18]. We consider a discrete distribution of sources described by the distance to the nearest source, D_{min}, in such a way that the number of sources in a shell with distance iD_{min} is i^2.

---

[1] Throughout we do not consider small angles deflections, which would alter the transition from diffusive to ballistic and, thus, the growth of higher order multipoles.

A. Coefficients of the spherical harmonics for an ensemble of sources

As proposed in Sec. II, given the source distance, the magnetic field and the particle energy and charge, it is possible to analytically obtain the arriving angular distribution of cosmic rays for that source, $dN_i/d\cos\theta$, and consequently its harmonic coefficients, $\Phi_\ell^{(s)}$, where (s) denotes the source. In this section, we discuss the approach for obtaining a total arriving angular distribution, $dN_{\mathrm{tot}}/d\cos\theta$.

Given two angular distributions, with two preferred angles, $dN_1/d\cos\theta_1$ and $dN_2/d\cos\theta_2$, one can obtain $dN_{\mathrm{sum}}/d\cos\theta_{\mathrm{sum}} = dN_1/d\cos\theta_1 + dN_2/d\cos\theta_2$, with $b_\ell^{(\mathrm{sum})}(\theta_{\mathrm{sum}}) = 0$, for every ℓ. Its harmonic coefficients will be given by

$$\Phi_0^{(\mathrm{sum})} = \Phi_0^{(1)} + \Phi_0^{(2)}$$

$$\Phi_\ell^{(\mathrm{sum})} = \sqrt{(\Phi_\ell^{(1)})^2 + (\Phi_\ell^{(2)})^2 + 2\Phi_\ell^{(1)}\Phi_\ell^{(2)}\cos(\alpha)}, \qquad (14)$$

where α is the angle between θ_1 and θ_2. If we consider sources randomly distributed, then $\langle\cos(n\alpha)\rangle = 0$. Therefore, the coefficients of the angular distribution from an ensemble of sources will be given by

$$\Phi_0^{(\mathrm{tot})}(E) = \sum_s n_s(E, r_s)$$

$$\Phi_{\ell>0}^{(\mathrm{tot})}(E) = \sqrt{\sum_s [\Phi_\ell(E, r_s) n_s(E, r_s)]^2}, \qquad (15)$$

where n_s denotes the arriving cosmic ray density, and the sum over s denotes the sum over all sources. The angular power spectrum, which contains the information about the dipolarity of the distribution, can then be obtained by

$$C_\ell^{(\mathrm{tot})}(E) = \frac{(\Phi_\ell^{(\mathrm{tot})}(E))^2/(2\ell+1)}{\sum_{n=0}^{\infty}(\Phi_n^{(\mathrm{tot})}(E))^2/(2n+1)}. \qquad (16)$$

B. The nearest source dipole and dilution from further sources

During propagation, cosmic rays may interact with the photon background via pair production, pion production, and photodisintegration, which leads to an energy-dependent propagation horizon [19–23]. Limitations on the propagation distance, which depend on the particle energy, are also expected due to the presence of extra-Galactic magnetic fields [8,24,25]. We use the semianalytical method proposed in Ref. [8] to calculate the contribution from each source to the spectrum, $n_i(E, r_i)$.

An understanding for the resultant dipole from an ensemble of sources is obtained from the consideration of Eq. (15). Specifically, it should be noted that the dipole term sums incoherently, whilst the isotropic term sums coherently. As further developed in Appendix B, to a first approximation the total dipole can be understood as the dipole from the closest source diluted by the ratio of the contribution of farther sources, i.e., $\delta \approx \delta_1 n_1/n_{\mathrm{tot}}$.

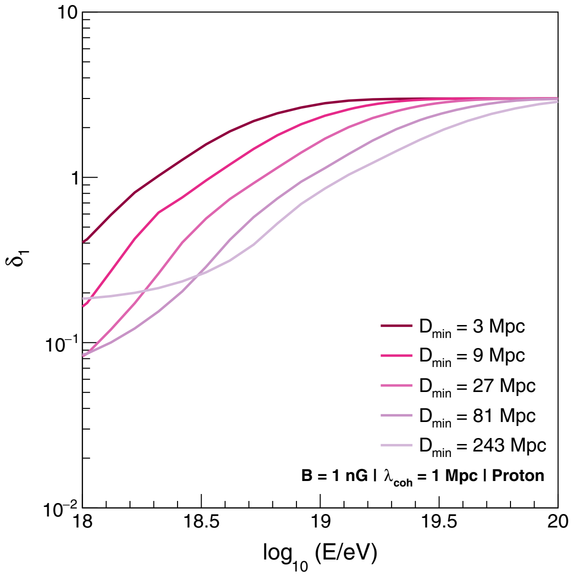

FIG. 4. Dipole from the closest source as a function of the energy. Each colored line represents a different distance to the nearest source. A proton primary is considered, but similar results are found for the other primaries.

Figures 4 and 5 show, respectively, the dipole for the closest source (δ_1) and the dilution factor (n_1/n_{tot}), i.e., the ratio between the cosmic ray density coming from the closest source and total cosmic ray density. Figure 4 can be appreciated as a reexpression of the relation shown in Fig. 3 in terms of energy.

Figure 5 shows the dilution factor level due to the contribution from more distant sources. For both lower and higher energies, this dilution factor is smaller. The growth of the dilution factor at lower energies is brought about by the magnetic horizon effect, which suppresses the cosmic ray contribution from more distant sources [8]. At higher energies, the role of the energy loss horizon sets in, which suppresses the cosmic rays from farther sources.

IV. EVOLUTION OF THE DIPOLE WITH ENERGY

With a clear understanding of the origin of an UHECR dipole, how the ensemble dipole evolves as a function of energy can be addressed. To obtain the dipole strength at each energy, the contribution of each source to both the spectrum and coefficients of the spherical harmonics must be obtained.

Following Eq. (15) and the semianalytical method to obtain the arriving cosmic ray rate considering energy losses and magnetic fields effects, we have calculated the

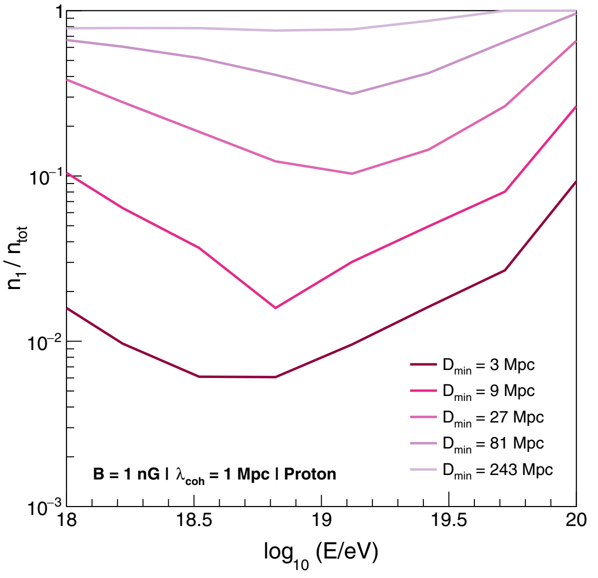

FIG. 5. Dilution factor of the dipole from the nearest source due to the contribution of the more distant sources. Each colored line represents a different distance to the nearest source. A proton primary is considered, but similar results are found for the other primaries.

evolution of the harmonic coefficients with energy for different ensembles. A spectral index of $\Gamma = 2$, a maximum rigidity of $R_{\max} = 10^{19}$ V and pure composition at the sources were considered. Several distances to the nearest source, $D_{\min}$, primary species, and magnetic field intensities, B, within the range set by observations [26–29] were treated.

The top panel of Fig. 6 shows the resulting dipole, δ, for an example case with $r_s = 27$ Mpc, $B = 1$ nG and nitrogen composition together the data measured the Pierre Auger Observatory [3]. The bottom panel shows the evolution of the power spectrum with energy. Two main regimes are found. For lower energies, the total angular distribution is dipolar, i.e., most of the power of the function is in the first two poles ($\ell = 0$ and $\ell = 1$). For this regime, the normalized distribution is well described by $1 + \delta \cos\theta$. For higher energies, the nondipolarity of the distribution increases and the power is divided in higher order multipoles. The transition between the regimes is quantified by f_{nondip} and we define the source to be in the dipolar regime when $f_{\text{nondip}} < 1\%$.

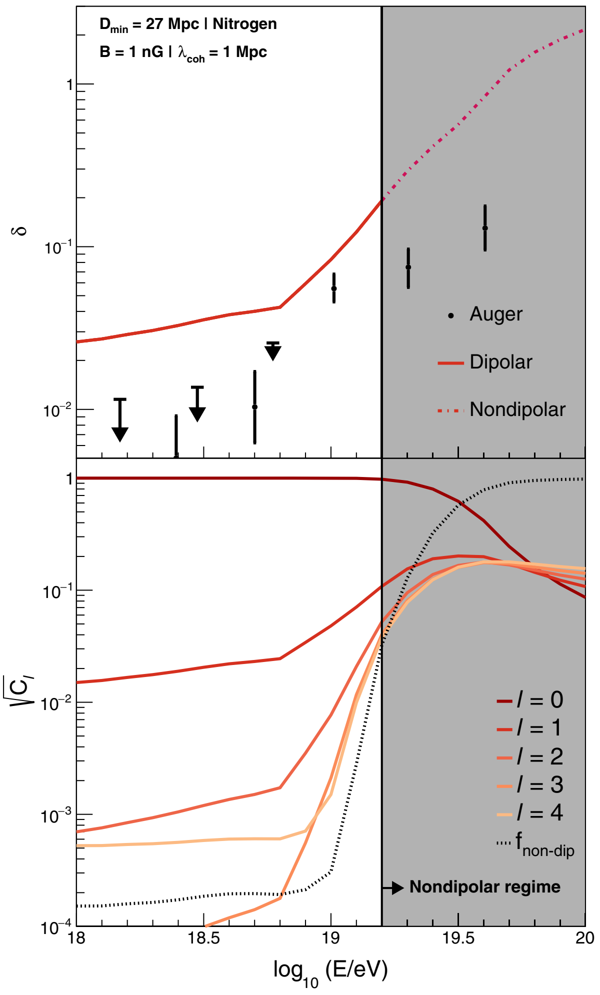

FIG. 6. Evolution of the total angular distribution with energy. The top panel shows the amplitude of the dipole calculated from the model and measured by the Pierre Auger Observatory [3]. The bottom panel shows the angular power spectrum. The shaded area represents the energy range on the nondipolar regime.

The analysis done by the Pierre Auger Collaboration shows that the measured distribution of arrival directions can be well described by just a dipolar expansion and the data is consistent with the assumption that no multipoles of higher order are present. Henceforth, the angular power spectrum in not being explicitly shown and the amplitude of δ for the astrophysical models will be represented by continuous and dashed lines. The change from continuous to dashed lines is to illustrate the energy at which the nondipolar behavior becomes important for each astrophysical model, i.e., $f_{\text{nondip}} > 1\%$. Continuous lines show the values of δ for energies at which $f_{\text{nondip}} < 1\%$ for each astrophysical model. Dashed lines, on the other hand, show the values of δ for energies at which $f_{\text{nondip}} > 1\%$.

A statistical comparison between the models and the data is beyond the scope of this work. However, it is important to note that a comparison of the models to the data would only be valid in the energy range delimited by the solid lines. In this energy range, both the data and the models can be well described by a pure dipolar expansion ($f_{\text{nondip}} < 1\%$) and, therefore, the comparison is consistent. A comparison of the value of δ obtained by the models to the data in the energy range shown by the dashed lines is

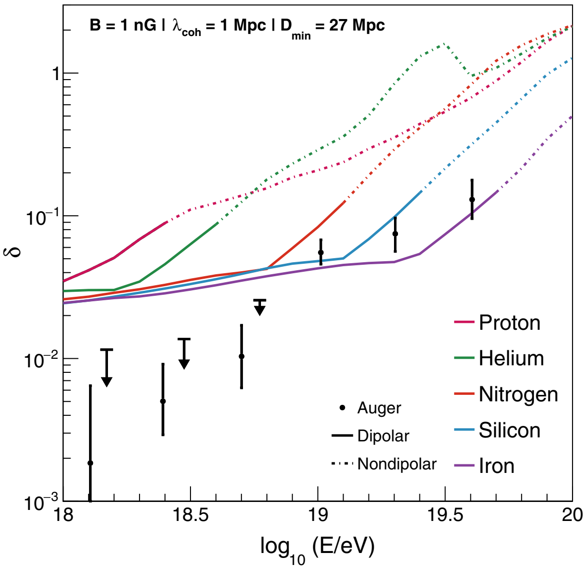

FIG. 7. Evolution of the amplitude of the dipole with energy. The data points show the amplitude of the large-scale dipole measured by the Pierre Auger Observatory [4]. The continuous lines show the region in which the angular distribution is dipolar, i.e., $f_{\text{nondip}} < 1\%$, while the dashed lines show the region in which the nondipolarity is significant.

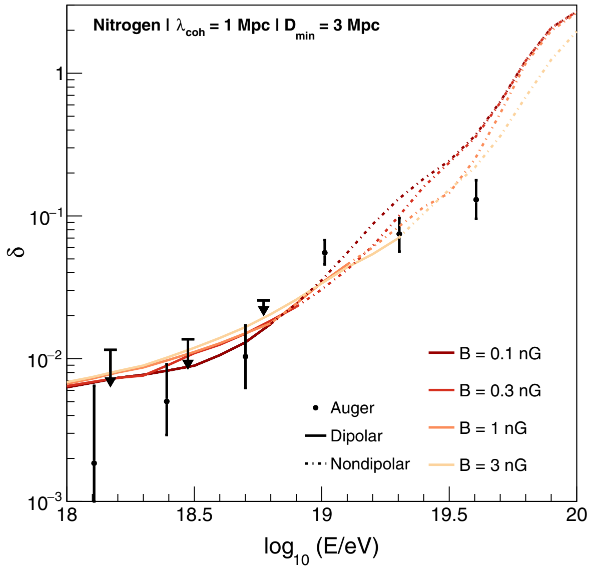

FIG. 8. Same as Fig. 7, but for a fixed distance to the nearest source and primary and different magnetic field intensities.

not valid because in this range the data can be described by a pure dipolar expansion as shown in the analysis of the Pierre Auger Collaboration while the models cannot.

Figure 7 shows the results for different species, for the case of a fixed distance to the nearest source and scattering length. For the cases considered, up to four regimes can be seen, which directly relate to the regimes on the contribution to the spectrum of sources from a distance shell (see Ref. [8] for a detailed explanation of these regimes). These regimes can be divided into the nondipolar (**A**, $f_{\text{nondip}} > 1\%$) and three subregimes within the dipolar (**B**, $f_{\text{nondip}} < 1\%$). From higher to lower energies:

(i) *AI: Nondipolar regime:* At the highest energies, the angular distribution is dominated by the closest sources, since the energy loss horizon prevents farther sources contributing to the arriving cosmic rays. These sources are in the ballistic regime and, therefore, the total angular distribution is nondipolar, i.e., $f_{\text{nondip}} > 1\%$;

(ii) *BI: Nonresonant scattering enhancement:* The dipole is dictated by the first source and diluted by the farther ones. In this regime λ_{scatt} grows as E^2, which is reflected in the dipole;

(iii) *BII: Resonant scattering enhancement:* Same as the previous one, but λ_{scatt}, and consequently the dipole grow as $E^{1/3}$;

(iv) *BIII: Low energy magnetic horizon:* In this regime the behavior of the dipole is dictated by the finite age of the Universe, which leads to the magnetic horizon.

Figure 8 shows the dependence of the dipole strength (assuming a fixed distance to the nearest source, CR species, and magnetic field coherence length) for a range of extra-Galactic magnetic field strength values. For most cases, the dipole strength is seen to not depend on the extra-Galactic magnetic field strength, B. In this case, CR transport from sources reaches the steady-state diffusive regime value, in which the dipole grows linearly with λ_{scatt}, whilst the contribution to the total CR density from the closest source grows with $1/\lambda_{\text{scatt}}$, resulting in less dilution. These two effects subsequently compensate each other. For larger distances, however, this is not true anymore since the effects of a finite source activity time, $t_{\max}$, become relevant. Also, as expected, the energy at which the nondipolar regime becomes dominant heavily depends on the magnetic field strength, B.

Finally, Fig. 9 shows the dipole dependence (assuming a fixed extra-Galactic magnetic field strength and coherence length) for different cosmic ray primary species and distances to the nearest source. The dependence on $D_{\min}$ follows from the fact that the dipole of the first source depends on $1/D_{\min}$, whilst the dilution factor, which depends inversely on the number of contributing sources, grows with $D^2_{\min}$. Consequently, lower values of $D_{\min}$ imply lower values for the dipole (i.e., the dilution effect wins), at least in the energy region below the nondipolar regime (i.e., for energies in which $f_{\text{nondip}} < 1\%$).

Although it is not our aim here to make strong comparisons to the results from the Pierre Auger Observatory, a few general comments are worth noting. While for the

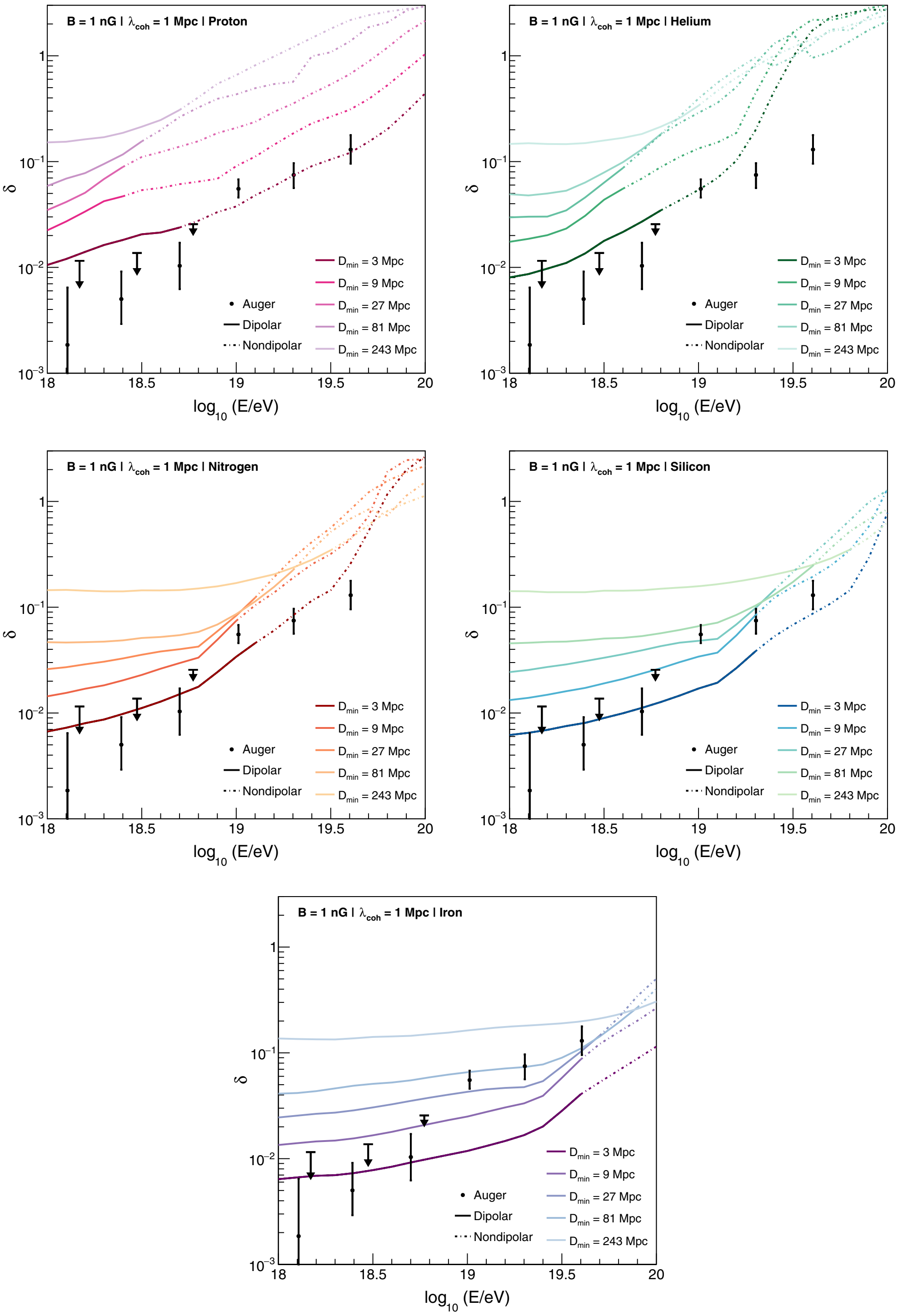

FIG. 9. Same as Fig. 7, but for a fixed magnetic field intensity and primary. Each line represents a distance to the nearest source and each panel represents a primary.

intermediate energies ($10^{18.9}$ eV $< E < 10^{19.4}$ eV), the evolution of the dipole is consistent with an intermediate composition, the distribution at the most energetic data point ($E \sim 10^{19.6}$ eV) needs to be driven by either heavier nuclei at the sources, such as Silicon and Iron, or strong extra-Galactic magnetic fields ($B > 1$ nG). Furthermore, a strong evolution of the dipole strength with energy was only found for cases in which the dipole contribution from the nearest source was in the steady-state diffusion regime. Lastly, in most of the cases, the distribution becomes nondipolar ($f_{\rm nondip} > 1\%$) at the highest energies, which might be consistent to the sky maps presented by the Pierre Auger Observatory in their anisotropy studies [30,31].

It is noteworthy that the calculations presented here consider the mean dipole strength obtained for an ensemble of randomly distributed sources. However, due to Poissonian fluctuations in the position of randomly distributed sources, a large variance of the order of the mean is expected, as estimated in Appendix B. A more rigorous comparison with the data would, thus, be extremely dependent on the considerations about the position of the sources.

V. CONCLUSIONS

In this work, we have further developed a picture for the development of a large-scale dipole in the CR arrival direction distribution due to their diffusion in extra-Galactic magnetic fields. We have proposed a simple general approach for calculating the angular distribution, and subsequently the dipole and angular power spectrum of arriving cosmic rays emanating from an ensemble of sources.

The dependency of the dipole and angular power spectrum on the particle scattering length, source distance, and activity age the sources, for a range of transport regimes, were found to have a simple origin. For intermediate values of $\lambda_{\rm scatt}/r_s$ ($r_s/t_{\rm max} \lesssim \lambda_{\rm scatt}/r_s \lesssim 1$), the steady-state diffusive regime result in which the dipole behaves as $\delta \approx \lambda_{\rm scatt}/r_s$, was verified. For lower values of $\lambda_{\rm scatt}/r_s$, the onset of a magnetic horizon which increases the dipole was shown. For large values of $\lambda_{\rm scatt}/r_s$, the transition to the ballistic regime was shown to be dominant, and a quantification of the nondipolarity of the distribution was proposed in the form of the term $f_{\rm nondip}$.

The combination of the general approach for the angular distribution of a single source proposed in this work with the semianalytical method for the propagation of UHECR proposed in our previous work [8] provides the necessary tools for studying the evolution with energy of the dipole from an ensemble of sources. Using this tool, a novel approach taking into account different contributions from each source due to energy losses and extra-Galactic magnetic fields effects as well as different primaries becomes possible.

We have covered and discussed the different regimes for the dipole strength evolution with energy, for different combinations of extra-Galactic magnetic field strength value, distance to the nearest source, age of activity of the sources, and primary cosmic ray species. Investigating the effect of changing the distance of the nearest source, the dipole was shown to be dictated by the closest sources, while diluted by the farther ones. From that, the distance to nearest source, $D_{\rm min}$, was found to control the amplitude of the dipole for the energies where the arriving distribution is dipolar. Smaller values of $D_{\rm min}$ gave rise to a larger number of contributing sources, acting overall to dilute the dipole and, consequently, reduce the overall dipole amplitude. Also, a steep energy evolution of the dipole is only found when steady-state diffusion regime is achieved. As shown in Fig. 9, this happens only if small values of $D_{\rm min}$ are considered. This general result further supports the previous findings that a local UHECR source must exist [8,24,32].

The transition from a dipolar to a nondipolar distribution and its importance to modeling the anisotropy data measured by the Pierre Auger Observatory were also discussed via an angular power spectrum analysis. We have shown that, for some realistic scenarios, the distribution is already expected to be significantly nondipolar at the highest energies. For these cases, a simple comparison of the amplitude of the calculated dipole to the dipole measured by the Pierre Auger Observatory is not consistent. A combination of more realistic models and further data on the higher poles of the distribution measured by the Pierre Auger Observatory as well as their evolution with energy (similarly to what has been done in Ref. [14]) can prove to be an essential key to decipher this question. A statistical comparison of the model developed here with data is outside of the scope of this work. The results presented here contribute to building up the understanding of the arrival direction of UHECR and to providing important insights for testing realistic models.

In summary, we have improved our understanding on the dipolar behavior in the distribution of arrival directions of UHECR and provided a relevant set of tools for pursuing the answer for the century-long question about their origin.

ACKNOWLEDGMENTS

R. G. L. and V. d. S. acknowledge FAPESP support No. 2015/15897-1, No. 2016/24943-0, and No. 2019/01653-4. R. G. L. and V. d. S. acknowledge the National Laboratory for Scientific Computing (LNCC/MCTI, Brazil) for providing HPC resources of the SDumont supercomputer, which have contributed to the research results reported within this paper [33]. R. G. L. thanks DESY Zeuthen for all the help and infrastructure provided while visiting the institution. V. d. S. thanks CNPq.

APPENDIX A: DEPENDENCY ON AGE OF ACTIVITY OF THE SOURCE AND ANGULAR RESOLUTION

As discussed in Sec. II, the evolution of the amplitude of the dipole with $\lambda_{\rm scatt}/r_s$ departs from the steady-state diffusive regimes for both low and high values of $\lambda_{\rm scatt}/r_s$.

The horizon at lower values of $\lambda_{\rm scatt}/r_s$ is related to the finite age of activity of the sources. Particles that went past Earth and must subsequently diffuse back might, in order to arrive, have a longer path than the age of the Universe, in contrast with head-on particles, which have a shorter path, increasing, thus, the dipole. This regime is significant for $\lambda_{\rm scatt}/r_s < r_s/ct_{\rm max}$.

In the ballistic regime, on the other hand, the dipolarity of the distribution is suppressed for large values of $\lambda_{\rm scatt}/r_s$ as shown by the angular power spectrum. From Eq. (5), it was expected that, in this regime, the angular distribution would be described by a delta function at $\theta = 0$. For such distribution, the amplitudes of a_0 and a_1 would tend to zero, while an infinite number of poles would be needed to describe it. A delta distribution, however, is nonphysical since the source has a given size and the experiments have a given angular resolution. Figure 10 shows the angular power spectrum when different angular resolutions, $\theta_{\rm res}$, are tested. C_ℓ tend to a finite value which is smaller the better the angular resolution and which follows $C_0 = C_1/3$, as

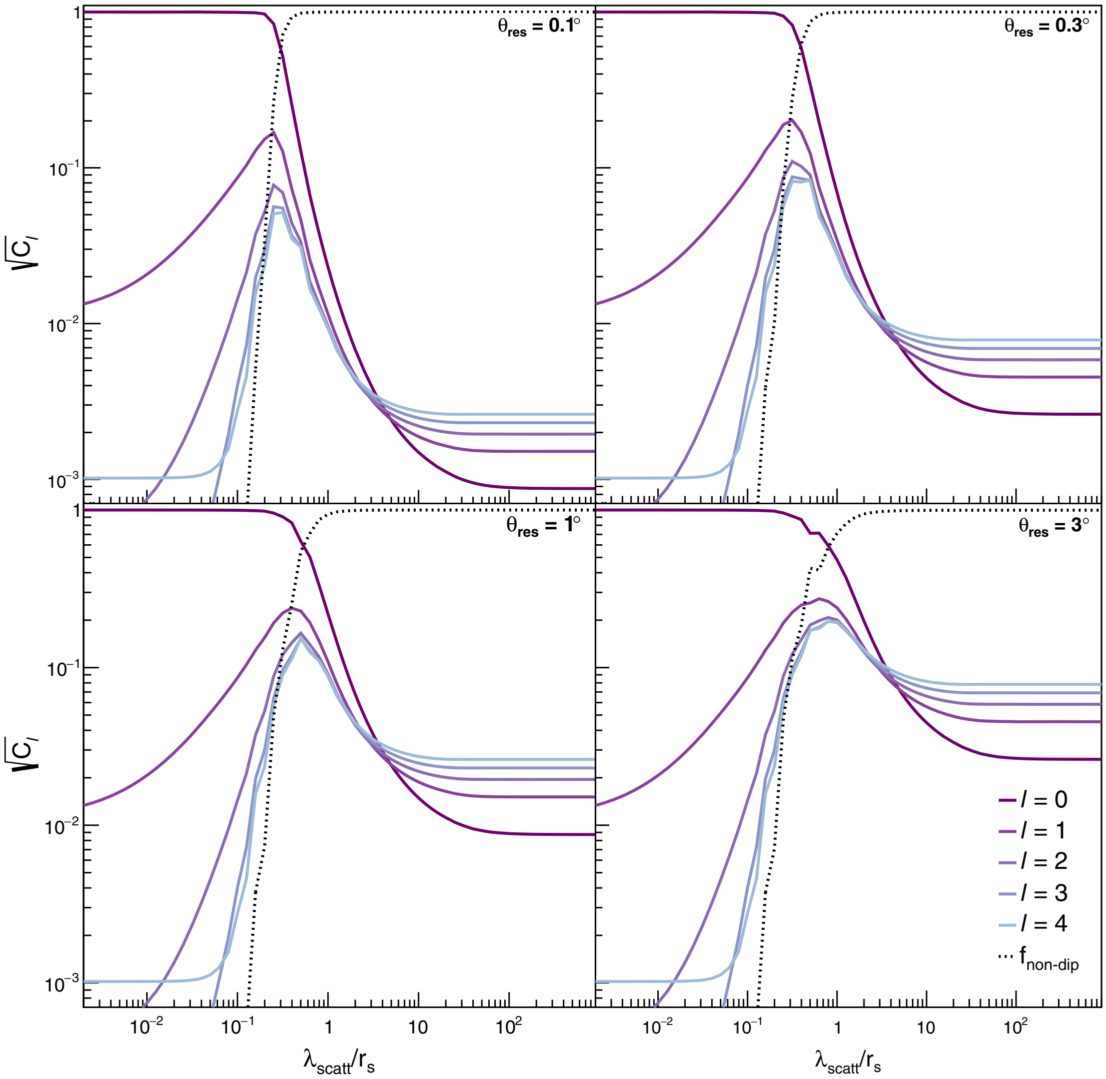

FIG. 10. Evolution of the angular power spectrum with λ/r_s. The panels are for $\theta_{\rm res} = \{0.1°, 0.3°, 1°, 3°\}$. Each continuous line represents a power, ℓ, and the dashed line represents the term $f_{\rm nondip}$.

expected from the definition in Eq. (10). Throughout the paper $\theta_{\mathrm{res}} = 1°$ is used.

APPENDIX B: FIRST APPROXIMATION AND VARIANCE OF THE TOTAL DIPOLE

We consider a set of distance shells, each located at iD_{min}, and containing i^2 number of sources within the shell volume. The contribution of each shell to the final dipole can be estimated as

$$\langle\Phi_1^{(i)}\rangle^2 = \frac{i^2(\Phi_1^{(s_i)} n_{s_i})^2}{n_{\mathrm{tot}}^2}, \tag{B1}$$

where n_{tot} is total cosmic ray density coming from all the sources, and $a_1^{(s_i)}$ and n_{s_i} are, respectively, the dipole term and the cosmic ray density from a single source in shell i. In the steady-state diffusion regime, the cosmic ray density from a single source in shell i behaves as $1/r_i = 1/(iD_{\mathrm{min}})$ and the dipole strength from such a source behaves as $\lambda_{\mathrm{scatt}}/r_i = \lambda_{\mathrm{scatt}}/(iD_{\mathrm{min}})$. The overall contribution of sources in shell i to the dipole can therefore be as a function of the contribution of the first source,

$$\langle\Phi_1^{(i)}\rangle^2 = \frac{i^2\left(\frac{\Phi_1^{(1)} n_1}{i^2}\right)^2}{n_{\mathrm{tot}}^2} = \left(\frac{\Phi_1^{(1)} n_1}{i n_{\mathrm{tot}}}\right)^2. \tag{B2}$$

Consequently, the total dipole can be approximated as

$$\langle\Phi_1^{(\mathrm{tot})}\rangle^2 \approx \sum_i \left(\frac{\Phi_1^{(1)} n_1}{i n_{\mathrm{tot}}}\right)^2 \Rightarrow$$

$$\delta = \langle\Phi_1^{(\mathrm{tot})}\rangle \approx \frac{\Phi_1^{(1)} n_1}{n_{\mathrm{tot}}}. \tag{B3}$$

Throughout the paper, we have considered sources randomly distributed, leading to $\langle\cos(n\alpha)\rangle = 0$ in Eq. (14). Therefore the Φ_1 term here calculated represents the mean dipole. It is important to estimate its variance.

We use Eq. (14) and consider sources in the same shell, i.e., with the same $\Phi_1^{(s)}$ term for the single source angular distribution. For the convenience of the notation, we define the dipole term of the summation of two angular distributions as [see Eq. (14)]

$$A = (2\Phi_1^{(\mathrm{sum})})^2. \tag{B4}$$

The variance will then be given by

$$\begin{aligned}
\langle A\rangle &= 2\Phi_1^2 + 2\Phi_1^2\langle\cos(\phi)\rangle = 2\Phi_1^2\\
\langle A^2\rangle &= (2\Phi_1^2)^2 + 4\Phi_1^4\langle\cos^2(\phi)\rangle + 4\Phi_1^4\langle\cos(\phi)\rangle\\
&= (2\Phi_1^2)^2 + 4\Phi_1^4\\
\sigma(A) &= \sqrt{\langle A^2\rangle - \langle A\rangle^2} = 2\Phi_1^2,
\end{aligned} \tag{B5}$$

from which one can obtain the total variance,

$$\begin{aligned}
\sigma(\Phi_1^{\mathrm{tot}}) = \sigma(\delta) &= \sqrt{\sum_i \left(\frac{\Phi_1^{(i)}}{\sqrt{i}}\right)^2}\\
&\approx \sqrt{\sum_i \left(\frac{\Phi_1^{(1)} n_1}{i^2 n_{\mathrm{tot}}}\right)^2} \approx \delta.
\end{aligned} \tag{B6}$$

Due to the Poissonian behavior, the variance is dictated by the closest shells, which contain fewer sources and, as demonstrated, are of the same order of the mean.

Another source of uncertainties in the model is the relation between the distance to the nearest source, D_{min}, and the average distance between sources, which is taken as the same for the hypothesis here considered. A large fluctuation is expected, though, for the distance to the nearest source, which is known to drive the dipole.

---

[1] R. Alves Batista *et al.*, Front. Astron. Space Sci. **6**, 23 (2019).

[2] A. Aab *et al.* (Pierre Auger Collaboration), Nucl. Instrum. Methods Phys. Res., Sect. A **798**, 172 (2015).

[3] A. Aab *et al.* (Pierre Auger Collaboration), Science **357**, 1266 (2017).

[4] A. Aab *et al.* (Pierre Auger Collaboration), Astrophys. J. **891**, 142 (2020).

[5] J. Abraham *et al.* (Pierre Auger Collaboration), Phys. Lett. B **685**, 239 (2010).

[6] A. Aab *et al.* (Pierre Auger Collaboration), Phys. Rev. Lett. **125**, 121106 (2020).

[7] A. Aab *et al.* (Pierre Auger Collaboration), Phys. Rev. D **102**, 062005 (2020).

[8] R. G. Lang, A. M. Taylor, M. Ahlers, and V. de Souza, Phys. Rev. D **102**, 063012 (2020).

[9] R. Schlickeiser, Astrophys. J. **336**, 243 (1989).

[10] S. O'Sullivan, B. Reville, and A. Taylor, Mon. Not. R. Astron. Soc. **400**, 248 (2009).

[11] D. Harari, S. Mollerach, and E. Roulet, Phys. Rev. D **89**, 123001 (2014).

[12] M. Ahlers and P. Mertsch, Prog. Part. Nucl. Phys. **94**, 184 (2017).

[13] D. Wittkowski and K.-H. Kampert, Astrophys. J. Lett. **854**, L3 (2018).
[14] A. Abeysekara *et al.* (HAWC, IceCube Collaborations), Astrophys. J. **871**, 96 (2019).
[15] D. Harari, S. Mollerach, and E. Roulet, Phys. Rev. D **92**, 063014 (2015).
[16] N. Globus and T. Piran, Astrophys. J. Lett. **850**, L25 (2017).
[17] A. Dundović and G. Sigl, J. Cosmol. Astropart. Phys. 01 (2019) 018.
[18] S. Mollerach and E. Roulet, Phys. Rev. D **101**, 103024 (2020).
[19] D. Hooper, S. Sarkar, and A. M. Taylor, Astropart. Phys. **27**, 199 (2007).
[20] D. Allard, Astropart. Phys. **39–40**, 33 (2012).
[21] M. Lemoine, Phys. Rev. D **71**, 083007 (2005).
[22] R. Aloisio and V. Berezinsky, Astrophys. J. **625**, 249 (2005).
[23] N. Globus, D. Allard, and E. Parizot, Astron. Astrophys. **479**, 97 (2008).
[24] A. M. Taylor, M. Ahlers, and F. A. Aharonian, Phys. Rev. D **84**, 105007 (2011).
[25] S. Mollerach and E. Roulet, J. Cosmol. Astropart. Phys. 10 (2013) 013.
[26] P. P. Kronberg and M. Simard-Normandin, Nature (London) **263**, 653 (1976).
[27] P. P. Kronberg, Rep. Prog. Phys. **57**, 325 (1994).
[28] P. Blasi, S. Burles, and A. V. Olinto, Astrophys. J. Lett. **514**, L79 (1999).
[29] D. R. Schleicher and F. Miniati, Mon. Not. R. Astron. Soc. **418**, L143 (2011).
[30] A. Aab *et al.* (Pierre Auger Collaboration), Astrophys. J. Lett. **853**, L29 (2018).
[31] A. di Matteo *et al.* (Pierre Auger, Telescope Array Collaboration), Proc. Sci., ICRC2019 (**2020**) 439.
[32] P. L. Biermann and V. de Souza, Astrophys. J. **746**, 72 (2012).
[33] http://sdumont.lncc.br.

12 CONCLUSIONS

In this thesis, we have used a phenomenological approach to study two paramount topics in astrophysics which are intrinsically related to the propagation of astroparticles: Lorentz invariance violation and the origin of ultra-high energy cosmic rays.

In Chapter 3, we argued the importance of testing LIV for both astrophysics and fundamental physics as well as the potential of using astroparticles in such. In Chapters 4-7, we presented several tests of LIV which look for LIV signatures in different data sets and instruments.

First, in Chapter 4, we have used the upper limits on the photon flux obtained by the Pierre Auger Observatory to impose limits on the effects of subluminal LIV in the propagation of GZK photons. We have improved previous analyses by using more up-to-date data, considering more realistic astrophysical assumptions, and doing a full simulation of the propagation of GZK photons in order to obtain their flux as a function of energy. GZK photons are emitted during the propagation of UHECR and, consequently, their flux depends significantly on the assumptions about the UHECR sources, such as their composition, spectral parameters and source evolution. Previous works have considered a pure proton composition (108,109) which is ruled out by $X_{\max}$ measurements of the Pierre Auger Observatory. Protons produce more GZK photons (see Chapter 7), which leads to an overestimation of the flux. For the first time, we have estimated the dependency on the astrophysical models of the LIV constraints obtained using this technique. For different source evolution models, a difference of up to 500% was found in the flux. The dependency on the composition and source parameters is even stronger and for some models which describe well the energy spectrum and composition data, the data was shown to be insensitive to LIV. For the reference scenario, C_3R_5, which best describes UHECR data, limits of $\delta_{\gamma,0} > -10^{-20}$, $\delta_{\gamma,1} > -10^{-38}$ eV^{-1} and $\delta_{\gamma,2} > -10^{-56}$ eV^{-2} were imposed. These constraints are more robust and up-to-date than previous limits using a similar technique and orders of magnitude more restrictive than those imposed using TeV gamma-rays due to the difference in the energy of the particles. Nevertheless, a direct comparison is not straightforward due to different systematics and strong model dependency.

In Chapter 6, we have proposed a new robust technique for testing LIV using multiple TeV spectra. Using multiple sources is desirable in order to improve statistics and justified as LIV is expected not to be a feature of the individual source. The proposed technique minimized the systematic biases coming from uncertainties in the EBL distribution, intrinsic spectral form and energy resolution. The effects of the systematics in the results were also evaluated. Using a dataset of 111 energy spectra from 38 sources, we have imposed limits on the LIV energy scale of $E^{(1)}_{\rm LIV}|_{2\sigma} = 12.08 \times 10^{28}$ eV, $E^{(1)}_{\rm LIV}|_{5\sigma} = 5.73 \times 10^{28}$ eV, $E^{(2)}_{\rm LIV}|_{2\sigma} = 2.38 \times 10^{21}$ eV and $E^{(2)}_{\rm LIV}|_{5\sigma} = 1.42 \times 10^{21}$ eV. These are the most constraining limits on subluminal LIV using TeV gamma-ray in the literature. The proposed technique, which contains a procedure for selecting relevant spectra and range of detected energy is suitable to be used in future LIV analyses with upcoming new measurements of TeV spectra and can be an important tool for LIV studies in the CTA era.

In Chapter 6, a contribution to the estimation of the potential of CTA to study LIV was presented. Two scenarios were simulated using ctools. First, we have shown that, if LIV effects of the order of current limits are present, CTA will be able to detect it with more than 50σ confidence level. Later, we have estimated the expected limits imposed by CTA using two TeV sources, Markarian 501 and 1ES 0229+200. The estimated limits are of the same order of current limits, even if just a single source is used. CTA is, thus, expected to be a key experiment in LIV studies in the next years. This work contributed with the evaluation of the systematics coming from the use of different analysis packages to a broader work from the CTA consortium on sensitivity of CTA for testing cosmological and fundamental physics in the propagation of gamma-rays. (113)

In Chapter 7, we tested LIV in the propagation of astroparticles using data from the Pierre Auger Observatory. Two cases were considered. Similarly to what was done in Chapter 4, subluminal LIV effects on the propagation of GZK photons were tested using the upper limits on the flux of EeV photons. Using the scenario obtained by the combined fit of spectrum and composition performed by the Pierre Auger Collaboration (76), the data was shown to be insensitive to LIV. In the second case, LIV in the hadronic sector was tested for the first time considering a more realistic mixed composition. A combined fit of both energy spectrum and composition was done under different LIV assumptions. Different models for the EBL distribution, hadronic interactions, and photohadronic cross-sections were tested. Limits of $\delta_{\rm had,0}|_{5\sigma} < 10^{-19}$ were imposed. The data is best described when some level of LIV is considered ($\delta_{\rm had,0} = 10^{-21}$ or $\delta_{\rm had,0} = 10^{-21}$, depending on the model). The data was, thus, shown to favor a scenario with fewer interactions, which could be caused by some level of LIV, but also by other features not covered by the simplistic astrophysical model considered, e.g., a higher relative contribution of local sources.

Finally, in Chapter 8, we presented a review of several astrophysical tests of LIV as well as a compilation of the currently most restrictive limits. Improvements in LIV studies in the future are expected with the advent of more robust data analyses and experimental data from new experiments such as CTA, the Southern Wide-field Gamma-ray Observatory (SWGO) (133), and AugerPrime.

The second topic covered in this thesis was the century-long question about the origin of ultra-high energy cosmic rays. In Chapter 9, we discussed the possibility of unveiling the distribution of UHECR sources using the energy spectrum, composition and arrival direction distribution.

In Chapter 10, we reaffirmed the need for a local source of UHECR. We have proposed a fast semi-analyitical method for the propagation of UHECR under turbulent magnetic fields, which reduces the computational cost of such simulations in several orders of magnitude. The relative contribution to the spectrum of sources at different distance shells was described in detail, and the onset of a magnetic enhancement and horizon was shown. Constraints on the distance to the nearest UHECR source of a few tens of Mpc were imposed, depending on composition and EGMF assumptions. This shows that the energy spectrum and composition of UHECR can provide important tools for understanding the radial distribution of UHECR sources and should be used complimentary to the arrival directions distribution.

Lastly, in Chapter 11, we have studied the evolution with energy of the dipole in the angular distribution of arrival directions. We have proposed a general analytical calculation for the poles and power spectrum of an angular distribution of UHECR coming from a single source in environments with turbulent EGMF. With the general approach proposed combined with the semi-analytical method for the propagation from Chapter 10, we have proposed a novel method for calculating the strength of the dipole as a function of the energy for an ensemble of sources. The resulting regimes in the dipole evolution as well as their dependency on composition, source density, distance to the nearest source and magnetic field assumptions were discussed. We have also argued for the importance of evaluating the dipolarity of the distribution and showed that for realistic astrophysical assumptions the predicted angular distribution becomes non-dipolar in the energy range measured by the Pierre Auger Observatory.

Although a more rigorous comparison with experimental data is out of the scope of this work, forming a solid understanding of the processes that leads to the behavior of measured data as well as its dependency on several astrophysical assumptions is crucial for building a robust path towards finding the origin of UHECR.

REFERENCES

1 HESS, V. F. The highest-energy cosmic rays. **Physikalische Zeitschrift**, v. 13, p. 1084, 1912.

2 MILLIKAN, R. A.; CAMERON, G. H. The origin of the cosmic rays. **Physical Review**, American Physical Society, v. 32, p. 533–557, Oct. 1928. DOI: 10.1103/PhysRev.32.533.

3 AUGER, P. *et al.* Extensive cosmic-ray showers. **Reviews of Modern Physics**, American Physical Society, v. 11, p. 288–291, July 1939. DOI: 10.1103/RevModPhys.11.288.

4 ANDERSON, C. D. The positive electron. **Physical Review**, American Physical Society, v. 43, p. 491–494, Mar. 1933. DOI: 10.1103/PhysRev.43.491.

5 NEDDERMEYER, S. H.; ANDERSON, C. D. Note on the nature of cosmic-ray particles. **Physical Review**, American Physical Society, v. 51, p. 884–886, May 1937. DOI: 10.1103/PhysRev.51.884.

6 STREET, J. C.; STEVENSON, E. C. New evidence for the existence of a particle of mass intermediate between the proton and electron. **Physical Review**, American Physical Society, v. 52, p. 1003–1004, Nov. 1937. DOI: 10.1103/PhysRev.52.1003.

7 LATTES, C. *et al.* Processes involving charged mesons. **Nature**, v. 159, p. 694–697, 1947. DOI: 10.1038/159694a0.

8 LATTES, C.; OCCHIALINI, G.; POWELL, C. Observations on the tracks of slow mesons in photographic emulsions. 2. **Nature**, v. 160, p. 486–492, 1947. DOI: 10.1038/160486a0.

9 EVOLI, C. **The cosmic-ray energy spectrum**. [S.l.]: Zenodo, 2018. DOI: 10.5281/zenodo.2360277.

10 MENN, W. *et al.* The PAMELA space experiment. **Advances in Space Research**, v. 51, n. 2, p. 209 – 218, 2013. DOI: 10.1016/j.asr.2011.06.030.

11 KOUNINE, A. The Alpha Magnetic Spectrometer on the International Space Station. **International Journal of Modern Physics E**, v. 21, n. 08, p. 1230005, 2012. DOI: 10.1142/S0218301312300056.

12 SEO, E. *et al.* Cosmic-ray energetics and mass (CREAM) balloon project. **Advances in Space Research**, v. 33, n. 10, p. 1777 – 1785, 2004. DOI: 10.1016/j.asr.2003.05.019.

13 ATWOOD, W. B. *et al.* The Large Area Telescope on the Fermi Gamma-Ray Space Telescope Mission. **Astrophysical Journal**, v. 697, n. 2, p. 1071, 2009. DOI: 10.1088/0004-637X/697/2/1071.

14 AARTSEN, M. *et al.* The IceCube Neutrino Observatory: instrumentation and online systems. **Journal of Instrumentation**, v. 12, n. 03, p. P03012, 2017. DOI: 10.1088/1748-0221/12/03/P03012.

15 HINTON, J. The status of the H.E.S.S. project. **New Astronomy Reviews**, v. 48, n. 5–6, p. 331–337, 2004. DOI: 10.1016/j.newar.2003.12.004.

16 HOLDER, J. *et al.* The first VERITAS telescope. **Astroparticle Physics**, v. 25, n. 6, p. 391–401, 2006. DOI: 10.1016/j.astropartphys.2006.04.002.

17 ALEKSIĆ, J. *et al.* The major upgrade of the MAGIC telescopes, part I: the hardware improvements and the commissioning of the system. **Astroparticle Physics**, v. 72, p. 61–75, 2016. DOI: 10.1016/j.astropartphys.2015.04.004.

18 ABEYSEKARA, A. *et al.* Observation of the Crab Nebula with the HAWC Gamma-Ray Observatory. **Astrophysical Journal**, v. 843, n. 1, p. 39, 2017. DOI: 10.3847/1538-4357/aa7555.

19 AAB, A. *et al.* The Pierre Auger Cosmic Ray Observatory. **Nuclear Instruments and Methods A**, v. 798, p. 172–213, 2015. DOI: 10.1016/j.nima.2015.06.058.

20 KAWAI, H. *et al.* Telescope Array experiment. **Nuclear Physics B:** proceedings supplements, v. 175-176, p. 221 – 226, 2008. DOI: 10.1016/j.nuclphysbps.2007.11.002.

21 ACHARYA, B. *et al.* Introducing the CTA concept. **Astroparticle Physics**, v. 43, p. 3 – 18, 2013. DOI: 10.1016/j.astropartphys.2013.01.007.

22 ACHARYA, B. *et al.* **Science with the Cherenkov Telescope Array**. 2018. DOI: 10.1142/10986 Available from: https://arxiv.org/abs/1709.07997. Accessible at: 8 Dec. 2020.

23 ALBERT, A. *et al.* Search for high-energy neutrinos from binary neutron star merger GW170817 with ANTARES, IceCube, and the Pierre Auger Observatory. **Astrophysical Journal Letters**, v. 850, n. 2, p. L35, 2017. DOI: 10.3847/2041-8213/aa9aed.

24 ABBOTT, B. P. *et al.* Multi-messenger observations of a binary neutron star merger. **Astrophysical Journal Letters**, v. 848, n. 2, p. L12, 2017. DOI: 10.3847/2041-8213/aa91c9.

25 ALVES BATISTA, R. *et al.* Open questions in cosmic-ray research at ultrahigh energies. **Frontiers in Astronomy and Space Sciences**, v. 6, p. 23, 2019. DOI: 10.3389/fspas.2019.00023.

26 GELMINI, G.; KALASHEV, O. E.; SEMIKOZ, D. V. GZK photons as ultra high energy cosmic rays. **Journal of Experimental and Theoretical Physics**, v. 106, p. 1061–1082, 2008. DOI: 10.1134/S106377610806006X.

27 ELLIS, J. R.; MAYES, V.; NANOPOULOS, D. V. Uhecr particle spectra from crypton decays. **Physical Review D**, v. 74, n. 11, p. 115003, 2006. DOI: 10.1103/PhysRevD.74.115003.

28 FERMI, E. On the origin of the cosmic radiation. **Physical Review**, v. 75, p. 1169–1174, 1949. DOI: 10.1103/PhysRev.75.1169.

29 AXFORD, W. Acceleration of cosmic rays by shock waves. **Annals of the New York Academy of Sciences**, v. 375, p. 297 – 313, Dec. 2006. DOI: 10.1111/j.1749-6632.1981.tb33702.x.

30 KRYMSKII, G. F. A regular mechanism for the acceleration of charged particles on the front of a shock wave. **Akademiia Nauk SSSR Doklady**, v. 234, p. 1306–1308, 1977. Available from: https://ui.adsabs.harvard.edu/abs/1977DoSSR.234.1306K. Accessible at: 8 Dec. 2020.

31 BELL, A. R. The acceleration of cosmic rays in shock fronts. I. **Monthly Notices of the Royal Astronomical Society**, v. 182, p. 147–156, 1978.

32 BLANDFORD, R.; OSTRIKER, J. Particle acceleration by astrophysical shocks. **Astrophysical Journal Letters**, v. 221, p. L29–L32, 1978. DOI: 10.1086/182658.

33 HILLAS, A. The origin of ultrahigh-energy cosmic rays. **Annual Reviews of Astronomy and Astrophysics**, v. 22, p. 425–444, 1984. DOI: 10.1146/annurev.aa.22.090184.002233.

34 ACKERMANN, M. *et al.* Detection of the characteristic pion-decay signature in supernova remnants. **Science**, v. 339, n. 6121, p. 807, 2013. DOI: 10.1126/science.1231160.

35 FUNK, S. High-energy gamma rays from supernova remnants. *In:* ALSABTI, A.; MURDIN, P. (ed.). **Handbook of Supernovae.** Cham: Springer, 2017. p. 1737-1750. DOI: 10.1007/978-3-319-21846-5_12.

36 HOOPER, D.; SARKAR, S.; TAYLOR, A. M. The intergalactic propagation of ultrahigh energy cosmic ray nuclei. **Astroparticle Physics**, v. 27, n. 2–3, p. 199–212, 2007. DOI: 10.1016/j.astropartphys.2006.10.008.

37 ALLARD, D. Extragalactic propagation of ultrahigh energy cosmic-rays. **Astroparticle Physics**, v. 39-40, p. 33 – 43, 2012. DOI: 10.1016/j.astropartphys.2011.10.011.

38 ALVES BATISTA, R. **On the cosmological propagation of high energy particles in magnetic fields**. 2015. Ph. D. Thesis (Doctor) - Department of Physics, Faculty of Mathematics, Informatics and Natural Sciences, Universität Hamburg, 2015.

39 GAMOW, G. Expanding universe and the origin of elements. **Physical Review**, v. 70, n. 7–8, p. 572–573, 1946. DOI: 10.1103/PhysRev7.0.572.

40 ALPHER, R. A.; HERMAN, R. Evolution of the Universe. **Nature**, v. 162, n. 4124, p. 774–775, 1948.

41 PENZIAS, A. A.; WILSON, R. W. A measurement of excess antenna temperature at 4080 mc/s. **Astrophysical Journal**, v. 142, p. 419–421, 1965. DOI: 10.1086/148307.

42 FIXSEN, D. J. The temperature of the cosmic microwave background. **Astrophysical Journal**, v. 707, n. 2, p. 916–920, Nov. 2009. DOI: 10.1088/0004-637x/707/2/916.

43 DWEK, E.; KRENNRICH, F. The extragalactic background light and the gamma-ray opacity of the universe. **Astroparticle Physics**, v. 43, p. 112–133, Mar. 2013. DOI: 10.1016/j.astropartphys.2012.09.003.

44 KNEISKE, T. M. *et al.* Implications of cosmological gamma-ray absorption. 2. Modification of gamma-ray spectra. **Astronomy and Astrophysics**, v. 413, p. 807–815, 2004. DOI: 10.1051/0004-6361:20031542.

45 FRANCESCHINI, A.; RODIGHIERO, G.; VACCARI, M. The extragalactic optical-infrared background radiations, their time evolution and the cosmic photon-photon opacity. **Astronomy and Astrophysics**, v. 487, p. 837, 2008. DOI: 10.1051/0004-6361:200809691.

46 FINKE, J. D.; RAZZAQUE, S.; DERMER, C. D. Modeling the extragalactic background light from stars and dust. **Astrophysical Journal**, v. 712, p. 238–249, 2010. DOI: 10.1088/0004-637X/712/1/238.

47 GILMORE, R. C. *et al.* Semi-analytic modeling of the EBL and consequences for extragalactic gamma-ray spectra. **Monthly Notices of the Royal Astronomical Society**, v. 422, p. 3189, 2012. DOI: 10.1111/j.1365-2966.2012.20841.x.

48 DOMINGUEZ, A. *et al.* Extragalactic background light inferred from AEGIS galaxy SED-type fractions. **Monthly Notices of the Royal Astronomical Society**, v. 410, p. 2556, 2011. DOI: 10.1111/j.1365-2966.2010.17631.x.

49 STECKER, F. W.; SCULLY, S. T.; MALKAN, M. A. An empirical determination of the intergalactic background light from UV to FIR wavelengths using FIR deep galaxy surveys and the gamma-ray opacity of the Universe. **Astrophysical Journal**, v. 827, n. 1, p. 6, 2016. [Erratum: Astrophys.J. 863, 112 (2018)] DOI: 10.3847/0004-637X/827/1/6.

50 ANJOS, R. C. **Propagação de raios cósmicos extragaláticos**. 2014. Ph. D. Thesis (Doctor in Science) - Instituto de Física de São Carlos, Universidade de São Paulo, São Carlos, 2014. Available from: https://teses.usp.br/teses/disponiveis/76/76131/tde-18082014-142550/en.php. Accessible at: 8 Dec. 2020.

51 DE ANGELIS, A.; GALANTI, G.; RONCADELLI, M. Transparency of the Universe to gamma rays. **Monthly Notices of the Royal Astronomical Society**, v. 432, p. 3245–3249, 2013. DOI: 10.1093/mnras/stt684.

52 GREISEN, K. End to the cosmic-ray spectrum? **Physical Review Letters**, v. 16, n. 17, p. 748–750, Apr. 1966. DOI: 10.1103/PhysRevLett.16.748.

53 ZATSEPIN, G. T.; KUZMIN, V. A. Upper limit of the spectrum of cosmic rays. **Journal of Experimental and Theoretical Physics Letters**, v. 4, n. 4, p. 78, 1966.

54 ALOISIO, R. *et al.* SimProp v2r4: Monte Carlo simulation code for UHECR propagation. **Journal of Cosmology and Astroparticle Physics**, v. 11, p. 009, 2017. DOI: 10.1088/1475-7516/2017/11/009.

55 ALVES BATISTA, R. *et al.* CRPropa 3 - a public astrophysical simulation framework for propagating extraterrestrial ultra-high energy particles. **Journal of Cosmology and Astroparticle Physics**, v. 05, p. 038, 2016. DOI: 10.1088/1475-7516/2016/05/038.

56 ALVES BATISTA, R. *et al.* Effects of uncertainties in simulations of extragalactic UHECR propagation, using CRPropa and SimProp. **Journal of Cosmology and Astroparticle Physics**, v. 10, p. 063, 2015. DOI: 10.1088/1475-7516/2015/10/063.

57 AAB, A. *et al.* A measurement of the cosmic-ray energy spectrum above 2.5×10^{18} eV using the Pierre Auger Observatory. **Physical Review D**, v. 102, n. 6, p. 062005, 2020. DOI: 10.1103/PhysRevD.102.062005.

58 AAB, A. *et al.* Depth of maximum of air-shower profiles at the Pierre Auger Observatory: measurements at energies above $10^{17.8}$ eV. **Physical Review D**, v. 90, n. 12, p. 122005, 2014. DOI: 10.1103/PhysRevD.90.122005.

59 AAB, A. *et al.* Depth of maximum of air-shower profiles at the Pierre Auger Observatory. II. composition implications. **Physical Review D**, v. 90, n. 12, p. 122006, 2014. DOI: 10.1103/PhysRevD.90.122006.

60 PATRIGNANI, C. *et al.* Review of particle physics. **Chinese Physics C**, v. 40, n. 10, p. 100001, 2016. DOI: 10.1088/1674-1137/40/10/100001.

61 KLAGES, H. *et al.* The Kascade experiment. **Nuclear Physics B:** proceedings supplements, v. 52, n. 3, p. 92 – 102, 1997. DOI: 10.1016/S0920-5632(96)00852-3.

62 APEL, W. *et al.* The KASCADE-Grande experiment. **Nuclear Instruments and Methods in Physics Research Section A:** accelerators, spectrometers, detectors and associated equipment, v. 620, n. 2, p. 202 – 216, 2010. DOI: 10.1016/j.nima.2010.03.147.

63 AAB, A. *et al.* Features of the energy spectrum of cosmic rays above 2.5×10^{18} eV using the Pierre Auger Observatory. **Physical Review Letters**, v. 125, n. 12, p. 121106, 2020. DOI: 10.1103/PhysRevLett.125.121106.

64 KAMPERT, K.-H.; UNGER, M. Measurements of the cosmic ray composition with air shower experiments. **Astroparticle Physics**, v. 35, n. 10, p. 660–678, 2012. DOI: 10.1016/j.astropartphys.2012.02.004.

65 PIEROG, T. *et al.* EPOS LHC: test of collective hadronization with data measured at the CERN Large Hadron Collider. **Physical Review C**, v. 92, n. 3, p. 034906, 2015. DOI: 10.1103/PhysRevC.92.034906.

66 RIEHN, F. *et al.* Hadronic interaction model Sibyll 2.3d and extensive air showers. **Physical Review D**, v. 102, n. 6, p. 063002, 2020. DOI: 10.1103/PhysRevD.102.063002.

67 OSTAPCHENKO, S. QGSJET-II: towards reliable description of very high energy hadronic interactions. **Nuclear Physics B:** proceedings supplements, v. 151, p. 143–146, 2006. DOI: 10.1016/j.nuclphysbps.2005.07.026.

68 YUSHKOV, A. Mass composition of cosmic rays with energies above 1017.2 eV from the hybrid data of the Pierre Auger Observatory. *In:* INTERNATIONAL COSMIC RAY CONFERENCE (ICRC2019), 36., 2019, Madison. **Proceedings**[...]. Madison: ICRC, 2020. p. 482. DOI: 10.22323/1.358.0482.

69 ANTONI, T. *et al.* KASCADE measurements of energy spectra for elemental groups of cosmic rays: Results and open problems. **Astroparticle Physics**, v. 24, p. 1–25, 2005. DOI: 10.1016/j.astropartphys.2005.04.001.

70 APEL, W. *et al.* KASCADE-Grande measurements of energy spectra for elemental groups of cosmic rays. **Astroparticle Physics**, v. 47, p. 54–66, 2013. DOI: 10.1016/j.astropartphys.2013.06.004.

71 APEL, W. *et al.* Kneelike structure in the spectrum of the heavy component of cosmic rays observed with KASCADE-Grande. **Physical Review Letters**, v. 107, p. 171104, 2011. DOI: 10.1103/PhysRevLett.107.171104.

72 APEL, W. *et al.* KASCADE-Grande measurements of energy spectra for elemental groups of cosmic rays. **Astroparticle Physics**, v. 47, p. 54–66, 2013. DOI: 10.1016/j.astropartphys.2013.06.004.

73 BEREZINSKY, V.; GAZIZOV, A.; GRIGORIEVA, S. Dip in UHECR spectrum as signature of proton interaction with CMB. **Physics Letters B**, v. 612, p. 147–153, 2005. DOI: 10.1016/j.physletb.2005.02.058.

74 SOUZA, V. Testing the agreement between the Xmax distributions measured by the Pierre Auger and Telescope Array Observatories. *In:* INTERNATIONAL COSMIC RAY CONFERENCE (ICRC2017), 35., 2017, Bexco, Busan, Korea. **Proceedings**[. . .].Bexco, Busan, Korea: ICRC, 2018. p. 522, 2018. DOI: 10.22323/1.301.0522.

75 GLOBUS, N.; ALLARD, D.; PARIZOT, E. A complete model of the cosmic ray spectrum and composition across the galactic to extragalactic transition. **Physical Review D**, v. 92, n. 2, p. 021302, 2015. DOI: 10.1103/PhysRevD.92.021302.

76 AAB, A. *et al.* Combined fit of spectrum and composition data as measured by the Pierre Auger Observatory. **Journal of Cosmology and Astroparticle Physics**, v. 04, p. 038, 2017. [Erratum: JCAP 03, E02 (2018)] DOI: 10.1088/1475-7516/2017/04/038.

77 AAB, A. *et al.* Observation of a large-scale anisotropy in the arrival directions of cosmic rays above 8×10^{18} eV. **Science**, v. 357, n. 6537, p. 1266–1270, 2017. DOI: 10.1126/science.aan4338.

78 AAB, A. *et al.* Cosmic-ray anisotropies in right ascension measured by the Pierre Auger Observatory. **Astrophysical Journal**, v. 891, p. 142, 2020. DOI: 10.3847/1538-4357/ab7236.

79 AAB, A. *et al.* An indication of anisotropy in arrival directions of ultra-high-energy cosmic rays through comparison to the flux pattern of extragalactic gamma-ray sources. **Astrophysical Journal Letters**, v. 853, n. 2, p. L29, 2018. DOI: 10.3847/2041-8213/aaa66d.

80 PEDREIRA, F. Bounds on diffuse and point source fluxes of ultra-high energy neutrinos with the Pierre Auger Observatory *In:* INTERNATIONAL COSMIC RAY CONFERENCE (ICRC2019), 36., 2019, Madison. **Proceedings**[. . .]. Madison: ICRC, 2019. p. 979, 2020. DOI: 10.22323/1.358.0979.

81 RAUTENBERG, J. Limits on ultra-high energy photons with the Pierre Auger Observatory. *In:* INTERNATIONAL COSMIC RAY CONFERENCE (ICRC2019), 36., 2019, Madison. **Proceedings**[. . .]. Madison: ICRC, 2020. p. 398. DOI: 10.22323/1.358.0398.

82 AAB, A. *et al.* Probing the origin of ultra-high-energy cosmic rays with neutrinos in the EeV energy range using the Pierre Auger Observatory. **Journal of Cosmology and Astroparticle Physics**, v. 10, p. 022, 2019.

83 SAGAWA, H. Telescope Array extension: TAx4. *In:* INTERNATIONAL COSMIC RAY CONFERENCE (ICRC2015), 34., 2015, Hague, Netherlands. **Proceedings**[. . .].Hague, Netherlands: ICRC, 2016. p. 657. DOI: 10.22323/1.236.0657.

84 ABREU, P. *et al.* Antennas for the detection of radio emission pulses from cosmic-ray induced air showers at the Pierre Auger Observatory. **Journal of Instrumentation**, IOP Publishing, v. 7, n. 10, p. P10011–P10011, Oct. 2012. DOI: 10.1088/1748-0221/7/10/p10011.

85 CASTELLINA, A. AugerPrime: the Pierre Auger Observatory Upgrade. **EPJ Web of Conferences**, v. 210, p. 06002, 2019. DOI: 10.1051/epjconf/201921006002.

86 ÁLVAREZ-MUÑIZ, J. *et al.* The Giant Radio Array for Neutrino Detection (GRAND): science and design. **Science China Physics, Mechanics Astronomy**, v. 63, n. 1, p. 219501, 2020. DOI: 10.1007/s11433-018-9385-7.

87 OLINTO, A. V. et al. POEMMA: probe of extreme multi-messenger astrophysics. *In:* INTERNATIONAL COSMIC RAY CONFERENCE (ICRC2017), 35., 2017. Bexco, Busan, Korea. **Proceedings**[. . .]. Bexco, Busan, Korea: ICRC, 2018. p. 542. DOI: 10.22323/1.301.0542.

88 BITEAU, J.; WILLIAMS, D. A. The extragalactic background light, the Hubble constant, and anomalies: conclusions from 20 years of TeV gamma-ray observations. **Astrophysical Journal**, v. 812, n. 1, p. 60, 2015. DOI: 10.1088/0004-637X/812/1/60.

89 NAUROIS, M.; MAZIN, D. Ground-based detectors in very-high-energy gamma-ray astronomy. **Comptes Rendus Physique**, v. 16, p. 610–627, 2015. DOI: 10.1016/j.crhy.2015.08.011.

90 OHM, S.; ELDIK, C. van; EGBERTS, K. γ/hadron separation in very-high-energy -ray astronomy using a multivariate analysis method. **Astroparticle Physics**, v. 31, n. 5, p. 383–391, June 2009. DOI: 10.1016/j.astropartphys.2009.04.001.

91 FUNK, S. Ground- and space-based gamma-ray astronomy. **Annual Review of Nuclear and Particle Science**, v. 65, p. 245–277, 2015. DOI: 10.1146/annurev-nucl-102014-022036.

92 COLLADAY, D.; KOSTELECKY, V. Lorentz violating extension of the standard model. **Physical Review D**, v. 58, p. 116002, 1998. DOI: 10.1103/PhysRevD.58.116002.

93 ALFARO, J. Quantum gravity and Lorentz invariance deformation in the standard model. **Physical Review Letters**, v. 94, p. 221302, 2005. DOI: 10.1103/PhysRevLett.94.221302.

94 MATTINGLY, D. Modern tests of Lorentz invariance. **Living Reviews in Relativity**, v. 8, p. 1–78, 2005. DOI: 10.12942/lrr-2005-5.

95 BLUHM, R. Observational constraints on local Lorentz invariance. *In:* ASHTEKAR, A.; PETKOV, V .(ed.). **Springer handbook of spacetime**. Berlin: Springer, 2014. p. 485–507. DOI: 10.1007/978-3-642-41992-$8_2$3.

96 COLEMAN, S.; GLASHOW, S. L. High-energy tests of Lorentz invariance. **Physical Review D**, v. 59, n. 11, p. 116008, 1999. DOI: 10.1103/PhysRevD.59.116008.

97 JACOBSON, T.; LIBERATI, S.; MATTINGLY, D. Threshold effects and Planck scale Lorentz violation: combined constraints from high-energy astrophysics. **Physical Review D**, v. 67, p. 124011, 2003. DOI: 10.1103/PhysRevD.67.124011.

98 SARKAR, S. Possible astrophysical probes of quantum gravity. **Modern Physics Letters A**, v. 17, p. 1025–1036, 2002. DOI: 10.1142/S0217732302007521.

99 KOSTELECKY, V.; RUSSELL, N. Data tables for Lorentz and CPT violation. **Reviews of Modern Physics**, v. 83, p. 11–31, 2011. DOI: 10.1103/RevModPhys.83.11.

100 VASILEIOU, V. *et al.* Constraints on Lorentz invariance violation from Fermi-Large Area Telescope observations of gamma-Ray bursts. **Physical Review D**, D87, n. 12, p. 122001, 2013. DOI: 10.1103/PhysRevD.87.122001.

101 ACCIARI, V. *et al.* Bounds on Lorentz invariance violation from MAGIC observation of GRB 190114C. **Physical Review Letters**, v. 125, n. 2, p. 021301, 2020. DOI: 10.1103/PhysRevLett.125.021301.

102 MARTíNEZ-HUERTA, H.; PéREZ-LORENZANA, A. Restrictions from Lorentz invariance violation on cosmic ray propagation. **Physical Review D**, v. 95, n. 6, p. 063001, 2017. DOI: 10.1103/PhysRevD.95.063001.

103 MARTÍNEZ-HUERTA, H. *et al.* Constraints on Lorentz invariance violation using HAWC observations above 100 TeV. *In:* **INTERNATIONAL COSMIC RAY CONFERENCE (ICRC2019)**, 36., 2019. Madison. **Proceedings** [. . .]. Madison: ICRC, 2020.

104 ALBERT, A. *et al.* Constraints on Lorentz invariance violation from HAWC observations of gamma rays above 100 TeV. **Physical Review Letters**, v. 124, p. 131101, 2020. DOI: 10.1103/PhysRevLett.124.131101.

105 RUBTSOV, G.; SATUNIN, P.; SIBIRYAKOV, S. Constraints on violation of Lorentz invariance from atmospheric showers initiated by multi-TeV photons. **Journal of Cosmology and Astroparticle Physics**, v. 1705, n. 05, p. 049, 2017. DOI: 10.1088/1475-7516/2017/05/049.

106 SATUNIN, P. New constraints on Lorentz Invariance violation from Crab Nebula spectrum beyond 100 TeV. **European Physical Journal C**, v. 79, n. 12, p. 1011, 2019. DOI: 10.1140/epjc/s10052-019-7520-y.

107 STECKER, F. W.; SCULLY, S. T. Lorentz invariance violation and the spectrum and source power of ultrahigh energy cosmic rays. **Astroparticle Physics**, v. 23, p. 203–209, 2005. DOI: 10.1016/j.astropartphys.2005.01.001.

108 GALAVERNI, M.; SIGL, G. Lorentz violation in the photon sector and ultra-high energy cosmic rays. **Physical Review Letters**, v. 100, p. 021102, 2008. DOI: 10.1103/PhysRevLett.100.021102.

109 GALAVERNI, M.; SIGL, G. Lorentz violation and ultrahigh-energy photons. **Physical Review D**, v. 78, p. 063003, 2008. DOI: 10.1103/PhysRevD.78.063003.

110 STECKER, F. W.; SCULLY, S. T. Searching for new physics with ultrahigh energy cosmic rays. **New Journal of Physics**, v. 11, p. 085003, 2009. DOI: 10.1088/1367-2630/11/8/085003.

111 COLOGNA, G. *et al.* The exceptional flare of Mrk 501 in 2014: combined observations with H.E.S.S. and FACT. **AIP Conference Proceedings**, v. 1792, n. 1, p. 050019, 2017. DOI: 10.1063/1.4968965.

112 LANG, R. G. Testing Lorentz invariance violation at the Pierre Auger Observatory. *In:* INTERNATIONAL COSMIC RAY CONFERENCE (ICRC2019), 36., 2019, Madison. **Proceedings**[. . .]. Madison: ICRC, 2020. p. 327, 2020. DOI: 10.22323/1.358.0327.

113 ABDALLA, H. *et al.* **Sensitivity of the Cherenkov Telescope Array for probing cosmology and fundamental physics with gamma-ray propagation**. Oct. 2020. Available from: https://arxiv.org/abs/2010.01349. Accessible at: 8 Dec. 2020.

114 BI, X.-J. *et al.* Testing Lorentz invariance with ultra high energy cosmic ray spectrum. **Physical Review D**, v. 79, p. 083015, 2009. DOI: 10.1103/PhysRevD.79.083015.

115 MACCIONE, L. *et al.* Planck-scale Lorentz violation constrained by Ultra-High-Energy Cosmic Rays. **Journal of Cosmology and Astroparticle Physics**, v. 04, p. 022, 2009. DOI: 10.1088/1475-7516/2009/04/022.

116 LANG, R. G. **Effects of Lorentz Invariance Violation on the ultra-high energy cosmic rays spectrum**. 2017. Dissertation (Master in Science) - Instituto de Física de São Carlos, Universidade de São Paulo, São Carlos, 2017. Available from https://teses.usp.br/teses/disponiveis/76/76131/tde-13042017-143220/en.php. Accessible at: 8 Dec. 2020.

117 PUGET, J.; STECKER, F.; BREDEKAMP, J. Photonuclear interactions of ultrahigh-energy cosmic rays and their astrophysical consequences. **Astrophysical Journal**, v. 205, p. 638–654, 1976. DOI: 10.1086/154321.

118 STECKER, F.; SALAMON, M. Photodisintegration of ultrahigh-energy cosmic rays: a new determination. **Astrophysical Journal**, v. 512, p. 521–526, 1999. DOI: 10.1086/306816.

119 KONING, A. J. *et al.* TALYS 1.0. *In:* INTERNATIONAL CONFERENCE ON NUCLEAR DATA FOR SCIENCE AND TECHNOLOGY, 2007. **Proceedings**[...]. Paris: EDP Science, 2008. p. 211–214. Available from: https://nd2007.edpsciences.org/articles/ndata/pdf/2007/01/ndata07767.pdf. Accessible at: 8 Dec. 2020.

120 VERZI, V. Measurement of the energy spectrum of ultra-high energy cosmic rays using the Pierre Auger Observatory. *In:* INTERNATIONAL COSMIC RAY CONFERENCE (ICRC2019), 36., 2019, Madison. **Proceedings**[. . .]. Madison: ICRC, 2020. p. 450.

121 DE DOMENICO, M. *et al.* Reinterpreting the development of extensive air showers initiated by nuclei and photons. **Journal of Cosmology and Astroparticle Physics**, v. 07, p. 050, 2013. DOI: 10.1088/1475-7516/2013/07/050.

122 UNGER, M.; FARRAR, G. R.; ANCHORDOQUI, L. A. Origin of the ankle in the ultrahigh energy cosmic ray spectrum, and of the extragalactic protons below it. **Physical Review D**, v. 92, n. 12, p. 123001, 2015. DOI: 10.1103/PhysRevD.92.123001.

123 MUZIO, M. S.; UNGER, M.; FARRAR, G. R. Progress towards characterizing ultrahigh energy cosmic ray sources. **Physical Review D**, v. 100, n. 10, p. 103008, 2019. DOI: 10.1103/PhysRevD.100.103008.

124 BIERMANN, P. L.; SOUZA, V. de. Centaurus A: the extragalactic source of cosmic rays with energies above the knee. **Astrophysical Journal**, American Astronomical Society, v. 746, n. 1, p. 72, Jan. 2012. DOI: 10.1088/0004-637x/746/1/72.

125 MOLLERACH, S.; ROULET, E. Ultrahigh energy cosmic rays from a nearby extragalactic source in the diffusive regime. **Physical Review D**, v. 99, n. 10, p. 103010, 2019. DOI: 10.1103/PhysRevD.99.103010.

126 TAYLOR, A. M.; AHLERS, M.; AHARONIAN, F. A. The need for a local source of UHE CR nuclei. **Physical Review D**, v. 84, p. 105007, 2011. DOI: 10.1103/PhysRevD.84.105007.

127 MATTEO, A. et al. Full-sky searches for anisotropies in UHECR arrival directions with the Pierre Auger Observatory and the Telescope Array. *In:* INTERNATIONAL COSMIC RAY CONFERENCE (ICRC2019), 36., 2019, Madison. **Proceedings**[...]. Madison: ICRC, 2020. p. 439. DOI: 10.22323/1.358.0439.

128 HARARI, D.; MOLLERACH, S.; ROULET, E. Anisotropies of ultrahigh energy cosmic rays diffusing from extragalactic sources. **Physical Review D**, v. 89, n. 12, p. 123001, 2014. DOI: 10.1103/PhysRevD.89.123001.

129 HARARI, D.; MOLLERACH, S.; ROULET, E. Anisotropies of ultrahigh energy cosmic ray nuclei diffusing from extragalactic sources. **Physical Review D**, v. 92, n. 6, p. 063014, 2015. DOI: 10.1103/PhysRevD.92.063014.

130 GLOBUS, N.; PIRAN, T. The extragalactic ultra-high energy cosmic-ray dipole. **Astrophysical Journal Letters**, v. 850, n. 2, p. L25, 2017. DOI: 10.3847/2041-8213/aa991b.

131 DUNDOVIĆ, A.; SIGL, G. Anisotropies of ultra-high energy cosmic rays dominated by a single source in the presence of deflections. **Journal of Cosmology and Astroparticle Physics**, v. 01, p. 018, 2019. DOI: 10.1088/1475-7516/2019/01/018.

132 MOLLERACH, S.; ROULET, E. Extragalactic cosmic rays diffusing from two populations of sources. **Physical Review D**, v. 101, n. 10, p. 103024, 2020. DOI: 10.1103/PhysRevD.101.103024.

133 ABREU, P. *et al.* **The Southern Wide-Field Gamma-Ray Observatory (SWGO): a next-generation ground-based survey instrument for VHE gamma-ray astronomy**. July 2019. Available from: https://arxiv.org/abs/1907.07737. Accessible at: 8 Dec. 2020.